

Advancing single-molecule instrumentation through nanoscale optics, fabrication, and surface functionalization

Ha, Seungkyu

DOI

[10.4233/uuid:addc45be-225e-4a52-acb6-59b3c967deb1](https://doi.org/10.4233/uuid:addc45be-225e-4a52-acb6-59b3c967deb1)

Publication date

2018

Document Version

Final published version

Citation (APA)

Ha, S. (2018). *Advancing single-molecule instrumentation through nanoscale optics, fabrication, and surface functionalization*. [Dissertation (TU Delft), Delft University of Technology].
<https://doi.org/10.4233/uuid:addc45be-225e-4a52-acb6-59b3c967deb1>

Important note

To cite this publication, please use the final published version (if applicable).
Please check the document version above.

Copyright

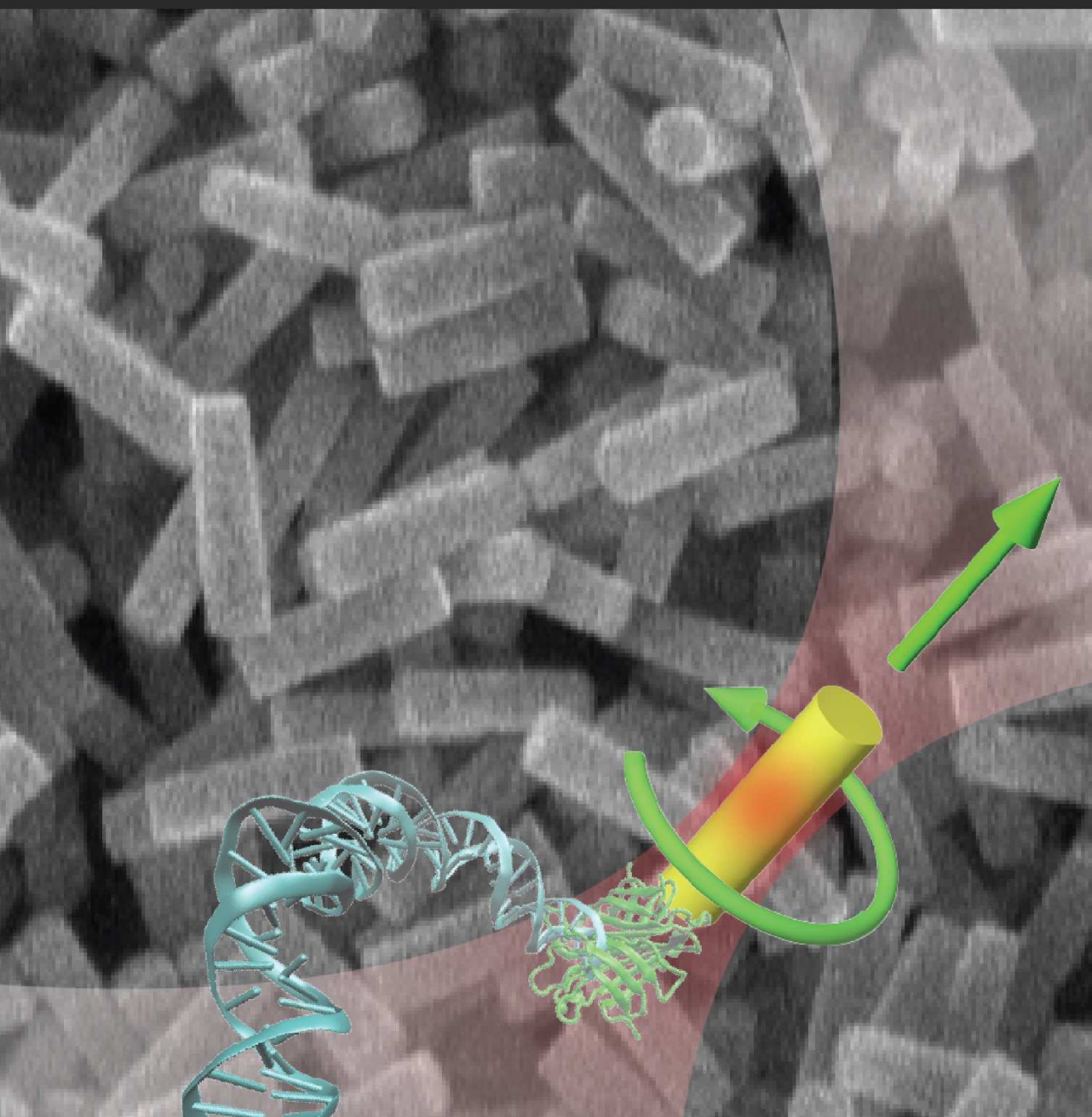
Other than for strictly personal use, it is not permitted to download, forward or distribute the text or part of it, without the consent of the author(s) and/or copyright holder(s), unless the work is under an open content license such as Creative Commons.

Takedown policy

Please contact us and provide details if you believe this document breaches copyrights.
We will remove access to the work immediately and investigate your claim.

Advancing Single-Molecule Instrumentation through Nanoscale Optics, Fabrication, and Surface Functionalization

Seungkyu Ha



**Advancing Single-Molecule Instrumentation
through Nanoscale Optics, Fabrication,
and Surface Functionalization**

**Advancing Single-Molecule Instrumentation
through Nanoscale Optics, Fabrication,
and Surface Functionalization**

Dissertation

for the purpose of obtaining the degree of doctor
at Delft University of Technology

by the authority of the Rector Magnificus Prof. dr. ir. T. H. J. J. van der Hagen
chair of the Board for Doctorates

to be defended publicly on
Tuesday 16 October 2018 at 12:30 hours

by

Seungkyu HA

Master of Science in Electrical Engineering and Computer Science,
Seoul National University, Korea
born in Ulsan, Korea

This dissertation has been approved by the promotor.

Composition of the doctoral committee:

Rector Magnificus chairperson
Prof. dr. N. H. Dekker Delft University of Technology, promotor

Independent members:

Prof. dr. P. H. Jones University College London, United Kingdom
Prof. dr. M. Rief Technische Universität München, Germany
Prof. dr. ir. S. J. Tans Delft University of Technology
Dr. F. Pedaci Centre de Biochimie Structurale de Montpellier, France
Dr. D. G. G. McMillan Delft University of Technology
Prof. dr. M. Dogterom Delft University of Technology, reserve member

Other members:

Dr. A. J. L. Adam Delft University of Technology



Keywords: biophysics, single-molecule, nano-optics, nanofabrication, surface functionalization, optical tweezers, optical torque wrench, DNA nanocurtain, fluorescence microscopy

Copyright © 2018 by Seungkyu Ha

Printed by: Ipskamp Printing, Enschede

Casimir PhD series 2018-37

ISBN 978-90-8593-367-0

An electronic copy of this dissertation is available at: <http://repository.tudelft.nl>

Contents

1. Introduction	1
1.1. Single-molecule biophysics	2
1.2. Single-molecule instrumentation	3
1.3. Guide to the contents of thesis	5
1.4. References	7
2. Optical Torque Wrench, Nanofabrication, and Surface Functionalization	11
2.1. Optical torque wrench	12
2.1.1. Optical angular momentum transfer	12
2.1.2. Configuration of the OTW setup	13
2.1.3. Torque and force calibrations in the OTW	15
2.1.4. Numerical modeling of force, torque, and drag	16
2.2. Nanofabrication and surface functionalization	17
2.2.1. Lithography	17
2.2.2. Etching	18
2.2.3. Surface functionalization	18
2.3. References	19
3. Tunable Top-Down Fabrication and Functional Surface Coating of Single-Crystal Titanium Dioxide Nanostructures and Nanoparticles	21
3.1. Introduction	22
3.2. Results and discussion	24
3.2.1. Selecting an etch mask for the plasma etching of single-crystal TiO ₂	24
3.2.2. Trifluoromethane (CHF ₃)-based plasma etching of single-crystal TiO ₂ nanocylinders	24
3.2.3. Sulfur hexafluoride (SF ₆)-based plasma etching of single-crystal TiO ₂ nanocylinders	26
3.2.4. Quantification of single-crystal TiO ₂ nanocylinder uniformity	27
3.2.5. Surface functionalization and bioconjugation of single-crystal TiO ₂	29
3.2.6. Degree of monodispersity in coated single-crystal TiO ₂ nanoparticles	31
3.2.7. Characterization of individual DNA molecules using single-crystal TiO ₂ nanocylinders	32
3.3. Conclusions	33
3.4. Methods	34
3.4.1. Fabrication and bioconjugation of single-crystal rutile TiO ₂ nanocylinders for OTW experiments	34
3.5. References	36
3.6. Supplementary Information	38

3.6.1. Supplementary Methods	38
3.6.1.1. Orientation of the optic axis in single-crystal rutile TiO ₂ nanocylinder for OTW experiment	38
3.6.1.2. Considerations for optimal fabrication of the Cr etch mask for single-crystal TiO ₂ etching	38
3.6.1.3. Surface functionalization procedure of single-crystal TiO ₂	39
3.6.1.4. Evaluation of single-crystal TiO ₂ surface functionalization efficiency via fluorescence microscopy	39
3.6.1.5. Preparation of DNA construct for OTW experiments	40
3.6.1.6. Preparation of flow cell for OTW experiments	40
3.6.1.7. Bioconjugation of DNA to single-crystal TiO ₂ nanocylinders for OTW experiments	41
3.6.1.8. OTW instrumentation and DNA measurements with single-crystal TiO ₂ nanocylinders	42
3.6.2. Supplementary Tables	43
3.6.3. Supplementary Figures	46
3.6.4. Supplementary References	56
4. Enhanced Linear and Angular Optical Trapping Using Single-Crystal Rutile TiO₂ Nanocylinders	57
4.1. Introduction	58
4.2. Results and Discussion	59
4.2.1. Optimization of rutile TiO ₂ particle geometry	59
4.2.1.1. Large birefringence for optimal angular momentum transfer	60
4.2.1.2. Large refractive index for enhanced linear momentum transfer	61
4.2.1.3. Cylindrical shape for stable 3D trapping	62
4.2.2. Linear and angular trapping of TiO ₂ nanoparticles	63
4.2.2.1. Dimensions of rutile TiO ₂ nanocylinders trappable in 3D	63
4.2.2.2. Rutile TiO ₂ nanocylinders optimized for high stiffness, low drag, and rapid response time	65
4.2.2.3. Rutile TiO ₂ nanocylinders transmit nN forces and nN-nm torques with excellent measurement precision	67
4.3. Conclusions	69
4.4. Methods	70
4.4.1. Fabrication and surface functionalization of rutile TiO ₂ nanocylinders	70
4.4.2. OTW setup and measurements	71
4.4.3. Numerical calculation of optical momentum transfer and hydrodynamic drag	72
4.5. References	73
4.6. Supplementary Information	76
4.6.1. Derivation of the analytical equation for optical torque transfer from a linearly polarized plane wave to an infinitely wide birefringent plate with uniform thickness	76
4.6.2. Supplementary Figures	78

4.6.3. Supplementary Tables	93
4.6.4. Supplementary References	96
5. Quantifying the Precision of Single-Molecule Torque and Twist Measurements Using Allan Variance	97
5.1. Introduction	98
5.2. Materials and Methods	98
5.2.1. Definition and properties of the Allan deviation	98
5.2.2. Computation of the Allan variance	99
5.2.3. Analytic expression for the Allan variance of a Brownian particle in a harmonic trap	100
5.2.4. Stochastic simulations of rotational motion	101
5.2.5. Allan deviation measurements with magnetic tweezers	101
5.2.6. Allan deviation measurements with optical tweezers	102
5.3. Results	102
5.3.1. Allan deviation analysis of simulated traces	103
5.3.2. Angle and torque precision in the MTT	104
5.3.3. Angle and torque precision in the eMTT at different fields	107
5.3.4. Angle and torque precision in eMTT for different bead sizes	109
5.3.5. Angle and torque measurements in the OTW	109
5.4. Discussion	111
5.5. References	113
5.6. Supplementary Information	115
5.6.1. Comparison of magnetic tweezers and optical tweezers in applying Allan variance	115
5.6.2. The effect of noise correlation in Allan variance	116
5.6.2.1. Independence of the difference between consecutive samples at a single integration time	116
5.6.2.2. Independence of the Allan variance at different integration times	117
5.6.3. The shape factor used for MLE fitting of Allan variance data	117
5.6.4. Matlab routine for angular Langevin dynamics simulation	118
5.6.5. Comparison of Allan variance to other variances	118
5.6.6. Comparison of Allan variance to power spectrum analysis	119
5.6.7. Rotational drag coefficient of a bead on a circular trajectory	120
5.6.8. Supplementary Figures	121
5.6.9. Supplementary References	132
6. Stretched and Oriented DNA Arrays Embedded in Microfluidic Device for Multiplexing Protein-DNA Investigation	133
6.1. Introduction	134
6.2. Results and discussion	136
6.2.1. Fabrication of nanoscale gold barrier and anchor array on glass coverslip	136
6.2.2. Fabrication of PDMS-based microfluidic device	138
6.2.3. Chemical functionalization of glass coverslip and gold nanostructures	140

6.2.4. Optimization of gold nanobarrier size for loading of single DNA molecules	142
6.2.5. Protein-DNA interaction observed by SODA microfluidic devices	143
6.3. Conclusions	145
6.4. Materials and Methods	146
6.4.1. Fabrication of SODA devices	146
6.4.1.1. Nanofabrication of gold nanostructures	146
6.4.1.2. Microfabrication of Si mold for PDMS block	147
6.4.1.3. Fabrication of PDMS microfluidic device	148
6.4.2. Surface coatings and bioassay for experiments with SODA devices	148
6.4.2.1. Surface functionalization	148
6.4.2.2. Bioassay preparation	149
6.4.2.3. Experiments with SODA devices	149
6.5. References	150
6.6. Supplementary Information	153
6.6.1. Supplementary Figures	153
7. Conclusions and Recommendations	161
7.1. Current research outcomes	162
7.1.1. Single-crystal rutile TiO ₂ probes for the optical torque wrench.....	162
7.1.2. Stretched and oriented DNA arrays	163
7.2. Suggestions for further development	164
7.2.1. Utilization of the various shapes of nanoparticle probes	164
7.2.2. Alternative routes for cleaving single-crystal nanocylinders	165
7.2.3. Mass fabrication of nanoparticle probes for OTW	165
7.2.4. Highly birefringent nanoparticles from the substrates of (001) orientation	166
7.2.5. Highly birefringent nanorods made from tailored metamaterials	167
7.2.6. Position and tilt calibration of nanocylinders in an OTW	169
7.2.7. Solid-state implementation of the optical torque wrench	169
7.2.8. More accessible stretched and oriented DNA arrays	170
7.3. References	171
Summary	173
Samenvatting	177
Curriculum Vitae	181
List of Publications	183

1

Introduction

This thesis is dedicated to the development of nanoscale tools to facilitate research in the field of single-molecule biophysics, using a combination of nanoscale optics, fabrication, and surface functionalization. This allows enhanced access to the features of biological molecules at the nanoscale, in particular molecular machines, at the corresponding timescales. Here, the framework and context of the research themes presented in this thesis are described. The main research project consists of the development of optically trappable and rotatable single-crystal rutile TiO₂ nanoparticle probes for accurate measurement and manipulation of force and torque of single biomolecules such as nucleic acids and proteins. A secondary research project is development of nanopatterned and chemically functionalized glass coverslips for an improved microfluidics platform to investigate individual protein-DNA interactions using high-throughput fluorescence microscopy. In this chapter, the research field of biophysics is introduced, followed by an overview showing how novel developments in single-molecule instrumentation have provided innovative methodologies to study biomolecules and biological motors. Then, the contents of this thesis are summarized in a concise manner.

1.1. Single-molecule biophysics

Only within a half-century, there has been an exponential growth in the understanding of life by human beings, for example, from discovery of DNA structure in 1953¹ to the sequencing of an entire human genome in 2003². The discovery of nucleic acids (i.e., DNA and RNA) as the information carriers in all forms of life, has played a crucial role. Such discovery was partially inspired by the pioneering work of Erwin Schrödinger, a physicist who tried to answer the long-standing question of humankind – “*What is life?*” – from the viewpoint of physics³. For example, his work influenced Watson, Crick, Wilkins, and Franklin, the main contributors to the discovery of the double-helical structure of DNA, a landmark finding from which the field of molecular biology developed⁴. Needless to say, this, and all other following key biological discoveries are indebted to the precise understanding of (bio)molecules and their chemical interactions based on the atomic and quantum theories in physics established at the early 20th century. The advent of modern biology therefore can be viewed as the outcome of a continuous process of interaction between biology, chemistry, and physics, exhibiting an interdisciplinary nature.

For the past decades, there have been efforts to understand biology in a more quantitative manner, as opposed to descriptions of a more qualitative nature. Such efforts have included investigations of behavior at the single-cell or single-molecule level, as opposed to the averaged behavior that necessarily derives from bulk observations. This trend has been possible through the active incorporation of tools and concepts from physics⁵, which have led to the development and application of diverse novel approaches such as atomic force microscopy (AFM)⁶, single-molecule fluorescence resonance energy transfer (smFRET)⁷, super-resolution microscopy^{8, 9}, cryo-electron microscopy (cryo-EM)^{10, 11}, optical tweezers (OT)^{12, 13}, and magnetic tweezers (MT)¹⁴. The large impact of these novel techniques has also been widely recognized by the Nobel prizes awarded, e.g., AFM in 1986, super-resolution microscopy in 2014, and optical tweezers in 2018. This approach is collectively recognized as “*biophysics*” and has been growing rapidly. Within this line of research, the ability to manipulate and observe single (bio)molecules has achieved many important discoveries and expanded our understandings of life. Such findings have complemented, and hence also enhanced, the discoveries made *via* standard ensemble techniques in which precise molecular mechanisms are obscured by the collective behavior of numerous biomolecules¹⁵.

Single-molecule methodologies can address three broad categories of research: i) physical properties of single biomolecules themselves, ii) dynamics of interactions between different biomolecules, and iii) working mechanism of sophisticated linear and rotary biomotors. The first category has revealed interesting mechanics and spatiotemporal behaviors of the basic building blocks of life, including stretching/twisting of single nucleic acid molecules¹⁶⁻¹⁹ and folding/unfolding of single proteins^{20, 21}. The efforts in the second category have been answering about questions for how diverse building blocks of life interact to maintain the key cellular processes within the frame of the central dogma of biology²², i.e., transcription, translation, and replication. They include, for example, the base-pair stepping

dynamics of RNA polymerase²³, DNA coiling by topoisomerase²⁴, DNA homologous recombination²⁵, ClpXP-mediated protein unfolding²⁶, target search of RNA-guided endonuclease²⁷, and DNA loop extrusion by condensin²⁸. Research in the third category has elucidated the functioning of many sorts of sophisticated biological nano-machines that are strikingly similar yet very different to the machines made by modern technology of humankind, for example, the linear motion of motor proteins such as myosin²⁹, the rotary motion of large protein complexes including F₁-ATPase³⁰, and the *Escherichia coli* (*E. coli*) bacterial flagellar motor³¹. These discoveries could have not been possible without using the single-molecule instruments which are specifically designed for each target biological system under investigation, as detailed in the following section.

1.2. Single-molecule instrumentation

The focus of single-molecule biophysics lies in elucidating the diverse biological processes that occur inside cells, either *in vivo* or *in vitro*. To study the behavior of sophisticated biological nanomachines including genome processing proteins and molecular motors, it is required to use appropriate tools to access features ranging from sizes of small biomolecules (~nm) to cells (~ μm)³². Simultaneously, in this size regime, the temporal scale of biological processes spans from catalytic rates of fast enzymes (from ~ns to ~ μs)³³ to folding times of large proteins (~s)³⁴, necessitating the comparable temporal resolutions for such tools. These requirements are order(s)-of-magnitude smaller for length scales and faster for time scales than those of daily equipment such as rulers (~mm) and clocks (~s).

Fortunately, the achievements in scientific research and technological development over the last century have allowed the design of such instruments. For example, the discovery of photo-electron effect in quantum physics spurred the development of photodetectors, and in combination with advanced microelectronics and computers, modern fast photo-diodes can record signals with bandwidths ranging from kHz to GHz, suitable for recording the fast dynamics of single molecules. There exist many more such examples including the fast charge-coupled device (CCD) or complementary metal-oxide-semiconductor (CMOS) cameras, piezo-driven high-precision translational stages, stable high-power lasers with different wavelengths, and improved optics such as high numerical aperture (NA) objective lens for improved imaging and optical trapping. Moreover, methodologies for more precise characterizations of instrumental measurement precision and temporal resolution have been developed, e.g., power spectral density³⁵ and Allan deviation analysis³⁶.

The most commonly employed single-molecule techniques can be broadly classified as the following: i) *tweezers* techniques that allow detection and manipulation of force and torque in biomolecules, thereby functioning as sensors and actuators. This classification includes optical tweezers (OT), optical torque wrench (OTW)³⁷, atomic force microscopy (AFM), magnetic tweezers (MT), (electro-)magnetic torque tweezers (MTT)^{38,39}, acoustic force spectroscopy (AFS)⁴⁰, and centrifugal force microscopy (CFM)⁴¹. Notably, the development of techniques such as OTW and MTT that enable measurements of torque and rotation are relatively recent compared to other force-based techniques and require further

development for their wide-spread use. In particular, MT, MTT, AFS, and CFM are developed for high throughput measurement capacity, which remains a limitation for OT, OTW, and AFM; ii) *imaging* techniques which allow spatial observation of biological structures or biomolecular interactions, including conventional fluorescence microscopy⁴², single-molecule fluorescence resonance energy transfer (smFRET), super-resolution microscopy, and cryogenic electron microscopy (cryo-EM). Particularly, the fluorescence-based techniques are advantageous in the aspect that different biomolecules can be readily distinguished by using diverse dyes; iii) *hybrid* techniques which combine the functionalities of both tweezing and imaging, such as OT combined with fluorescence microscopy⁴³, hydrodynamic force-based trapping and stretching⁴⁴, and DNA nanocurtains^{45,46}. These are capable of direct visualization of biomolecules, however, only DNA nanocurtains allow for high-throughput measurement at the expense of the precision in force control (force is applied to many biomolecules simultaneously in a less controlled manner, mostly through hydrodynamic drag in flowing buffer).

For implementation of single-molecule instrumentation, key enabling scientific principles and technologies include optics, fabrication, and surface functionalization at the nanoscale, especially for the instruments studied in this thesis, i.e., the OTW and DNA nanocurtains. The principles of nano-optics provides a versatile, relatively non-invasive means to manipulate and observe biomolecules. In both OT and OTW, a tightly focused laser beam of near-infrared wavelength (typically 1064 nm) allows contact-free application of force and torque on nanoparticles linked to biomolecules in aqueous solutions, while minimizing photodamage and attendant heating⁴⁷ due to relatively little absorption by water. In the OTW, torque application is enabled by controlling nanoscale angular momentum transfer through sophisticated management of trapping beam polarization status. In the case of imaging techniques, fluorescence imaging of single biomolecules labeled with different dyes⁴⁸ or nanoparticles⁴⁹ that emit in the visible wavelength regime allows for real-time observation of biomolecule dynamics and interactions. Diverse optical layouts have been devised to enhance imaging under particular conditions. For example, in total internal reflection fluorescence (TIRF) microscopy⁵⁰, an evanescent wave generated by total internal reflection allows a very limited excitation volume that permits higher signal-to-noise ratio which is advantageous in single-molecule studies using DNA nanocurtains or smFRET. Another such example is two-photon fluorescence microscopy (TPM)⁵¹, in which a non-linear optical effect is exploited to enable high-resolution imaging within a highly scattering medium such as deep tissue and brain. Also, various super-resolution microscopy techniques overcome the light diffraction barrier of the conventional microscopy and provide unprecedented resolutions in optical imaging⁹. Overall, all these optical phenomena have been devised, characterized, and applied in the frame of nano-optics⁵². Notably, nanoscale light-matter interactions can be analytically complex, or defy analytical solution entirely, and hence numerical modeling can help to better understand and estimate such phenomena. For example, numerical calculations have aided in estimating the optical trapping behaviors of rutile TiO₂ nanoparticles in this thesis.

Nanofabrication processes make it possible to access the size scale ranging from nanometers to microns, which overlaps with the scale observed in biology, i.e., from simple molecules to cells. For different target applications, specifically designed micro- and nanoscale features, e.g., shapes, dimensions, and material properties, can be realized through nanofabrication. Particularly in optical trapping-based techniques, nanofabricated dielectric or metallic particles can serve as nanoscale probes for the investigation of single molecules^{44,53,54}, cells^{55,56}, or local environments such as the surrounding medium^{57,58} or the substrate surface⁵⁹. It is noteworthy that specific nanoparticles with well-controlled anisotropy (in either shape or material) are required to apply and detect torques. Meanwhile, nanostructure arrays fabricated on the surface of glass, polymer, or semiconductor substrates, can provide alternative experimental platforms to investigate single biomolecules²⁷ and cells⁶⁰ in imaging-based techniques exemplified by DNA nanocurtains, DNA microarrays⁶¹, and nanopillar arrays⁶². Nanofabrication is also indispensable for other single-molecule techniques that do not directly rely on optical principles, e.g., extremely sharp tips (radius of curvature < 10 nm) on micro-cantilevers of AFM and miniaturized piezo elements of AFS.

Surface functionalization can function as a glue between biomolecules and the surface of nanofabricated particles or structures for sensing and manipulation. In OT and OTW, single biomolecules are too small to be stably trapped and manipulated as they are. Therefore, their trapping becomes possible in an indirect manner by attaching "handles" (i.e., larger micro- or nanoscale particles suitable for trapping) to them. As an example, the surface of oxide particles (e.g., SiO₂ or TiO₂) can be functionalized with silane linkers to attach diverse biomolecules such as DNA strands or proteins through chemically stable bonds⁶³. Importantly, there should be at least two or more attachment points at the interface of a handle and a single-molecule to form a torsionally constrained linkage that allows for application of torques. In case of DNA nanocurtains, single DNA molecules need to be also confined on the surface of a glass substrate to be imaged by TIRF microscopy. For this purpose, the glass substrate is coated by a supported lipid bilayer while a small fraction of lipids are linked to single DNA molecules. Such two-dimensionally confined DNA molecules can be eventually immobilized at desired positions by attaching them to nanofabricated gold structures *via* thiol-based chemistry. For reliable experimentation, it is also frequently crucial to perform surface passivation, in which surfaces are additionally treated to prevent aspecific attachment of biomolecules or undesirable aggregation of nanoparticles. It is noteworthy that nanofabrication processes should be adapted or optimized for each nanoparticle/nanostructure-coating strategy to provide both clean and compatible surfaces to the chemicals used during functionalization.

1.3. Guide to the contents of thesis

The major achievement of this thesis has been to extend the physical limits of the application and measurement of torque and rotation using the OTW. The motivation for this development is to push the limit of torque spectroscopy and enable measurements on

biomolecules and biomotors that were not feasible with the previously existing techniques. One direction of this development is to enable the measurements of biomolecules in the regime of rapid (milliseconds-to-seconds) and subtle modulation of torque (~ 1 pN·nm) and angle ($\sim 1^\circ$) that is crucial in plenty of cellular processes^{53,64}. The other development goal is to substantially expand the accessible torque-speed space, facilitating the measurement of extremely high torque (1–10 nN·nm) and rotational frequency (1–10 kHz) that are characteristics of diverse important biological rotary motors⁶⁵. Based on the examination of diverse candidate materials considering these development goals, the use of single-crystal rutile TiO₂ nanocylinders has been suggested in this thesis, as a nearly ideal material for an advanced optical angular probe. Single-crystal rutile TiO₂ is a material with which the optical trapping community is less familiar, despite its multiple tremendous advantages. This lack of familiarity can be understood from the challenges inherent in rutile TiO₂ particle production and trapping that are addressed in this thesis.

Another achievement presented in this thesis has been to develop an optimized DNA nanocurtain platform. It is designated in this thesis with a more descriptive term, stretched and oriented DNA arrays (SODA), as DNA molecules are stretched by buffer flow, oriented with respect to their sequence, and precisely aligned along the gold nanostructure arrays. The significance of using SODA lies in their capacities for multiplexing and direct visualization of biomolecule locations, which complements other low-throughput and indirect-detection techniques including OT and OTW. The specific aim of this optimization is to elucidate the detailed dynamics of diverse protein complexes working on nucleic acids such as the eukaryotic replisome. In addition, technical advances in device fabrication and coupling with magnetic tweezers are explored.

Leading up to these achievement, **Chapter 2** provides details of instrumentation, calibration, and numerical modeling for OTW, and an overview of nanofabrication and surface functionalization processes that are applied throughout this thesis. From **Chapter 3** to **Chapter 5**, the results from the development of a novel torque probe for OTW are presented. **Chapter 3** describes the solutions to rutile TiO₂ nanoparticle production issues, i.e., tunable top-down nanofabrication and highly-efficient surface functionalization. These developments allow reproducible production of rutile TiO₂ particles with desired shapes and dimensions with high structural uniformity and permit reliable attachment of diverse (bio)molecules. **Chapter 4** details the requirements for the shape and dimensions of rutile TiO₂ nanoparticles for stable three-dimensional optical trapping and maximized optical torque transfer. The results are experimentally verified by the characterization of linear and angular trapping of differently sized rutile TiO₂ nanocylinders, and additional verifications are given by numerical calculations. In addition, the achievable measurement precision of physical quantities (i.e., force, torque, position, and angle) and temporal resolution are assessed with Allan deviation analysis as a function of signal averaging time. In **Chapter 5**, the angular precision and temporal resolution achieved in the OTW setup are compared with those of (electro)magnetic torque tweezers, together with an extended explanation on the validity of Allan deviation analysis in torque spectroscopy. The presented results from the thorough investigation of rutile TiO₂ nanoparticles, starting from its production carried

through to its utilization, will pave the way to a more wide-spread use of this probe material and facilitate further development of optical torque spectroscopy in single-molecule biophysics.

In **Chapter 6**, the development of SODA is presented. A fabrication process with higher flexibility in device design is demonstrated, in which maskless lithography techniques are employed for both gold nanostructures and Si molds for microfluidic channels. In addition, a protocol to render SODA compatible with magnetic tweezers is suggested. The applied surface coatings including supported lipid bilayers function as expected, and the size of gold nanobarriers is also optimized to confine single DNA strands with a high probability. With this optimally-sized gold nanostructures, a proof-of-concept experiments and data analysis are performed on nucleoprotein filament formation dynamics of Rad51 DNA binding proteins. These proven approaches to obtain integrated and functioning SODA devices are expected to be further developed and extensively utilized as a complementary tool to investigate single-molecule behaviors.

Finally, **Chapter 7** provides the conclusion of this thesis, and the recommendations and preliminary experimental results with respect to future developments. I am convinced that this overview of my research and accomplishments in developments of single-molecule instrumentation provides practical information and guidelines for the readers from the same or other disciplines. Thereby it will inspire all to continue to look at the "*bottom*", because indeed there is still "*plenty of room*" there, nearly sixty years after the original suggestion to do so was made by visionary physicist Richard Feynman in 1959⁶⁶.

1.4. References

1. Watson, J. D. & Crick, F. H. C. Molecular structure of nucleic acids: a structure for deoxyribose nucleic acid. *Nature* **171**, 737 (1953).
2. International Human Genome Sequencing Consortium, Finishing the euchromatic sequence of the human genome. *Nature* **431**, 931 (2004).
3. Schrödinger, E. *What Is Life? the physical aspect of the living cell and mind* (Cambridge University Press, Cambridge, 1944).
4. Cobb, M. *Life's greatest secret: The race to crack the genetic code* (Hachette UK, 2015).
5. Nelson, P. & Doniach, S. Biological physics: energy, information, life. *Physics Today* **57**, 63-64 (2004).
6. Hughes, M. L. & Dougan, L. The physics of pulling polyproteins: a review of single molecule force spectroscopy using the AFM to study protein unfolding. *Reports on Progress in Physics* **79**, 076601 (2016).
7. Sasmal, D. K., Pulido, L. E., Kasal, S. & Huang, J. Single-molecule fluorescence resonance energy transfer in molecular biology. *Nanoscale* **8**, 19928-19944 (2016).
8. Sydor, A. M., Czymmek, K. J., Puchner, E. M. & Mennella, V. Super-resolution microscopy: from single molecules to supramolecular assemblies. *Trends in Cell Biology* **25**, 730-748 (2015).
9. Vangindertael, J., Camacho, R., Sempels, W., Mizuno, H., Dedecker, P. & Janssen, K. P. F. An introduction to optical super-resolution microscopy for the adventurous biologist. *Methods and Applications in Fluorescence* **6**, 022003 (2018).
10. Bai, X.-C., McMullan, G. & Scheres, S. H. W. How cryo-EM is revolutionizing structural biology. *Trends in Biochemical Sciences* **40**, 49-57 (2015).
11. Fernandez-Leiro, R. & Scheres, S. H. W. Unravelling biological macromolecules with cryo-electron microscopy. *Nature* **537**, 339 (2016).
12. Moffitt, J. R., Chemla, Y. R., Smith, S. B. & Bustamante, C. Recent advances in optical tweezers. *Annual Review of Biochemistry* **77**, 205-228 (2008).
13. Gao, D. et al. Optical manipulation from the microscale to the nanoscale: fundamentals, advances and prospects. *Light: Science & Applications* **6**, e17039 (2017).

14. Sarkar, R. & Rybenkov, V. V. A guide to magnetic tweezers and their applications. *Frontiers in Physics* **4**, 48 (2016).
15. Miller, H., Zhou, Z., Shepherd, J., Wollman, A. J. M. & Leake, M. C. Single-molecule techniques in biophysics: a review of the progress in methods and applications. *Reports on Progress in Physics* **81**, 024601 (2018).
16. Wang, M. D., Yin, H., Landick, R., Gelles, J. & Block, S. M. Stretching DNA with optical tweezers. *Biophysical Journal* **72**, 1335-1346 (1997).
17. Oberstrass, F. C., Fernandes, L. E., Lebel, P. & Bryant, Z. Torque spectroscopy of DNA: base-pair stability, boundary effects, backbending, and breathing dynamics. *Physical Review Letters* **110**, 178103 (2013).
18. Lipfert, J. et al. Double-stranded RNA under force and torque: similarities to and striking differences from double-stranded DNA. *Proceedings of the National Academy of Sciences* **111**, 15408 (2014).
19. Marin-Gonzalez, A., Vilhena, J. G., Perez, R. & Moreno-Herrero, F. Understanding the mechanical response of double-stranded DNA and RNA under constant stretching forces using all-atom molecular dynamics. *Proceedings of the National Academy of Sciences* **114**, 7049 (2017).
20. Bornschlöggl, T. & Rief, M. Single-molecule protein unfolding and refolding using atomic force microscopy. In *Single Molecule Analysis: Methods and Protocols* (ed Peterman, E. J. G., Wuite, G. J. L.) 233-250 (Humana Press, 2011).
21. Jiao, J., Rebane, A. A., Ma, L. & Zhang, Y. Single-molecule protein folding experiments using high-precision optical tweezers. In *Optical Tweezers: Methods and Protocols* (ed Gennerich, A.) 357-390 (Springer New York, 2017).
22. Alberts, B., Bray, D., Lewis, J., Raff, M., Roberts, K. & Watson, J. D. *Molecular Biology of the Cell* (Garland, 1994).
23. Abbondanzieri, E. A., Greenleaf, W. J., Shaevitz, J. W., Landick, R. & Block, S. M. Direct observation of base-pair stepping by RNA polymerase. *Nature* **438**, 460 (2005).
24. Koster, D. A., Croquette, V., Dekker, C., Shuman, S. & Dekker, N. H. Friction and torque govern the relaxation of DNA supercoils by eukaryotic topoisomerase IB. *Nature* **434**, 671 (2005).
25. Kaniecki, K., De Tullio, L. & Greene, E. C. A change of view: homologous recombination at single-molecule resolution. *Nature Reviews. Genetics* **19**, 191 (2017).
26. Aubin-Tam, M.-E., Olivares, Adrian O., Sauer, Robert T., Baker, Tania A. & Lang, Matthew J. Single-Molecule Protein Unfolding and Translocation by an ATP-Fueled Proteolytic Machine. *Cell* **145**, 257-267 (2011).
27. Sternberg, S. H., Redding, S., Jinek, M., Greene, E. C. & Doudna, J. A. DNA interrogation by the CRISPR RNA-guided endonuclease Cas9. *Nature* **507**, 62 (2014).
28. Ganji, M. et al. Real-time imaging of DNA loop extrusion by condensin. *Science* (2018).
29. Kodera, N., Yamamoto, D., Ishikawa, R. & Ando, T. Video imaging of walking myosin V by high-speed atomic force microscopy. *Nature* **468**, 72 (2010).
30. Noji, H., Yasuda, R., Yoshida, M. & Kinosita Jr, K. Direct observation of the rotation of F1-ATPase. *Nature* **386**, 299 (1997).
31. Nord, A. L., Pedaci, F. & Berry, R. M. Transient pauses of the bacterial flagellar motor at low load. *New Journal of Physics* **18**, 115002 (2016).
32. Southern, J. et al. Multi-scale computational modelling in biology and physiology. *Progress in Biophysics and Molecular Biology* **96**, 60-89 (2008).
33. Voet, D. *Biochemistry* (John Wiley, New York, 1995).
34. Naganathan, A. N. & Muñoz, V. Scaling of folding times with protein size. *Journal of the American Chemical Society* **127**, 480-481 (2005).
35. Berg-Sørensen, K. & Flyvbjerg, H. Power spectrum analysis for optical tweezers. *Review of Scientific Instruments* **75**, 594-612 (2004).
36. van Oene, M. M. et al. Quantifying the precision of single-molecule torque and twist measurements using Allan variance. *Biophysical Journal* **114**, 1970-1979 (2018).
37. La Porta, A. & Wang, M. D. Optical torque wrench: angular trapping, rotation, and torque detection of quartz microparticles. *Physical Review Letters* **92**, 190801 (2004).
38. Lipfert, J., Kerssemakers, J. W. J., Jager, T. & Dekker, N. H. Magnetic torque tweezers: measuring torsional stiffness in DNA and RecA-DNA filaments. *Nature Methods* **7**, 977 (2010).
39. Janssen, X. J. A., Lipfert, J., Jager, T., Daudey, R., Beekman, J. & Dekker, N. H. Electromagnetic torque tweezers: a versatile approach for measurement of single-molecule twist and torque. *Nano Letters* **12**, 3634-3639 (2012).
40. Sitters, G., Kamsma, D., Thalhammer, G., Ritsch-Marte, M., Peterman, E. J. G. & Wuite, G. J. L. Acoustic force spectroscopy. *Nature Methods* **12**, 47 (2014).
41. Yang, D., Ward, A., Halvorsen, K. & Wong, W. P. Multiplexed single-molecule force spectroscopy using a centrifuge. *Nature Communications* **7**, 11026 (2016).

42. Shashkova, S. & Leake, M. C. Single-molecule fluorescence microscopy review: shedding new light on old problems. *Bioscience Reports* (2017).
43. Sirinakis, G., Ren, Y., Gao, Y., Xi, Z. & Zhang, Y. Combined versatile high-resolution optical tweezers and single-molecule fluorescence microscopy. *Review of Scientific Instruments* **83**, 093708 (2012).
44. Perkins, T. T., Smith, D. E. & Chu, S. Single Polymer dynamics in an elongational flow. *Science* **276**, 2016 (1997).
45. Finkelstein, I. J. & Greene, E. C. Supported lipid bilayers and DNA curtains for high-throughput single-molecule studies. In *DNA Recombination: Methods and Protocols* (ed Tsubouchi, H.) 447-461 (Humana Press, 2011).
46. Collins, B. E., Ye, L. F., Duzdevich, D. & Greene, E. C. Chapter 12 - DNA curtains: novel tools for imaging protein–nucleic acid interactions at the single-molecule level. In *Methods in Cell Biology* (ed Waters, J. C., Wittman, T.) **123**, 217-234 (Academic Press, 2014).
47. Neuman, K. C., Chadd, E. H., Liou, G. F., Bergman, K. & Block, S. M. Characterization of photodamage to *Escherichia coli* in optical traps. *Biophysical Journal* **77**, 2856-2863 (1999).
48. Terai, T. & Nagano, T. Small-molecule fluorophores and fluorescent probes for bioimaging. *Pflügers Archiv - European Journal of Physiology* **465**, 347-359 (2013).
49. Ng, S. M., Koneswaran, M. & Narayanaswamy, R. A review on fluorescent inorganic nanoparticles for optical sensing applications. *RSC Advances* **6**, 21624-21661 (2016).
50. Martin-Fernandez, M. L., Tynan, C. J. & Webb, S. E. D. A 'pocket guide' to total internal reflection fluorescence. *Journal of Microscopy* **252**, 16-22 (2013).
51. So, P. T. C., Dong, C. Y., Masters, B. R. & Berland, K. M. Two-photon excitation fluorescence microscopy. *Annual Review of Biomedical Engineering* **2**, 399-429 (2000).
52. Novotny, L. & Hecht, B. *Principles of nano-optics* (Cambridge university press, 2012).
53. Forth, S., Sheinin, M. Y., Inman, J. & Wang, M. D. Torque measurement at the single-molecule level. *Annual Review of Biophysics* **42**, 583-604 (2013).
54. Forties, Robert A. & Wang, Michelle D. Discovering the power of single molecules. *Cell* **157**, 4-7 (2014).
55. Wu, T. et al. A photon-driven micromotor can direct nerve fibre growth. *Nature Photonics* **6**, 62 (2011).
56. Craig, D., McDonald, A., Mazilu, M., Rendall, H., Gunn-Moore, F. & Dholakia, K. Enhanced optical manipulation of cells using antireflection coated microparticles. *ACS Photonics* **2**, 1403-1409 (2015).
57. Yao, A., Tassieri, M., Padgett, M. & Cooper, J. Microrheology with optical tweezers. *Lab on a Chip* **9**, 2568-2575 (2009).
58. Arita, Y., McKinley, A. W., Mazilu, M., Rubinsztein-Dunlop, H. & Dholakia, K. Picoliter rheology of gaseous media using a rotating optically trapped birefringent microparticle. *Analytical Chemistry* **83**, 8855-8858 (2011).
59. Schäffer, E., Nørrelykke, S. F. & Howard, J. Surface forces and drag coefficients of microspheres near a plane surface measured with optical tweezers. *Langmuir* **23**, 3654-3665 (2007).
60. Abbott, J. et al. CMOS nanoelectrode array for all-electrical intracellular electrophysiological imaging. *Nature Nanotechnology* **12**, 460 (2017).
61. Bumgarner, R. Overview of DNA Microarrays: Types, Applications, and Their Future. *Current Protocols in Molecular Biology* **101**, 22.21.1-22.21.11 (2013).
62. Abdul Kaf, M., El-Said, W. A., Kim, T.-H. & Choi, J.-W. Cell adhesion, spreading, and proliferation on surface functionalized with RGD nanopillar arrays. *Biomaterials* **33**, 731-739 (2012).
63. Ha, S., Janissen, R., Ussembayev, Y. Y., van Oene, M. M., Solano, B. & Dekker, N. H. Tunable top-down fabrication and functional surface coating of single-crystal titanium dioxide nanostructures and nanoparticles. *Nanoscale* **8**, 10739-10748 (2016).
64. Lebel, P., Basu, A., Oberstrass, F. C., Tretter, E. M. & Bryant, Z. Gold rotor bead tracking for high-speed measurements of DNA twist, torque and extension. *Nature Methods* **11**, 456 (2014).
65. Beeby, M., Ribardo, D. A., Brennan, C. A., Ruby, E. G., Jensen, G. J. & Hendrixson, D. R. Diverse high-torque bacterial flagellar motors assemble wider stator rings using a conserved protein scaffold. *Proceedings of the National Academy of Sciences* **113**, E1917 (2016).
66. Feynman, R. P. There's plenty of room at the bottom. *Journal of Microelectromechanical Systems* **1**, 60-66 (1992).

2

Optical Torque Wrench, Nanofabrication, and Surface Functionalization

This chapter provides an overview for setup and calibration of optical torque wrench (OTW), nanofabrication processes, and surface functionalization strategies, which are the fundamentals for the subsequent chapters. First, details of OTW instrumentation is provided, including the physical principles, instrumental design, calibration of trapped particles, and numerical modeling of particle trapping behaviors, as they form a basis of the developments presented in **Chapters 3-5**. The wide-spread use of the conventional optical force spectroscopy has been facilitated by the existence of commercially available standard optical probes, i.e., polystyrene or silica microspheres, that are homogeneous in composition, highly uniform in geometry, and versatile in surface coatings. However, no such particles are available for OTW yet. Hence, further developments of the fabrication and surface functionalization of OTW probes are important and a promising approach is offered by a top-down process developed in this thesis (**Chapter 3**). For this top down approach, lithography and etching processes are crucial and hence introduced here. These techniques are also utilized for the fabrication of gold nanostructures and silicon molds with microfluidic channels for protein-DNA interaction studies in **Chapter 6**. In addition, an introduction to the general surface functionalization methodology is provided as such approaches are applied to attach single biomolecules to nanoparticles or nanostructures in this thesis (**Chapter 3** and **Chapter 6**).

2.1. Optical torque wrench

The optical torque wrench (OTW) allows control of torque and angle, in addition to force and position. It is an extension of the conventional optical tweezers (OT) in which only force and position can be controlled. However, the wide-spread use of OTW has been hampered by its higher complexity in experimental setup, birefringent probe particle preparation, trap calibration, and theoretical modeling, which are discussed in this section. The substantially enhanced force and torque achieved with single-crystal rutile TiO₂ nanocylinders in this thesis require several modifications of the trap calibration methods, which are developed for the conventional angular probes, e.g., quartz SiO₂. Also, the cylindrical geometry and the optical anisotropy require numerical approaches rather than analytical ones for precise estimation of the optical and hydrodynamic properties of rutile TiO₂ nanocylinders, unlike the conventional isotropic spherical particles for which analytical solutions are available.

2.1.1. Optical angular momentum transfer

The physical principle behind OTW operation is based on the light-matter interaction, more precisely, the linear and angular momentum transfer from photons to a particle. The transfer of linear optical momentum to the particle enables optical trapping by generating field gradient force, and the same principle is used in OT. For application of torque on the trapped particle, angular momentum transfer is utilized. Historically, the existence of the linear momentum (i.e., electromagnetic radiation pressure) of light was predicted by Johannes Kepler in early 17th century¹. However, only at the beginning of the 20th century, the linear momentum was mathematically formulated by John H. Poynting^{2,3}, and the experimental proof was given by Pyotr Lebedev, Ernest F. Nichols, and Gordon F. Hull^{4,5}. For the light angular momentum, John H. Poynting expected its existence in 1909⁶, and Richard Beth experimentally verified it in 1936 using circularly polarized light and a quartz plate held by a thin wire⁶.

Since the invention of laser in 1960⁷ and the subsequent first demonstration of the laser-based optical trapping in 1970⁸, the optical angular momentum transfer started to be investigated with higher precision using OT platforms^{9,10} and led to the development of OTW^{11,12}. These research were mainly based on spin angular momentum (SAM) of light (in either linearly or circularly polarized beam), while orbital angular momentum (OAM) of light was discovered only later in 1992 by Les Allen and others¹³. Although both SAM and OAM can be utilized to exert torques, the OTW setup utilized in this thesis employs SAM. The advantages of using SAM include: i) more straightforward control and measurement of torque; and ii) the convenience of directly using the conventional laser output mode (linearly polarized TEM₀₀ beam) without the need of a complicated mode conversion (e.g., to Laguerre-Gaussian beam).

2.1.2. Configuration of the OTW setup

The details of the configuration of the OTW setup utilized for the research in this thesis (Chapters 3-5) are presented in this section (Fig. 2.1). The basic elements of the OTW setup are almost identical to those of the conventional optical tweezers systems, to allow for application of light gradient force to stably trap particles. However, the major difference from the conventional optical tweezers lies in the addition of various polarization optics for precise manipulation and detection of light polarization states¹⁴, including electro-optic modulator (EOM), waveplates, and polarizing beam splitter (PBS).

The first part of the beam path is for conditioning the laser beam regarding power and beam size. A diode-pumped solid-state laser (1064 nm-wavelength, continuous wave, TEM₀₀) is coupled with an optical isolator (ISO) to prevent possible damage to the laser head in case of any intense backscattering events. The laser power is controlled using a combination of a half-wave plate (HWP) and a PBS. The unused portion of the laser power (i.e., the beam reflected by the PBS) is dissipated by a beam block (BB). A beam shutter is installed to block the laser beam when necessary. Then, a reducing telescope (~1:4) is used to obtain a reduced beam diameter which is small enough to pass the given size of the apertures of the acousto-optic modulator (AOM) and EOM. The AOM and a photodiode (PD) consist a feedback loop which stabilizes intensity fluctuation of the laser beam. An iris is installed after the AOM, to select only the 0th order output beam from the AOM. The advantages of using 0th order AOM output instead of 1st order are: i) less power is required for the radio frequency (RF) signal that drives the AOM, resulting in a reduction of heating that might induce a larger drift in the setup; ii) the setup can be operated with turned-off AOM when necessary, e.g., for optical beam path alignment.

The next part of the beam path is added for polarization control. A Glan laser polarizer (GLP) is used to further purify the polarization states and increase the extinction ratio (1:10⁵) between *p*- and *s*- polarization components. An HWP is placed at the input of EOM for alignment purpose, to slightly rotate the input linear polarization direction and therefore exactly matching the required $\pi/4$ offset angle from the fast axis of the EOM crystal. Another HWP is placed at the output of EOM, also for alignment purposes, to rotate the output linear polarization to match with the PBS orientation at the torque detection unit. The fine tuning of these two HWP offers a convenient alternative approach to align the laser beam polarization with respect to EOM because the EOM holder does not support fine-tuning of EOM body's rotation angle. Due to the divergent nature of the focused Gaussian beam, one additional reducing telescope (~1:2) is placed after EOM to reduce the beam diameter once again, rendering the beam width suitable to enter the beam expander (BE; with a beam expansion ratio of ~4) input aperture window. A non-polarizing beam splitter (NPBS) is located just before the BE, and another output from the NPBS is used for reference torque detection. In this reference torque detection unit, two quarter wave plates (QWPs) mimic the actual angular trap without any trapped particle, thereby precisely reports the status of

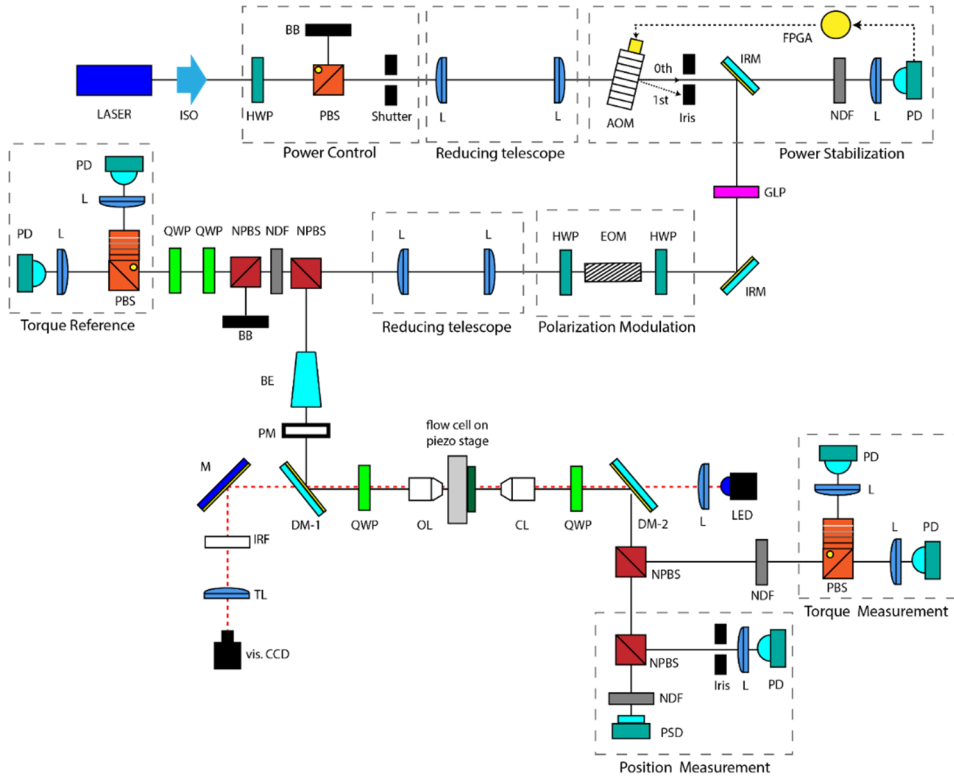


Figure 2.1. The schematic of OTW setup. The 1064 nm-wavelength trapping laser beam path is displayed as black solid lines, while the visible light (LED) microscopy illumination beam path is shown as red dotted lines. The abbreviations of components are as follows: optical isolator (ISO), beam block (BB), half-wave plate (HWP), quarter-wave plate (QWP), polarizing beam splitter (PBS), 50:50 non-polarizing beam splitter (NPBS), Glan laser polarizer (GLP), infrared lens (L), infrared mirror (IRM), neutral density filter (NDF), fast InGaAs photodiode (PD), data acquisition system for feedback control based on field programmable gate array (FPGA), acousto-optic modulator (AOM), electro-optic modulator (EOM), beam expander (BE), power meter (PM; put into the beam path only when necessary), dichroic mirror (DM), visible wavelength mirror (M), infrared filter (IRF), objective lens (OL), condenser lens (CL), light-emitting diode (LED), position sensitive detector (PSD), tube lens (TL), and visible-wavelength charge-coupled device camera (vis. CCD).

beam polarization without being biased by any trapped object or medium. The expanded beam after BE is reflected at a dichroic mirror (DM-1), and then passes a QWP and an objective lens (OL). The beam becomes highly focused by OL, to be able to trap particles within a flow cell chamber. The output beam is then collected by a condenser lens (CL). The position of CL is adjusted so that the output beam from CL becomes collimated. The use of two identical objective lenses, as OL and CL, facilitates collimation of the output beam and calibration of the laser power at focal plane. The output beam passes a QWP and is then reflected by a dichroic mirror (DM-2), being transferred to the position and torque detection units.

Besides the trapping beam path, an additional beam path is utilized to consist an optical microscope based on Köhler illumination system¹⁵, for observation of particles within a flow cell. A high-power blue LED is used for illumination, and infrared mirrors (IRM) are used as DMs, because visible light is mostly transmitted through

IRMs rather than being reflected. Together with a visible-wavelength mirror (M), a tube lens (TL), and a visible charge-coupled device (CCD) camera, visual observation of trapped particle is possible through this microscope configuration. The added infrared filter (IRF) blocks the scattered laser beam entering the CCD when necessary.

The rest of the beam path allows detection of both torque and force. The torque detection unit after DM-2 has the same symmetric configuration as the aforementioned reference torque detection unit. For both torque detection units, coupled PBS cubes are used to compensate the asymmetric extinction ratios (among p - and s - polarization components) of each PBS and offer the same level of extinction ratio for both p - and s -output polarization components. To further suppress unexpected polarization modulation, the beam path and placement of the optic components are carefully designed to compensate such asymmetries in polarization that can be induced by the optics components such as NPBS and DM. For example, the additional NPBS before the reference torque unit is installed solely for such a purpose. By using two PDs in the torque detection unit, the measured intensities of the left- and right-circularly polarized beam components provide a direct measure of angular momentum transfer to the trapped particle¹⁶.

The optical force is then deduced from the particle position measurement. An NPBS relays a half of the output beam to the position sensing detector (PSD) for the radial measurements (x, y), while another half is guided to the photodiode (PD) for the axial measurement (z). An iris is positioned before the PD and its opening is optimized to properly capture the Gouy phase¹⁷ shift of the trapped particle. The PSD alone can also measure all three spatial coordinates (x, y, z) of a trapped particle, however, this separated detection permits simultaneous optimization for both radial and axial measurements as they have conflicting requirements for iris opening¹⁸. The results shown in **Chapter 4** were measured with this improved position detection method, while those in **Chapter 3** were measured with PSD only.

For high-precision measurements, noise from various sources needs to be blocked or suppressed. In this OTW setup, the laser beam path is enclosed by metallic tubes wherever possible, to prevent turbulent air currents that can induce unwanted fluctuation and noise on the measured signals. Further, the entire setup is enclosed in a box made of thick plates to attenuate the transmission of acoustic noise. Every PD is powered by a lead battery instead of a power supply to reduce possible interferences from high-frequency electrical noise. In addition, the AOM is operated at only low RF power level, as high-power driving of the AOM results in excess heating and causes instrumental drift that appears as a large amount of low-frequency noise.

2.1.3. Torque and force calibrations in the OTW

The purpose of trap calibration process in OTW or optical tweezers is to obtain two physical parameters that describe the behavior of a particle in an optical trap (i.e., trap stiffness and drag coefficient). For the case of using the conventional spherical beads, their precise drag can be analytically calculated once their diameter and viscosity of the

surrounding medium are known. Then their stiffness can be calibrated by only measuring their spatial fluctuations over time. In contrast, an active modulation of force or torque is required to obtain both drag and stiffness without the prior knowledge on drag of particle and viscosity of medium. The latter is more suitable considering the non-conventional geometry of rutile TiO_2 nanoparticles (i.e., cylinder), for which analytical solution of drag is valid only for a certain range of aspect ratios.

For linear trap calibration of rutile TiO_2 nanoparticles in the OTW, the well-established back focal plane interferometry combined with sinusoidal-modulation is used ¹⁹ (as explained in **Chapter 3**). For angular trap calibration, two separate measurements (similar to Refs. 12, 16) are performed, one for angular fluctuation without any active modulation of torque and another with scanning polarization rotation frequency (PRF). Then the maximum torque value (in the unit of raw signal, volts) found in the frequency scanning is combined with the fitted parameters from the power spectral density of angular fluctuation data, resulting in all three calibrated angular trapping parameters (drag coefficient, trap stiffness, and detector sensitivity), as like the case of linear trap calibration.

However, for the application of these calibration processes, the use of single-crystal rutile TiO_2 nanocylinders (**Chapters 3-5**) requires several modifications to obtain more precise linear and angular trapping stiffnesses and drag coefficients. The necessity for such modification in calibration processes results from the substantially increased linear and angular stiffnesses offered by rutile TiO_2 nanocylinders. First, the high rotation frequency of 1–10 kHz resulting from the large birefringence of rutile TiO_2 (compare with ~ 100 Hz of quartz SiO_2 microcylinders ²⁰) makes it challenging to measure torque as a function of polarization rotation frequency (PRF) ¹⁶, with a small step of increment in PRF values to precisely detect the maximum torque. To address this issue, the frequency-sweep method has been suggested and utilized in this thesis as a more rapid and reliable method to measure the response of a trapped birefringent particle over a wide range of PRF values. Second, the tighter linear trapping resulting from the high refractive index of rutile TiO_2 makes it necessary to consider the hydrodynamic resonance effect (i.e., hydrodynamic memory effect)^{21, 22} in its power spectrum fitting ²³, because the simple Lorentzian model ²³ is not capable of fitting such power spectral density plots with resonance peaks. Notably, the occurrence of the hydrodynamic effect not only requires a more sophisticated fitting algorithm but also functions as a direct measure for the extremely large trap stiffness achieved by the trapping system. More details about these modified calibration approaches and relevant datasets can be found in **Chapter 4**.

2.1.4. Numerical modeling of force, torque, and drag

The theoretical calculations of optical force, torque, and hydrodynamic drag coefficients are valuable in the interpretation of measured probe behavior, and in the design of optimized probes for OTW. However, for cylindrical geometry, unlike spherical geometry, analytical equations that can be applied to any value of cylinder aspect ratio

do not exist to calculate these physical parameters. Moreover, for optical calculations, the anisotropic optical property (i.e., birefringence) of rutile TiO₂ further complicates the analytical approach. Therefore, a numerical approach is more desirable and finite element method (FEM) is utilized in this thesis (**Chapter 4**). For optical force and torque calculation, Maxwell stress tensor (MST) is utilized²⁴, and for viscous drag calculation, Navier-Stokes equations²⁵ are solved.

2.2. Nanofabrication and surface functionalization

The modern nanofabrication techniques originate from the IC (integrated circuit, e.g., computing chips from Intel or AMD) industry. It started as "microfabrication" techniques which were capable of producing ~10 μm-width signal lines. However, during the past decades, to meet the Moore's law (i.e., the number of transistors within an IC chip doubles every 24 months), the techniques have been continuously optimized to be able to fabricate feature sizes in the sub-micron scale. The ability to access micro- and nanoscales revolutionized not only the IC chip industry, but also the nanoscale science and engineering. In this section, a brief introduction is provided for the essential steps in nanostructure fabrication, i.e., lithography and etching. In addition, the principal concepts of organic surface functionalization are introduced, which is crucial in application of the fabricated nanoparticles/nanostructures to biomolecule measurements. These nanofabrication and functionalization techniques form the core of the developments shown in **Chapter 3** and **Chapter 6**.

2.2.1. Lithography

Originally, the term "lithography" reflects a technique for industrial printing or artwork. The similar process is used in micro/nanolithography for patterning micro/nanostructures on a substrate. The most established forms of lithography are photolithography and electron-beam (e-beam) lithography. In photolithography, photo-sensitive polymer (i.e., photoresist), mask, and light source are required. A substrate coated with photoresist is irradiated with photons from a light source through a mask that allows photons to pass through specific patterns scribed on the mask. Depending on the tone of the photoresist, the irradiated region of the resist layer can either remain or be removed at the end of lithography process (i.e., negative or positive resist, respectively). The photolithography is able to pattern a large area rapidly, but preparation of each photomask is costly and time-consuming. Therefore, a maskless photolithography technique, direct laser writing (DLW), is also available. In DLW, a desired pattern is made with a laser beam, similarly to drawing a sketch on a sheet of paper with a pen. As a consequence, the patterning speed itself is slower when compared to the conventional photolithography that uses a mask.

The achievable pattern resolution for photolithography is typically limited to ~1 μm due to the diffraction limit of the photons. Instead, e-beam lithography can be

used to produce submicron scale patterns because electrons have much shorter wavelength than photons. E-beam lithography is a maskless technique, very similar to DLW, but it utilizes electron-sensitive polymer (i.e., e-beam resist) and an electron gun. In this thesis, e-beam lithography is used in **Chapter 3** and **Chapter 6** to define the diameter of rutile TiO₂ nanocylinders and the shape and size of gold nanostructures. DLW is used in **Chapter 6**, to define desired microfluidic channel dimensions.

2.2.2. Etching

Similar to lithography process, etching procedure has a long history that emerged from industrial printing or artwork. The similar process in nanofabrication has the same nomenclature, designating the processes in which an unwanted part of a material is removed. There are two broad categories in this technique: wet etching and dry etching. For wet etching, acid or base is used in aqueous solution to selectively remove unwanted material by chemically dissolving it. This process is simple and controllable, but it is not suitable for nanocylinder etching due to its isotropic nature in etching direction. On the other hand, dry etching is based on reactive plasma in which directionally moving ions remove material physically and/or chemically. As it is possible to obtain a straight etched sidewall, the heights of rutile TiO₂ nanocylinders (**Chapter 3**) and microfluidic channels (**Chapter 6**) are defined by dry etching process in this thesis.

2.2.3. Surface Functionalization

The surface functionalization, or surface modification, is a crucial step to enable diverse applications of the fabricated nanostructures or nanoparticles. In this process, desired chemical functional groups and molecules can be attached onto a surface. For example, for single-molecule experiments, biomolecules are tethered to functionalized nanoparticles so that the biomolecules can be measured or manipulated *via* the nanoparticles. For (bio)sensors, a functionalized surface allows a selective adsorption of molecules, enabling detection of molecules of interest.

In this thesis, an optimized organic surface functionalization protocol is developed and demonstrated for rutile TiO₂ (**Chapter 3**). In general, it has been known that TiO₂ is more difficult to functionalize than other common materials such as SiO₂²⁶. By testing many different potential organic surface linkers, epoxysilane (GPDMS) is chosen as it offers dense and uniform functionalization on single-crystal rutile TiO₂ surface with only few preparation steps, being time-efficient as well. Hence, this new functionalization protocol allowed measuring of single DNA molecules with rutile TiO₂ nanocylinders. Moreover, additional attachment of physically and chemically inert poly(ethylene glycol) (PEG) to nanocylinder surfaces reduce their self-aggregation and increased the fraction of monodispersed cylinders. For the high-throughput observation of protein-DNA interactions in SODA devices (**Chapter 6**), a similar surface functionalization protocols are utilized. A supported lipid bilayer formed on a glass

coverslip and the functionalized gold nanostructures allow controlled DNA attachment and simultaneous observation of large number of single DNA molecules.

2.3. References

1. Kepler, J. *De cometis libelli tres* (1619).
2. Poynting, J. H. Radiation in the solar system: its effect on temperature and its pressure on small bodies. *Philosophical Transactions of the Royal Society of London. Series A, Containing Papers of a Mathematical or Physical Character* **202**, 525-552 (1904).
3. Wisniak, J. John Henry Poynting. *Educación Química* **22**, 340-348 (2011).
4. Lebedew, P. Untersuchungen über die druckkräfte des lichtetes. *Annalen der Physik* **311**, 433-458 (1901).
5. Nichols, E. F. & Hull, G. F. A preliminary communication on the pressure of heat and light radiation. *Physical Review (Series I)* **13**, 307-320 (1901).
6. Beth, R. A. Mechanical detection and measurement of the angular momentum of light. *Physical Review* **50**, 115-125 (1936).
7. Maiman, T. H. Stimulated optical radiation in ruby. *Nature* **187**, 493-494 (1960).
8. Ashkin, A. Acceleration and trapping of particles by radiation pressure. *Physical Review Letters* **24**, 156-159 (1970).
9. Ashkin, A. Applications of laser radiation pressure. *Science* **210**, 1081 (1980).
10. Santamato, E., Daino, B., Romagnoli, M., Settembre, M. & Shen, Y. R. Collective rotation of molecules driven by the angular momentum of light in a nematic film. In *Optical Effects in Liquid Crystals* (ed Jánosy, I.) 158-161 (Springer Netherlands, 1991).
11. Friese, M. E. J., Nieminen, T. A., Heckenberg, N. R. & Rubinsztein-Dunlop, H. Optical alignment and spinning of laser-trapped microscopic particles. *Nature* **394**, 348 (1998).
12. La Porta, A. & Wang, M. D. Optical torque wrench: angular trapping, rotation, and torque detection of quartz microparticles. *Physical Review Letters* **92**, 190801 (2004).
13. Allen, L., Beijersbergen, M. W., Spreeuw, R. J. C. & Woerdman, J. P. Orbital angular momentum of light and the transformation of Laguerre-Gaussian laser modes. *Physical Review A* **45**, 8185-8189 (1992).
14. Santybayeva, Z. & Pedaci, F. Optical torque wrench design and calibration. In *Optical Tweezers: Methods and Protocols* (ed Gennerich, A.) 157-181 (Springer New York, 2017).
15. Arecchi, A. V., Messadi, T. & Koshel, R. J. *Field guide to illumination* (SPIE Press, 2007).
16. Pedaci, F., Huang, Z., van Oene, M. & Dekker, N. H. Calibration of the optical torque wrench. *Optics Express* **20**, 3787-3802 (2012).
17. Gittes, F. & Schmidt, C. F. Interference model for back-focal-plane displacement detection in optical tweezers. *Optics Letters* **23**, 7-9 (1998).
18. Friedrich, L. & Rohrbach, A. Surface imaging beyond the diffraction limit with optically trapped spheres. *Nature Nanotechnology* **10**, 1064 (2015).
19. Tolić-Nørrelykke, S. F., Schäffer, E., Howard, J., Pavone, F. S., Jülicher, F. & Flyvbjerg, H. Calibration of optical tweezers with positional detection in the back focal plane. *Review of Scientific Instruments* **77**, 103101 (2006).
20. Huang, Z., Pedaci, F., van Oene, M., Wiggin, M. J. & Dekker, N. H. Electron Beam Fabrication of Birefringent Microcylinders. *ACS Nano* **5**, 1418-1427 (2011).
21. Franosch, T. et al. Resonances arising from hydrodynamic memory in Brownian motion. *Nature* **478**, 85 (2011).
22. Jannasch, A., Demirors, A. F., van Oostrum, P. D. J., van Blaaderen, A. & Schaffer, E. Nanonewton optical force trap employing anti-reflection coated, high-refractive-index titania microspheres. *Nature Photonics* **6**, 469-473 (2012).
23. Berg-Sørensen, K. & Flyvbjerg, H. Power spectrum analysis for optical tweezers. *Review of Scientific Instruments* **75**, 594-612 (2004).
24. Novotny, L. & Hecht, B. *Principles of nano-optics* (Cambridge University Press, 2012).
25. White, F. M. *Fluid mechanics* (McGraw-Hill, 1998).
26. Pujari, S. P., Scheres, L., Marcelis, A. T. M. & Zuilhof, H. Covalent surface modification of oxide surfaces. *Angewandte Chemie International Edition* **53**, 6322-6356 (2014).

3

Tunable Top-Down Fabrication and Functional Surface Coating of Single-Crystal Titanium Dioxide Nanostructures and Nanoparticles

Titanium dioxide (TiO_2) is a key component in diverse optical and electronic applications that exploit its exceptional material properties. In particular, the use of TiO_2 in its single-crystalline phase can offer substantial advantages over its amorphous and polycrystalline phases for existing and yet-to-be-developed applications. However, the implementation of single-crystal TiO_2 has been hampered by challenges in its fabrication and subsequent surface functionalization. Here, we introduce a novel top-down approach that allows for batch fabrication of uniform high aspect-ratio single-crystal TiO_2 nanostructures with targeted sidewall profiles. We complement our fabrication approach with a functionalization strategy that achieves dense, uniform, and area-selective coating with a variety of biomolecules. This allows us to fabricate single-crystal rutile TiO_2 nanocylinders tethered with individual DNA molecules for use as force- and torque-transducers in an optical torque wrench. These developments provide the means for increased exploitation of the superior material properties of single-crystal TiO_2 at the nanoscale.

This chapter has been published as: **Seungkyu Ha**, Richard Janissen, Yera Y. Ussembayev, Maarten M. van Oene, Belen Solano, and Nynke H. Dekker, "Tunable Top-Down Fabrication and Functional Surface Coating of Single-Crystal Titanium Dioxide Nanostructures and Nanoparticles", *Nanoscale* 8, pp. 10739–10748 (2016).

3.1. Introduction

Micro- and nanostructures based on titanium dioxide (TiO_2) have been utilized in numerous applications that exploit the unique properties of this material (**Supplementary Fig. S3.1**). For example, the high photocatalytic activity of TiO_2 is used for water splitting¹ and air purification². The electrical properties of TiO_2 , which include a tunable resistance, a high dielectric constant, carrier transport abilities, and a wide band gap, render it a preferred material for sensors³, memory devices⁴, transistors⁵, solar cells⁶, and batteries^{7,8}. Furthermore, the optical properties of TiO_2 , e.g. high refractive index and optical nonlinearity, find its use in optical waveguides⁹, photonic crystals¹⁰, and optical trapping¹¹.

In particular, the use of TiO_2 in its single-crystalline phase can offer substantial advantages over its amorphous and polycrystalline phases for existing and new applications. For instance, single-crystal TiO_2 allows improved control of surface properties, e.g. photochemical reactivity¹² and surface wettability¹³, by making use of the different crystallographic orientations. The higher carrier mobility of single-crystal TiO_2 renders it a promising material for transistors and (bio)sensors¹⁴ and may enhance the efficiency of dye-sensitized solar cells¹⁵. Furthermore, optical waveguides and photonic crystals composed of single-crystal TiO_2 ^{16,17} are expected, due to its highly ordered atomic structures, to exhibit improved light transmission and nonlinear response^{18,19}. Lastly, the single-crystal rutile polymorph of TiO_2 has an exceptionally large optical birefringence, which makes it an excellent candidate for incorporation into torque transducers for e.g. single-molecule spectroscopy²⁰.

To facilitate the application of TiO_2 in its single-crystalline phase, major challenges in both fabrication and surface functionalization must be addressed. First, it is important to control structural parameters such as feature size, shape, and pitch that determine the resulting physical responses of fabricated TiO_2 nanostructures. Such physical responses impact e.g. gas sensing performance³, light scattering efficiency⁶, light propagation behavior⁹, and optical trapping capabilities¹¹. Mainstream bottom-up approaches for TiO_2 nanofabrication²¹, e.g. hydrothermal growth method^{1,22} and electrochemical anodization⁶, while capable of high throughput, lack sufficient flexibility in controlling dimensions and geometries. A number of bottom-up methods are capable of fabricating single-crystal TiO_2 nanostructures, but these lack control of the crystallographic orientations and are limited to a certain crystalline polymorph, e.g. anatase²³ or rutile¹⁵. Hybrid fabrication methods, such as atomic layer deposition array defined by etch-back technique^{24,25}, can achieve high aspect-ratio but are limited to the fabrication of amorphous or polycrystalline TiO_2 ²⁶. These limitations can be overcome by employing top-down nanofabrication methods based on plasma etching, which can target single-crystal TiO_2 substrate with any desired

crystalline polymorph or crystallographic orientation. However, as TiO₂ is substantially more difficult to etch than comparable materials (e.g., silicon (Si), silicon dioxide (SiO₂), and silicon nitride (Si₃N₄))^{27,28}, such etching processes are currently limited to low aspect-ratio and largely positive sidewall angle.

Second, it is key to achieve highly efficient surface functionalization and bioconjugation of TiO₂ for applications such as (bio)sensors²⁹, force transducers³⁰, and torque transducers³¹. However, surface functionalization of TiO₂, using common alkoxy silane surface linkers, is known to be less efficient in terms of linker density and uniformity than that of other oxide materials (e.g., SiO₂ and aluminum oxide (Al₂O₃))^{32,33}. Furthermore, the majority of described bioconjugation methods for TiO₂ surfaces require long incubation time and additional crosslinker molecules²⁹ that could decrease the overall conjugation efficiency and harm the biomolecule functionality. Peculiarly for single-crystal TiO₂ nanostructures, the lack of extensive quantitative and qualitative comparisons of different surface functionalization strategies hinders the selection of an optimal procedure.

Here, we present a successful top-down fabrication and surface functionalization of single-crystal TiO₂ nanostructures and nanoparticles. We focus our efforts on the rutile polymorph of single-crystal TiO₂ (100), in order to harness its exceptionally large optical birefringence and precisely oriented optic axis for effective torque transfer (**Supplementary Methods**) in an optical torque wrench (OTW)²⁰. Using high aspect-ratio nanocylinders suitable for optical trapping as our target structures, we demonstrate how these can be mass-produced with well-defined sizes and etch profiles that display excellent overall structural uniformity. We achieve dense, uniform surface coating of TiO₂ nanocylinders using different linker molecules, and we demonstrate subsequent covalent conjugation of biological and organic molecules such as DNA, streptavidin, biotin, and biocompatible poly(ethylene glycol) (PEG). We successfully exploit these developments to fabricate and functionalize TiO₂ nanocylinders with single DNA molecules, and demonstrate full rotational control of individual nanocylinders in an OTW. This provides a particularly stringent test, as proper functioning of the OTW relies on both the correctly oriented optic axis and tightly controlled dimension of the single-crystal TiO₂ nanocylinder, and the quality and reliability of the surface coating. Rutile being the polymorph of TiO₂ that is most difficult to etch³⁴, our approach provides the means for increased exploitation of the superior material properties of single-crystal TiO₂ in any desired polymorph for diverse applications.

3.2. Results and discussion

3.2.1. Selecting an etch mask for the plasma etching of single-crystal TiO₂

One of the major issues in top-down nanofabrication of single-crystal TiO₂ is its high etch resistance. Plasma generated by fluorine-based gases is capable of etching TiO₂ only under more aggressive etching conditions – in terms of plasma ion density and energy – than the ones employed for the dry etching of comparable materials e.g. Si, SiO₂, and Si₃N₄. The increased difficulty in etching TiO₂ compared to e.g. SiO₂ stems from differences in the volatility of their etch byproducts: whereas SiF_x is volatile, TiF_x is not²⁷. The more aggressive physical etching conditions for TiO₂ necessitate careful selection of the etch mask material: while a typical polymer-based mask (e.g., photoresist, electron beam (e-beam) resist, or polystyrene spheres) can provide sufficient etch selectivity (defined as the ratio of the substrate and mask etch rates) for e.g. SiO₂³¹, this is not the case for TiO₂. The low etch selectivity imposes a thicker mask for a target etch depth, which is challenging as the applicable mask thickness is always limited (**Supplementary Methods**). Also, masks can suffer from excessive edge erosion during etching, which in turn reduces both feature sizes and the ability to perform anisotropic etching³⁵.

To overcome these challenges, we have searched for a mask material for the dry etching of single-crystal TiO₂ that achieves sufficiently high etch selectivity to permit the fabrication of nanostructures in a wide range of dimensions and sidewall profiles. We have compared different mask materials (**Supplementary Fig. S3.2**), such as chromium (Cr)³⁶, tungsten (W), e-beam resist, and amorphous Si. We observe that in particular Cr provides a significantly higher etch selectivity in fluorine-based etching of rutile TiO₂ (up to ~28:1 under specific etching conditions; an overview of etch selectivity values for different etching conditions can be found in **Supplementary Fig. S3.3**) than the other tested materials. We therefore select Cr as an appropriate etch mask material. To fabricate the Cr mask, we create circular apertures in a poly(methyl methacrylate) (PMMA) layer using e-beam lithography (**Fig. 3.1, step 1–3**). The aperture diameters can be tuned within 100–600 nm by means of defocusing e-beam. Subsequent Cr deposition and the following lift-off define the mask (**Fig. 3.1, step 4–5**).

3.2.2. Trifluoromethane (CHF₃)-based plasma etching of single-crystal TiO₂ nanocylinders

With the objectives to maximize the etch rate with a sufficiently high etch selectivity (>10:1, in order to achieve etch depths up to 1–2 μm at the practical upper limit of Cr mask thickness, ~150 nm; **Supplementary Methods**) and to produce single-crystal TiO₂ nanocylinders with vertical sidewall angles, we have

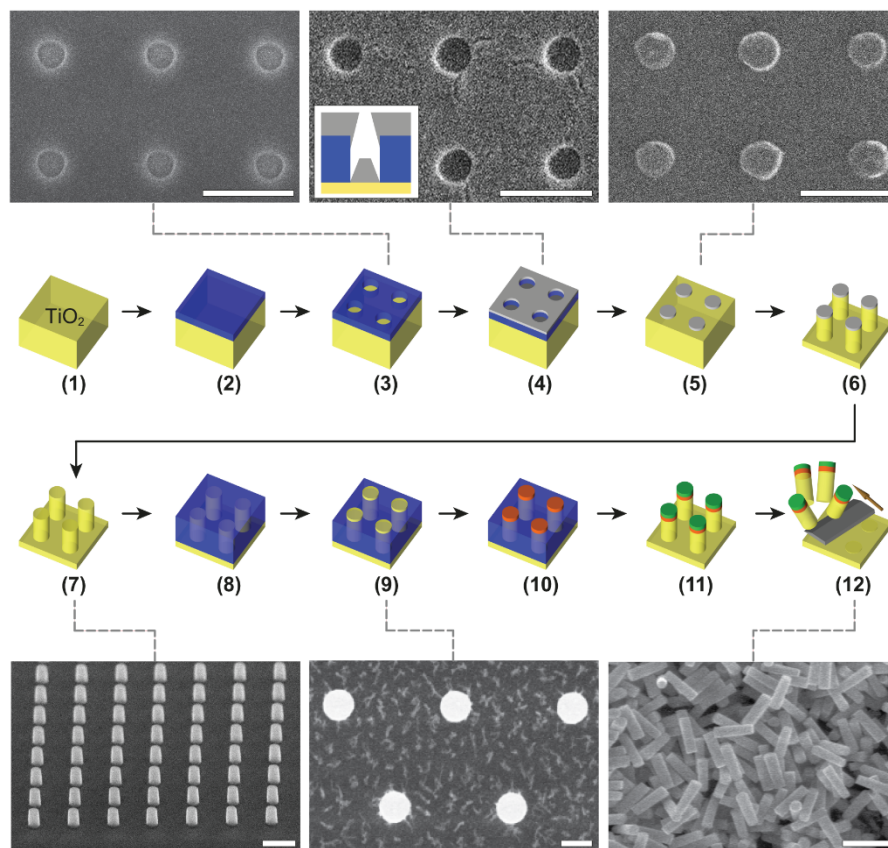


Figure 3.1. Schematic diagram of the fabrication protocol for single-crystal TiO_2 nanostructures and nanoparticles. Each SEM image is linked to the corresponding step by a gray dashed line. Scale bars denote 500 nm. **(Step 1)** Cleaning of a single-crystal TiO_2 substrate (yellow). **(Step 2)** PMMA (blue) spin-coating for e-beam lithography. **(Step 3)** E-beam patterning and subsequent development to generate evaporation windows that define the desired nanostructure sizes. The corresponding SEM image in the inset shows the TiO_2 surfaces (circles) following exposure and development of the PMMA layer. **(Step 4)** Deposition of the Cr layer (light gray) through evaporation. The Cr layer covers both the accessible TiO_2 surfaces (circles) and the PMMA layer (inset SEM image). The inset illustration shows a cross-section that highlights the formation of a Cr mask. **(Step 5)** Lift-off of PMMA layer and the resulting Cr etch mask. The SEM image in the inset displays the Cr mask (circles) formed on the TiO_2 substrate. **(Step 6)** Dry etching step to obtain the desired heights and sidewall profiles. **(Step 7)** Removal of the Cr mask following usage generates the complete nanostructures, and surface cleaning prepares these for subsequent surface functionalization. The SEM image (60° tilt) in the inset shows an array of the fabricated nanocylinders. **(Step 8)** Spin-coating of a temporary PMMA layer for area-selective functionalization. **(Step 9)** Etching of the temporary PMMA layer renders the tops of the nanostructures accessible. The SEM image in the inset shows the TiO_2 nanostructures (white circles) amidst the etched PMMA layer. **(Step 10)** Selective surface functionalization with linker molecules (orange). **(Step 11)** Removal of the temporary PMMA layer and the following conjugation with biomolecules (green). **(Step 12)** Mechanical cleavage of the nanostructures using a microtome blade (dark gray) to generate isolated individual nanoparticles. The inset shows an SEM image of a batch of cleaved nanocylinders. For further details, see **Methods**.

optimized parameters for the fluorine-based plasma etching process (**Fig. 3.1, step 6**). We start with a reactive ion etching (RIE) system in which

trifluoromethane (CHF_3) is the major etchant, and oxygen (O_2) and argon (Ar) are additive gases. The major etchant gas CHF_3 supplies both the reactive etching species and the fluorocarbon (C_xF_y) surface passivation layer-forming species³⁷. To optimize the process, we systematically vary the radio frequency (RF) power, chamber pressure, and ratios of the etch gases ($\text{CHF}_3:\text{O}_2:\text{Ar}$) (**Supplementary Table S3.1**). Our optimized etching conditions (**Supplementary Table S3.2**) result in a high single-crystal TiO_2 etch rate of ~ 40 nm/min at a sufficient etch selectivity of $\sim 14:1$ over the Cr mask, which enables the formation of TiO_2 nanocylinders with vertical sidewalls ($\sim 90^\circ$; **Fig. 3.2a**). We have successfully implemented this protocol on a second, nominally identical RIE system (**Fig. 3.2b**), requiring only minor tuning in the O_2 flow rate (4–8 sccm compared to ~ 0.5 sccm), most likely due to differences in instrument calibration.

Notably, we observe that tuning a single process parameter, namely the O_2 flow rate, allows us to drastically alter sidewall etch profiles and even cross-sectional shapes (**Supplementary Fig. S3.3**). For example, at low O_2 flow rates (0–1 sccm), we can modulate the sidewall angles from positive to negative, thereby including vertical sidewalls (**Fig. 3.2a,b**). At significantly higher O_2 flow rates (5–10 sccm), we can obtain hourglass-shaped etch profiles (**Fig. 3.2c**).

3.2.3. Sulfur hexafluoride (SF_6)-based plasma etching of single-crystal TiO_2 nanocylinders

While maintaining the identical objectives as above (high etch selectivity and vertical sidewall angles), we have also optimized the plasma etching of TiO_2 using another major etchant, sulfur hexafluoride (SF_6), in inductively coupled plasma (ICP)-RIE systems. We achieve higher etch rates of 100–200 nm/min (compared to those of 30–100 nm/min in RIE systems) using two different ICP-RIE systems (one equipped with SF_6 , methane (CH_4), and Ar gases, **Fig. 3.2d**; the other equipped with SF_6 and helium (He) gases, **Fig. 3.2e,f**), making it possible to fabricate TiO_2 nanocylinders with heights up to 1–2 μm while reducing the time of exposure to the plasma. The latter is important because longer etch durations tend to induce a drift in the etching conditions which in turn leads to irregular etch profiles. The higher TiO_2 etch rates that we obtain result from the increased density of plasma generated in ICP-RIE versus RIE systems²⁸ and a reduced level of C_xF_y sidewall surface passivation. Decreased levels of C_xF_y passivation are attributed to an excess of hydrogen plasma³⁸ and to the lack of a carbon source for the cases of $\text{SF}_6:\text{CH}_4:\text{Ar}$ and $\text{SF}_6:\text{He}$, respectively. Furthermore, SF_6 -etched nanocylinders show cleaner, smoother surfaces in high-resolution scanning electron microscope (SEM) images (**Fig. 3.2d**) compared to those of CHF_3 -etched cylinders (**Fig. 3.2c**).

When we use non-optimized SF_6 -based plasma etching conditions, etch profiles displaying highly positive sidewall angles are obtained. Since the high plasma densities of ICP-RIE systems also significantly increase the Cr etch rates,

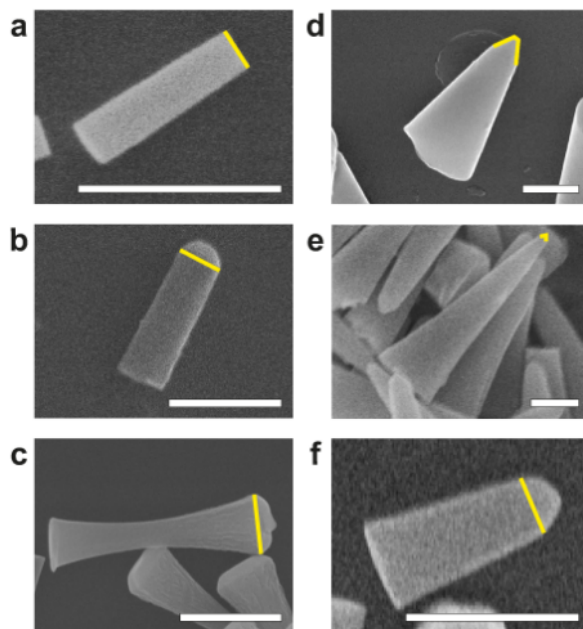


Figure 3.2. Control of single-crystal TiO_2 nanocylinder shapes using different conditions in plasma etching. In each SEM image, the top surface of the nanocylinder is marked by a yellow line (remnants of the Cr mask prior to its removal are visible in **(b,c,f)**). Scale bars denote 500 nm. In the following, the height (H), the averaged diameter (D), and the resulting aspect-ratio ($\text{AR} = H/D$) of each nanocylinder are shown. **(a)** A nanocylinder with a vertical sidewall (89°) that results from an optimized $\text{CHF}_3:\text{O}_2$ dry etching in an RIE system (H: 430 nm, D: 110 nm, AR: 3.9). **(b)** A nanocylinder with a vertical sidewall (89°) etched from the optimized $\text{CHF}_3:\text{O}_2$ dry etching in a second, nominally identical RIE system (H: 605 nm, D: 205 nm, AR: 3.0). **(c)** An hourglass-shaped nanocylinder that results from $\text{CHF}_3:\text{O}_2:\text{Ar}$ dry etching in an RIE system (H: 1020 nm, D: 200 nm, AR: 5.1). **(d)** A cone-shaped nanocylinder that results from $\text{SF}_6:\text{CH}_4:\text{Ar}$ dry etching in an ICP-RIE system (H: 1385 nm, D: 490 nm, AR: 2.8). **(e)** A cone-shaped nanocylinder that results from $\text{SF}_6:\text{He}$ dry etching in an ICP-RIE system (H: 2160 nm, D: 390 nm, AR: 5.5). **(f)** A nearly vertical (85°) nanocylinder that results from an optimized $\text{SF}_6:\text{He}$ dry etching in an ICP-RIE system (H: 470 nm, D: 210 nm, AR: 2.2).

we observe that the Cr mask tends to be completely etched away during the process, hence resulting in the formation of cone-shaped nanocylinders³⁵ (**Fig. 3.2d,e**). Under our optimized etching conditions (**Supplementary Table S3.2**), which rely on a reduced ICP power to generate moderate plasma density, we are able to achieve sufficient etch selectivity over the Cr mask ($\sim 16:1$) and nearly vertical sidewall angles ($\sim 85^\circ$; **Fig. 3.2f**) with high single-crystal TiO_2 etch rates of ~ 120 nm/min.

3.2.4. Quantification of single-crystal TiO_2 nanocylinder uniformity

To quantify both the local and global structural uniformity of fabricated single-crystal TiO_2 nanocylinders over an entire substrate, we have analyzed SEM images of high aspect-ratio (3.6) nanocylinders fabricated using the CHF_3 plasma-based protocol (**Fig. 3.3**; etching conditions in **Supplementary Table S3.2**). Qualitatively, the high uniformity of nanocylinder diameters and heights

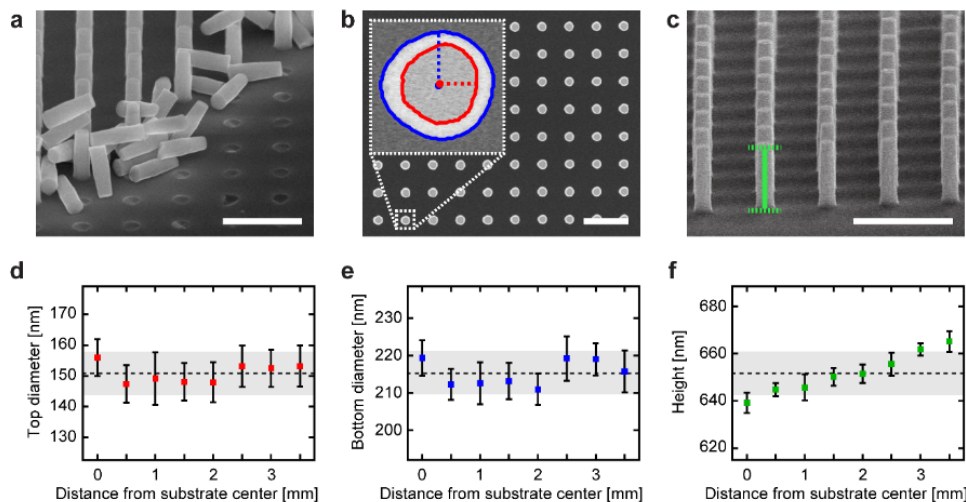


Figure 3.3. Dimensions of fabricated single-crystal TiO_2 nanocylinders. **(a-c)** SEM images of etched TiO_2 nanocylinders (light gray). Scale bars denote $1\ \mu\text{m}$. **(a)** Tilted-view (60°) of partially cleaved TiO_2 nanocylinders. An array of rigidly fixed nanocylinders is visible in top-left corner, and the cleaved substrate surface is bottom-right corner. The released nanocylinders are positioned at the interface of these regions. **(b)** Top-view of the nanocylinders. The inset shows the boundaries of the top (red contour line) and bottom (blue contour line) surface areas detected using the custom-written image analysis software routine. The dotted horizontal red (vertical blue) line and the red (blue) dot display the equivalent radius and the center of the top (bottom) surface, respectively. **(c)** Tilted-view (75°) together with an illustration of the image analysis procedure used to extract nanocylinder heights. The green vertical line measures the distance between the centers of the top and bottom surfaces (indicated by the green dotted horizontal lines). This distance is converted to actual height using the tilting angle. **(d-f)** Quantification of nanocylinder diameters and heights over the substrate. Measurement points are spaced by $0.5\ \text{mm}$ from the center of the substrate to its edge. At each point, the diameters (heights) are calculated from $n = 12$ ($n = 10$) different nanocylinders. The square markers and the error bars in the graphs represent the mean and the standard deviation of the local uniformity, respectively. The horizontal dotted black lines and the top and bottom sides of the gray shaded boxes in the graphs represent the mean and the standard deviation of the global uniformity, respectively. **(d)** Top diameters, **(e)** bottom diameters, and **(f)** heights are shown as a function of distance from the substrate center.

can be observed from the SEM image of a cleaved nanocylinder substrate (**Fig. 3.3a**). To quantify this, we measure the dimensions of nanocylinders at radial distances from the substrate center out to $3.5\ \text{mm}$ and spaced by $0.5\ \text{mm}$ (thus covering the entire circularly patterned area with radius $\sim 4\ \text{mm}$ on the $10 \times 10\ \text{mm}^2$ -sized substrate). From analysis of top-view SEM images (**Fig. 3.3b**), we observe that the top (**Fig. 3.3d**) and bottom diameters (**Fig. 3.3e**) exhibit excellent local uniformity, defined as the uniformity at each measurement position (averaged relative standard deviation (RSD) of 4.4% (top) and 2.3% (bottom)). The global uniformity across the substrate displayed similar values (RSD of 4.7% (top) and 2.7% (bottom)). Fluctuations in diameters likely result from the instability of the e-beam during the patterning process of the Cr etch mask. The observation that the top diameters are nonetheless slightly less uniform than the bottom diameters may result from the fact that etching erodes

the Cr mask in a non-uniform fashion depending on the roughness of the mask surface³⁹, as is backed up by an analysis of the roundness of the top and bottom nanocylinder surfaces (**Supplementary Fig. S3.4**). From tilted-view SEM images (**Fig. 3c**), we also extract the nanocylinder heights (**Fig. 3.3f**), which similarly show very good uniformity both locally (averaged RSD of 0.6%) and globally (RSD of 1.4%). We attribute the nearly monotonic increase in heights outward from the substrate center to the well-known loading effect, in which the transport and depletion of etching species along a substrate contribute to etch rate nonuniformity⁴⁰. The analysis of a batch of low aspect-ratio (1.6) nanocylinders reveals identical trends (**Supplementary Fig. S3.4** and **Supplementary Table S3.3**; etching conditions in **Supplementary Table S3.2**), thereby proving that our protocol can be used to generate both low and high aspect-ratio nanoscale structures with high uniformity.

3.2.5. Surface functionalization and bioconjugation of single-crystal TiO₂

We now demonstrate highly efficient and versatile surface functionalization and bioconjugation of single-crystal rutile TiO₂ (**Fig. 3.4a**). We perform the functionalization experiments on single-crystal TiO₂ nanostructures fabricated using our developed SF₆-based plasma etching process presented earlier. Compared with CHF₃-based etching, this process results in a lower degree of surface contamination by C_xF_y, and hence a higher surface linker coverage.

To quantitatively characterize the surface coating efficiency of different covalently bound surface linkers, we first test functionalization on single-crystal rutile TiO₂ substrates with large-scale square micro-patterns (25 × 25 μm²) embedded in a thick (1–2 μm) PMMA layer (**Fig. 3.4b**). Similarly to other oxide materials, the surface of TiO₂ is populated by hydroxyl groups that allow it to be functionalized with different types of linker molecules, such as silanes and other organic molecules with covalent hydroxyl-binding capacity^{33,41}. Here, we have tested four different surface linker molecules: an aminoalcohol (ethanolamine hydrochloride; ETA), an epoxysilane ((3-glycidoxypropyl)dimethylethoxysilane; GPDMS), a widely used alkoxy silane ((3-aminopropyl)dimethylethoxysilane; APDMS), and a cyclic azasilane (N-n-Butyl-aza-2,2-dimethoxysilacyclopentane; BADMSCP). Additionally, since PEG coatings are widely used for surface passivation⁴² and as biocompatibility layers⁴³, we have also tested the covalent attachment of heterobifunctional PEG to ETA-coated surfaces (**Supplementary Methods, Supplementary Fig. S3.5**). To compare the coating efficiency of these different linkers, we covalently bind fluorophores (ATTO 647N; λ_{excitation} = 640 nm, λ_{emission} = 669 nm) to the functionalized micro-patterns and measure the fluorescence intensity using quantitative fluorescence microscopy (**Supplementary Methods**). The fluorescence measurements report successful surface functionalization for all surface linkers used (**Supplementary Fig. S3.5**).

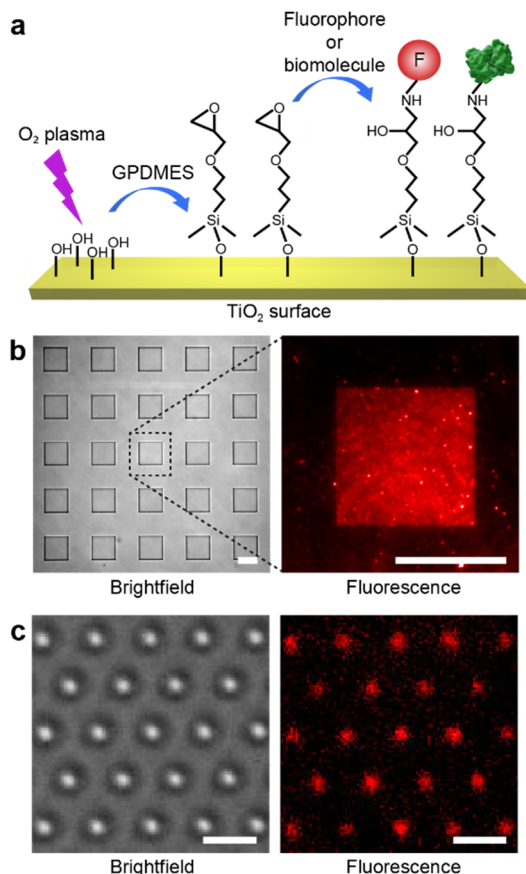


Figure 3.4. Characterization of the efficiency of surface functionalization of single-crystal TiO₂ structures using fluorescence microscopy. **(a)** Illustration of the surface coating steps. First, single-crystal TiO₂ surfaces are O₂ plasma-treated to generate hydroxyl groups (-OH). Then epoxysilanes (GPDMES) are covalently bound to the surface hydroxyl groups. Consequently, either fluorophores (red) or biomolecules (e.g., streptavidin (green)) are bound covalently to the reactive epoxy functional group. **(b)** Functionalized micro-patterns for quantitative characterization of the efficiency of surface functionalization. The brightfield image (left panel) shows squares (25 × 25 μm²) patterned on PMMA-coated TiO₂ substrate. The corresponding zoom-in fluorescence image (right panel) of a square shows successful covalent binding of the amino-labeled fluorophores (ATTO 647N) to the epoxysilane functionalized surface. Scale bars denote 20 μm. **(c)** Functionalized nanostructures for qualitative characterization of the efficiency of surface functionalization. Brightfield (left panel) and corresponding fluorescence (right panel) images of top-area functionalized TiO₂ nanocylinders using the same method as above. Scale bars denote 2 μm.

Regarding subsequent bioconjugation to TiO₂ surfaces, several considerations lead us to select epoxysilane (GPDMES) as the most appropriate surface linker. To start, epoxysilanes are widely used for their demonstrated reliability in surface functionalization⁴⁴ and biomolecule attachment⁴⁵. Furthermore, GPDMES-coated TiO₂ surfaces demonstrate high surface linker coating density and homogeneity (**Fig. 3.4b**). Indeed, while GPDMES coatings provide a slightly lower surface linker density than ETA or PEGylated ETA

coatings, their coating efficiency is significantly higher than the one obtained using BADMSCP and comparable to that of commonly used APDMES (**Supplementary Fig. S3.5**).

More importantly, the greatest advantages of using GPDMEs compared to other surface linkers are: first the ability of the epoxy group to react directly with the primary amino groups of biomolecules that permits bioconjugation in absence of additional crosslinkers, avoiding conditions that could harm the structural and functional integrity of the target biomolecules; and second the rapid surface functionalization process (e.g., ~15 min compared to ~12 h of all the other linkers; **Supplementary Methods**). With this procedure in hand, epoxysilane-functionalized TiO₂ surfaces can readily be used for the covalent conjugation of a majority of biomolecules. We apply this bioconjugation process to the single-crystal TiO₂ nanocylinder arrays on the substrate (**Fig. 3.1, step 7–11**) prior to their mechanical cleaving (**Fig. 3.1, step 12**) to avoid additional, subsequent purification procedures. At this stage, functionalization can be applied to specific areas of the TiO₂ nanocylinders through partial PMMA coating (**Fig. 3.1, step 8–10**). Using this approach, we are able to functionalize and bioconjugate only the top parts of the TiO₂ nanocylinders (**Fig. 3.1, step 11**). Fluorescence microscopy has also been used to qualitatively demonstrate the successful functionalization of individual TiO₂ nanocylinders (**Fig. 3.4c**).

3.2.6. Degree of monodispersity in coated single-crystal TiO₂ nanoparticles

Our ability to functionalize single-crystal TiO₂ nanoparticles with high surface linker density and homogeneity can also be beneficial in different contexts. For example, following the mechanical cleaving that liberates the nanocylinders from the TiO₂ substrate, it is necessary to prevent their aggregation in aqueous environments. Generally speaking, the aggregation of nanoparticles depends on both the surface composition of the nanoparticles and the type of solution in which they are immersed⁴⁶. We have tested different surface coatings and buffer solutions that effectively prohibit single-crystal TiO₂ nanoparticle aggregation and have evaluated those using dynamic light scattering (DLS) measurements (**Supplementary Fig. S3.6**). We find that non-coated TiO₂ nanocylinders aggregate substantially over time in deionized (DI) water, in contrast to what occurs in physiological phosphate buffered saline (PBS) solution at similar pH (7.4). We also find that the addition of bovine serum albumin (BSA, 2% (m/v)), which is widely used as surface passivation agent⁴⁷, deteriorates substantially the monodispersity of TiO₂ nanocylinders in both DI water and PBS solution. When we apply a PEG coating – widely implemented for passivating nanoparticle surfaces to decrease aggregation and enhancing their biocompatibility⁴³ – to TiO₂ nanocylinders, we observe no aggregation in either DI water or PBS solution. Such PEG-coated TiO₂ nanocylinders refrain from aggregation even when they are conjugated to biomolecules such as biotin or DNA. Likewise, the

GPDMES-coated TiO₂ nanocylinders with bioconjugated streptavidin show no aggregation at physiological condition (PBS solution) and therefore have been chosen for the single-molecule OTW experiments.

3.2.7. Characterization of individual DNA molecules using single-crystal TiO₂ nanocylinders

To demonstrate the potential of our developed fabrication and surface coating processes for diverse applications, we tether single-crystal TiO₂ nanocylinders to individual linear, double-stranded DNA molecules and perform stretching and twisting experiments in an OTW. For these measurements, we use GPDMES-functionalized, streptavidin-coated single-crystal TiO₂ nanocylinders fabricated in SF₆ plasma (**Methods**), and test their response to force and torque applied on torsionally constrained 20.6 kbp DNA (contour length of $\sim 7 \mu\text{m}$; **Supplementary Methods**). A biotinylated handle on one extremity of the DNA is designed to bind to the streptavidin-coated nanocylinders, whereas the other extremity of the DNA includes digoxigenin to allow it to bind to the digoxigenin antibodies that are covalently bound to a heterobifunctional PEG-coated flow cell channel (**Fig. 3.5a, Supplementary Methods**).

Prior to performing measurements on these DNA-tethered single-crystal TiO₂ nanocylinders in an OTW (**Supplementary Methods**), we calibrate the optical trap by using individual non-tethered nanocylinders to measure its trap stiffness (**Supplementary Fig. S3.7**). We can then apply a force to a tethered nanocylinder and stretch the DNA (**Fig. 3.5b**). The obtained force-extension data are fitted to the worm-like chain (WLC) model⁴⁸ (red line in **Fig. 3.5b**) and yield a persistence length of $45 \pm 1 \text{ nm}$ and contour length of $6.8 \pm 0.2 \mu\text{m}$ (means and standard deviations for $n = 5$ different DNA tethers), in excellent agreement with previous reports^{30,31,48}. We additionally rotate the nanocylinder at low constant force (0.5 pN) or medium constant force (1.8 pN) to supercoil the tethered DNA molecule. The resulting extension-rotation relation (**Fig. 3.5c**) shows the characteristic symmetric (asymmetric) response of twisted DNA in the low (medium) force regime, also in agreement with previous reports^{31,49–52}. We note that the OTW provides an excellent platform to evaluate the quality of our top-down fabrication of single-crystal TiO₂ nanostructures, as only nanocylinders with precisely controlled dimensions and uniformity are appropriate for stable and reproducible optical trapping. Furthermore, use of the OTW to stretch and twist DNA molecules provides a stringent test of the applied surface functionalization, as these processes (notably twisting) are only possible provided that the surface functionalization and bioconjugation processes are sufficiently efficient to allow for the formation of multiple stable bonds at either DNA extremity⁵².

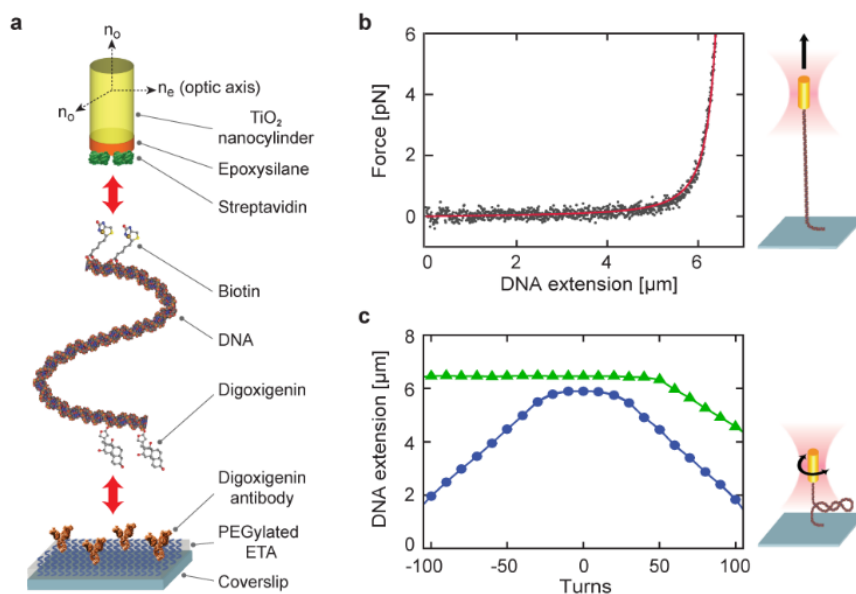


Figure 3.5. Application of DNA-tethered single-crystal rutile TiO_2 nanocylinders in an OTW. **(a)** Schematic of a DNA tethered at one extremity to a single-crystal rutile TiO_2 nanocylinder and at the other extremity to a flow cell channel surface. For the nanocylinder, the orientations of ordinary (n_o) and extraordinary (n_e) refractive indices are indicated. First, we functionalize the flow cell channel surface with ETA, PEG, and digoxigenin antibodies. Then the end of the DNA containing the digoxigenin-enriched handle is attached to the flow cell channel surface via an antigen-antibody binding. The other extremity of the DNA that contains the biotin-enriched handle binds to the streptavidin-coated nanocylinder. **(b)** The extension of tethered DNA as a function of force. The gray dots represent force-extension data while the red line is a fit to the WLC model. The illustration depicts a fully stretched DNA. **(c)** The response of DNA to rotation at different stretching forces (blue circles and green triangles for 0.5 pN and 1.8 pN, respectively). The corresponding illustration represents a supercoiled DNA.

3.3. Conclusions

We have developed and optimized processes for the fabrication, surface functionalization, and bioconjugation of single-crystal TiO_2 nanostructures and nanoparticles. Using two top-down etching approaches, we demonstrate the fabrication of highly uniform nanostructures and nanoparticles with controllable shapes and dimensions. The CHF_3 -based etching process provides a wider range of etch geometries, while the SF_6 -based etching process results in improved surface quality allowing homogenous and dense coating. We are able to etch single-crystal TiO_2 into various nanoscale shapes, including cylinders, cones, and hourglass-shaped structures. The fabricated nanostructures have diameters in the range of 100-600 nm, with heights up to 1-2 μm under etching conditions that yield high etch rate and selectivity. Using SF_6 -etched single-crystal TiO_2 nanocylinders, we show how they can be functionalized with high efficiency and be conjugated covalently to a majority of biomolecules. We

demonstrate the use of these coated TiO₂ nanocylinders by stretching and twisting individually tethered DNA molecules, an application that exploits the tight dimensional control and high-quality surface functionalization of nanocylinders etched from a rutile (100) single-crystal TiO₂ substrate. Our developed fabrication and surface functionalization methods will likely find utilization in diverse optical and electronic applications of single-crystal TiO₂, including applications in life science-oriented fields through e.g. the development of biosensors and single-molecule techniques.

3.4. Methods

3.4.1. Fabrication and bioconjugation of single-crystal rutile TiO₂ nanocylinders for OTW experiments

We use single-side polished single-crystal rutile TiO₂ (100) substrates (Latech, Singapore), 10 × 10 mm² in size and 0.5 mm in thickness, to produce nanocylinders. We clean the substrates in fuming nitric acid (99.5%, Sigma-Aldrich, The Netherlands) using ultrasonication for 10 min followed by thorough rinsing in DI water and drying under a nitrogen (N₂) stream (**Fig. 3.1, step 1**). We then subject the substrates to an O₂ plasma (TePla300, PVA TePla, Germany), after which we spin-coat ~250 nm-thick e-beam resist layer (PMMA 950k A4, MicroChem, Germany) at 500 rpm for 5 s and then 3000 rpm for 55 s. We bake the resist-coated substrates on a hotplate for 30 min at 175 °C (**Fig. 3.1, step 2**). The substrates do not require an additional conductive layer to prevent charge accumulation during e-beam patterning since it has sufficiently high electrical conductivity.

We then use an e-beam patterning system (EBPG 5000+, Leica, UK; the acceleration voltage is set to 100 kV and the aperture diameter to 400 μm) to pattern the PMMA layer by a defocused e-beam with circular cross-section and tunable diameter. The patterning of each circular shape is performed by a single-pixel e-beam exposure, defining the shapes of the Cr mask for subsequent nanocylinder etching. Using an e-beam condition (current of 85 nA, defocusing of 100–200 nm, and dose of 2000 μC/cm²), we pattern circles with 600 nm pitch on a circular patterning area with radius ~4 mm (~140 million masks in total) in <30 min. We develop the patterned substrate using a solution of methyl isobutyl ketone (MIBK, Sigma-Aldrich, The Netherlands) and isopropyl alcohol (IPA, Sigma-Aldrich, The Netherlands) (1:3 MIBK:IPA) for 60 s with constant hand agitation at room temperature. We then rinse the substrate in IPA for 30 s and dry it under a N₂ stream (**Fig. 3.1, step 3**).

We deposit the Cr mask layer using either an e-beam evaporator (Temescal FC-2000, Ferrotec, Germany) or a thermal evaporator (L560, Leybold Heraeus, Germany) loaded with Cr pieces (purity of 99.95%, Kurt J. Lesker, Germany), using the patterned PMMA layer as evaporation windows. We use

slow Cr deposition rates ($\leq 1.0 \text{ \AA/s}$) to obtain high quality Cr layers (**Fig. 3.1, step 4**). We finalize Cr mask formation in a lift-off process by soaking the substrate into preheated ($80 \text{ }^\circ\text{C}$) resist stripper (PRS-3000, JTBaker, The Netherlands) for 20 min with constant agitation using magnetic spinner. Then we thoroughly rinse the substrate in DI water and dry it under a N_2 stream (**Fig. 3.1, step 5**).

We etch TiO_2 nanocylinders using the optimized conditions (**Supplementary Table S3.2**) for vertical sidewall angles (**Fig. 3.1, step 6**). We etch nanocylinders with either an RIE system (Fluor Z401S, Leybold Heraeus, Germany; **Fig. 3.2a,b**) or an ICP-RIE system (Plasmalab system 100, Oxford Instr., UK; **Fig. 3.2f**). For dimensional analysis of the etched nanocylinders, we employ SEM systems (Hitachi S4800 FESEM, FEI XL30S FEG SEM, or FEI Nova NanoSEM). We remove the used Cr mask using a wet etchant (Chrome etch n°1, MicroChemicals, Germany) and then perform surface cleaning using fuming nitric acid and O_2 plasma (TePla300) for the subsequent surface functionalization (**Fig. 3.1, step 7**).

Optionally, if area-selective functionalization on top of the nanocylinders is required, we cover their sidewalls with a temporary protection layer. We cover the substrate with PMMA 950k resist at a chosen concentration to provide a spin-coated thickness larger than the heights of the nanocylinders (**Fig. 3.1, step 8**). Consequently, we etch the PMMA layer to render the tops of the nanocylinders accessible, using either O_2 plasma (TePla300) or MIBK solution (**Fig. 3.1, step 9**). Note that we do not bake the resist in order to allow for its straightforward removal afterwards.

To attach biomolecules to TiO_2 nanocylinders, we first activate the nanocylinder substrates by O_2 plasma treatment (Plasma-PREEN I, Plasmatic Systems Inc., USA). Then we bind GPDMS to the substrate for 15 min at $75 \text{ }^\circ\text{C}$ using non-diluted GPDMS solution, and wash the substrate in chloroform (CHROMASOLV plus, for HPLC, $\geq 99.9\%$, Sigma-Aldrich, The Netherlands) three times for 15 s each, followed by drying under a N_2 stream (**Fig. 3.1, step 10**). (If a temporary PMMA layer is used for area-selective functionalization, we first wash the substrate in ethanol three times for 15 s each directly after the incubation with GPDMS, followed by drying under a N_2 stream. We then remove the temporary PMMA layer in chloroform for 15 min at room temperature, followed by additional washing in fresh chloroform three times for 15 s each and drying under a N_2 stream.)

We then bind streptavidin molecules to the epoxy group of GPDMS, by incubating the nanocylinders with $2 \text{ } \mu\text{M}$ streptavidin (Sigma-Aldrich, The Netherlands) in PBS solution (pH 7.4, Sigma-Aldrich, The Netherlands) for 1 h at room temperature. After washing three times for 15 s each with PBS/TWEEN® solution (pH 7.4, PBS containing 0.1% (v/v) TWEEN® 20 (Sigma-Aldrich, The Netherlands)), we wash with PBS solution (pH 7.4) another three times for 15 s each (**Fig. 3.1, step 11**).

We cleave TiO₂ nanocylinders mechanically from the substrate using a diamond microtome blade (DT315D50, C.L. Sturkey, USA) inside a PBS/Triton™ droplet (pH 7.4, PBS containing 0.05% (v/v) Triton™ X-100 (Sigma-Aldrich, The Netherlands)), followed by suction of the droplet by a micropipette (**Fig. 3.1, step 12**). These cleaved, streptavidin-coated TiO₂ nanocylinders can be further coupled with biomolecules of interest, e.g. DNA with biotinylated handles, by incubating them in a flow cell channel for OTW experiments (**Supplementary Methods**).

3.5. References

1. Wang, G. et al. Hydrogen-treated TiO₂ nanowire arrays for photoelectrochemical water splitting. *Nano Letters* **11**, 3026-3033 (2011).
2. Yu, H., Zhang, K. & Rossi, C. Experimental study of the photocatalytic degradation of formaldehyde in indoor air using a nano-particulate titanium dioxide photocatalyst. *Indoor and built Environment* **16**, 529-537 (2007).
3. Hwang, S. et al. A near single crystalline TiO₂ nanohelix array: enhanced gas sensing performance and its application as a monolithically integrated electronic nose. *Analyst* **138**, 443-450 (2013).
4. Gale, E. TiO₂-based memristors and ReRAM: materials, mechanisms and models (a review). *Semiconductor Science and Technology* **29**, 104004 (2014).
5. Shih, W. S., Young, S. J., Ji, L. W., Water, W. & Shiu, H. W. TiO₂-based thin film transistors with amorphous and anatase channel layer. *Journal of the Electrochemical Society* **158**, H609-H611 (2011).
6. Liu, X. et al. Large-diameter titanium dioxide nanotube arrays as a scattering layer for high-efficiency dye-sensitized solar cell. *Nanoscale Research Letters* **9**, 362 (2014).
7. Tang, Y. et al. Unravelling the correlation between the aspect ratio of nanotubular structures and their electrochemical performance to achieve high-rate and long-life lithium-ion batteries. *Angewandte Chemie* **126**, 13706-13710 (2014).
8. Tang, Y. et al. Conductive inks based on a lithium titanate nanotube gel for high-rate lithium-ion batteries with customized configuration. *Advanced Materials* **28**, 1567-1576 (2015).
9. Bradley, J. D. B. et al. Submicrometer-wide amorphous and polycrystalline anatase TiO₂ waveguides for microphotonic devices. *Optics Express* **20**, 23821-23831 (2012).
10. Wang, X., Fujimaki, M. & Awazu, K. Photonic crystal structures in titanium dioxide (TiO₂) and their optimal design. *Optics Express* **13**, 1486-1497 (2005).
11. Jannasch, A., Demirörs, A. F., van Oostrum, P. D. J., van Blaaderen, A. & Schäffer, E. Nanonewton optical force trap employing anti-reflection coated, high-refractive-index titania microspheres. *Nature Photonics* **6**, 469 (2012).
12. Morris Hotsenpiller, P. A., Bolt, J. D., Farneth, W. E., Lowekamp, J. B. & Rohrer, G. S. Orientation dependence of photochemical reactions on TiO₂ surfaces. *The Journal of Physical Chemistry B* **102**, 3216-3226 (1998).
13. Wang, R., Sakai, N., Fujishima, A., Watanabe, T. & Hashimoto, K. Studies of surface wettability conversion on TiO₂ single-crystal surfaces. *The Journal of Physical Chemistry B* **103**, 2188-2194 (1999).
14. Baik, J. M. et al. High-yield TiO₂ nanowire synthesis and single nanowire field-effect transistor fabrication. *Applied Physics Letters* **92**, 242111 (2008).
15. Feng, X., Zhu, K., Frank, A. J., Grimes, C. A. & Mallouk, T. E. Rapid charge transport in dye-sensitized solar cells made from vertically aligned single-crystal rutile TiO₂ nanowires. *Angewandte Chemie International Edition* **51**, 2727-2730 (2012).
16. Bi, Z.-F. et al. Optical waveguides in TiO₂ formed by He ion implantation. *Optics Express* **20**, 6712-6719 (2012).
17. Awazu, K., Fujimaki, M., Ohki, Y. & Komatsubara, T. Photonic crystals of titanium dioxide fabricated by swift heavy ions. *Radiation Measurements* **40**, 722-729 (2005).
18. Agarwal, A. M., Liao, L., Foresi, J. S., Black, M. R., Duan, X. & Kimerling, L. C. Low-loss polycrystalline silicon waveguides for silicon photonics. *Journal of Applied Physics* **80**, 6120-6123 (1996).
19. Stone, A. et al. Direct laser-writing of ferroelectric single-crystal waveguide architectures in glass for 3D integrated optics. *Scientific Reports* **5**, 10391 (2015).
20. Lipfert, J., van Oene, M. M., Lee, M., Pedaci, F. & Dekker, N. H. Torque spectroscopy for the study of rotary motion in biological systems. *Chemical Reviews* **115**, 1449-1474 (2015).

21. Wang, Y., He, Y., Lai, Q. & Fan, M. Review of the progress in preparing nano TiO₂: an important environmental engineering material. *Journal of Environmental Sciences (China)* **26**, 2139-2177 (2014).
22. Tang, Y. et al. Mechanical force-driven growth of elongated bending TiO₂-based nanotubular materials for ultrafast rechargeable lithium ion batteries. *Advanced Materials* **26**, 6111-6118 (2014).
23. Miao, Z., Xu, D., Ouyang, J., Guo, G., Zhao, X. & Tang, Y. Electrochemically induced sol-gel preparation of single-crystalline TiO₂ nanowires. *Nano Letters* **2**, 717-720 (2002).
24. Huang, Y., Pandraud, G. & Sarro, P. M. The atomic layer deposition array defined by etch-back technique: a new method to fabricate TiO₂ nanopillars, nanotubes and nanochannel arrays. *Nanotechnology* **23**, 485306 (2012).
25. Shkondin, E. et al. Fabrication of high aspect ratio TiO₂ and Al₂O₃ nanogratings by atomic layer deposition. *Journal of Vacuum Science and Technology A* **34**, 031605 (2016).
26. Jeong, H. Y., Lee, J. Y. & Choi, S.-Y. Direct observation of microscopic change induced by oxygen vacancy drift in amorphous TiO₂ thin films. *Applied Physics Letters* **97**, 042109 (2010).
27. Dekker, J., Kolari, K. & Puurunen, R. Inductively coupled plasma etching of amorphous Al₂O₃ and TiO₂ mask layers grown by atomic layer deposition. *Journal of Vacuum Science and Technology B* **24**, 2350-2355 (2006).
28. Karouta, F. A practical approach to reactive ion etching. *Journal of Physics D: Applied Physics* **47**, 233501 (2014).
29. Tang, J., Wang, Y., Li, J., Da, P., Geng, J. & Zheng, G. Sensitive enzymatic glucose detection by TiO₂ nanowire photoelectrochemical biosensors. *Journal of Materials Chemistry A* **2**, 6153-6157 (2014).
30. Wang, M. D., Yin, H., Landick, R., Gelles, J. & Block, S. M. Stretching DNA with optical tweezers. *Biophysical Journal* **72**, 1335-1346 (1997).
31. Huang, Z., Pedaci, F., van Oene, M., Wiggin, M. J. & Dekker, N. H. Electron beam fabrication of birefringent microcylinders. *ACS Nano* **5**, 1418-1427 (2011).
32. Pujari, S. P., Scheres, L., Marcelis, A. T. M. & Zuilhof, H. Covalent surface modification of oxide surfaces. *Angewandte Chemie International Edition* **53**, 6322-6356 (2014).
33. Kim, W.-J. et al. Enhanced protein immobilization efficiency on a TiO₂ surface modified with a hydroxyl functional group. *Langmuir* **25**, 11692-11697 (2009).
34. Wang, Y. et al. TiO₂ micro-devices fabricated by laser direct writing. *Optics Express* **19**, 17390-17395 (2011).
35. Kaliasas, R., Baltrusaitis, J., Mikolajūnas, M., Jakučionis, L. & Viržonis, D. Scaling down lateral dimensions of silicon nanopillars fabricated by reactive ion etching with Au/Cr self-assembled clusters as an etch mask. *Thin Solid Films* **520**, 2041-2045 (2012).
36. Milenin, A., Jamois, C., Geppert, T., Gösele, U. & Wehrspohn, R. SOI planar photonic crystal fabrication: Etching through SiO₂/Si/SiO₂ layer systems using fluorocarbon plasmas. *Microelectronic Engineering* **81**, 15-21 (2005).
37. Suzuki, K., Youn, S.-W., Wang, Q., Hiroshima, H. & Nishioka, Y. Fabrication of sub 20-nm wide grooves in a quartz mold by space narrowing dry etching. *Microelectronic Engineering* **110**, 432-435 (2013).
38. Somashekhar, A., Ying, H., Smith, P. B., Aldrich, D. B. & Nemanich, R. J. Hydrogen plasma removal of post-RIE residue for backend processing. *Journal of The Electrochemical Society* **146**, 2318-2321 (1999).
39. Mohamed, K. & Alkaisi, M. M. Investigation of a nanofabrication process to achieve high aspect-ratio nanostructures on a quartz substrate. *Nanotechnology* **24**, 015302 (2013).
40. Giapis, K. P., Scheller, G. R., Gottscho, R. A., Hobson, W. S. & Lee, Y. H. Microscopic and macroscopic uniformity control in plasma etching. *Applied Physics Letters* **57**, 983-985 (1990).
41. Diebold, U. The surface science of titanium dioxide. *Surface Science Reports* **48**, 53-229 (2003).
42. Chandradoss, S. D., Haagsma, A. C., Lee, Y. K., Hwang, J.-H., Nam, J.-M. & Joo, C. Surface passivation for single-molecule protein studies. *Journal of Visualized Experiments* 50549 (2014).
43. Li, H., Zhang, X., Zhang, X., Wang, K., Liu, H. & Wei, Y. Facile preparation of biocompatible and robust fluorescent polymeric nanoparticles via PEGylation and cross-linking. *ACS Applied Materials & Interfaces* **7**, 4241-4246 (2015).
44. Chen, L., Yang, B. & Zhang, J. Preparation and tribological properties of polymer film covalently bonded to silicon substrate via an epoxy-terminated self-assembled monolayer. *Journal of Adhesion Science and Technology* **28**, 1725-1738 (2014).
45. Nam, Y., Branch, D. W. & Wheeler, B. C. Epoxy-silane linking of biomolecules is simple and effective for patterning neuronal cultures. *Biosensors and Bioelectronics* **22**, 589-597 (2006).
46. Ji, Z. et al. Dispersion and stability optimization of TiO₂ nanoparticles in cell culture media. *Environmental Science and Technology* **44**, 7309-7314 (2010).
47. Sweryda-Krawiec, B., Devaraj, H., Jacob, G. & Hickman, J. J. A new interpretation of serum albumin surface passivation. *Langmuir* **20**, 2054-2056 (2004).

48. Bouchiat, C., Wang, M., Allemand, J.-F., Strick, T., Block, S. & Croquette, V. Estimating the persistence length of a worm-like chain molecule from force-extension measurements. *Biophysical Journal* **76**, 409-413 (1999).
49. Koster, D. A., Croquette, V., Dekker, C., Shuman, S. & Dekker, N. H. Friction and torque govern the relaxation of DNA supercoils by eukaryotic topoisomerase IB. *Nature* **434**, 671 (2005).
50. Gutiérrez-Medina, B., Andreasson, J. O. L., Greenleaf, W. J., LaPorta, A. & Block, S. M. An optical apparatus for rotation and trapping. *Methods in Enzymology* **475**, 377-404 (2010).
51. Li, P. C., Chang, J. C., La Porta, A. & Yu, E. T. Fabrication of birefringent nanocylinders for single-molecule force and torque measurement. *Nanotechnology* **25**, 235304 (2014).
52. Strick, T. R., Allemand, J. F., Bensimon, D., Bensimon, A. & Croquette, V. The elasticity of a single supercoiled DNA molecule. *Science* **271**, 1835 (1996).

3.6. Supplementary Information

3.6.1. Supplementary Methods

3.6.1.1. Orientation of the optic axis in single-crystal rutile TiO₂ nanocylinder for OTW experiment

To control polarization-based rotation of optically trapped nanoparticles in an OTW, birefringent positive uniaxial single-crystals are desirable substrate materials. Single-crystal rutile TiO₂ is such a material, and it has an exceptionally high birefringence that is advantageous for effective torque transfer in an OTW. In particular, cylindrically shaped nanoparticles align their long axis with the direction of laser beam propagation, fixing two of the three rotational degrees of freedom (DOF). The remaining rotational DOF is controllable via the polarization of the laser beam provided that the optic axis is perpendicular to the nanocylinder's long axis (**Fig. 3.5a**). To appropriately control the orientation of this optic axis within the nanocylinders, it is necessary to etch into (100)-cut single-crystal rutile TiO₂ substrates. A similar approach has been employed for the case of X-cut single-crystal quartz SiO₂ substrates¹⁻⁵.

3.6.1.2. Considerations for optimal fabrication of the Cr etch mask for single-crystal TiO₂ etching

We consider the optimal fabrication of the Cr etch mask for the desired size of single-crystal TiO₂ nanostructures. The deposited Cr layer should be sufficiently thick for the mask to remain functional until the end of etching process, taking into account the fact that the mask top surface will not be perfectly flat. Also, the overall thickness of the Cr mask is limited by that of the used PMMA layer. The thickness of the PMMA should be 2–3 times larger than that of the Cr mask to facilitate complete lift-off, but it has an upper limit determined by its concentration. In practice, Cr layers thicker than ~150 nm tend to cause more severe deformation in patterned PMMA layers, resulting in higher nonuniformity. This deformation is presumably due to the built-up stress in Cr layers during physical vapor deposition⁶. A further consideration in mask fabrication is that mask shapes tend to be more cone-like when thicker Cr layers and/or smaller patterned apertures are used⁷ (**Fig. 3.1, step 4, inset illustration**). Such masks are not

suitable for anisotropic etching for vertical sidewall due to more rapid erosion of their thinner edges.

3.6.1.3. Surface functionalization procedure of single-crystal TiO₂

For the surface functionalization of single-crystal TiO₂ substrates, we have compared four different surface linker molecules (**Supplementary Fig. S3.5**): ETA (Sigma-Aldrich, The Netherlands), GPDMS (Sigma-Aldrich, The Netherlands), APDMES (Sigma-Aldrich, The Netherlands), and BADMSCP (abcr GmbH, Germany). For the binding of ETA linker, we dissolve ETA in anhydrous dimethyl sulfoxide (DMSO) (Sigma-Aldrich, The Netherlands) to a final concentration of 5 M. We use this ETA/DMSO solution to incubate the substrates for 12 h at room temperature, followed by washing the substrates with DI water. For the binding of epoxysilane linker (GPDMS), we incubate the substrates for 15 min at 75 °C using non-diluted GPDMS solution, followed by chloroform washing. For the binding of the APDMES and BADMSCP linkers, we incubate the substrates in ethanol containing either 5% (v/v) of APDMES or BADMSCP. We carry out the silanization reaction for 12 h at 70 °C and then wash with chloroform (or ethanol). Additionally, we perform PEGylation of ETA-coated surfaces with heterobifunctional NHS-PEG-COOH (MW 5,000, LaysanBio, USA) ⁸. We incubate the surfaces with 2 mM PEG dissolved in 100 mM 2-(N-morpholino)ethanesulfonic acid (MES) buffer (pH 4.7, Sigma-Aldrich, The Netherlands) for 1 h at room temperature. Afterwards, we wash the PEGylated surfaces with DI water. For every washing step involved, we wash three times for 15 s each, and then dry the substrates under a N₂ stream. The above protocols can also be applied to other oxidized surfaces, e.g. quartz (SiO₂) (**Supplementary Fig. S3.5**), silicon (Si), silicon nitride (Si₃N₄), and non-noble metals.

3.6.1.4. Evaluation of single-crystal TiO₂ surface functionalization efficiency via fluorescence microscopy

We fabricate 25 × 25 μm² micro-patterns of PMMA on single-crystal rutile TiO₂ and quartz SiO₂ substrates for quantitative evaluation of the surface linker functionalization efficiencies via fluorescence microscopy. To fabricate the PMMA micro-patterns, we utilize a similar protocol as described for TiO₂ nanocylinders (**Methods**). The main differences include spin-coating PMMA 950k A11 to achieve a ~1.9 μm-thick layer and altered e-beam settings (a current of 312 nA, a diameter of 300 nm through defocusing the beam, and a dose of 1000 μC/cm²). For the quartz SiO₂ substrates (X-cut, University Wafer, USA) alone, we sputter a 30 nm-thick gold (Au) layer (EM ACE600, Leica, The Netherlands) onto the spin-coated PMMA layer to prevent charging. Following e-beam patterning, we remove the Au layer by a wet etchant (TFA, Transene, USA). As described in **Methods**, we treat the micro-patterned substrates with O₂ plasma (Plasma-PREEN I) prior to the functionalization process.

For the evaluation of the surface functionalization efficiencies of the different linkers to single-crystal TiO₂ (and SiO₂) substrates, we use amino and NHS-ester

modified fluorophores (ATTO 647N, ATTO-TEC GmbH, Germany). They are covalently added to the organic functional groups of the surface linkers employed. For the substrates coated with ETA, APDMES, and BADMSCP, we dissolve NHS-ester labeled fluorophores in PBS buffer (pH 8.4, Sigma-Aldrich, The Netherlands) to a final concentration of 10 μM and add to the functionalized surfaces. After the reaction time of 1 h, we wash the substrates three times each with PBS/TWEEN® buffer (pH 7.4) and DI water to remove residual physisorbed molecules, and dry under a N_2 stream. For GPDMS-coated and PEGylated surfaces, we add 10 μM of amino-labeled fluorophores to PBS buffer (pH 7.4) and MES/EDC buffer (100 mM MES (pH 4.7) containing 50 mM EDC (1-Ethyl-3-(3-dimethylaminopropyl)carbodiimid, Sigma-Aldrich)), respectively, and the fluorophore coupling reactions take place for 1 h. We wash the substrates with PBS/TWEEN® buffer (pH 7.4) and DI water, followed by drying under a N_2 stream, as stated before.

We perform the fluorescence measurements of the functionalized surfaces and nanocylinders using an epifluorescence microscope (IX-81, Olympus, The Netherlands) equipped with a Peltier-cooled back-illuminated electron multiplying charge coupled device (EMCCD) camera (IXON, 512 \times 512 pixels, Andor, Ireland), in combination with an oil-immersion objective lens (100 \times /NA1.3, UPLNFLN, Olympus, The Netherlands). The fluorophores are excited using a diode laser ($\lambda = 640$ nm, Cell Laser System, Olympus, The Netherlands). For quantitative measurements, we measure the fluorescence intensity (in photon counts per second) of an area of 12.5 \times 12.5 μm^2 for different square micro-patterns on each sample. We calculate the average intensity – normalized to the area of 1 μm^2 – and the corresponding standard deviations to compare the different linker molecule coverages (**Supplementary Fig. S3.5**).

3.6.1.5. Preparation of DNA construct for OTW experiments

We carry out the DNA extension and supercoiling measurements (**Fig. 3.5**) on a linear 21.8 kbp DNA that contains biotin and digoxigenin modified nucleotides (biotin-16-dUTP and digoxigenin-11-dUTP, respectively, Roche Diagnostics, The Netherlands) at the opposite extremities (600 bp each). We prepare the DNA by ligating the biotin- and digoxigenin-enriched handles to a 20.6 kbp DNA fragment that is obtained via a *NotI/XhoI* digestion of Supercos1-lambda 1,2 plasmid (Agilent Technologies, USA). We create the DNA handles by PCR amplification of a 1.2 kbp fragment from pBlueScript II SK+ (Agilent Technologies, USA) using the primers – 5'-GACCGAGATAGGGTTGAGTG and 5'-CAGGGTCGGAACAGGAGAGC – in the presence of either biotin-16-dUTP or digoxigenin-11-dUTP. Prior to ligation using T4 DNA ligase (New England Biolabs, UK), the biotin and digoxigenin containing handles are digested with *NotI* and *XhoI*, respectively⁹.

3.6.1.6. Preparation of flow cell for OTW experiments

We perform OTW experiments (**Fig. 3.5**) in a custom-made flow cell assembled from two 24 \times 60 mm² borosilicate coverslips (#1.5, ~170 μm thickness, Menzel GmbH,

Germany) separated by a single-layer Parafilm® (Sigma-Aldrich, The Netherlands) spacer^{1,8,10}. We drill two holes of ~1 mm diameter in the top coverslips using a sand blaster, to connect with inlet and outlet tubings. Prior to flow cell assembly, we clean the coverslips using a 4% (v/v) aqueous Hellmanex® III (Hellma GmbH, Germany) solution and then DI water, in both cases by sonication for 20 min at 40 °C. We dry the cleaned coverslips under a N₂ stream. For the bottom coverslips, we perform surface functionalization to attach biomolecules. To increase the density of surface hydroxyl groups, which allows for denser, more homogeneous functionalization, we treat the bottom coverslips with O₂ plasma (Plasma-PREEN I) for 1 min with O₂ flow rate of 3 scfh and RF power of 200 W. We incubate these coverslips in DMSO solution containing 5 M ETA for 12 h at room temperature. Afterwards, we wash the functionalized coverslips thoroughly with DI water and dry them under a N₂ stream. Single-layer Parafilm® spacers are prepared by cutting out the desired flow cell channel shape, which is properly aligned to the holes in the top coverslips. Finally, we assemble the flow cells and seal the channels by melting the Parafilm® spacers between the coverslips on a hotplate for 30 s at 90 °C.

3.6.1.7. Bioconjugation of DNA to single-crystal TiO₂ nanocylinders for OTW experiments

In an OTW, we are able to carry out the extension and coiling measurements on individual, torsionally constrained DNA molecules.¹⁻⁵ We tether the DNA molecules to the bottom surface of the flow cell channel via digoxigenin:anti-digoxigenin coupling and to the functionalized single-crystal rutile TiO₂ nanocylinders via biotin:streptavidin coupling (**Fig. 3.5a**). To do so, we perform three steps. First, we PEGylate the ETA-coated flow cell channel both to covalently attach digoxigenin antibodies and to ensure an effective surface passivation against non-specific physisorption of streptavidin-coated TiO₂ nanocylinders. We achieve this by incubating the channel with 2 mM PEG dissolved in 100 mM MES buffer (pH 4.7) for 1 h. After washing with DI water, we incubate for 1 h with 8 μM digoxigenin IgG antibodies (Roche Diagnostics, The Netherlands) dissolved in MES/EDC buffer (pH 4.7). We wash the channel with PBS buffer (pH 7.4) and incubate BlockAid™ (Life Technologies, USA) for 1 h for additional surface passivation. Subsequently, we wash the channel with PBS buffer (pH 7.4). Second, we attach individual DNA molecules via the digoxigenin handles to the digoxigenin antibody-covered flow cell channel by incubating 5 pM of DNA for 1 h. We remove non-specifically adhered DNA molecules by washing the channel with PBS buffer (pH 7.4). Third, we attach the DNA via the biotinylated handles to the streptavidin-coated TiO₂ nanocylinders (**Methods**) by incubating them in the flow cell channel for ~30 min. We remove non-attached nanocylinders by flushing 1:1 diluted (v/v) BlockAid™ in PBS/Triton™ buffer (pH 7.4). We perform all DNA extension and coiling measurements in PBS/Triton™ buffer.

3.6.1.8. OTW instrumentation and DNA measurements with single-crystal TiO₂ nanocylinders

For optical trapping of single-crystal TiO₂ nanocylinders in our OTW setup (**Fig. 3.5b,c**), we expand and collimate a linearly polarized laser ($\lambda = 1064$ nm, Compass CW 1064-4000M, Coherent, The Netherlands) beam using a beam expander (4401-181-000-20, LINOS, Germany) to fill properly the input aperture of an objective lens (60 \times /NA1.2, CFI-PLAN-APO-VC-60XA-WI, Nikon, The Netherlands). The power entering the objective lens is always set to 100 mW during experiments. The objective lens focuses the laser beam into a flow cell, generating an optical trap.

To calibrate the optical trap, we monitor the fluctuations of an isolated, optically trapped TiO₂ nanocylinder using a position-sensitive detector (PSD) (DL100-7PCBA3, Pacific Silicon Sensor, The Netherlands) that acquires at 100 kHz (**Supplementary Fig. S3.7**). The nanocylinder trapping position is ~ 7 μm above from the bottom surface of the flow cell channel, to conserve the similar measurement conditions with the case of DNA-tethered nanocylinders¹¹. We can calculate the restoring force acting on a nanocylinder displaced from the trap center, by multiplying the measured displacement with the calibrated trap stiffness. Precise linear translation of the flow cell is possible using a piezo-actuator (P-517.3CD, Physik Instrumente, Germany) in x, y, and z directions.

For the force-induced DNA-extension experiments, we move the flow cell along the axis of laser beam propagation (axial direction) at a constant speed (~ 1 $\mu\text{m/s}$) while maintaining the laser beam at a fixed position. As the flow cell moves away from the laser beam focus, the increased DNA-tethered nanocylinder's displacement from the trap center induces higher axial force to the DNA molecule. For the DNA coiling experiments, a constant axial force should be applied to the trapped, DNA-tethered nanocylinder since whether the DNA twists or forms plectonemic supercoils strongly influenced by the tension applied to the molecule¹². We use a feedback loop between the piezo-actuator and PSD to clamp the axial force at the specified setpoint. By simultaneously rotating the linear input polarization of the laser beam, we apply torque to the TiO₂ nanocylinder, coiling the DNA molecule. The polarization can be rotated either by manual rotation of a half-wave plate (PWPS-1064-10-2, CVI Melles Griot, Germany), or by a fast electro-optical modulator (EOM) (LM 0202-LT, LINOS, Germany) in combination with quarter-wave plates (PWPS-1064-10-4, CVI Melles Griot, Germany).

3.6.2. Supplementary Tables

Table S3.1. Dry etching conditions for single-crystal TiO₂ during optimization of the CHF₃-RIE process.^{a)}

Sample	CHF ₃ flow [sccm]	O ₂ flow [sccm]	Ar flow [sccm]	RF power [W]	Chamber pressure [μbar]	TiO ₂ etch rate [nm/min]	Cr etch rate [nm/min]	Etch selectivity [TiO ₂ :Cr]
Ra1	50	5	30	200	50	68	3.7	18
Ra2	50	5	30	165	50	58	3.2	18
Ra3	50	5	30	100	50	30	1.7	18
Ra4	50	5	30	200	10	30	8.3	4
Rb1	50	5	30	200	50	77	4.1	19
Rb2	50	5	0	200	50	73	3.5	21

^{a)}The bold red numbers denote altered process parameters compared to the reference samples (Ra1 and Rb1).

Dry etching conditions for single-crystal TiO₂ during optimization of the CHF₃-RIE process

We show the representative etching conditions (**Supplementary Table S3.1**) used during optimization of the CHF₃-based plasma etching of single-crystal TiO₂ in an RIE system. Throughout the optimization, we fix the flow rate of CHF₃ gas, the main etchant, at the maximum value of 50 sccm, and set the flow rate of O₂ gas at 5 sccm which is the median value of our target range (0–10 sccm). More accurate comparisons are possible within the same batches of the applied Cr etch mask, designated as Ra (H: 100 nm, D: 535 nm) and Rb (H: 100 nm, D: 345 nm). The samples Ra1 and Rb1 are the reference samples, while the other samples differ by a single process parameter (designated as bold red numbers in **Supplementary Table S3.1**).

As an elevated RF power increases the etch rates of TiO₂ while maintaining nearly constant etch selectivity (compare samples Ra1, Ra2, and Ra3 in **Supplementary Table S3.1**), we select the highest available power (200 W). We find that an increase in the chamber pressure (from 10 to 50 μbar) enhances the etch selectivity by increasing the TiO₂ etch rates and decreasing the Cr etch rates (compare samples Ra1 and Ra4 in **Supplementary Table S3.1**). However, we do not utilize chamber pressures exceeding 50 μbar, as higher values result in excessive deposition of fluorocarbon passivation layers¹³ that are sufficiently thick to reduce the TiO₂ etch rates again. With these parameters fixed, we vary the gas composition. The addition of Ar gas, which results in harsher physical etching by heavy ions, generally increases etch rates.¹⁴ Indeed, upon its addition (at 30 sccm) both the Cr and TiO₂ etch rates are increased; however, as the increase in the Cr etch rate surpasses that of TiO₂, a deteriorated etch selectivity results (compare samples Rb1 and Rb2 in **Supplementary Table S3.1**). Our optimized process condition thus consists of CHF₃ at 50 sccm, a chamber pressure of 50 μbar, and an RF power of 200 W. With these fixed parameters, we vary O₂ gas flow rate from 0 sccm to 10 sccm to control sidewall profiles (**Supplementary Fig. S3.3**), and vertical sidewall can be obtained with 0.5 sccm of O₂.

Table S3.2. Dry etching conditions for single-crystal TiO₂ nanofabrication. ^{a)}

Figure	Etching System	Etching conditions
Fig. 3.2a	F1	Cr etch mask (H: 45 nm, D: 175 nm), CHF₃ :O ₂ = 50:0.5 sccm, RF 200 W, chamber pressure 50 μbar, DC bias -950 V, etch time 11 min (optimized).
Fig. 3.2b	F2	Cr etch mask (H: 100 nm, D: 255 nm), CHF₃ :O ₂ = 50:8 sccm, RF 200 W, chamber pressure 50 μbar, DC bias -1100 V, etch time 15 min (optimized).
Fig. 3.2c	F1	Cr etch mask (H: 100 nm, D: 535 nm), CHF₃ :O ₂ :Ar = 50:5:30 sccm, RF 165 W, chamber pressure 50 μbar, DC bias -855 V, etch time 15 min.
Fig. 3.2d	F3	Cr etch mask (H: 100 nm, D: 535 nm), SF₆ :CH ₄ :Ar = 15:30:50 sccm, ICP:RF = 2500:300 W, chamber pressure 30 μbar, DC bias -50 V, etch time 10 min, sample holder temperature 0 °C, chamber temperature 200 °C.
Fig. 3.2e	F4	Cr etch mask (H: 130 nm, D: 185 nm), SF₆ :He = 50:100 sccm, ICP:RF = 800:200 W, chamber pressure 50 μbar, DC bias -475 V, etch time 12 min, chamber temperature 25 °C.
Fig. 3.2f	F4	Cr etch mask (H: 120 nm, D: 205 nm), SF₆ :He = 20:100 sccm, ICP:RF = 300:300 W, chamber pressure 100 μbar, DC bias -835 V, etch time 4 min, chamber temperature 25 °C (optimized).
Fig. 3.3	F2	Cr etch mask (H: 60 nm, D: 220 nm), CHF₃ :O ₂ = 50:4 sccm, RF 200 W, chamber pressure 50 μbar, DC bias -1100 V, etch time 15 min (optimized).
Fig. 3.5	F4	Cr etch mask, the same etching condition as Fig. 3.2f (SF₆).
Fig. S3.2	F3	Various etch mask materials, SF₆ :CH ₄ :Ar = 15:30:50 sccm, ICP:RF = 1500:250 W, chamber pressure 30 μbar, DC bias -55 V, etch time 10 min, sample holder temperature 0 °C, chamber temperature 200 °C.
Fig. S3.3	F1	Cr etch mask (H: 100 nm, D: 345 nm), the same etching condition as Fig. 3.2a (CHF₃), except for the etch time (15 min) and the O ₂ gas flow rate (0, 0.5, 1, 5, or 10 sccm).
Fig. S3.4	F2	Cr etch mask (H: 30 nm, D: 190 nm), the same etching condition as Fig. 3.3 (CHF₃), except for the etch time (8 min).
Fig. S3.7	F4	Cr etch mask, the same etching condition as Fig. 3.2f (SF₆).

^{a)}The bold red letters denote the main etchant gas in each condition.

Dry etching conditions for single-crystal TiO₂ nanofabrication

We use etching systems that are denoted as F1 (Fluor Z401S, Leybold Heraeus, Germany), F2 (Fluor Z401S, Leybold Heraeus, Germany), F3 (AMS100 I-speeder, Adixen, France), and F4 (Plasmalab System 100, Oxford Instr., UK). The F1 and F2 are two nominally identical RIE systems, while F3 and F4 are two distinct ICP-RIE systems. We summarize the etching conditions for each batch of TiO₂ nanocylinders in **Supplementary Table S3.2**.

Table S3.3. Dimensional analysis of high and low aspect-ratio TiO₂ nanocylinders.

Sample	Statistical parameter	Top diameter	Bottom diameter	Height	Top roundness	Bottom roundness	Volume
Fig. 3.3 (15 min etch)	Average	151 nm	215 nm	652 nm	0.97	0.98	0.017 μm^3
	Local RSD	4.4%	2.3%	0.6%	1.0%	0.5%	4.5%
	Global RSD	4.7%	2.7%	1.4%	1.1%	0.5%	5.2%
Fig. S3.4 (8 min etch)	Average	149 nm	187 nm	273 nm	0.98	0.99	0.006 μm^3
	Local RSD	1.5%	0.9%	1.3%	0.5%	0.3%	2.1%
	Global RSD	2.4%	1.7%	3.1%	0.6%	0.4%	4.1%

Dimensional analysis of high and low aspect-ratio TiO₂ nanocylinders

We have analyzed SEM images of high and low aspect-ratio nanocylinder batches to quantify both the local and global structural uniformity. We summarize the obtained statistical parameters for each batch of TiO₂ nanocylinders in **Supplementary Table S3.3**, and present the corresponding graphs in **Fig. 3.3d-f** (high aspect-ratio: 3.6) and **Supplementary Fig. S3.4d-i** (low aspect-ratio: 1.6).

3.6.3. Supplementary Figures

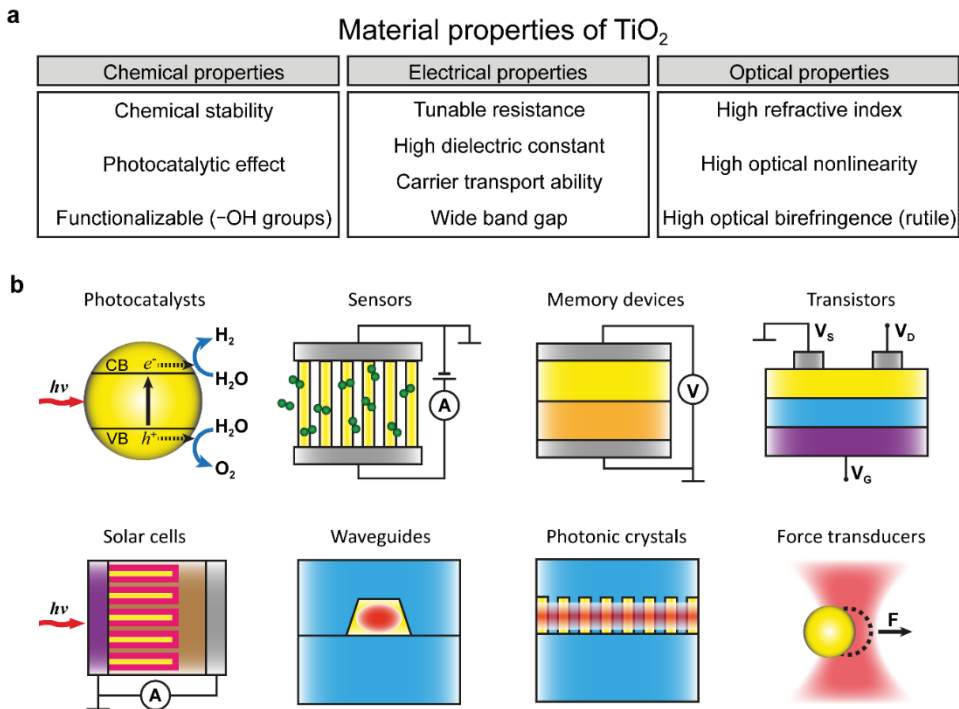


Figure S3.1. Diverse applications of TiO_2 at the nanoscale. **(a)** Overview of the chemical, electrical, and optical properties that make TiO_2 a versatile material for different applications. **(b)** Illustrations of nanoscale applications of TiO_2 (yellow). Top, left to right: a TiO_2 nanoparticle serves as a photocatalyst for water splitting into oxygen and hydrogen gases ($h\nu$: input radiation energy, CB: conduction band, VB: valence band, e^- : electron, h^+ : hole); a TiO_2 nanopillar array acts as a gas sensor (gray: metal electrodes, green: gas molecules, A: current as a sensing signal); a TiO_2 thin film acts as a tunable resistance material in a resistive random access memory device (gray: metal electrodes, orange: TiO_{2-x} , V: voltage as a read/write signal); a TiO_2 thin film can be used as a channel layer in a transparent transistor (gray: metal electrodes, blue: gate insulator, purple: transparent electrode, V_s , V_d , and V_g denote voltages at source, drain, and gate terminals, respectively). Bottom, left to right: a TiO_2 nanorod array acts as a photoanode in a solar cell ($h\nu$: radiation energy from the sun, gray: metal electrode, purple: transparent electrode, magenta: sensitization layer e.g. dye molecules or quantum dots, brown: electrolyte, A: current as converted energy); a nanostructured TiO_2 forms the core of a strip waveguide to support lightwave propagation (blue: cladding layers, red: confined lightwave); a two-dimensional TiO_2 photonic crystal slab used to manipulate the flow of lightwave (blue: cladding layers, red: confined lightwave); an optically trapped TiO_2 nanoparticle used as a force transducer (red: focused laser beam, dotted circle: trap center, F: force induced by the displacement of the nanoparticle).

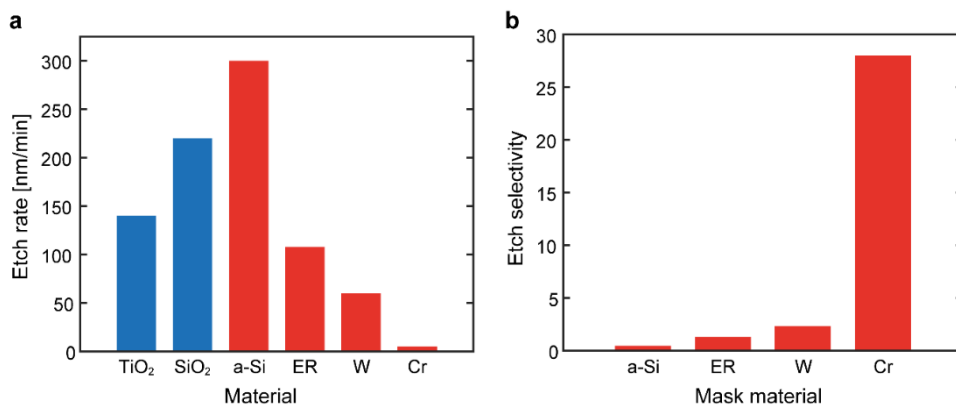


Figure S3.2. The etch rates and etch selectivities of different mask materials. **(a)** The etch rates for substrate (blue bars) materials (TiO₂: (100)-cut rutile single crystal, ~140 nm/min; SiO₂: X-cut quartz single crystal, ~220 nm/min) and mask (red bars) materials (a-Si: amorphous silicon layer deposited by a plasma-enhanced chemical vapor deposition system (Plasmalab 80 Plus, Oxford Instr., UK), ~300 nm/min; ER: spin-coated and baked e-beam resist layer (NEB-22A2E, Sumitomo Chemical, Belgium), ~110 nm/min; W: tungsten layer deposited by an e-beam evaporator (Temescal FC-2000, Ferrotec, Germany), ~60 nm/min; Cr: chromium layer deposited by the same evaporator, ~5 nm/min). All results are obtained under the same dry etching conditions (using the F3 etching system; etching conditions in **Supplementary Table S3.2**). **(b)** Etch selectivity of each mask material for single-crystal TiO₂ dry etching, which is the etch rate of TiO₂ divided by that of the mask material (a-Si: 0.5, ER: 1.3, W: 2.3, Cr: 28).

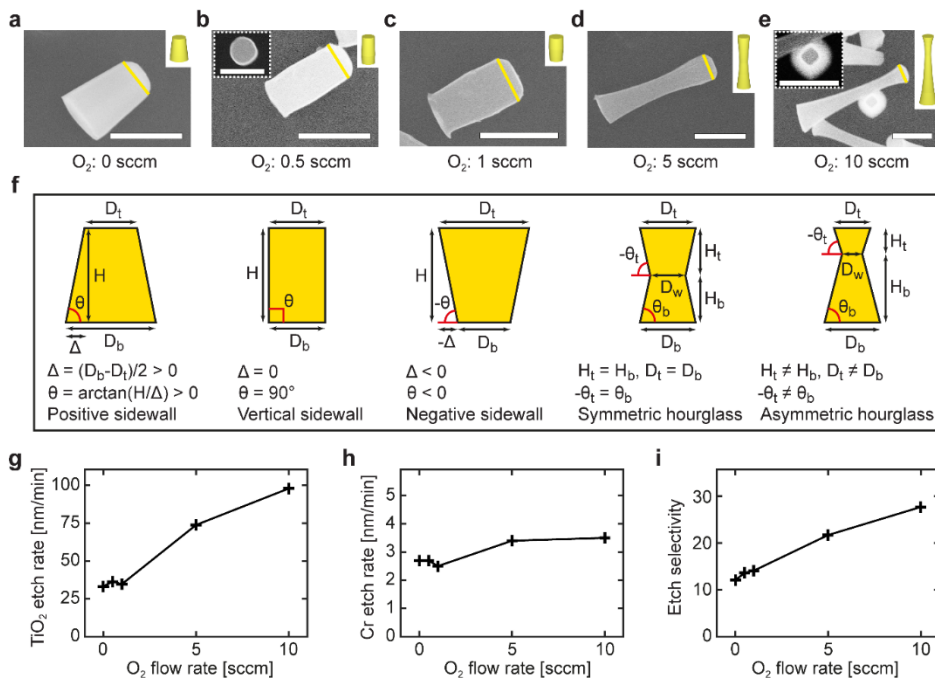


Figure S3.3. Control of sidewall profiles and etch characteristics in single-crystal TiO_2 nanocylinders by variation of O_2 flow rate in the CHF_3 -RIE process. **(a-e)** SEM images of single-crystal TiO_2 nanocylinders produced under identical etching conditions (using the F1 etching system; etching conditions in **Supplementary Table S3.2**) apart from the O_2 flow rate (values shown at the bottom of each image). Scale bars denote 500 nm. Top surfaces of the nanocylinders are marked with yellow lines because the remaining Cr masks are also visible in these images. The insets in top-right corner illustrate (to scale) the corresponding three-dimensional shapes of the nanocylinder SEM images. The types of obtained nanocylinder shapes include **(a)** positive sidewall angles, **(b)** vertical sidewall angles, **(c)** negative sidewall angles, **(d)** symmetric hourglass shapes, and **(e)** asymmetric hourglass shapes. In **(b)** and **(e)**, the insets in top-left corner (scale bars denote 500 nm) show top-view SEM images of nanocylinders cut at their middle, displaying cross-sections that are **(b)** circular or **(e)** diamond-shaped. **(f)** For the analysis of sidewall angles (θ), we use two-dimensional models as defined here. The definition of sidewall angles is illustrated for the cases of positive, vertical, and negative angles, using the measured heights (H) and diameters of top (D_t) and bottom (D_b). The hourglass-shaped nanocylinders possess two sidewall angles and heights for both top (θ_t , H_t) and bottom (θ_b , H_b) sides, and an additional waist diameter (D_w). **(g-i)** The etch characteristics are shown as a function of the O_2 flow rate: the etch rates of **(g)** TiO_2 , **(h)** Cr, and **(i)** the resulting etch selectivities (TiO_2 :Cr). The measured dimensions extracted from the SEM images **(a-e)** are as follows: **(a)** D_t : 285 nm, D_b : 395 nm, H : 500 nm, θ : 84° ; **(b)** $D_t = D_b$: 275 nm, H : 545, θ : 90° ; **(c)** D_t : 305 nm, D_b : 260 nm, H : 520 nm, θ : -88° ; **(d)** $D_t = D_b$: 260 nm, D_w : 175 nm, $H_t = H_b$: 555 nm, $-\theta_t = \theta_b$: 86° ; **(e)** D_t : 245 nm, D_b : 370 nm, D_w : 135 nm, H_t : 385 nm, H_b : 1085 nm, θ_t : -82° , θ_b : 84° .

Control mechanism for sidewall profiles in CHF_3 -etched single-crystal TiO_2 nanocylinders

We observe that tuning the O_2 flow rate during the single-crystal TiO_2 etching process allows us to control the sidewall profile of the nanostructures. We attribute the formation of different sidewall profiles (positive, vertical, negative, and hourglass-shaped) to underlying changes in the thickness of a sidewall passivation layer that

result from the interplay between CHF_3 and O_2 plasma. The thickness variation permits both the formation of positive sidewall angles in the absence of O_2 flow and the formation of vertical (or negative) sidewall angles at an O_2 flow of 0.5 (1.0) sccm (**Supplementary Fig. S3.3a-c**). The hourglass-shaped etch profiles likely result from substantially reduced TiO_2 surface passivation combined with the random trajectories of reactive ions^{15,16} (**Supplementary Fig. S3.3d,e**).

Control mechanism for cross-sectional shapes and etch selectivity in CHF_3 -etched single-crystal TiO_2 nanocylinders

We find that the single-crystal TiO_2 nanocylinders etched at low O_2 flow rates (0–1 sccm) exhibit circular cross-sections (**Supplementary Fig. S3.3b, inset** in top-left corner), while those etched at high O_2 flow rates (5–10 sccm) feature diamond-shaped cross-sections (**Supplementary Fig. S3.3e, inset** in top-left corner). These differences may result from changes in the predominant etching mode: at low O_2 flow rates, the initial shape of the etch masks (circular in the case of **Supplementary Fig. S3.3**) should be directly transferred to the etched nanostructures, as the dominance of physical etching by ion bombardment results in the same etch rate independently of crystallographic orientation; conversely, at high O_2 flow rates, chemical etching may predominate than physical etching, resulting in etch rates that vary per orientation of the crystal planes in the single-crystal TiO_2 substrates¹⁷. Moreover, the above reasoning is supported by the fact that TiO_2 etch rates (**Supplementary Fig. S3.3g**) increase significantly (~3-fold) while Cr etch rates (**Supplementary Fig. S3.3h**) remain nearly the constant (~3 nm/min), as we increase O_2 flow rate. The removal of Cr mask layer is possible only by the physical etching but not by the chemical etching based on fluorine chemistry while both etching modes induce TiO_2 etching. We attribute this to a decreased thickness of the CHF_3 plasma-generated fluorocarbon passivation layer on TiO_2 surfaces in the presence of O_2 plasma¹⁸. As such a layer protects TiO_2 surfaces from chemical reaction with etching species, its decreased thickness results in an increase of the TiO_2 etch rates whilst those of Cr remain nearly unaffected, enhancing etch selectivity (**Supplementary Fig. S3.3i**).

The reproducibility of different sidewall profiles in CHF_3 -etched single-crystal TiO_2 nanocylinders

A repetition of this experiment in the second nominally identical RIE system yields the similar trends but at slightly altered O_2 flow rates (using the F2 etching system; etching conditions in **Supplementary Table S3.2**). For example, etching nanocylinders with vertical sidewall angles requires an O_2 flow rate of 4–8 sccm (compared to ~0.5 sccm in the first RIE system (**Supplementary Fig. S3.3b**)). Similarly, etching nanocylinders into hourglass-shapes requires an O_2 flow rate of ~16 sccm (compared to 5–10 sccm in the first RIE system (**Supplementary Fig. S3.3d,e**)). We attribute these discrepancies in parameters to the differences in instrument calibration, e.g. of the mass flow controllers for the control and measurement of O_2 flow rates.

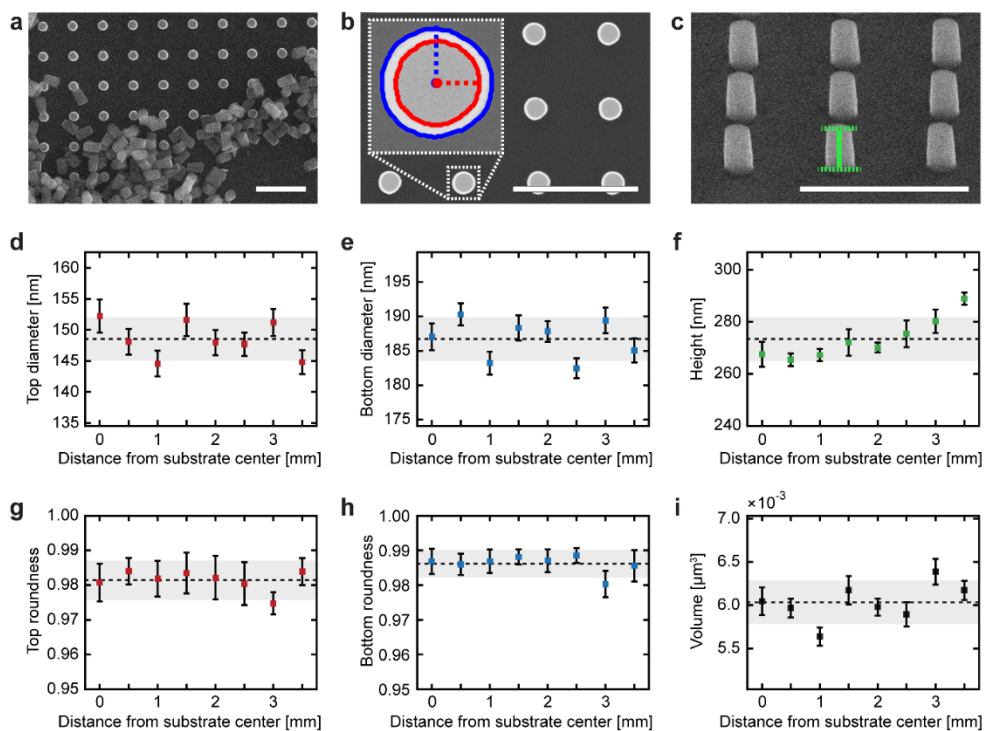


Figure S3.4. Dimensions of fabricated single-crystal TiO_2 nanocylinders. **(a-c)** SEM images of etched single-crystal TiO_2 nanocylinders (light gray). Scale bars denote $1\ \mu\text{m}$. **(a)** Top-view of a single-crystal TiO_2 substrate with partially cleaved nanocylinders. An array of rigidly fixed nanocylinders is visible in the top left corner, and the cleaved substrate surface is bottom right corner. The released nanocylinders are positioned at the interface of these regions. **(b)** Top-view of a substrate with etched nanocylinders. The inset shows a zoom-in as an example for image analysis. The red (blue) contour, dotted line, and dot represent the boundary, equivalent radius, and center of nanocylinder top (bottom) surface, respectively. **(c)** Tilted-view (60°) of a substrate with etched nanocylinders. The green dotted horizontal lines are crossing the centers of top and bottom surfaces, and the green vertical line indicates the height that will be converted to the actual height considering the tilting angle. **(d-i)** Nanocylinder dimensions extracted from the SEM images. The graphs display the **(d)** top diameter, **(e)** bottom diameter, **(f)** height, **(g)** top roundness, **(h)** bottom roundness, and **(i)** volume as a function of the radial distance from the substrate center. The roundness (defined as $4\pi A/P^2$, A: area, P: perimeter) measures how closely the shape of a nanocylinder's cross section resembles that of a circle, where 1 corresponds to a perfect circle and smaller values imply deviations from circular. Measurement points are spaced by $0.5\ \text{mm}$ from the center of the substrate to its edge. At each point, the diameters (heights) are calculated from $n = 12$ ($n = 10$) different nanocylinders. The square markers and the error bars in the graphs represent the mean and the standard deviation of the local uniformity, respectively. The horizontal dotted black lines and the top and bottom sides of the gray shaded boxes in the graphs represent the mean and the standard deviation of the global uniformity, respectively.

Distributions of fabricated single-crystal TiO_2 nanocylinder dimensions

The comparison between single-crystal TiO_2 nanocylinder dimensions presented in **Supplementary Fig. S3.4** and those presented earlier (**Fig. 3.3**) provides more information for the analysis of the nanocylinder dimensions. We etch the different

batches of nanocylinders under the same conditions, except for the etch duration (**Supplementary Table S3.2**). The etch time of the nanocylinders analyzed in **Supplementary Fig. S3.4** (8 min) is approximately twice less than that of the nanocylinders shown in **Fig. 3.3** (15 min). Both etch times demonstrate a similar trend regarding the nanocylinder dimensions (analysis results are summarized in **Supplementary Table S3.3**). The observed irregular Cr mask erosion effect, which depends on the roughness of the mask surface, causes stronger deformation of the top surface geometry than the bottom of the nanocylinders; we expect that the bottom surface geometry is mostly determined by the initial round shape of etch mask while the top surface geometry is the same as the eroded etch mask until the end of the etching process. This geometry deformation is also observable in the roundness analysis, in which the top roundness values are smaller than the bottom roundness values for both batches of nanocylinders. For this reason, the top diameters show less local uniformity than the bottom diameters. As this effect is more profound for extended etch times, etch time of 15 min results in less local uniformity than etch time of 8 min for both top and bottom diameters. For each measurement point, the top and bottom diameters are directly correlated as observable in **Supplementary Fig. S3.4** and **Fig. 3.3**. However, variations in the top and bottom diameters across a substrate are random, possibly due to the instability of e-beam size or current during e-beam patterning process. Regardless of these variations, the top and bottom diameters exhibit still high global uniformity for both batches of nanocylinders (RSD $\leq 5\%$), which lie in the same order of magnitude as their local uniformity. Further, we observe high global uniformity in nanocylinder heights across the substrates (RSD $\leq 3\%$) regardless of the loading effect. These excellent global uniformity in both diameters and heights leads to nanocylinder volumes with high global uniformity (RSD $\leq 5\%$) across a substrate which is desirable for the application of torque in an OTW¹.

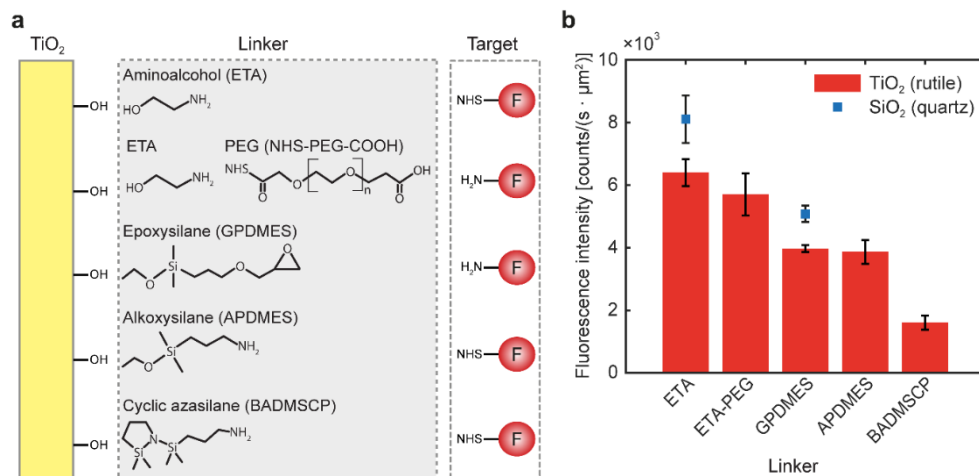


Figure S3.5. Quantitative comparison of surface functionalization efficiencies on single-crystal TiO₂ for different linker molecules. **(a)** Schematic of the different functionalization strategies. At left, the TiO₂ (or other oxide materials, e.g. SiO₂) surface provides hydroxyl groups (-OH) to which the linkers bind covalently. In the center, the used linker molecules (ETA, GPDMS, APDMES, and BADMSCP) are shown with their molecular structures, including the PEGylation of ETA-coated surface. At right, target molecules are NHS-ester or amine modified ATTO 647N fluorophores (F), binding to the different functional group of each linker (**Supplementary Methods**). The fluorophores allow quantitative measurements via fluorescence microscopy. However, in the same manner, other organic molecules, such as biomolecules or polymers, can be bound to the surface linkers. **(b)** Quantitative comparison of differently functionalized single-crystal rutile TiO₂ (red bars) and quartz SiO₂ (blue squares) substrates. The measured fluorescence intensity represents the surface coating density while the error bar (standard deviation) reflects the homogeneity of the coatings (**Supplementary Methods**).

Comparison of TiO₂ and SiO₂ in surface functionalization efficiency

It is known that TiO₂ has lower functionalization efficiency compared to other widely used oxide materials, e.g. SiO₂ and Al₂O₃^{19,20}. To quantify this difference in functionalization efficiency, we compare the surface coating efficiency of TiO₂ (rutile) with that of SiO₂ (quartz). We select two linkers for this comparison: ETA, based on its highest coating efficiency on TiO₂ surfaces (**Supplementary Fig. S3.5b**), and GPDMS that we used for TiO₂ nanostructure functionalization (**Fig. 3.4c**) and OTW measurements (**Fig. 3.5**). For SiO₂ substrates, which are functionalized under the same conditions as TiO₂, both ETA and GPDMS coatings show ~30% higher functionalization density than on TiO₂. However, the coating efficiencies of TiO₂ are sufficient to perform single molecule OTW experiments (**Fig. 3.5b,c**). If higher coating density is required, TiO₂ substrates can be treated with extended O₂ plasma-treatment time to increase the density of surface hydroxyl groups²⁰.

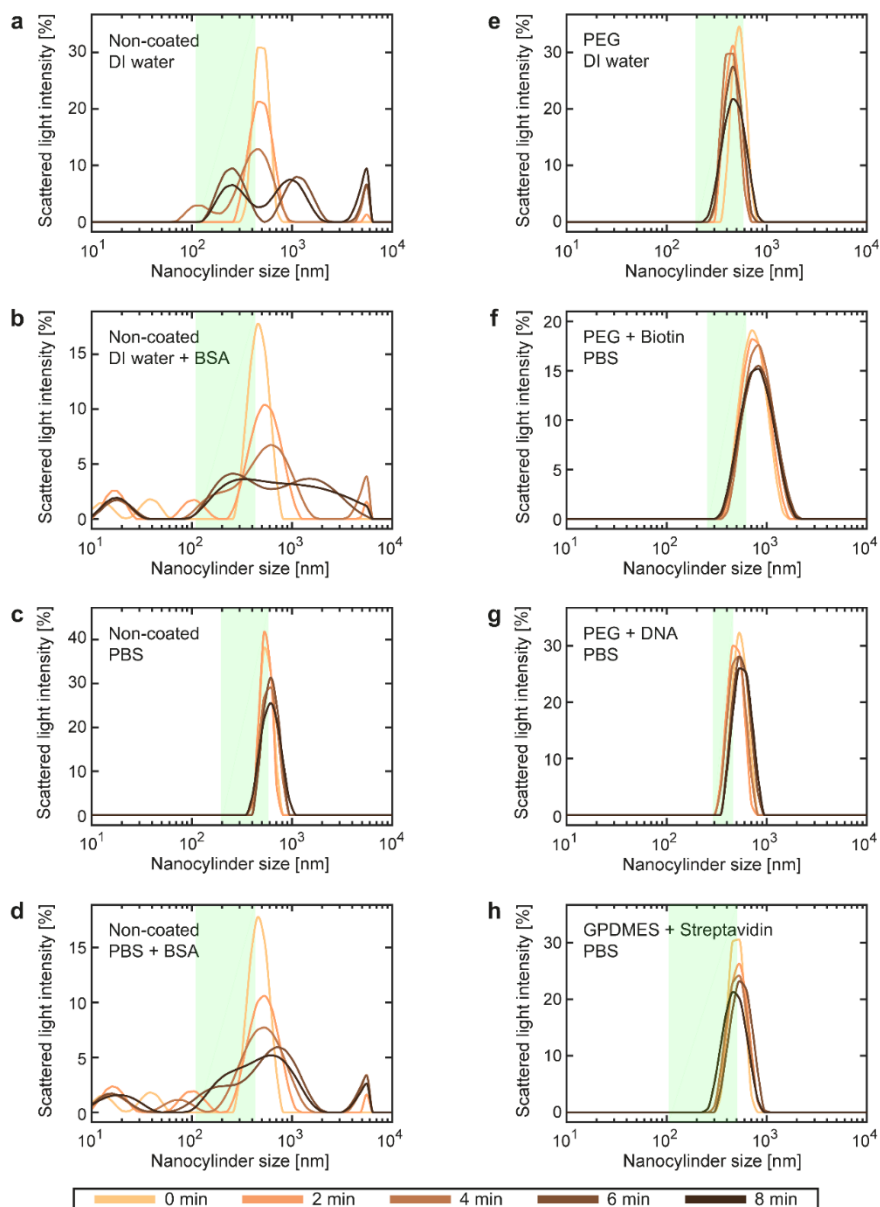


Figure S3.6. DLS measurements of single-crystal TiO₂ nanocylinder aggregation in relation to surface coatings and buffer conditions. In the DLS graphs, each curve is an average of 10 measurements with a duration of 10 s each, with 2 min between successive curves (see legend at bottom of figure). Each green shaded box within the panels displays the range of nanocylinder sizes measured previously in SEM (left edge: diameter, right edge: height). Top-left corner denotes the individual test conditions, which are surface coating (1st row) and buffer solution (2nd row). **(a-d)** Results for non-coated nanocylinders dispersed in **(a)** DI water, **(b)** DI water with 2% (m/v) BSA (New England Biolabs, UK), **(c)** PBS buffer (pH 7.4), and **(d)** PBS buffer (pH 7.4) with 2% BSA. **(e-g)** DLS data for PEGylated nanocylinders in **(e)** DI water, and in PBS buffer (pH 7.4) after bioconjugation with **(f)** biotin and **(g)** DNA. **(h)** Result for GPDMEs-coated nanocylinders with bound

streptavidin in PBS buffer (pH 7.4): this condition is used for the presented single-molecule OTW experiments (**Fig. 3.5**). The SEM-measured nanocylinder dimensions are as follows where D (H) denotes diameters (heights): **(a,b,d)** D: ~110 nm, H: ~430 nm; **(c,e)** D: ~195 nm, H: ~585 nm; **(f)** D: ~255 nm, H: ~625 nm; **(g)** D: ~290 nm, H: ~460 nm; **(h)** D: ~105 nm, H: ~505 nm.

Measurements and analysis of DLS data

We probe the aggregation of cleaved, isolated single-crystal TiO₂ nanocylinders with different surface coatings and buffer solutions via DLS (Zetasizer Nano ZS, Malvern, UK). We compare the degree of nanocylinder aggregations by characterizing the nanocylinder size distributions with 173° backscattering angle at 25 °C. To achieve monodispersed nanocylinders in aqueous solution, we vortex the nanocylinder solutions for 1 min before each measurement. However, for the nanocylinders in **Supplementary Fig. S3.6a** and **Supplementary Fig. S3.6b**, vortexing is insufficient to obtain monodispersity. For these samples, we sonicate the solutions for 10 min before measurements. We attribute the mismatch between nanocylinder dimensions (green boxes) based on SEM image analysis and size measurements via DLS to the highly scattering nature of TiO₂ and non-spherical shape of the nanocylinders. Besides the aggregated nanocylinder solutions (**Supplementary Fig. S3.6a,b,d**) which are apparent from the severe broadening of the size distributions, the monodispersed nanocylinder solutions (**Supplementary Fig. S3.6c,e-h**) exhibit only sedimentation of nanocylinders over time, observable by intensity decrease.

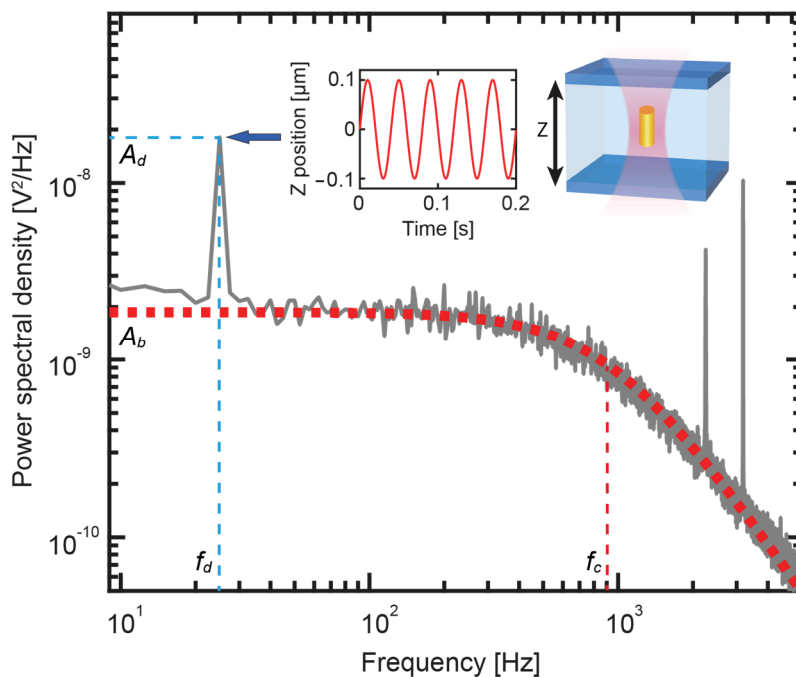


Figure S3.7. Optical trap calibration of single-crystal TiO_2 nanocylinders. The power spectral density (gray curve) of a trapped TiO_2 nanocylinder with a Lorentzian fit (red dotted line) provides corner frequency (f_c) and baseline amplitude (A_b). A piezo stage drives the flow cell sinusoidally in time (with amplitude of $0.1 \mu\text{m}$ and frequency of 25 Hz) along the z -axis (inset) to induce a drag force to the trapped nanocylinder. The driving frequency (f_d) of this modulation appears as a spike in the power spectrum (blue arrow), with amplitude A_d . Analysis of the three measured values (A_b , A_d , and f_c) yields the three necessary parameters for the force calibration in an OTW: nanocylinder drag coefficient, PSD sensitivity, and trap stiffness ²¹.

3.6.4. Supplementary References

1. Huang, Z., Pedaci, F., van Oene, M., Wiggin, M. J. & Dekker, N. H. Electron beam fabrication of birefringent microcylinders. *ACS Nano* **5**, 1418-1427 (2011).
2. Deufel, C., Forth, S., Simmons, C. R., Deigosha, S. & Wang, M. D. Nanofabricated quartz cylinders for angular trapping: DNA supercoiling torque detection. *Nature Methods* **4**, 223-225 (2007).
3. Li, P. C., Chang, J. C., La Porta, A. & Yu, E. T. Fabrication of birefringent nanocylinders for single-molecule force and torque measurement. *Nanotechnology* **25**, 235304 (2014).
4. Gutiérrez-Medina, B., Andreasson, J. O. L., Greenleaf, W. J., LaPorta, A. & Block, S. M. An optical apparatus for rotation and trapping. *Methods in Enzymology* **475**, 377-404 (2010).
5. Lipfert, J., van Oene, M. M., Lee, M., Pedaci, F. & Dekker, N. H. Torque spectroscopy for the study of rotary motion in biological systems. *Chemical Reviews* **115**, 1449-1474 (2015).
6. Steingoetter, I. & Fouckhardt, H. Deep fused silica wet etching using an Au-free and stress-reduced sputter-deposited Cr hard mask. *Journal of Micromechanics and Microengineering* **15**, 2130 (2005).
7. Chen, H., Zhang, Q. & Chou, S. Y. Patterning of light-extraction nanostructures on sapphire substrates using nanoimprint and ICP etching with different masking materials. *Nanotechnology* **26**, 085302 (2015).
8. Janissen, R., Berghuis, B. A., Dulin, D., Wink, M., van Laar, T. & Dekker, N. H. Invincible DNA tethers: covalent DNA anchoring for enhanced temporal and force stability in magnetic tweezers experiments. *Nucleic Acids Research* **42**, gku677 (2014).
9. Lipfert, J., Koster, D. A., Vilfan, I. D., Hage, S. & Dekker, N. H. Single-molecule magnetic tweezers studies of type IB topoisomerases. In *DNA Topoisomerases: Methods and Protocols (Methods in Molecular Biology, Vol. 582)*, 71-89 (Humana Press, 2009).
10. Lipfert, J., Kerssemakers, J. W., Jager, T. & Dekker, N. H. Magnetic torque tweezers: measuring torsional stiffness in DNA and RecA-DNA filaments. *Nature Methods* **7**, 977-980 (2010).
11. Felgner, H., Müller, O. & Schliwa, M. Calibration of light forces in optical tweezers. *Applied Optics* **34**, 977-982 (1995).
12. Koster, D. A., Crut, A., Shuman, S., Bjornsti, M.-A. & Dekker, N. H. Cellular strategies for regulating DNA supercoiling: a single-molecule perspective. *Cell* **142**, 519-530 (2010).
13. Suzuki, K., Youn, S.-W., Wang, Q., Hiroshima, H. & Nishioka, Y. Fabrication of sub 20-nm wide grooves in a quartz mold by space narrowing dry etching. *Microelectronic Engineering* **110**, 432-435 (2013).
14. Mohamed, K. & Alkai, M. M. Investigation of a nanofabrication process to achieve high aspect-ratio nanostructures on a quartz substrate. *Nanotechnology* **24**, 015302 (2013).
15. Peng, Y. et al. Optimization of inductively coupled plasma etching for low nanometer scale air-hole arrays in two-dimensional GaAs-based photonic crystals. *Journal of Semiconductors* **31**, 012003 (2010).
16. Shul, R. J. et al. High-density plasma etching of compound semiconductors. *Journal of Vacuum Science and Technology A* **15**, 633-637 (1997).
17. Mishima, T., Terao, K., Takao, H., Shimokawa, F., Oohira, F. & Suzuki, T. Crystalline anisotropic dry etching for single crystal silicon. In *Proceedings of the 24th International Conference on Micro Electro Mechanical Systems (IEEE)*, 221-224 (2011).
18. Kaspar, P., Jeyaram, Y., Jäckel, H., Foelske, A., Kötz, R. & Bellini, S. Silicon nitride hardmask fabrication using a cyclic CHF₃-based reactive ion etching process for vertical profile nanostructures. *Journal of Vacuum Science and Technology B* **28**, 1179-1186 (2010).
19. Pujari, S. P., Scheres, L., Marcelis, A. T. M. & Zuilhof, H. Covalent surface modification of oxide surfaces. *Angewandte Chemie International Edition* **53**, 6322-6356 (2014).
20. Kim, W.-J. et al. Enhanced protein immobilization efficiency on a TiO₂ surface modified with a hydroxyl functional group. *Langmuir* **25**, 11692-11697 (2009).
21. Tolić-Nørrellykke, S. F., Schäffer, E., Howard, J., Pavone, F. S., Jülicher, F. & Flyvbjerg, H. Calibration of optical tweezers with positional detection in the back focal plane. *Review of Scientific Instruments* **77**, 103101 (2006).

4

Enhanced Linear and Angular Optical Trapping Using Single-Crystal Rutile TiO₂ Nanocylinders

Optical trapping of (sub)micron-sized particles is broadly employed in nanoscience and engineering. The materials commonly employed for these particles, however, have physical properties that limit the transfer of linear or angular momentum (or both). This reduces the magnitude of forces and torques, and the spatiotemporal resolution, achievable in linear and angular traps. Here, we overcome these limitations through the use of single-crystal rutile TiO₂, which has an exceptionally large optical birefringence, a high index of refraction, good chemical stability, and is amenable to geometric control at the nanoscale. We show that rutile TiO₂ nanocylinders form powerful joint force and torque transducers in aqueous environments by using only moderate laser powers to apply nN·nm torques at kHz rotational frequencies to tightly trapped particles. In doing so, we demonstrate how rutile TiO₂ nanocylinders outperform other materials and offer unprecedented opportunities to expand the control of optical force and torque at the nanoscale.

This chapter has been submitted as: **Seungkyu Ha***, Ying Tang*, Maarten M. van Oene, Richard Janissen, Roland M. Dries, Belen Solano, Aurèle J. L. Adam, and Nynke H. Dekker, "Enhanced Linear and Angular Optical Trapping Using Single-Crystal Rutile TiO₂ Nanocylinders" (2018). (*equal contribution)

4.1. Introduction

The ability of optical tweezers to apply torque to, and thereby control the rotation of, micron- scale (or smaller) particles^{3,4} complements their well-known control of force and position and provides the opportunities for diverse novel applications at the nanoscale. For example, in biological physics, angular optical tweezers have been utilized in single-molecule torque spectroscopy^{5,6}, rotational microrheology⁷, and in the manipulation of cellular growth dynamics⁸. In quantum physics, rotational optomechanical effects within angular optical traps⁹ are under active investigation. And in engineering applications, angular optical tweezers enable optically-driven microfluidic actuators such as micro-gears¹⁰ and fluidic pumps¹¹.

Linear optical tweezers achieve stable 3D-trapping of either dielectric or metal particles using Gaussian (TEM₀₀) beams, and have been extensively described¹². To achieve additional angular optical control, specialized forms of laser beams or trapping particles (or both) are required⁶. One of the most practical implementations for angular optical tweezers makes use of a linearly polarized Gaussian beam together with optically anisotropic (i.e., birefringent) dielectric particles^{2,13-16}. This choice of beam enables straightforward control of torque and angle^{2,14} while obviating mode changes (e.g., into the Laguerre-Gaussian mode)¹⁷ or modulation of the laser beam power¹⁸. While metal particles have been successfully trapped and rotated^{19,20}, the use of dielectric particles presents several advantages. Firstly, torque detection is direct because only dielectric materials have transmitted light components that are proportional to the transfer of angular momentum¹⁶. Secondly, highly transparent dielectric materials do not suffer from the extreme heating of absorptive metals²¹. Thirdly, the reduced light scattering from dielectric materials relative to metals is more favorable for three-dimensional (3D) trapping. Extensive scattering from metals destabilizes axial trapping, and hence metal particles with dimensions exceeding a few hundred nanometers support only two-dimensional (2D) trapping^{19,20}. Finally, unlike inherently isotropic metals, optically anisotropic dielectric crystals make it possible to simultaneously confine all three rotational degrees of freedom (RDOF), which is advantageous for high-accuracy sensing applications. Among the wide range of dielectric materials, uniaxial crystals such as quartz SiO₂ have been popular choices due to their well-defined refractive index (n), birefringence (Δn), and optic axis⁶.

Nonetheless, the full potential of combined linear and angular optical manipulation using dielectric force and torque transducers has not been achieved due to the limited performance offered by conventional dielectric materials. For example, quartz SiO₂ has a relatively low index of refraction ($n = 1.54$) that limits the efficient transfer of linear momentum (and hence the achievable maximum force^{22,23}), as well as a low birefringence ($\Delta n = 0.009$) that prohibits the efficient transfer of angular momentum (limiting the achievable maximum torque⁶). Other materials, e.g., vaterite or calcite CaCO₃, have higher birefringence ($\Delta n = 0.1$ or $|\Delta n| = 0.16$, respectively), but a similarly low refractive index ($n = 1.6$ or $n = 1.56$, respectively)^{4,24}. Attempts to

overcome these material limitations have come with adverse side effects. For example, one may compensate for inefficient momentum transfer by increasing the power (and hence the momentum) in the input beam, but this enhances the risk of photodamage in biological applications²⁵. Alternatively, one may employ larger particles to achieve higher force and torque, but the increased frictional drag will decrease the achievable spatiotemporal resolution in these parameters (and their conjugate variables, position and angle)¹.

Rutile TiO₂ has several key features that make it a highly propitious candidate for overcoming these drawbacks. To start, rutile TiO₂ exhibits the highest birefringence ($\Delta n = 0.26$)²⁶ of all known naturally occurring dielectric crystals, ~ 29 -fold larger than that of quartz SiO₂. Next, its refractive index ($n = 2.6$)²⁶ is one of the largest among dielectric crystals, comparable to that of anatase TiO₂ ($n = 2.5$)²⁶, previously selected to demonstrate the generation of very large optical forces²³, and again much larger than that of quartz SiO₂. Furthermore, rutile TiO₂ in its pure single-crystalline form can be maintained at the nanoscale level via top-down fabrication²⁷. This makes it possible to harness its full nominal birefringence and optical index, without any of the reduction observed in porous poly-crystalline structures prepared by bottom-up processes^{28,29}. Lastly, rutile TiO₂ has demonstrated bio-compatibility and bio-functionalizability and is chemically, mechanically, and thermally stable²⁷. This means that it may be employed under tougher conditions (e.g., high pressure, high temperature, or prolonged exposure to aqueous and biological environments) relative to other birefringent materials such as CaCO₃ (which dissolves in aqueous environments²⁴).

Here, we demonstrate how these favorable properties collectively render rutile TiO₂, when shaped into nanocylinders, into an ideal, joint transducer of optical force and torque. To do so, we show that single-crystal rutile TiO₂ nanocylinders, even those with larger volumes, can be trapped in 3D using moderate laser powers, with no need for secondary antireflection coatings²³ or modified optics^{22,30}. We then perform measurements of differently sized nanocylinders in an optical torque wrench (OTW)¹⁵ to quantify the applied forces and torques, which show excellent agreement with numerical calculations based on finite element methods (FEM). This allows us to show that tightly trapped rutile TiO₂ nanocylinders outperform other available dielectric materials by sustaining nN·nm torques at kHz rotational frequencies in aqueous environments. This, together with the excellent joint resolution in force, torque and their conjugate variables (exceeding 1 pN and 1 nm; 1 pN·nm and 1 degree) achieved, expands our control of forces and torques at the nanoscale.

4.2. Results and Discussion

4.2.1. Optimization of rutile TiO₂ particle geometry

In this section, we describe the optimization of rutile TiO₂ nanoparticle geometry for optical trapping. First, we describe how particle selection based on height can maximize

the efficiency of birefringence-based torque transfer, for which the exceptionally high birefringence of rutile TiO_2 is advantageous. Then we discuss how the high refractive index of rutile TiO_2 enhances the applied force compared to other commonly-used dielectric materials. Finally, we show that a cylindrical geometry permits improved 3D trapping and full RDOF confinement.

4.2.1.1. Large birefringence for optimal angular momentum transfer

The optical torque τ that a linearly polarized beam can apply to a birefringent particle with uniform thickness is given by:

$$\tau = -A \sin(hk_o \Delta n) \sin(2\theta), \quad (\text{Equation 4.1})$$

where $A = S \epsilon_o n c (E_o)^2 / (2\omega)$ and S is the particle cross-sectional area, ϵ_o is the vacuum permittivity, $n = (n_e + n_o)/2$ is mean of the particle's optical indices along the extraordinary (n_e) and ordinary (n_o) axes, c is the speed of light in vacuum, E_o is the electric field amplitude of light in the particle, and ω is the angular frequency of the input beam. In the first sine term, h is the particle height along the direction of beam propagation, k_o is the wavenumber of the input laser beam in vacuum, and $\Delta n = n_e - n_o$ is the particle's birefringence. The torque is modulated according to the offset angle θ between the input beam linear polarization direction and the particle optic axis as described by the second sine term, and thus the maximal torque $\tau_o = A \sin(hk_o \Delta n)$ appears at $\theta = \pm 45^\circ$. Note that **Eq. 4.1** does not precisely describe the torque experienced by nanoparticles trapped at a beam focus (**Supplementary Fig. S4.1**), as it is derived in the context of a plane wave that imparts angular momentum to an infinitely wide plate (**Supplementary Text S4.6.1**). Nonetheless, **Eq. 4.1** provides a reasonable starting point for torque transducer design.

As **Eq. 4.1** shows, for a given particle material, the particle height h can be optimized to maximize the torque transfer efficiency. For materials with low birefringence, the optimal particle height is excessively large (e.g., $\sim 30 \mu\text{m}$ for quartz SiO_2). This size scale not only presents a challenge to fabrication but also far exceeds the favorable particle size range for stable 3D trapping in typical single-beam optical tweezers, i.e., $< \sim 1 \mu\text{m}$, below the size of a tightly focused beam. The conventional torque transducers of heights $\sim 1 \mu\text{m}$ ^{13, 15, 24} are made of low birefringence materials and cannot transfer the full angular momentum carried by the laser beam (**Fig. 4.1a**). However, in the case of rutile TiO_2 with its exceptionally large birefringence, a torque transfer efficiency of 100% should be achievable for 1-micron particles (**Fig. 4.1a**).

The ability to reach larger maximal torques (τ_o) for smaller particles (i.e., particles with lower rotational drag γ_θ) has several implications for optical torque transducers. (i) The faster maximal rotation speed ($f_o = \tau_o / (2\pi\gamma_\theta)$) allows access to a larger torque-speed space. (ii) The increased angular trap stiffness ($\kappa_\theta = 2\tau_o$) and low drag improve measurement precision for both torque and angle, as they are

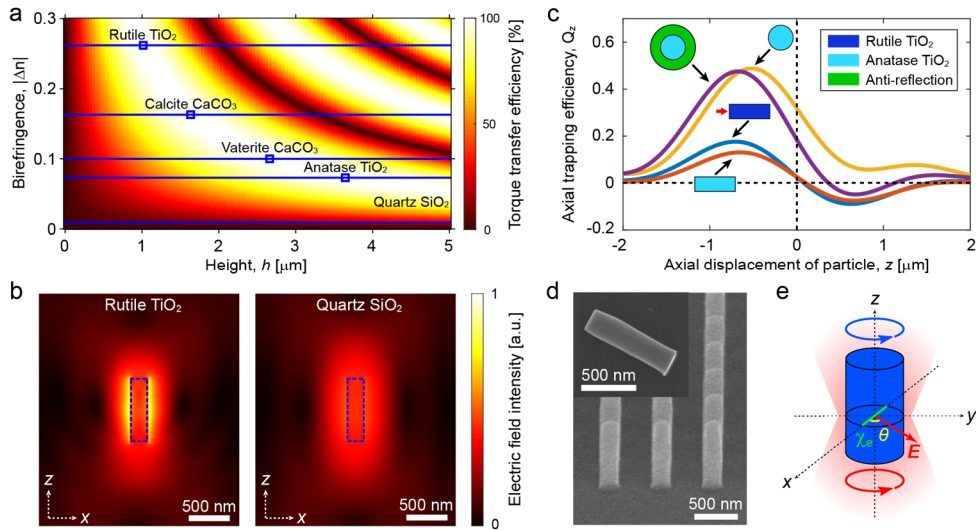


Figure 4.1. Design principles for force and torque transducers in optical tweezers. (a) Map of the torque transfer efficiency $(|\sin(hk_0\Delta n)| \times 100)$; derived from Eq. 4.1) as a function of particle height (h) and birefringence ($|\Delta n|$) of different dielectric materials. The blue squares indicate the smallest particle heights at which 100% torque transfer efficiency can be achieved ($\sim 30 \mu\text{m}$ for quartz SiO_2). (b) FEM-calculated electric field intensity around nanocylinders (blue dashed line) made of different materials, located at the laser beam focus ($z = 0$) in water. (c) FEM-calculated axial trapping efficiency (Q_z) curves for various TiO_2 nanoparticle geometries at fixed volumes. An anatase TiO_2 ($n = 2.3$; light blue) sphere ($d = 430 \text{ nm}$) cannot be trapped in 3D, but it becomes trappable upon the addition of an anti-reflection coating (green), or when reshaped (at constant volume) into a cylinder ($d = 220 \text{ nm}$, $AR = 5$). A rutile TiO_2 ($n = 2.6$; dark blue) cylinder with the same dimensions is also trappable. The trapping orientation of each cylinder with respect to the beam propagation direction (red arrow) is as drawn. (d) SEM micrograph (60° tilted view) of a fabricated rutile TiO_2 nanocylinder batch prior to mechanical cleaving. The inset shows a cleaved single nanocylinder. (e) Experimental scheme of the OTW. The x -, y -, and z -axes are in the reference frame of the nanocylinder, which has the optic axis along the x -axis (as indicated by the extraordinary electric susceptibility χ_e). The laser beam propagates along the z -axis and the optical gradient force traps the nanocylinder in 3D. When a nonzero offset angle θ exists between the optic axis and the direction of the input beam linear polarization (electric field vector E in the xy -plane), the optical torque is applied on the nanocylinder.

proportional to $(\gamma_\theta)^{1/2}$ and $(\gamma_\theta)^{1/2}/\kappa_\theta$, respectively ¹. (iii) The shorter angular trap relaxation time ($t_{c,\theta} = \gamma_\theta/\kappa_\theta$) results in enhanced temporal resolution ¹.

4.2.1.2. Large refractive index for enhanced linear momentum transfer

Compared to conventional dielectric materials employed in angular trapping such as quartz SiO_2 , vaterite CaCO_3 , and calcite CaCO_3 ($n = 1.5$ – 1.6), rutile TiO_2 possesses a substantially larger optical index ($n = 2.6$ on average) ²⁶. This implies a larger index difference with the surrounding medium (e.g., water, $n = 1.33$) and correspondingly stiffer linear trapping ^{22,23}. This can be visualized through FEM calculations (Fig. 4.1b), which show more intense scattering at the interface between the particle and the medium that leads to a higher field gradient and hence an enhanced trapping force. Thus, the use of rutile TiO_2 enhances the transfer of not only angular but also linear

momentum. This simultaneous enhancement is unique to rutile TiO₂, as other materials that have high birefringence possess only low refractive indices (e.g., calcite CaCO₃).

4.2.1.3. Cylindrical shape for stable 3D trapping

The advantage of being able to generate high forces comes at a cost, as a higher index mismatch leads to increased scattering. This implies that radiation pressure from the incident laser beam is more likely to perturb axial trapping. Therefore, 3D trapping of high-index particles in single-beam optical traps is limited to those smaller than a certain threshold size, which is determined by the material and the particle geometry. To compensate for the adverse effect of scattering on trapping, diverse solutions have been developed. One solution is to alter the optical configuration by implementing counter-propagating beams²² or a donut-shaped beam³⁰ for trapping. Another solution is to modify the particle by introducing an anti-reflection coating²³. However, this increased sophistication in optical configuration or fabrication prevents its straightforward wide-spread implementation.

Instead, we can overcome the adverse effects of scattering by using a cylindrical shape for rutile TiO₂ nanoparticles, as shown for previously described dielectric torque transducers^{2,13-16}. This geometry decreases light scattering for a fixed volume of a particle by reducing the surface area encountered by the input laser beam. This effect is explicitly demonstrated by our numerically calculated trapping force curves comparing differently shaped high-index particles (**Fig. 4.1c**). Our FEM calculations show that rutile TiO₂ spheres cannot be trapped in 3D if their diameter exceeds ~346 nm (**Supplementary Fig. S4.2**), in agreement with previously reported calculations³¹. However, as we describe in detail below, we use an OTW to demonstrate stable 3D trapping of fabricated rutile TiO₂ nanocylinders (**Fig. 4.1d,e**) with volumes that exceed the volume threshold for the trappability of spheres. Having an increased range of trappable particle volumes available allows the application of increased force or torque. Furthermore, the omission of antireflection coatings reduces drag and thus improves the achievable maximum angular speed, temporal resolution, and measurement precision.

The use of cylindrically shaped rutile TiO₂ nanoparticles includes another important advantage, namely the full confinement of the three RDOF. For a positive or negative uniaxial birefringent sphere, the birefringence-originated torque constrains only two or one RDOF. This has the drawback that unconstrained RDOF may introduce unexpected angular fluctuations into torque and angle signals. The geometrical anisotropy provided by a non-spherical particle shape such as a cylinder can avoid these complications (**Supplementary Fig. S4.3**) and is hence a requirement for certain applications, e.g., high-precision single-molecule torque spectroscopy.

4.2.2. Linear and angular trapping of TiO₂ nanoparticles

4.2.2.1. Dimensions of rutile TiO₂ nanocylinders trappable in 3D

We fabricated multiple rutile TiO₂ nanocylinder batches (**Methods**) with different diameters $d = 150\text{--}400$ nm and heights $h = 0.5\text{--}1.5$ μm , with resulting aspect ratios ($AR = h/d$) ranging from 2.5 to 6.5 (**Supplementary Fig. S4.4**; precise dimensions measured by scanning electron microscopy (SEM) are shown in **Fig. 4.2** and **Supplementary Table S4.1**). We first tested whether these particles could be optically trapped in 3D in an aqueous environment (**Methods**), because stable 3D trapping is a prerequisite for the application of force and torque. We experimentally observed that rutile TiO₂ cylinders with small diameters (160–230 nm) could be stably trapped (T1–T7 in **Fig. 4.2**), even though their volumes are similar to or larger than that of the largest rutile TiO₂ sphere predicted to be trappable. In contrast, cylinders with diameters exceeding ~ 260 nm (U1–U6 in **Fig. 4.2**) were not trappable in 3D, but rather scattered away from the trap. Therefore, we defined an experimental threshold diameter d_{exp}^* for the trappability of the rutile TiO₂ cylinders as a function of their AR . For each AR , d_{exp}^* falls within the range 230–260 nm.

The behaviour of individual particles within cylinder batches is consistent with this transition. For example, the mean diameter of cylinder batch T8 ($AR = 4.4$) is 256 nm \pm 10 nm (**Fig. 4.2a**). While most cylinders from this batch were not trappable or could be trapped only temporarily (with particles exiting the trap within seconds or minutes), a few were stably trapped for hours. Such behavior is expected if a small fraction of the batch has diameters that fall below d_{exp}^* .

We compare these and subsequent findings with FEM calculations (**Methods**). The calculated axial stiffness (κ_z) map (**Fig. 4.2a**; other calculated linear trapping parameters are described in **Supplementary Fig. S4.5**), where black pixels indicate untrappable cylinder dimensions, reveals a higher threshold range for trappability, $d_{cal}^* \approx 255\text{--}315$ nm, defined as the minimum diameter which results in a black pixel for each aspect ratio. A few experimental factors that have not been considered in the calculations could explain the mismatch between the trappable cylinder dimensions found by experimental and numerical approaches. For example, cylinder batch U1 lies in a trappable regime of the calculated map but is experimentally untrappable. The calculations for the maps shown in **Fig. 4.2** incorporate the objective lens aperture filling ratio ($\alpha = 1.7$, **Methods**; **Supplementary Fig. S4.6**). However, they do not account for optical aberrations (see also section 4.2.2.2.) and, for a given cylinder geometry, they assume zero taper angle, whereas trapping behaviors are largely dependent on taper angle (**Supplementary Fig. S4.6**).

We have also calculated maps of the radial stiffness (κ_r ; **Fig. 4.2b**), the angular stiffness (κ_θ ; **Fig. 4.2c**), and the maximal rotation rate ($f_o = (\kappa_\theta/2)/(2\pi\gamma_\theta)$; **Fig. 4.2d**, obtained using FEM-calculated drag coefficients (γ_θ ; **Supplementary Fig. S4.7**) and angular stiffnesses (κ_θ ; **Fig. 4.2c**), which we compare to our experimental results in the next subsections.

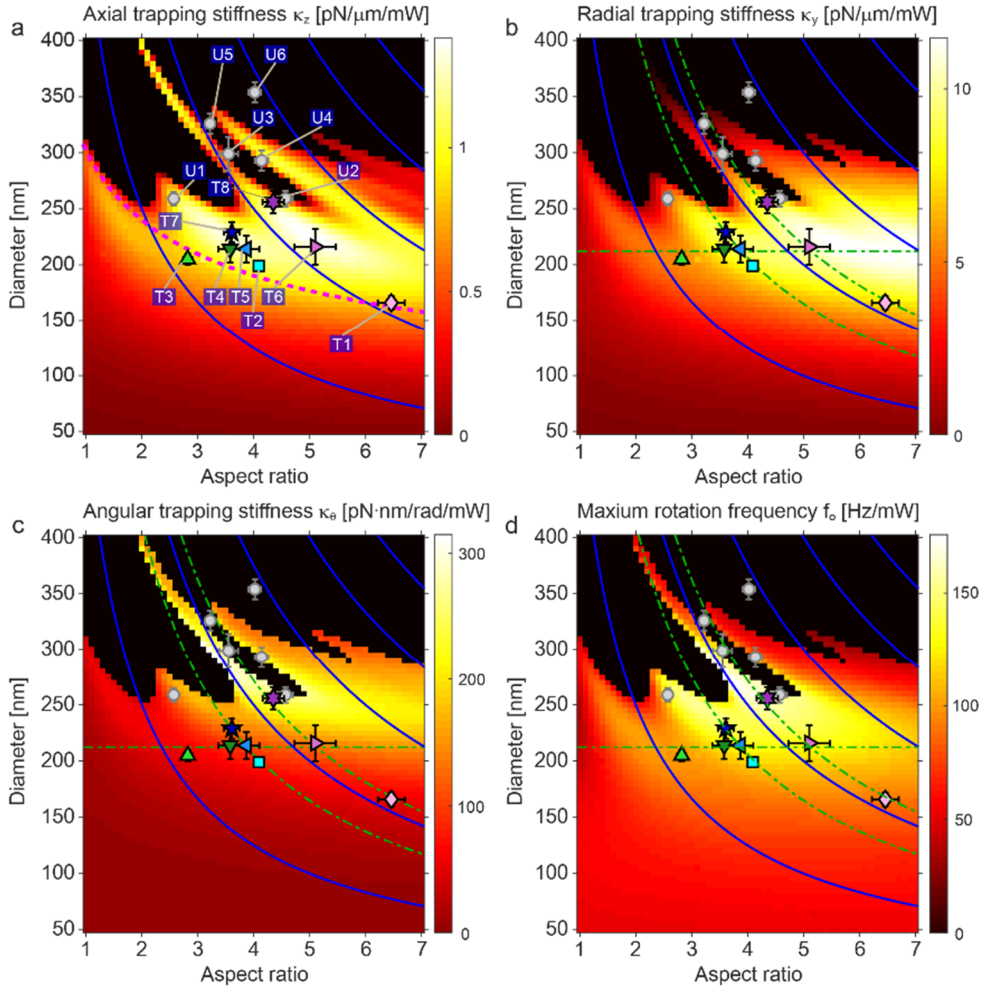


Figure 4.2. Calculated maps of linear and angular stiffness for rutile TiO₂ nanocylinders of varying dimensions, with experimentally assessed trappability per cylinder batch superimposed. (a-c) FEM-calculated (a) axial (κ_z), (b) radial (κ_r), and (c) angular (κ_θ) stiffness maps of rutile TiO₂ nanocylinders. The stiffness values are calculated with the zero-taper angle for each cylinder dimension and the measured aperture filling ratio ($\alpha = 1.7$) from our OTW setup, and normalized by the input beam power. (d) Maximum rotation frequency ($f_\theta = \tau_o / (2\pi\gamma_\theta)$) map of rutile TiO₂ nanocylinders obtained from FEM-calculated maximum torque ($\tau_o = \kappa_\theta / 2$; derived from data in panel (c)) and drag (γ_θ ; **Supplementary Fig. S4.7**). In panel (a), the region above the dashed magenta curve includes nanocylinders with volumes exceeding that of the largest trappable rutile TiO₂ sphere with $d \approx 346$ nm. In panels (b-d), dimensions relevant for the analysis in **Fig. 4.3** are displayed: the horizontal dash-dotted green line represents $d \approx 213$ nm; the leftmost dash-dotted green curve represents $h \approx 825$ nm; and the rightmost dash-dotted green curve represents $h \approx 1096$ nm. In all panels, the maps are plotted as a function of the cylinder aspect ratio ($AR = 1-7$, with step size 0.1) and the cylinder diameter ($d = 100-400$ nm, with step size 5 nm). The black pixels indicate cylinders with untrappable dimensions (for which axial stiffnesses cannot be calculated). The solid blue curves are iso-height contours (500–2500 nm from left to right, with a step size of 500 nm). Trappable fabricated cylinder batches (labeled as T1–T8) are indicated by distinct symbols and colors. Untrappable fabricated cylinder batches (labeled as U1–U6) are shown as gray filled circles. Symbols and error bars denote the averages and standard deviations of the SEM-measured cylinder dimensions, respectively ($N = 5-10$; **Supplementary Table S4.1**).

4.2.2.2. Rutile TiO₂ nanocylinders optimized for high stiffness, low drag, and rapid response time

The stiffness and drag are the two primary physical parameters that describe the behavior of optically trapped particles¹. Therefore, we experimentally determined the trap stiffness (linear and angular) and the corresponding drag coefficient for each trappable rutile TiO₂ cylinder batch, with the results summarized in **Fig. 4.3**. We used laser powers less than 100 mW to demonstrate the high performance of rutile TiO₂ cylinders even in the low-power regime. However, we present the trapping stiffness normalized by laser power for comparison with other studies. To highlight the effect of geometrical parameters, the experimental stiffness values are plotted as a function of diameter or height at a fixed height or diameter in **Fig. 4.3a,b,d,e**. In **Fig. 4.2b-d**, the dash-dotted green lines represent the fixed heights $h \approx 1096$ nm and $h \approx 825$ nm, and the fixed diameter $d \approx 213$ nm. The results of FEM calculations based on mean particle geometries (with actual sidewall profiles as quantified by SEM and displayed in **Supplementary Fig. S4.4**) are co-plotted in **Fig. 4.3a,b,d,e** for comparison. In the case of linear trapping, we display the trapping parameters as measured in the y -dimension. Because the input beam is polarized along the x -dimension (**Methods**), trapping is strongest along the y -dimension (twofold and tenfold stronger than trapping in the x - and z -dimensions, respectively; **Supplementary Fig. S4.5**). Overall, increases in either cylinder diameter (**Fig. 4.3a,d**) or height (**Fig. 4.3b,e**) that enhance the light-matter interaction volume tend to result in greater linear and angular trap stiffnesses. Particularly, for angular trapping, an increased cylinder diameter at a fixed height corresponds to a wider cross-sectional area S in **Eq. 4.1**, and hence also a higher value of the angular stiffness (**Fig. 4.3d**). For a fixed diameter, taller cylinders yield increased angular stiffness, until saturation occurs close to the height h in **Eq. 4.1** for optimal torque transfer (**Fig. 4.3e**). These trends agree very well with the FEM-based predictions. Exact quantitative agreement between the experimental observations and FEM predictions is achieved upon scaling the calculated stiffnesses by $42\% \pm 14\%$ (**Supplementary Fig. S4.8**), which we attribute to optical aberrations that distort the electric field distribution at the beam focus³², an experimental limitation that is challenging to include in calculations. The measured drag coefficients, which are not similarly influenced by aberrations, equal $104\% \pm 17\%$ of the values calculated by FEM (**Supplementary Fig. S4.8**), implying high accuracy of our calibrated measurements.

The ratio of the measured drag (**Methods**) and stiffness reports on the response times of trapped rutile TiO₂ cylinders. When the measured translational or rotational drag is plotted against the corresponding trap stiffness, a linear relationship is observed (**Fig. 4.3c,f**). Within the range of cylinder dimensions tested, this reflects the above-mentioned trend of increased stiffness with increased diameter or height (corresponding to increased drag). The slope of the fitted lines yields the overall trap relaxation time ($t_{c,y} = \gamma_y/\kappa_y$ or $t_{c,\theta} = \gamma_\theta/\kappa_\theta$), with a shorter t_c reflecting a more rapid response time and increased temporal resolution.

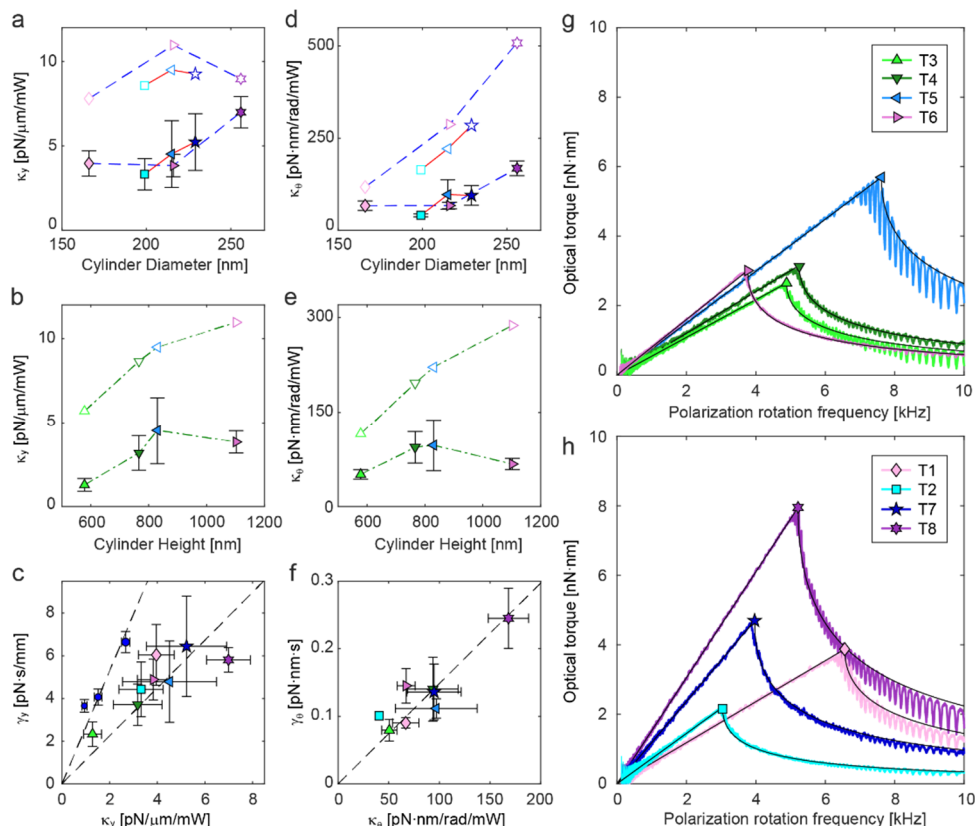


Figure 4.3. Experimentally measured linear and angular trapping performances of rutile TiO₂ nanocylinders. (a,b,d,e) Measured stiffness (κ_y , κ_θ) values plotted versus cylinder diameter or height, together with calculated values for comparison. The OTW-measured values are represented by filled symbols and associated error bars. The FEM-calculated values (which make use of SEM-measured cylinder geometries with actual sidewall profiles) are represented by empty symbols. For ease of visualization, in panel (a,d), data points from the cylinders of similar height $h \approx 1096$ nm (825 nm) are connected with dashed blue lines (solid red lines), and in panel (b,e), data points from the cylinders of similar diameter $d \approx 213$ nm are connected with dash-dotted green lines. (c,f) Measured drag coefficients (γ_y , γ_θ) plotted versus measured stiffness values (κ_y , κ_θ). The slope of a linear fit (dashed black line, forced through the origin) reports on the trap relaxation time ($t_{c,y} = 11 \mu\text{s}$ at 100 mW, $t_{c,\theta} = 15 \mu\text{s}$ at 100 mW). The measurement results from PS spheres are overlaid in panel (c) for comparison (filled blue circles; the mean diameters of batches P1, P2, and P3 are 370 nm, 505 nm, and 746 nm, respectively). A linear fit to PS data results in $t_{c,y} = 26 \mu\text{s}$ at 100 mW. (g,h) Moving-averaged optical torque as a function of input beam polarization rotation frequency (PRF), measured at 92 mW. Each curve represents the data obtained from a single cylinder, and its fit to the theory ² is overlaid (black line). When the PRF exceeds the maximum rotation frequency of a cylinder (denoted by the corresponding colored symbol), the particle begins to slip and thus exhibits a decreased torque ². The cylinders with similar diameters ($d \approx 213$ nm, T3–T6) are compared in panel (g), and those with similar heights ($h \approx 1096$ nm, T1 and T8; $h \approx 825$ nm, T2 and T7) are compared in panel (h). For the symbols employed in panels (a–h), the shape and color coding are as in Fig. 4.2.

For linear trapping, we compare the results obtained with rutile TiO₂ cylinders to those obtained with standard polystyrene (PS) spheres (representative of low-index force transducers). The linear trap stiffness of rutile TiO₂ nanocylinders is

approximately two-fold higher than that of PS spheres of comparable drag, a direct consequence of the higher refractive index of rutile TiO₂ ($n = 2.6$) compared to PS ($n = 1.57$). Correspondingly, rutile TiO₂ nanocylinders enable a nearly two-fold increase in temporal response ($t_{c,y} = 11 \mu\text{s}$ for rutile TiO₂, versus $t_{c,y} = 26 \mu\text{s}$ for PS at 100 mW; **Fig. 4.3c**). These effects can be appreciated by comparing the rutile TiO₂ cylinder batch T2 with the PS sphere batch P2 ($d = 505 \text{ nm}$), which both have drag coefficients of $\sim 4 \text{ pN}\cdot\text{s}/\text{mm}$ (**Fig. 4.3c**). For angular trapping, the trap relaxation time of rutile TiO₂ nanocylinders ($t_{c,\theta} = 15 \mu\text{s}$ at 100 mW; **Fig. 4.3f**) is again considerably shorter due to the high angular trap stiffness (**Fig. 4.2c**, deriving from the large birefringence) achievable with such low rotational drag (**Supplementary Fig. S4.7**). As the trap relaxation time is inversely proportional to the laser beam power, it can be further tuned using this parameter.

4.2.2.3. Rutile TiO₂ nanocylinders transmit nN forces and nN·nm torques with excellent measurement precision

To deduce the range of applicable forces using trapped rutile TiO₂ nanocylinders, we examine their measured linear stiffnesses and estimate the range of their harmonic regime. The high radial trapping stiffness of rutile TiO₂ nanocylinders should permit the application of large forces up to $\sim \text{nN}$, as demonstrated for anti-reflection coated anatase TiO₂ spheres²³. For example, a rutile TiO₂ nanocylinder with radial trap stiffness $\kappa_y = \sim 7 \text{ pN}/\mu\text{m}/\text{mW}$ (cylinder batch T8) should experience a $\sim 1 \text{ nN}$ restoring force at $\sim 1.4 \text{ W}$ laser power (not measured due to the limitation of available power in our setup) upon displacement of $\sim 100 \text{ nm}$ from the trap center, well within the estimated harmonic potential regime (**Supplementary Fig. S4.5**). This represents an order of magnitude improvement over the typical $\sim 100 \text{ pN}$ limit of optical tweezers³³.

The exceptionally large birefringence of rutile TiO₂ makes it possible to simultaneously achieve very high torques ($1\text{--}10 \text{ nN}\cdot\text{nm}$) and rotational speeds ($1\text{--}10 \text{ kHz}$) at only moderate laser powers ($< 100 \text{ mW}$) in aqueous solution (**Fig. 4.3g,h**). Such an expansive torque-speed range is not achievable in similar measurement conditions using other dielectric particles with much lower birefringence^{13, 15}. To provide a guideline for selecting cylinder dimensions, we compare the torque-speed curves of differently sized nanocylinders (**Fig. 4.3g,h**). We first compare cylinders with similar diameters ($d \approx 213 \text{ nm}$, batches T3–T6) but different heights (**Fig. 4.3g**). Here, the rotational drag coefficients are similar, as observable from the slopes ($\gamma_\theta = \tau_o/\omega_o$) in the linear part of the torque-speed curves. Using a cylinder with an optimal height for torque transfer efficiency (within this dataset, batch T5) results in a higher maximum torque and increased rotational frequency. Differently stated, for a fixed cylinder diameter, the height provides a means to tune the torque transfer efficiency. We next compare two groups of cylinders with similar heights ($h \approx 1096 \text{ nm}$, batches T1 and T8; $h \approx 825 \text{ nm}$, batches T2 and T7) but different diameters (**Fig. 4.3h**). Within each group of cylinders, the torque transfer efficiencies are similar, but the drag coefficients differ substantially. A smaller drag coefficient is preferable in general for a higher rotation

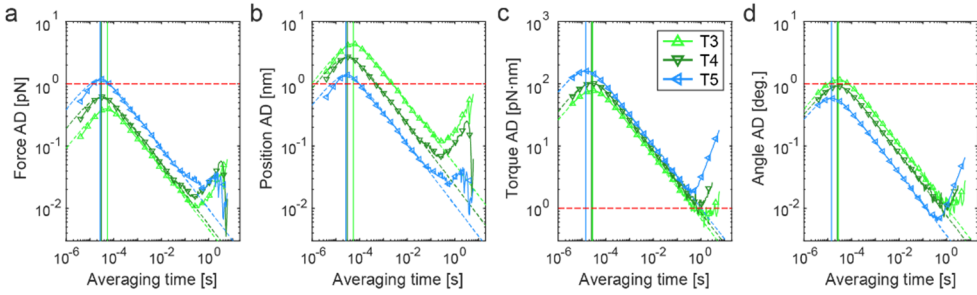


Figure 4.4. Temporal resolution and measurement precision in force, position, torque, and angle, achieved with rutile TiO₂ nanocylinders. (a-d) Allan deviation (AD) as a function of averaging time for three selected rutile TiO₂ cylinder batches (T3–T5, in order of increasing linear and angular stiffness; the same symbols and colors as in Fig. 4.2). AD plots for four different physical quantities are shown: (a) force, (b) position, (c) torque, and (d) angle. Each colored solid curve represents the normal AD obtained from a single cylinder measured at 92 mW. Colored symbols reflect the octave-sampled overlapping AD, and their fit to the theory¹ is overlaid as a dashed curve. The AD values report on the achievable measurement precision for a given averaging time, and the horizontal dashed red lines indicate the typical precisions required for measurements of individual biomolecules. For each cylinder, the trap relaxation time (t_c) can be deduced from the timescale at which the AD curve peaks ($1.8926t_c$; designated by the colored vertical lines)¹. This relaxation time forms the lower bound of the achievable temporal resolution.

frequency (e.g., compare batches T1 and T8 in Fig. 4.3h). However, a reduction in drag does not always guarantee an increased rotation frequency even if torque transfer efficiency is maintained (e.g., compare batches T2 and T7 in Fig. 4.3h). This is because the resulting rotation frequency ($f_o \propto \kappa_\theta / \gamma_\theta$) is dependent on the relative rates of change between stiffness κ_θ and drag γ_θ , which are distinct functions of particle dimensions. Hence, for a fixed cylinder height, one should select the suitable cylinder diameter to access the desired torque-speed regime.

Utilizing the high linear and angular stiffnesses achievable with low-drag rutile TiO₂ nanocylinders, we employ Allan deviation (AD) analysis¹ to demonstrate the ensuing improvements in measurement precision. For the primary quantities of physical interest – force, torque, position, and angle – we demonstrate in Fig. 4.4 that one can achieve excellent precisions below 1 pN, 1 pN·nm, 1 nm, and 1 degree, respectively, on short timescales between (sub)milliseconds and seconds. To quantify trapping, signal averaging times longer than the time at which the AD peak (colored vertical lines in Fig. 4.4) occurs are appropriate. This regime corresponds to the thermal limit, i.e., the harmonic trapping regime. AD values within this region determine the measurement precision as a function of the averaging time. Theoretically, longer averaging times increase the measurement precision, but there is a practical lower bound on the measurement precision because of long-term drift or other measurement noise¹. In our setup, this lower bound occurs at an averaging time between ~ 0.1 s and ~ 10 s.

We illustrate here how the main trapping parameters affect the magnitude of the AD curve, in turn increasing or decreasing the achievable measurement precision. As an example, we selected a subset of the cylinder batches, i.e., T3–T5, that exhibits the

order of increasing linear and angular stiffnesses. The force AD (**Fig. 4.4a**) and torque AD (**Fig. 4.4c**) are functions of drag only ($\propto (\gamma)^{1/2}$). Therefore, the best force and torque precisions are obtained from the cylinder with the smallest linear and angular drag coefficients (batch T3). However, the position AD (**Fig. 4.4b**) and angle AD (**Fig. 4.4d**) are functions of both drag and stiffness ($\propto (\gamma)^{1/2}/\kappa$). As differences in stiffness values are more significant in the chosen dataset, the best position and angle precisions are achieved with the highest linear and angular stiffnesses (batch T5).

Finally, we compare the stiffness, torque-speed regime, measurement precision, and temporal resolution between rutile TiO₂ and other common dielectric crystals, i.e., quartz SiO₂ and calcite CaCO₃. We chose to compare only calculated results because of the difficulty of fabricating different materials into an identical geometry. As experimentally demonstrated here (**Fig. 4.3, Supplementary Fig. S4.8**), we can reliably predict the overall trends in both linear and angular trapping parameters by numerical modeling. This comparison shows that rutile TiO₂ is indeed the most competent material as a combined force and torque transducer (**Supplementary Fig. S4.9**).

4.3. Conclusions

In this work, we have employed experimental measurements and numerical calculations based on finite-element methods to demonstrate how the collective optical properties of single-crystalline rutile TiO₂ (including high refractive index and exceptionally large birefringence), together with its shaping into nanocylinders of appropriate dimensions, make it possible to develop joint optical force and torque transducers with outstanding properties. We show that rutile TiO₂ nanocylinders exhibit high stiffness in both linear and angular domains, allowing for the application of \sim nN-scale forces and unprecedentedly high 1–10 nN·nm torques. Given their low drag coefficients, our fabricated rutile TiO₂ nanocylinders should exhibit excellent time response, which we have verified experimentally and exploited to highlight how rutile TiO₂ torque transducers can sustain high 1–10 kHz rotation frequencies in aqueous solution, even at a moderate trapping laser power not exceeding 100 mW. Furthermore, we show how optically trapped rutile TiO₂ nanocylinders enable high measurement precision in the key physical parameters of force, torque, position, and angle.

We expect that this coalescence of exceptional trapping properties into single rutile TiO₂ particles will open up opportunities for micro- and nanoscale applications. For example, the ability to transmit \sim nN·nm torques at \sim kHz rotation frequency will render measurements on systems with a wide torque-speed regime, e.g., the bacterial flagellar motor³⁴, accessible. Similarly, the high temporal resolution and excellent measurement precision will permit investigations of fast dynamics in other bio-molecules^{5,35}. Moreover, the small size, bio-compatibility, and chemical inertness of rutile TiO₂ nanocylinders, together with their low laser power requirements compared

to other materials, will facilitate their usage in *in-vivo* microrheology³⁶ or cellular manipulation^{8,37}. Alternatively, these force and torque transducers could provide an enhanced platform for studies of quantum phenomena such as cavity cooling⁹ and Casimir effects³⁸. Finally, we foresee potential applications for rutile TiO₂ nanocylinders in engineering applications such as optically-driven nanomachines^{10,11}, excitability-based sensors¹⁵, or photonic force microscopy³⁹.

4.4. Methods

4.4.1. Fabrication and surface functionalization of rutile TiO₂ nanocylinders

To produce rutile TiO₂ nanocylinders (**Fig. 4.1d**), we use our developed top-down fabrication protocol (more details can be found in Ref. 27). We use a high-quality (100) single-crystal rutile TiO₂ substrate (1 cm × 1 cm, ~500 μm thickness, MTI Corp.). The optic axis is precisely aligned in every produced nanocylinder, using the (100) crystal orientation in which the optic axis is perpendicular to the substrate surface normal. This configuration allows the precise angular manipulation around z-axis, with a trapping beam linearly polarized in *xy*-plane (as depicted in **Fig. 4.1e**). Compared to our previously reported fabrication protocol²⁷, we further optimized the chromium mask shape and thickness to obtain more circular cross sections and smaller taper angles (see details in **Supplementary Fig. S4.10**). The steps in the nanofabrication protocol that control nanocylinder diameter and height are electron-beam lithography (EBPG 5000 or EBPG 5200, Vistec) and plasma etching (Fluor Z401S, Leybold Heraeus or Plasmalab System 100, Oxford Instr.), respectively. As shown in **Supplementary Table S4.1**, this optimization leads to excellent structural uniformity among the fabricated TiO₂ nanocylinders (relative standard deviation 2–8% for diameters and 0.1–1.5% for heights, measured for 5–15 particles per batch), as deduced from the SEM images (S4800 FESEM, Hitachi) (**Supplementary Fig. S4.4**). As a result, our nanoparticles more closely resemble ideal cylinders and display more reproducible behavior. Otherwise, for example, deviations in the taper angle can lead to a substantial change in the trap stiffness (**Supplementary Fig. S4.6**).

To increase the probability of trapping single isolated nanocylinders in OTW measurements, it is crucial to prolong the monodispersed status of the nanocylinders in aqueous solution. For this purpose, the nanocylinders are coated with amino-terminated monofunctional polyethylene glycol (NH₂-PEG) molecules (MW 5000, PEG1154, Iris Biotech) *via* epoxysilane linkers (3-Glycidoxypropyldimethylethoxysilane, 539260, Sigma-Aldrich) using our previously developed TiO₂ surface functionalization protocol²⁷. The PEGylated nanocylinders are mechanically cleaved in phosphate buffered saline (PBS) buffer (pH 7, Sigma-Aldrich) droplets by scratching the substrate surface with a sharpened home-made plastic blade. The plastic blade is softer than the TiO₂ substrate and minimizes the production of TiO₂ dust particles. We note that the presence of short PEG molecules does not affect the trapping and rotational

dynamics of our nanocylinders²¹, and have observed that the monodispersity of PEGylated TiO₂ particles is maintained upon sonication and vortexing, even after year-long storage (in plastic tubes at 4°C).

4.4.2. OTW setup and measurements

We conducted OTW experiments with our home-built setup (1064 nm-wavelength single-beam optical trap with polarization control; more details can be found in Refs.^{15, 16, 27}). We use a custom-made flow cell assembled with two borosilicate glass coverslips (No. 1.5H, Marienfeld) separated by a single-layer Parafilm® spacer of ~100 μm thickness. The use of coverslips with high-precision thickness (170 μm ± 5 μm for No. 1.5H) reduces possible variations in optical trap quality that might occur when the conventional coverslips with large thickness variation (e.g., 160–190 μm for No. 1.5) are used⁴⁰. The PBS buffer containing the nanocylinders are injected into the flow cell channel and both input and output of the channel are sealed by vacuum grease (18405, Sigma-Aldrich). After ~1 h, most of the nanocylinders in the solution are sedimented to the bottom of the flow cell. Among these nanocylinders, only a chosen nanocylinder can be lifted from the bottom by focusing the laser beam on the particle to generate a pushing force *via* light scattering. Using rutile TiO₂ is beneficial in this lifting process because its large refractive index induces stronger scattering for a given laser power. Afterwards, we can trap and measure the freed nanocylinder without any hydrodynamic coupling effect that can occur if the particle concentration is too high⁴¹. Also, it is possible to measure for extended times (tested up to ~3 h) without losing the particle by collision with other particles entering the optical trap. The nanocylinder trapping position is kept as 18–20 μm above the bottom surface of the flow cell channel, to effectively avoid any hydrodynamic interaction with the flow cell.

We measured 14 different rutile TiO₂ nanocylinder batches (**Supplementary Table S4.1**), and 3–10 particles were recorded for each trappable batch (**Fig. 4.3**, **Supplementary Fig. S4.8**, **Supplementary Table S4.2**). For calibration of linear and angular trapping properties, we adapted the previously developed methods^{16, 42}. For measurement of linear and angular fluctuations of a trapped cylinder, we employed an input beam which is linearly polarized along the *x*-axis. The large radial stiffness of the rutile TiO₂ particles lead to hydrodynamic effects, which contribute colored noise to the power spectrum^{23, 43}. We have considered this in our analysis (**Supplementary Fig. S4.10**). The linear and angular fluctuation data are acquired at 250 kHz sampling frequency. We developed and employed an improved method to more precisely measure torque-speed curves (**Supplementary Fig. S4.10**). In our method, each curve is measured by continuously scanning the polarization rotation frequency in the range of 0–15 kHz for a few seconds using a waveform generator (33120A, Agilent), with 100 kHz sampling frequency. Compared to the conventional time-consuming method in which separate torque traces are recorded at multiple different frequency values, this high-speed recording over a wide frequency range avoids the distortion of the measured curve caused by setup drift. The downward spikes shown at high PRF in **Fig.**

4.3g,h are attributed to the peculiarities of the setup, such as the finite time required for the polarization reversal of electro-optic modulator (EOM) voltage ^{2,14}, and appear regardless of the chosen torque-speed measurement method.

In addition, we measured linear trapping properties of PS microspheres (Polybead® Microspheres, Polysciences) (**Fig. 4.3c, Supplementary Fig. S4.8, Supplementary Table S4.3**) since they are one of the *de facto* standards among optical trapping community. In general, the characteristics of optical traps are not identical among different optical tweezers due to the difference in the specifications of the laser beam, objective lens, immersion medium, and flow cell design. Therefore, comparing the results from the standard commercial PS beads with high compositional and geometrical uniformity provides a means with which experimentalists can estimate the expected trapping properties of rutile TiO₂ nanocylinders in their own instruments.

4.4.3. Numerical calculation of optical momentum transfer and hydrodynamic drag

The cylindrical geometry and anisotropic optical property of our rutile TiO₂ particles require a numerical approach to precisely estimate their viscous drag coefficients and optical trapping force and torque. It is because the exact analytical solutions do not exist for anisotropic cylinders with arbitrary aspect ratios, unlike the commonly used isotropic spherical probes. We utilize FEM ⁴⁴ with one of its commercial implementations (COMSOL Multiphysics v5.2a, COMSOL Inc.). In general, FEM is more computationally demanding than other approaches such as T-matrix formulations ³¹. However, it is more flexible and versatile in the aspect of modeling anisotropic material and irregular geometry. Using FEM is straightforward even with cylinders of small aspect ratio and exotic shapes such as tapered cylinders (**Supplementary Fig. S4.6**), cones, and hour-glass shapes. The validations of our numerical models are shown in **Supplementary Fig. S4.10**. We note that the properties (size, density, quality, etc.) of geometry meshing in FEM models should be optimized properly to obtain precise results.

To calculate linear and angular optical trapping properties, we locate a rutile TiO₂ nanocylinder at the center of the calculation domain. The cylinder is enclosed by a uniform medium (water, $n = 1.33$) of spherical shape, and the medium is terminated with a perfect matching layer to treat the size of the medium as infinite by coordinate transformation. We use the exact focus beam equation without any approximations to calculate the input background field ⁴⁵. The beam shape is defined by the vacuum wavelength ($\lambda = 1064$ nm), objective lens numerical aperture ($NA = 1.2$), filling ratio ($\alpha = \infty$ or 1.7), linear polarization direction (along x -axis), and index of medium ($n = 1.33$). Here, the filling ratio $\alpha (= w_o/r_o)$ is defined as the ratio of the $1/e^2$ radius of input beam w_o and effective input aperture radius of objective lens $r_o (= f NA$, where f is the focal length of the objective lens). We use $\alpha = \infty$ as an ideal configuration in which input beam is a plane wave, and $\alpha = 1.7$ as the measured value in our OTW setup. The time-averaged optical force and torque on the cylinder is obtained by integrating the Maxwell stress

tensor over the surface of a virtual sphere enclosing the cylinder⁴⁶. We first obtain the axial force (F_z) curves, from which the axial equilibrium trapping positions (z_{eq}) are derived (**Supplementary Fig. S4.5**). Then we calculate radial force (F_x, F_y) and maximal torque (τ_o) at z_{eq} . The optical force is calculated at the zero-torque condition ($\theta = 0^\circ$ in **Eq. 4.1**), while the torque is calculated at the maximum torque transfer condition ($\theta = 45^\circ$ in **Eq. 4.1**).

To calculate hydrodynamic drag coefficients, the surrounding medium (water at 23 °C, dynamic viscosity of 0.933 mPa·s) is set to flow translationally (rotationally), inducing viscous drag force (torque) on the nanocylinder. The solutions of Navier-Stokes equations⁴⁷ result in force and torque as a function of the speed of medium flow, from which the drag coefficients can be extracted. We calculated two translational (axial, radial) and one rotational (around z-axis) drag coefficients: i) for each ideal cylinder (**Supplementary Fig. S4.7**) to use in calculations of angular speeds (**Fig. 4.2d**, **Supplementary Fig. S4.9**) and AD values (**Supplementary Fig. S4.9**), ii) for each fabricated nanocylinder batch (**Supplementary Fig. S4.8**) to compare with our experimentally obtained values. For the case of ideal cylinders, like ideal spheres⁴⁸, analytical expressions for the translational⁴⁹ and rotational⁵⁰ viscous drag exist. However, these are valid for only a limited range of aspect ratios and hence we used our numerical approach.

4.5. References

1. van Oene, M. M. et al. Quantifying the precision of single-molecule torque and twist measurements using Allan variance. *Biophysical Journal* **114**, 1970-1979 (2018).
2. Santybayeva, Z. & Pedaci, F. Optical torque wrench design and calibration. In *Optical Tweezers: Methods and Protocols, Methods in Molecular Biology* (ed Gennerich, A.) **1486**, 157-181 (Springer New York, 2017).
3. Beth, R. A. Mechanical detection and measurement of the angular momentum of light. *Physical Review* **50**, 115-125 (1936).
4. Friese, M. E. J., Nieminen, T. A., Heckenberg, N. R. & Rubinsztein-Dunlop, H. Optical alignment and spinning of laser-trapped microscopic particles. *Nature* **394**, 348-350 (1998).
5. Forth, S., Sheinin, M. Y., Inman, J. & Wang, M. D. Torque measurement at the single-molecule level. *Annual Review of Biophysics* **42**, 583-604 (2013).
6. Lipfert, J., van Oene, M. M., Lee, M., Pedaci, F. & Dekker, N. H. Torque spectroscopy for the study of rotary motion in biological systems. *Chemical Reviews* **115**, 1449-1474 (2015).
7. Arita, Y., McKinley, A. W., Mazilu, M., Rubinsztein-Dunlop, H. & Dholakia, K. Picoliter rheology of gaseous media using a rotating optically trapped birefringent microparticle. *Analytical Chemistry* **83**, 8855-8858 (2011).
8. Wu, T. et al. A photon-driven micromotor can direct nerve fibre growth. *Nature Photonics* **6**, 62-67 (2011).
9. Arita, Y., Mazilu, M. & Dholakia, K. Laser-induced rotation and cooling of a trapped microgyroscope in vacuum. *Nature Communications* **4**, 2374 (2013).
10. Neale, S. L., MacDonald, M. P., Dholakia, K. & Krauss, T. F. All-optical control of microfluidic components using form birefringence. *Nature Materials* **4**, 530-533 (2005).
11. Leach, J., Mushfique, H., di Leonardo, R., Padgett, M. & Cooper, J. An optically driven pump for microfluidics. *Lab on a Chip* **6**, 735-739 (2006).
12. Jones, P. H., Maragò, O. M. & Volpe, G. *Optical tweezers: principles and applications* (Cambridge University Press, 2015).
13. La Porta, A. & Wang, M. D. Optical torque wrench: angular trapping, rotation, and torque detection of quartz microparticles. *Physical Review Letters* **92**, 190801 (2004).

14. Gutiérrez-Medina, B., Andreasson, J. O. L., Greenleaf, W. J., LaPorta, A. & Block, S. M. An optical apparatus for rotation and trapping. In *Methods in Enzymology* (ed Walter, N. G.) **475**, 377-404 (Academic Press, 2010).
15. Pedaci, F., Huang, Z., van Oene, M., Barland, S. & Dekker, N. H. Excitable particles in an optical torque wrench. *Nature Physics* **7**, 259-264 (2010).
16. Pedaci, F., Huang, Z., van Oene, M. & Dekker, N. H. Calibration of the optical torque wrench. *Optics Express* **20**, 3787-3802 (2012).
17. Allen, L., Beijersbergen, M. W., Spreeuw, R. J. C. & Woerdman, J. P. Orbital angular momentum of light and the transformation of Laguerre-Gaussian laser modes. *Physical Review A* **45**, 8185-8189 (1992).
18. Funk, M., Parkin, S. J., Stilgoe, A. B., Nieminen, T. A., Heckenberg, N. R. & Rubinsztein-Dunlop, H. Constant power optical tweezers with controllable torque. *Optics Letters* **34**, 139-141 (2009).
19. Lehmuskero, A., Ogier, R., Gschneidner, T., Johansson, P. & Käll, M. Ultrafast spinning of gold nanoparticles in water using circularly polarized light. *Nano Letters* **13**, 3129-3134 (2013).
20. Shao, L., Yang, Z.-J., Andrés, D., Johansson, P. & Käll, M. Gold nanorod rotary motors driven by resonant light scattering. *ACS Nano* **9**, 12542-12551 (2015).
21. Jauffred, L., Taheri, S. M., Schmitt, R., Linke, H. & Oddershede, L. B. Optical trapping of gold nanoparticles in air. *Nano Letters* **15**, 4713-4719 (2015).
22. van der Horst, A., van Oostrum, P. D. J., Moroz, A., van Blaaderen, A. & Dogterom, M. High trapping forces for high-refractive index particles trapped in dynamic arrays of counterpropagating optical tweezers. *Applied Optics* **47**, 3196-3202 (2008).
23. Jannasch, A., Demirörs, A. F., van Oostrum, P. D. J., van Blaaderen, A. & Schäffer, E. Nanonewton optical force trap employing anti-reflection coated, high-refractive-index titania microspheres. *Nature Photonics* **6**, 469-473 (2012).
24. Arita, Y. et al. Rotational dynamics and heating of trapped nanovaterite particles. *ACS Nano* **10**, 11505-11510 (2016).
25. Neuman, K. C., Chadd, E. H., Liou, G. F., Bergman, K. & Block, S. M. Characterization of photodamage to *Escherichia coli* in optical traps. *Biophysical Journal* **77**, 2856-2863 (1999).
26. Polyanskiy, M. N. *Refractive index database*. <https://refractiveindex.info/> (2018).
27. Ha, S., Janissen, R., Ussembayev, Y. Y., van Oene, M. M., Solano, B. & Dekker, N. H. Tunable top-down fabrication and functional surface coating of single-crystal titanium dioxide nanostructures and nanoparticles. *Nanoscale* **8**, 10739-10748 (2016).
28. Parkin, S. J. et al. Highly birefringent vaterite microspheres: production, characterization and applications for optical micromanipulation. *Optics Express* **17**, 21944-21955 (2009).
29. Demirörs, A. F., Jannasch, A., van Oostrum, P. D., Schaffer, E., Imhof, A. & van Blaaderen, A. Seeded growth of titania colloids with refractive index tunability and fluorophore-free luminescence. *Langmuir* **27**, 1626-1634 (2011).
30. Simpson, N. B., McGloin, D., Dholakia, K., Allen, L. & Padgett, M. J. Optical tweezers with increased axial trapping efficiency. *Journal of Modern Optics* **45**, 1943-1949 (1998).
31. Nieminen, T. A. et al. Optical tweezers computational toolbox. *Journal of Optics A: Pure and Applied Optics* **9**, S196-S203 (2007).
32. Rohrbach, A. & Stelzer, E. H. K. Trapping forces, force constants, and potential depths for dielectric spheres in the presence of spherical aberrations. *Applied Optics* **41**, 2494-2507 (2002).
33. Neuman, K. C. & Nagy, A. Single-molecule force spectroscopy: optical tweezers, magnetic tweezers and atomic force microscopy. *Nature Methods* **5**, 491-505 (2008).
34. Beeby, M., Ribardo, D. A., Brennan, C. A., Ruby, E. G., Jensen, G. J. & Hendrixson, D. R. Diverse high-torque bacterial flagellar motors assemble wider stator rings using a conserved protein scaffold. *Proceedings of the National Academy of Sciences* **113**, E1917-E1926 (2016).
35. Capitanio, M. & Pavone, F. S. Interrogating biology with force: single molecule high-resolution measurements with optical tweezers. *Biophysical Journal* **105**, 1293-1303 (2013).
36. Daniels, B. R., Masi, B. C. & Wirtz, D. Probing single-cell micromechanics in vivo: the microrheology of *C. elegans* developing embryos. *Biophysical Journal* **90**, 4712-4719 (2006).
37. Craig, D., McDonald, A., Mazilu, M., Rendall, H., Gunn-Moore, F. & Dholakia, K. Enhanced optical manipulation of cells using antireflection coated microparticles. *ACS Photonics* **2**, 1403-1409 (2015).
38. Xu, Z. & Li, T. Detecting Casimir torque with an optically levitated nanorod. *Physical Review A* **96**, 033843 (2017).
39. Phillips, D. B. et al. Surface imaging using holographic optical tweezers. *Nanotechnology* **22**, 285503 (2011).
40. Reihani, S. N. S., Shahid, A. M., Andrew, C. R. & Lene, B. O. Significant improvement of optical traps by tuning standard water immersion objectives. *Journal of Optics* **13**, 105301 (2011).

41. Meiners, J.-C. & Quake, S. R. Direct Measurement of hydrodynamic cross correlations between two particles in an external potential. *Physical Review Letters* **82**, 2211-2214 (1999).
42. Tolić-Nørrelykke, S. F., Schäffer, E., Howard, J., Pavone, F. S., Jülicher, F. & Flyvbjerg, H. Calibration of optical tweezers with positional detection in the back focal plane. *Review of Scientific Instruments* **77**, 103101 (2006).
43. Franosch, T. et al. Resonances arising from hydrodynamic memory in Brownian motion. *Nature* **478**, 85-88 (2011).
44. Wei, X., Wachtors, A. J. & Urbach, H. P. Finite-element model for three-dimensional optical scattering problems. *Journal of the Optical Society of America A* **24**, 866-881 (2007).
45. Novotny, L. *Principles of nano-optics*, 2nd edn (Cambridge University Press, 2012).
46. Chen, J., Ng, J., Lin, Z. & Chan, C. T. Optical pulling force. *Nature Photonics* **5**, 531-534 (2011).
47. White, F. M. *Fluid mechanics*, 8th edn (McGraw-Hill Education, 2016).
48. Leach, J. et al. Comparison of Faxen's correction for a microsphere translating or rotating near a surface. *Physical Review E* **79**, 026301 (2009).
49. Khatibzadeh, N. et al. Determination of motility forces on isolated chromosomes with laser tweezers. *Scientific Reports* **4**, 6866 (2014).
50. Ortega, A. & García de la Torre, J. Hydrodynamic properties of rodlike and disklike particles in dilute solution. *The Journal of Chemical Physics* **119**, 9914-9919 (2003).

4.6. Supplementary Information

4.6.1. Derivation of the analytical equation for optical torque transfer from a linearly polarized plane wave to an infinitely wide birefringent plate with uniform thickness

The purpose of this section is to confirm the validity of **Eq. 4.1**, as in the literature many different forms of this equation exist in the absence of detailed derivation¹⁻⁴. First, we start with torque on a single dipole in a plate:

$$\vec{\tau} = \vec{p} \times \vec{E}, \quad (\text{Equation S4.1})$$

where \vec{p} is the electric dipole moment and \vec{E} is the electric field in the plate⁵. We can derive the torque per unit volume of a dielectric plate of uniform thickness perpendicular to the beam propagation direction by considering multiple dipoles in a given volume:

$$N\vec{\tau} = N\vec{p} \times \vec{E} = \vec{P} \times \vec{E} = \varepsilon_0 \underline{\chi} \vec{E} \times \vec{E}, \quad (\text{Equation S4.2})$$

where N is the number of dipoles, \vec{P} is the polarization per unit volume, ε_0 is the vacuum permittivity, and $\underline{\chi}$ is the electric susceptibility tensor in the plate. The input beam is set to be a plane wave that propagates in the z -direction, being linearly polarized in x - y plane. Thus, the electric field \vec{E} has zero intensity in the z -dimension ($E_z = 0$) and hence torque is applied in the z -direction only:

$$N\vec{\tau} = \varepsilon_0 \begin{bmatrix} \chi_x & 0 & 0 \\ 0 & \chi_y & 0 \\ 0 & 0 & \chi_z \end{bmatrix} \begin{bmatrix} E_x \\ E_y \\ 0 \end{bmatrix} \times \begin{bmatrix} E_x \\ E_y \\ 0 \end{bmatrix} = \varepsilon_0 \begin{bmatrix} 0 \\ 0 \\ (\chi_x - \chi_y)E_x E_y \end{bmatrix}. \quad (\text{Equation S4.3})$$

Using the known relationship $\chi = n^2 - 1$, the torque in the z direction can be described as:

$$N\tau_z = \varepsilon_0 (\chi_x - \chi_y) E_x E_y = \varepsilon_0 (n_x^2 - n_y^2) E_x E_y. \quad (\text{Equation S4.4})$$

In **Eq. S4.4**, the electric field vectors (E_x, E_y) in time t and space z are defined as:

$$\begin{aligned} E_x &= E_x(z, t) = E_{0,x} \cos(k_x z - \omega t), \\ E_y &= E_y(z, t) = E_{0,y} \cos(k_y z - \omega t), \end{aligned} \quad (\text{Equation S4.5})$$

where $E_{0,x} = E_0 \cos(\theta)$, $E_{0,y} = E_0 \sin(\theta)$, and θ is the angle between the x -axis and the linear polarization direction of the electric field with amplitude E_0 in the plate. Also, $k_x = k_0 n_x$, $k_y = k_0 n_y$, while n_x, n_y are refractive indices of the plate along the x - and y -axis, k_x, k_y are wavenumbers in the plate along the x - and y -axis, and $k_0 = \frac{\omega}{c}$ is the wavenumber in vacuum (here, ω is the laser optical frequency and c is the speed of light in vacuum). We rewrite **Eq. S4.5** similarly to Beth's derivation³:

$$\begin{aligned} E_x(z, t) &= E_{0,x} \cos\left(\frac{k_x+k_y}{2}z + \frac{k_x-k_y}{2}z - \omega t\right) = E_{0,x} \cos(Z + D), \\ E_y(z, t) &= E_{0,y} \cos\left(\frac{k_x+k_y}{2}z - \frac{k_x-k_y}{2}z - \omega t\right) = E_{0,y} \cos(Z - D), \end{aligned} \quad (\text{Equation S4.6})$$

where $Z = kz - \omega t$ and $D = \frac{\Delta k}{2}z$ (here, $k = \frac{k_x+k_y}{2}$, $\Delta k = k_x - k_y = k_0(n_x - n_y) = k_0\Delta n$). Using trigonometric identities, we can further simplify the factor $E_x E_y$ in **Eq. S4.4**. This allows us to express the z -component of the instantaneous torque per unit volume as:

$$N\tau_z = \varepsilon_0(n_x^2 - n_y^2)E_x E_y = \frac{\varepsilon_0(n_x^2 - n_y^2)E_0^2}{4} \sin(2\theta) (\cos(2Z) + \cos(2D)), \quad (\text{Equation S4.7})$$

and its time-averaged variant as:

$$\langle N\tau_z \rangle = \frac{1}{T} \int_0^T dt N\tau_z = \frac{\varepsilon_0(n_x^2 - n_y^2)E_0^2}{4} \sin(2\theta) \cos(z\Delta k). \quad (\text{Equation S4.8})$$

To obtain the torque per unit area for a given plate thickness (i.e., height) h , we integrate along the z -axis:

$$\begin{aligned} \int_0^h dz \langle N\tau_z \rangle &= hN\langle \tau_z \rangle = \frac{\varepsilon_0(n_x^2 - n_y^2)E_0^2}{4} \sin(2\theta) \left(\frac{1}{\Delta k} [\sin(z\Delta k)]_0^h\right) \\ &= \frac{\varepsilon_0 c(n_x^2 - n_y^2)E_0^2}{4\omega\Delta n} \sin(2\theta) \sin(h\Delta k) = \frac{\varepsilon_0 n c E_0^2}{2\omega} \sin(2\theta) \sin(hk_0\Delta n), \end{aligned} \quad (\text{Equation S4.9})$$

where n is the mean index (i.e., $n = \frac{n_x+n_y}{2}$) of the plate. Finally, the torque per plate volume can be obtained by rewriting $N = \frac{N_d}{V} = \frac{N_d}{hS}$, where N_d is the total number of dipoles within the plate and S is the area of the plate surface with which the beam interacts:

$$\langle \tau_{z,total} \rangle = N_d \langle \tau_z \rangle = \frac{S\varepsilon_0 n c E_0^2}{2\omega} \sin(hk_0\Delta n) \sin(2\theta), \quad (\text{Equation S4.10})$$

which is identical to the amplitude of torque in **Eq. 4.1** in the main text. We note that this equation is derived under the idealized condition of a plane wave interacting only with an infinitely wide plate of uniform thickness. It does not take into account the surrounding medium, and as such, the accompanying reflections at the material interfaces. When we use such idealized conditions in our FEM calculations, we obtain results identical to those predicted by **Eq. 4.1 (Supplementary Fig. S4.10)**; although a plate of finite size, e.g., 300 nm \times 300 nm surface area, is required by FEM models, it is equivalent to the infinite case when light diffraction near the plate edges is ignored). Therefore, torque values acquired under non-ideal but realistic conditions deviate from the predictions of **Eq. 4.1**. As further detailed in **Supplementary Fig. S4.1**, one such example is a particle with a finite size trapped by a tightly-focused beam, e.g., rutile TiO₂ experiments in OTW as shown in **Fig. 4.1e**.

4.6.2. Supplementary Figures

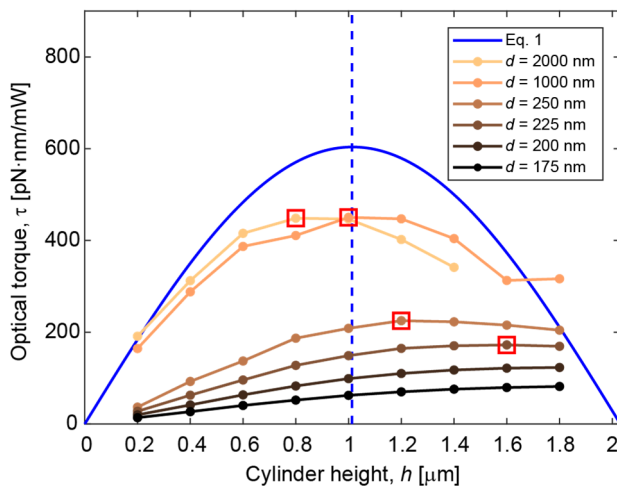


Figure S4.1. FEM-calculated rutile TiO_2 nanocylinder height for maximal torque transfer efficiency at different fixed diameters. The maximal optical torque (circles) of rutile TiO_2 nanocylinders as a function of their height ($h = 0.2\text{--}1.8 \mu\text{m}$) for different diameters ($d = 175\text{--}2000 \text{ nm}$), FEM-calculated at $z_{\text{eq}} = 0 \text{ nm}$ and $\theta = 45^\circ$ (for the largest diameter $d = 2000 \text{ nm}$, calculation is performed up to $h = 1.4 \mu\text{m}$ due to the limitation of computing memory). Calculations are performed assuming a focus beam with the vacuum wavelength $\lambda = 1064 \text{ nm}$, objective lens $NA = 1.2$, an objective lens filling ratio $\alpha = \infty$, and a surrounding medium index $n = 1.33$. For comparison, the analytical prediction (blue curve, using Eq. 4.1 from the main text) assuming a plane wave interacting with a rutile TiO_2 plate of $300 \text{ nm} \times 300 \text{ nm}$ surface area is co-plotted. The vertical dashed blue line ($h \approx 1 \mu\text{m}$) indicates the analytical prediction of optimal cylinder height for the maximal torque transfer efficiency, while the numerical predictions are designated by red squares if they exist within the calculated range. Note that nanoparticles with diameters smaller than the beam wavelength ($d = 175\text{--}250 \text{ nm}$) deviate most from the analytical prediction. Cylinders with diameters comparable to or larger than the beam wavelength ($d = 1000\text{--}2000 \text{ nm}$) show optical torque that more closely approximates the analytical prediction, as their geometry is closer to that of a rutile TiO_2 plate.

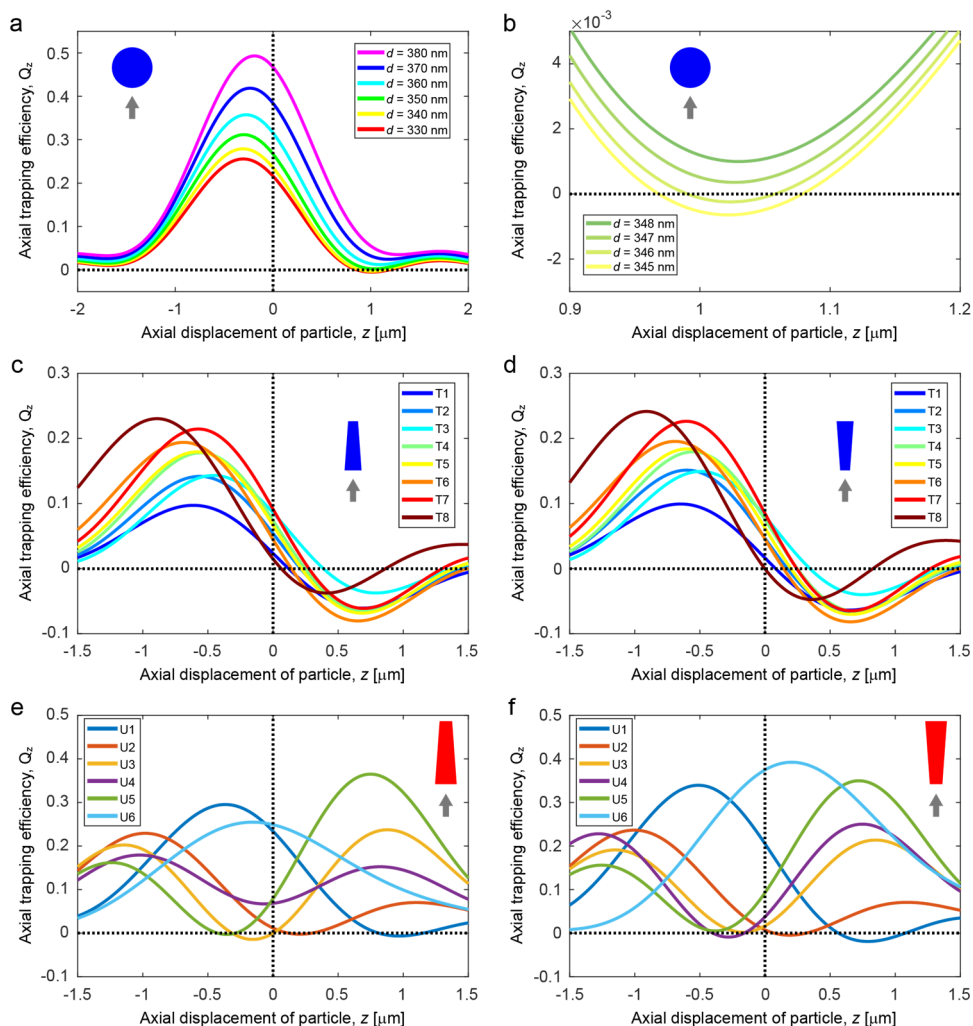


Figure S4.2. FEM-calculated optical trappability of rutile TiO_2 spheres and cylinders. (a) The FEM-calculated axial trapping efficiency (Q_z) curves (i.e., normalized axial force (F_z) curves; $Q_z = F_z/(nP/c)$, where n is the refractive index of the surrounding medium, P is the trapping laser beam power, and c is the speed of light in vacuum) for rutile TiO_2 spheres with diameters of 330–380 nm, demonstrating that spheres with large volume ($\geq \sim 350$ nm) are not trappable. (b) FEM-calculations of Q_z with 1 nm-step in sphere diameter (345–348 nm) reveal that the diameter of the largest trappable rutile TiO_2 sphere is ~ 346 nm. (c–f) The FEM-calculated axial trapping efficiency (Q_z) curves for all fabricated rutile TiO_2 nanocylinder batches, using average SEM-measured dimensions with actual sidewall profiles as input parameters. The trap strengths (as defined in **Supplementary Fig. S4.5**) of trappable cylinders (T1–T8; (c,d)) are much larger than those of non-trappable cylinders (U1–U6; (e,f)). As the cylinders are not symmetric in the z -dimension, two different trapping orientations exist for each cylinder (with the positive (c,e) or negative (d,f) taper angle with respect to the input beam as shown in the inset diagram). For trappable cylinders (T1–T8; (c,d)), as their taper angles are small (0.1 – 1.6° , **Supplementary Table S4.1**), the trapping orientation does not significantly contribute to trapping behavior (**Supplementary Fig. S4.6**). All calculations in (a–f) are performed assuming a focus beam with objective lens $NA = 1.2$, an objective lens filling ratio $\alpha = 1.7$, and a surrounding medium index $n = 1.33$.

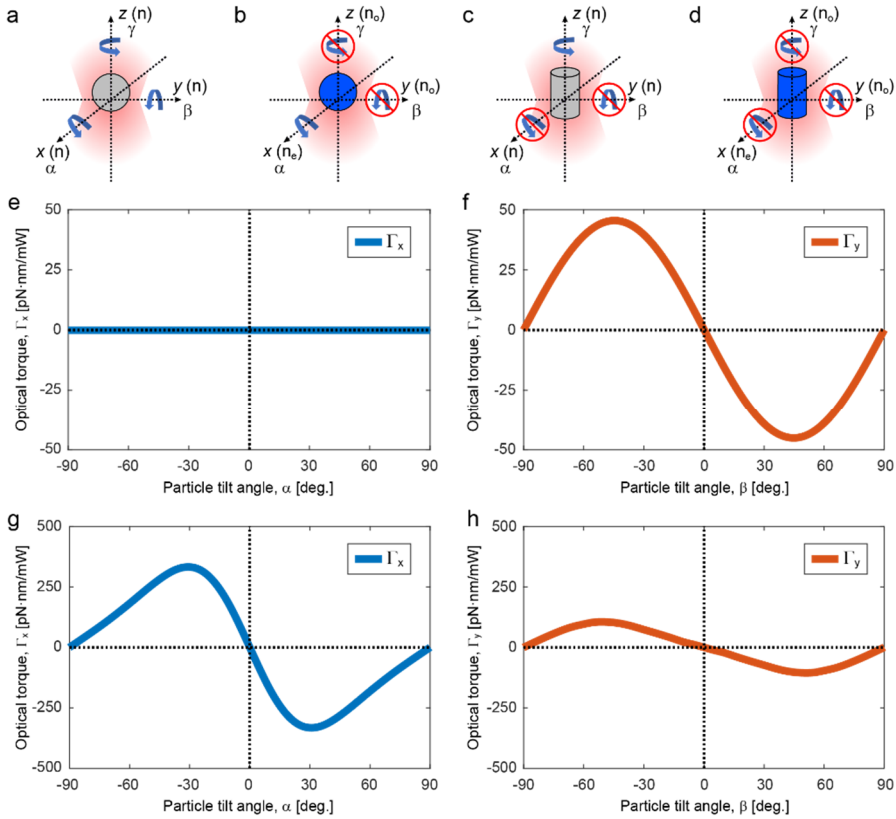


Figure S4.3. FEM-calculated RDOF confinement torque of rutile TiO_2 spheres and cylinders. Visual representation of the mechanism of RDOF confinement, supported by numerical calculations. (a-d) Illustrations of achievable confinement of the RDOF depending on the degree of geometrical or optical anisotropy. An optically isotropic particle (gray, e.g., polystyrene) has a constant refractive index (n) along its principal axes (x, y , and z), while a birefringent particle (blue, e.g., rutile TiO_2) includes an extraordinary index (n_e) that differs from the other two ordinary indices (n_o). Here, a positively birefringent crystal (e.g., rutile TiO_2) is assumed, and thus $n_e > n_o$. A blue curved arrow indicates free rotation in the absence of confinement, while an overlaid prohibitory traffic sign indicates the restriction in rotation due to confined RDOF. The incident trapping beam is assumed to be linearly polarized in the x -dimension. (a) A non-birefringent sphere, which is fully isotropic, has no confined RDOF. (b) A positively birefringent sphere that has optical anisotropy only, has two confined RDOF. (c) A non-birefringent cylinder that has geometrical anisotropy only, has two confined RDOF. (d) A positively birefringent cylinder, which is fully anisotropic, has fully confined RDOF. (e,f) FEM-calculated optical torque components for a positively birefringent sphere (rutile TiO_2 , $d = 150$ nm), i.e., configuration in panel (b). The result shows that indeed the angle α is not confined, as (e) Γ_x remains zero at any angle, while the angle β is confined by the restoring torque (f) Γ_y from the optical birefringence. (g,h) FEM-calculated optical torque components for a positively birefringent cylinder (rutile TiO_2 , $d = 200$ nm and $AR = 5$), i.e., configuration in panel (d). The confinement in the angle α results from the restoring torque (g) Γ_x generated by the uneven radiation pressure distribution on a tilted cylinder (no such geometrical effect would occur in the case of a tilted sphere). The angle β is doubly confined by the restoring torque (h) Γ_y from both geometrical and optical anisotropy. The confinement of the RDOF in the angle γ by the restoring torque Γ_z that results from particle birefringence is common to both sphere and cylinder. All calculations in (e-h) are performed assuming the vacuum wavelength of input beam $\lambda = 1064$ nm, an equilibrium axial trapping position $z_{eq} = 0$, a focus beam with objective lens $NA = 1.2$, an objective lens filling ratio $\alpha = \infty$, and a surrounding medium index $n = 1.33$.

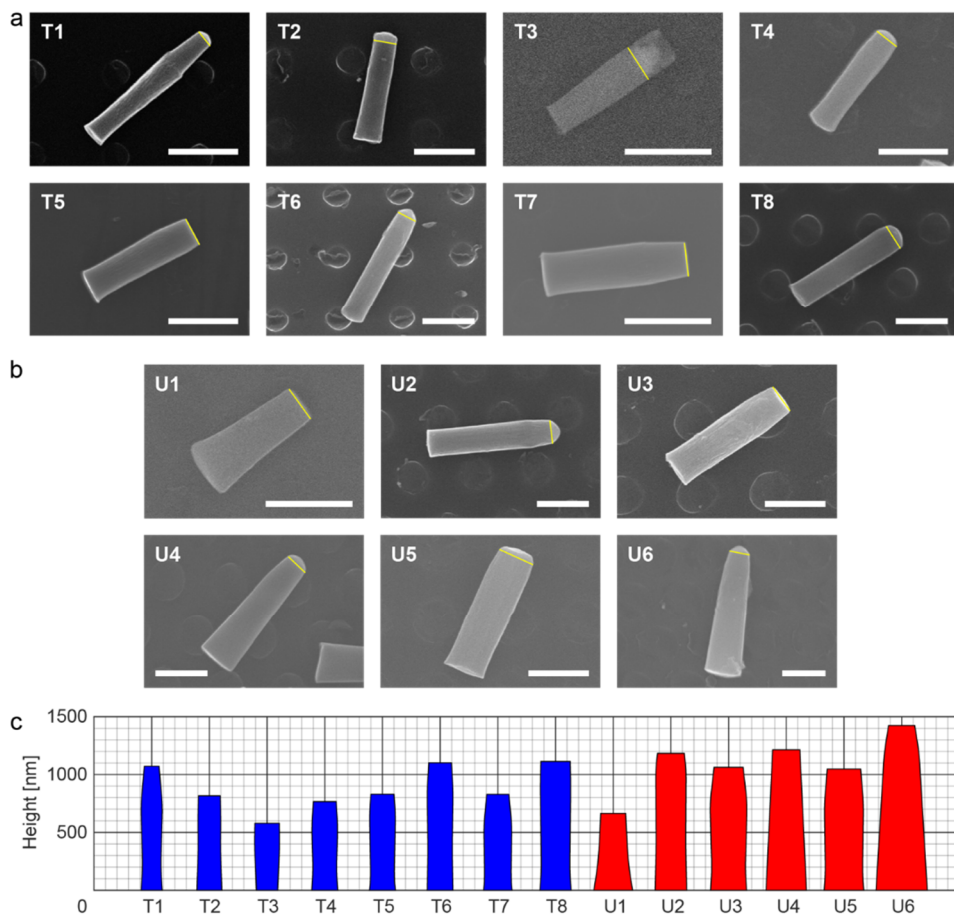


Figure S4.4. SEM micrographs of top-down fabricated single-crystal rutile TiO_2 nanocylinder batches. (a,b) A representative SEM micrograph of each cylinder batch is shown: (a) trappable nanocylinder batches (T1–T8); (b) untrappable nanocylinder batches (U1–U6). All scale bars are 500 nm. The yellow lines indicate the top surfaces of cylinders, and the structures just above them are Cr masks that remain when SEM images are taken prior to Cr removal by wet etching. (c) Geometries of trappable (blue) and untrappable (red) nanocylinders drawn up on the same scale with the mean dimensions obtained from multiple SEM images (**Supplementary Table S4.1**). Both vertical and horizontal grid lines have the same spacing (100 nm-step for thin lines and 500 nm-step for thick lines).

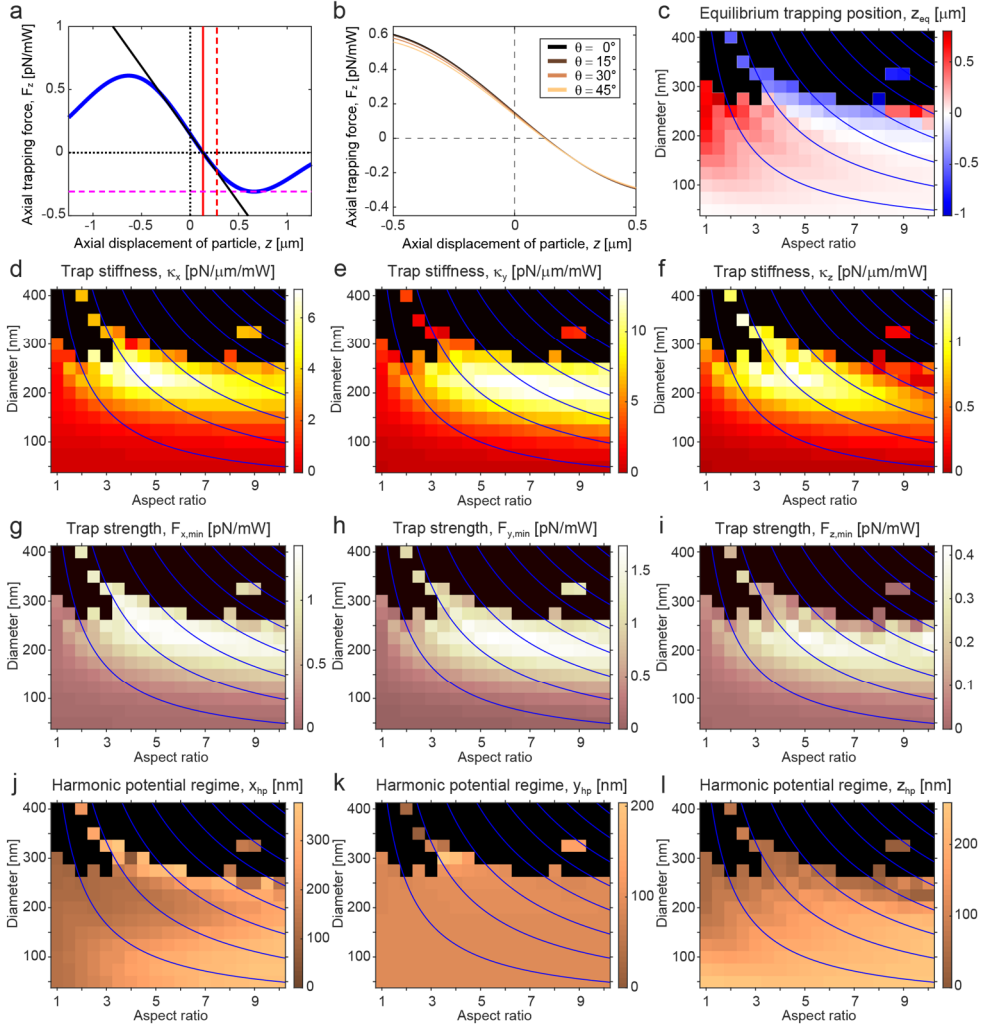


Figure S4.5. FEM-calculated parameters describing the linear optical trapping behavior of rutile TiO_2 nanocylinders. Linear trapping parameters deduced from FEM-calculated force curves, plotted as a function of cylinder diameter and aspect ratio. (a) The definitions of these parameters are graphically summarized with an axial force curve (the blue curve, for a nanocylinder with $d = 200$ nm and $AR = 5$ as an example): the axial equilibrium trapping position z_{eq} (the vertical red line which is the x -intercept of the force curve), the axial trap stiffness κ_z (the gradient of force at z_{eq} designated by the solid black tangential line which approximates the harmonic potential well), the axial trap strength $F_{z,min}$ (the horizontal magenta dashed line over which the particle will escape from the trap), and the axial harmonic potential regime x_{hp} (the distance from z_{eq} to the nearest position at which the deviation of the actual force from the ideal harmonic approximation starts to exceed 10% which is the conventional cutoff threshold^{6,7}, represented by the vertical red dashed line). (b) The changing axial force curve shape upon rotation of the same rutile TiO_2 cylinder in (a) from $\theta = 0^\circ$ to $\theta = 45^\circ$ (with the rotation angle θ as defined in Eq. 4.1 from the main text). In this range, the deviation of z_{eq} is almost negligible (~ 6 nm) compared to the cylinder height (1 μm). As this behavior is similar to other cylinder dimensions as well, it is still valid to calculate the maximum optical torque (which occurs at $\theta = 45^\circ$) with z_{eq} obtained at $\theta = 0^\circ$ (Fig. 4.3c, Supplementary Fig. S4.9). (c) The map of z_{eq} . For each black colored pixel, z_{eq} does not exist (i.e., the axial force curve has no x -intercept) and hence 3D-trapping is not possible for cylinders of the corresponding dimensions. We do not calculate radial trapping parameters

at these positions, since we are interested in 3D-trappable cylinder dimensions only. For 3D-trappable cylinder dimensions, the radial trapping parameters are calculated at z_{eq} . **(d-f)** The linear trap stiffness maps ($\kappa_x, \kappa_y, \kappa_z$). **(g-i)** The linear trap strength maps ($F_{x,min}, F_{y,min}, F_{z,min}$). **(j-l)** The linear harmonic potential regime maps (x_{hp}, y_{hp}, z_{hp}). The blue curves are iso-height contours (500–4000 nm from left to right, with a step size of 500 nm). The resolution of the maps is $\Delta AR = 0.5$ and $\Delta d = 25$ nm. All calculations in (a-l) are performed assuming the vacuum wavelength of input beam $\lambda = 1064$ nm, a focus beam with objective lens $NA = 1.2$, an objective lens filling ratio $\alpha = \infty$, and a surrounding medium index $n = 1.33$.

Additional explanation of the linear trapping parameters

In addition to the axial trap stiffness κ_z , various other axial trapping parameters should be considered when choosing appropriate cylinder dimensions for specific practical applications. For example, the axial trap strength $F_{z,min}$ can be used as a criterion to assess stable 3D trapping. If the axial trap strength of a cylinder is very weak, despite the trap itself having high axial stiffness (e.g., the nanocylinder with $d = 300$ nm and $AR = 3.5$), then such a particle is difficult to exploit since it will escape from the trap at the slightest external perturbation. Also, the extent of the linear axial force regime z_{hp} , combined with κ_z , provides information about the maximum applicable axial force under the assumption that the axial trap is a harmonic potential well (i.e., a linear Hookean spring). This information is valuable as proper trap calibration is easiest in this regime. The above definitions and reasoning apply similarly to radial trapping in x - and y -dimensions.

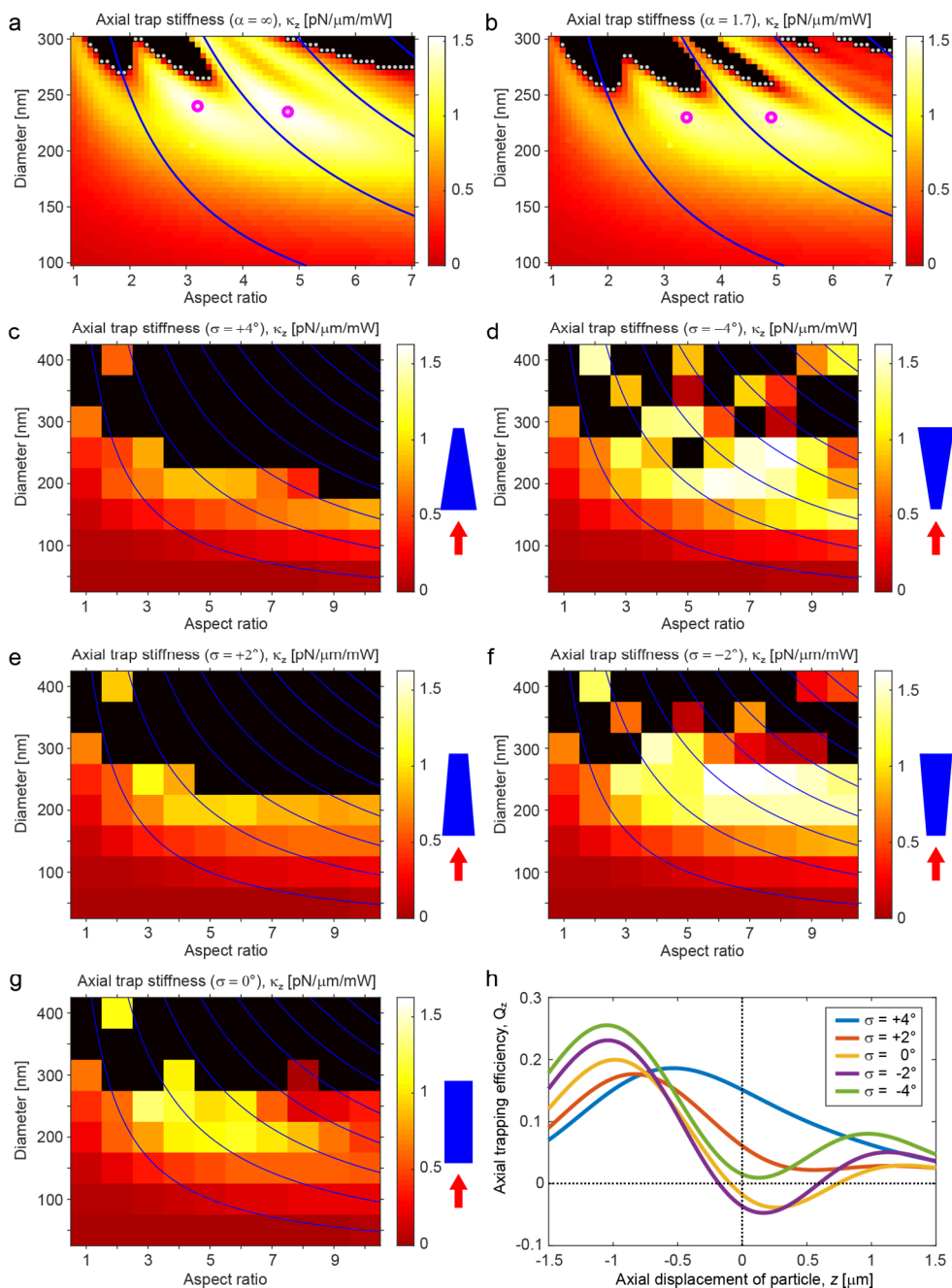


Figure S4.6. FEM-calculated maps of axial stiffness and curves of axial trapping efficiency for rutile TiO_2 nanocylinders with different objective lens aperture filling ratios and taper angles. (a,b) The FEM-calculated high-resolution maps of axial stiffness κ_z for rutile TiO_2 nanocylinders with (a) ideal ($\alpha = \infty$) and (b) measured ($\alpha = 1.7$; the same data as Fig. 4.2a) aperture filling ratios. The calculated threshold diameter d_{cal}^* for each aspect ratio is displayed as a gray dot, and the magenta circles indicate the local maxima of stiffness. Calculations based on the measured filling ratio (b) result in a narrower range of 3D-trappable cylinder diameters for aspect ratios between 1 and 5. The stiffness values at the local maxima are also reduced

by $\sim 10\%$, due to the less tight beam focusing for a smaller filling ratio. The blue curves are iso-height contours (500–2000 nm from left to right, with a step size of 500 nm). The resolution of the maps is $\Delta AR = 0.1$ and $\Delta d = 5$ nm. (c–f) κ_z maps of nanocylinders with a taper angle σ of (c) $+4^\circ$, (d) -4° , (e) $+2^\circ$, and (f) -2° , as a function of the aspect ratio and average diameter d_{av} (with ideal aperture filling ratio $\alpha = \infty$). The schematics to the right of the maps illustrate the taper angle (not to scale) and orientation of the cylinder body with respect to the laser beam propagation direction (red arrow). (g) κ_z map of perfectly straight nanocylinders (the same data as shown in panel (a) and **Supplementary Fig. S4.9**), displayed for straightforward comparison with the maps of tapered cylinders. The blue curves are iso-height contours (500–4000 nm from left to right, with a step size of 500 nm). The resolution of the maps is $\Delta AR = 1$ and $\Delta d = 50$ nm. (h) Axial trapping efficiency Q_z as a function of taper angle for a representative cylinder batch with $d_{av} = 250$ nm and $AR = 5$. All calculations in (a–h) are performed assuming the vacuum wavelength of input beam $\lambda = 1064$ nm, a focus beam with objective lens $NA = 1.2$, and a surrounding medium index $n = 1.33$.

Effects of nanocylinder taper angle on axial trapping properties

The dry etching process can result in nanocylinders with small taper angle (0 – 5° ; T1–T8 and U1–U6 shown in **Supplementary Fig. S4.4** and **Supplementary Table S4.1**), and such geometrical asymmetry can alter the optical trapping characteristics^{8,9}. To investigate this effect in rutile TiO_2 nanocylinders, we calculated axial trapping force F_z and then extracted axial stiffness κ_z for cylinders with taper angle σ of $\pm 2^\circ$ and $\pm 4^\circ$ while keeping the cylinder height and average diameter constant (thus, both the surface area and volume of the tapered cylinders are nearly the same as those of straight cylinders, allowing an unbiased comparison). For a tapered cylinder, two trapping orientations are possible with respect to the beam propagation direction. When the larger facet of a tapered cylinder is facing the source of the laser beam, the trappable regime shrinks and overall the trap stiffness decreases. This might be due to the increased light scattering at the larger entering surface of the particle, which destabilizes the trap. In contrast, when the tapered cylinder is flipped, and the smaller facet faces the beam source, the trappable regime expands and overall the trap stiffness increases. However, for each individual cylinder dimension, these changes are not proportional but nonlinearly correlated with the taper angle. For example, in the case of $d = 250$ nm and $AR = 5$ cylinder (**Supplementary Fig. S4.6h**), changing taper angle from 0° to -2° enhances trap stiffness, but -4° taper renders the cylinder untrappable. Importantly, this result also advises us about what are the fabrication error-tolerant cylinder sizes, with which the particles can be always 3D-trapped even with small variations in taper angles. For example, $d = 200$ nm and $AR = 4$ – 6 cylinders can be 3D-trapped regardless of the taper angle variations of $\pm 4^\circ$. For the fabricated and optically trappable rutile TiO_2 nanocylinder batches (T1–T8), taper angles are rather small (0.1 – 1.6°) and hence their trapping behaviors are expected to be similar to those of perfectly straight cylinders.

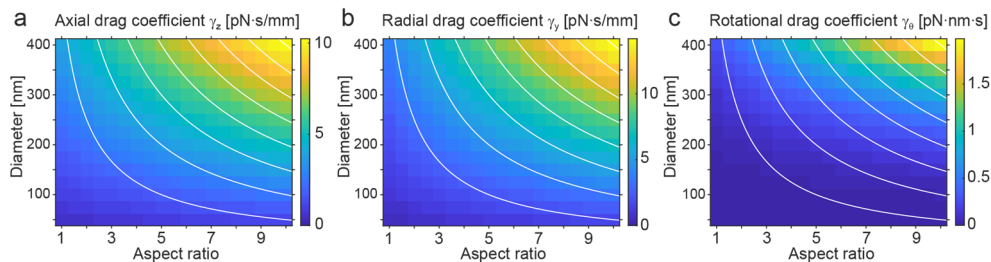


Figure S4.7. FEM-Calculated translational and rotational hydrodynamic drag coefficients of nanocylinders. (a,b) The drag coefficients for translational movements of nanocylinders in water are FEM-calculated as a function of cylinder diameter and aspect ratio: (a) the axial linear drag coefficients (movement along the z -axis), (b) the radial linear drag coefficients (movement along either the x -axis or the y -axis). (c) The drag coefficients for rotational motion of nanocylinders (rotation about the z -axis). These rotational drag coefficients are used to calculate the maps of the maximum rotation frequency (Fig. 4.2d and Supplementary Fig. S4.9). The resolution of the maps in (a-c) is $\Delta AR = 0.5$ and $\Delta d = 25$ nm. For Fig. 4.2d in the main text, we used a drag map with higher resolution, $\Delta AR = 0.1$ and $\Delta d = 5$ nm. The white curves are iso-height contours (500–4000 nm from left to right, with a step size of 500 nm).

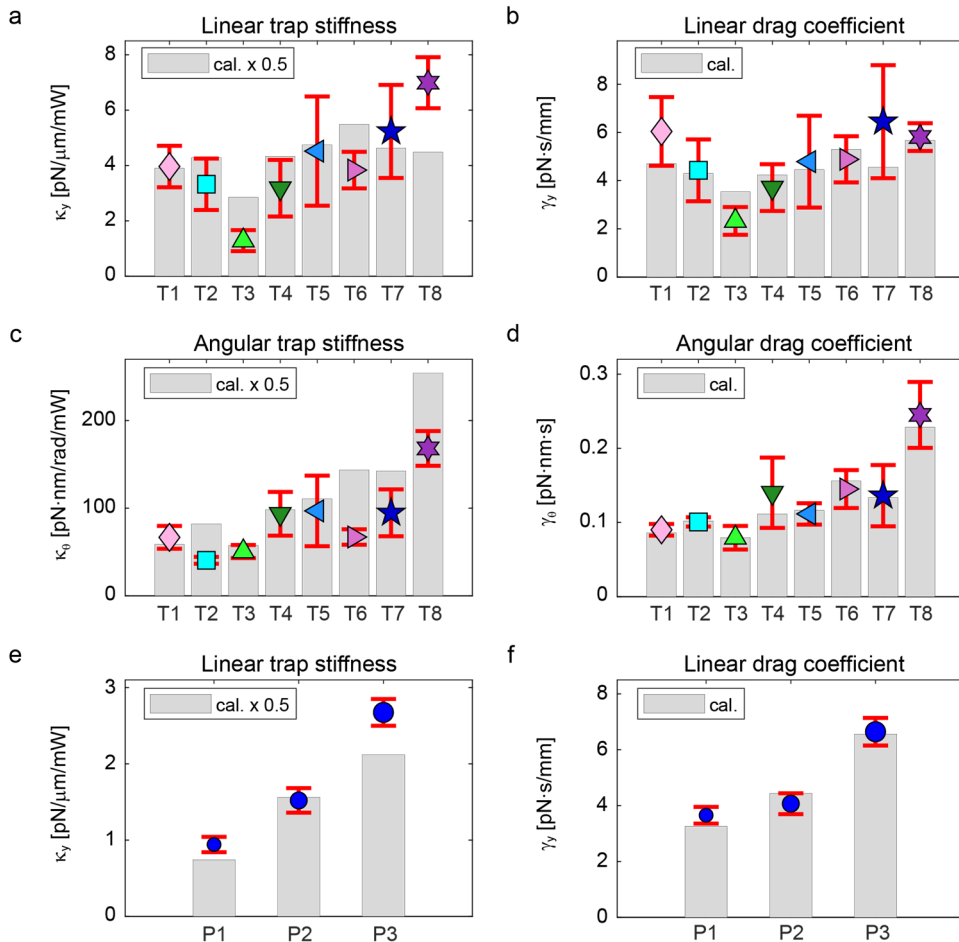


Figure S4.8. Comparison of experimentally and theoretically obtained stiffnesses and drag coefficients for trapping of rutile TiO_2 cylinders and PS spheres. For all trappable nanocylinder batches (T1–T8) and measured PS sphere batches (P1–P3), the trapping parameters obtained by both FEM calculations and OTW measurements are shown. The FEM calculations used the SEM-measured average dimensions for the cylinders and the average diameter provided by the supplier for the spheres. (a) The linear trap stiffness (κ_y), (b) linear drag coefficient (γ_y), (c) angular trap stiffness (κ_θ), and (d) angular drag coefficient (γ_θ) of the rutile TiO_2 nanocylinders (summarized in **Supplementary Table S4.2**). (e) The linear trap stiffness (κ_y) and (f) linear drag coefficient (γ_y) of the PS spheres (summarized in **Supplementary Table S4.3**). In all panels, the gray bars indicate the FEM-calculated values, while the colored symbols (mean) and red error bars (SD) indicate the experimental values obtained by OTW-measurements of multiple particles per batch ($N = 3$ –10). The FEM-calculated stiffness values (a,c,e) are scaled down by 50% for a direct comparison with experimental values (designated as cal. $\times 0.5$). The mean ratios between FEM-calculated and measured values averaged over all batches are (a) for κ_y : $46\% \pm 16\%$, (b) for γ_y : $104\% \pm 22\%$, (c) for κ_θ : $38\% \pm 11\%$, and (d) for γ_θ : $103\% \pm 9\%$ in case of rutile TiO_2 , and (e) for κ_y : $58\% \pm 7\%$ and (f) for γ_y : $102\% \pm 8\%$ (mean \pm SD) in case of PS. By averaging the linear values (a) and (c) and the angular values (b) and (d) of rutile TiO_2 , we arrived at the values quoted in the main text, for κ : $42\% \pm 14\%$ and for γ : $104\% \pm 17\%$, respectively. Overall, the calculations properly predict all observed trends in drag and stiffness.

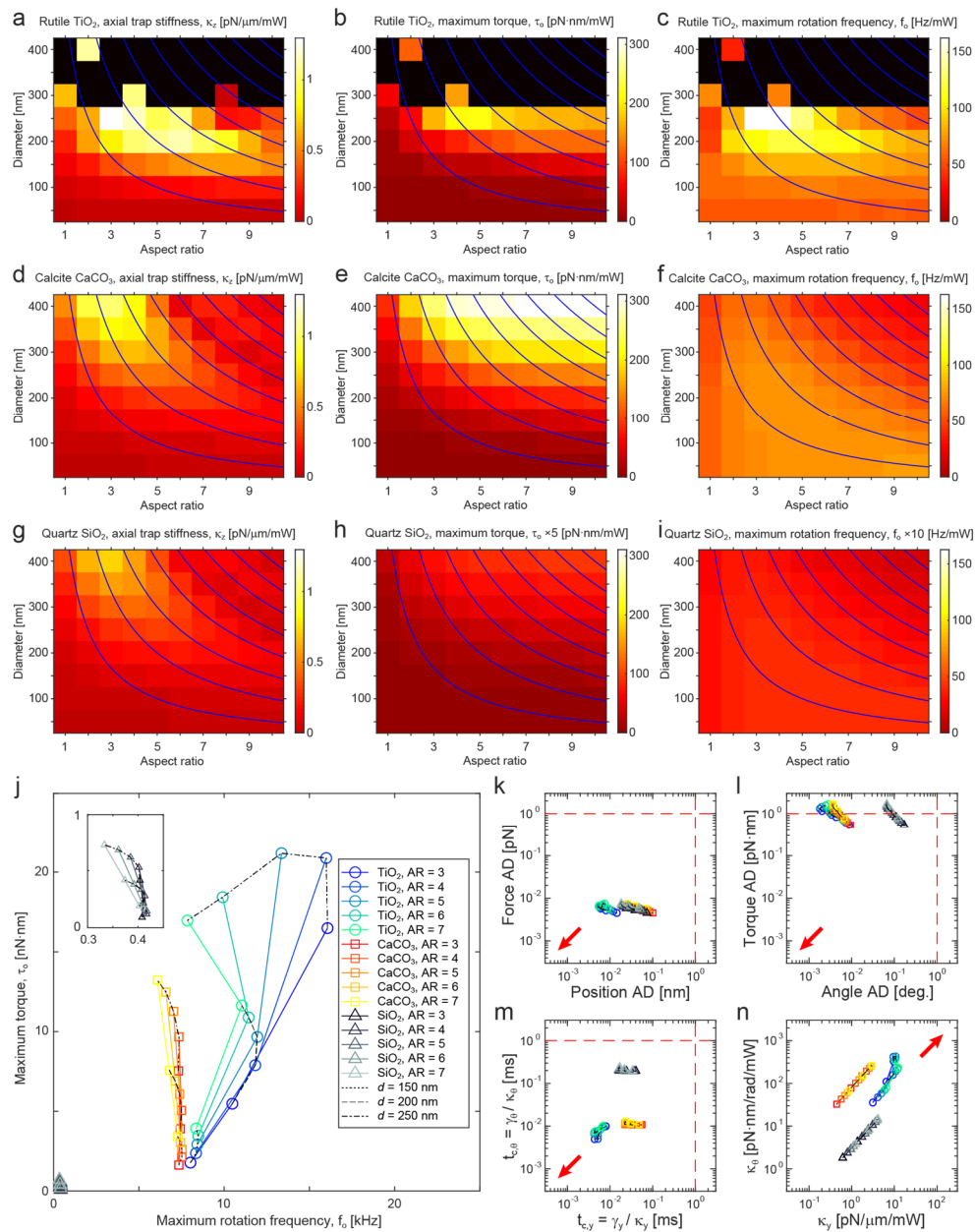


Figure S4.9. FEM-calculated linear and angular trapping parameters for different birefringent crystals. (a-i) For an unbiased comparison with the trapping parameters of (a-c) rutile TiO_2 nanocylinders, we performed similar FEM calculations for nanocylinders made of other birefringent crystals that are frequently used for OTW applications, including (d-f) calcite CaCO_3 and (g-i) quartz SiO_2 . The calculated parameters are (a,d,g) the axial trapping stiffness κ_z , (b,e,h) the maximum torque τ_o , and (c,f,i) the maximum rotation frequency f_o . The maximum rotation frequency ($f_o = \tau_o / (2\pi\gamma_\theta)$) maps are obtained using the FEM-calculated angular drag coefficients γ_θ (Supplementary Fig. S4.7). Within the calculated range of cylinder dimensions ($d = 50\text{--}400$ nm, $AR = 1\text{--}10$), only rutile TiO_2 has dimensions that are not 3D-trappable (black pixels) due to

its highest refractive index. Each parameter is displayed with the same color scale across the maps of different materials. Quartz SiO₂ has the smallest birefringence, and its angular parameters (τ_o and f_o) are very small (peak values are only 18.7 pN·nm/mW and 4.3 Hz/mW, respectively; for visibility, values are scaled up by (h) five-fold and (i) ten-fold, respectively). The calculations are performed with $\lambda = 1064$ nm, $NA = 1.2$, $\alpha = \infty$, and $n = 1.33$. The blue curves are iso-height contours (500–4000 nm from left to right, with a step size of 500 nm). The resolution of the maps is $\Delta AR = 1$ and $\Delta d = 50$ nm. (j–n) Using the FEM-calculated optical trapping parameters shown in panels (a–i) and drag coefficients (**Supplementary Fig. S4.7**), the optical trapping performances of all three materials are predicted for cylinders with $d = 150$ – 250 nm and $AR = 3$ – 7 . All symbols and colors are drawn according to the legend in panel (j). (j) The achievable torque-speed regime. The location of each symbol denotes the maximum torque and the maximum rotation frequency. The inset shows a magnified view of the quartz SiO₂ results. (k–l) Allan deviation (AD) analysis¹⁰ to elucidate the (k) linear and (l) angular measurement precisions. All AD values are functions of signal averaging time and 1 s is assumed. (m) The linear and angular trap relaxation times that define the lower bounds of the temporal resolutions in measurements¹⁰. (n) The linear and angular trap stiffnesses. In panels (k–n), arrows indicate the preferable parameter regimes for the superior spatiotemporal resolutions in measurements. In panels (k–m), the vertical and horizontal red lines are the minimum desired spatiotemporal resolutions for diverse nanoscale experiments, particularly for single biomolecules (1 pN, 1 nm, 1 pN·nm, 1 degree, and 1 ms). In panels (j–n), note that all parameters except force AD and torque AD are dependent on input beam power. A value of 100 mW is assumed for parameters shown in panels (j–m), while the stiffnesses are normalized by power in panel (n).

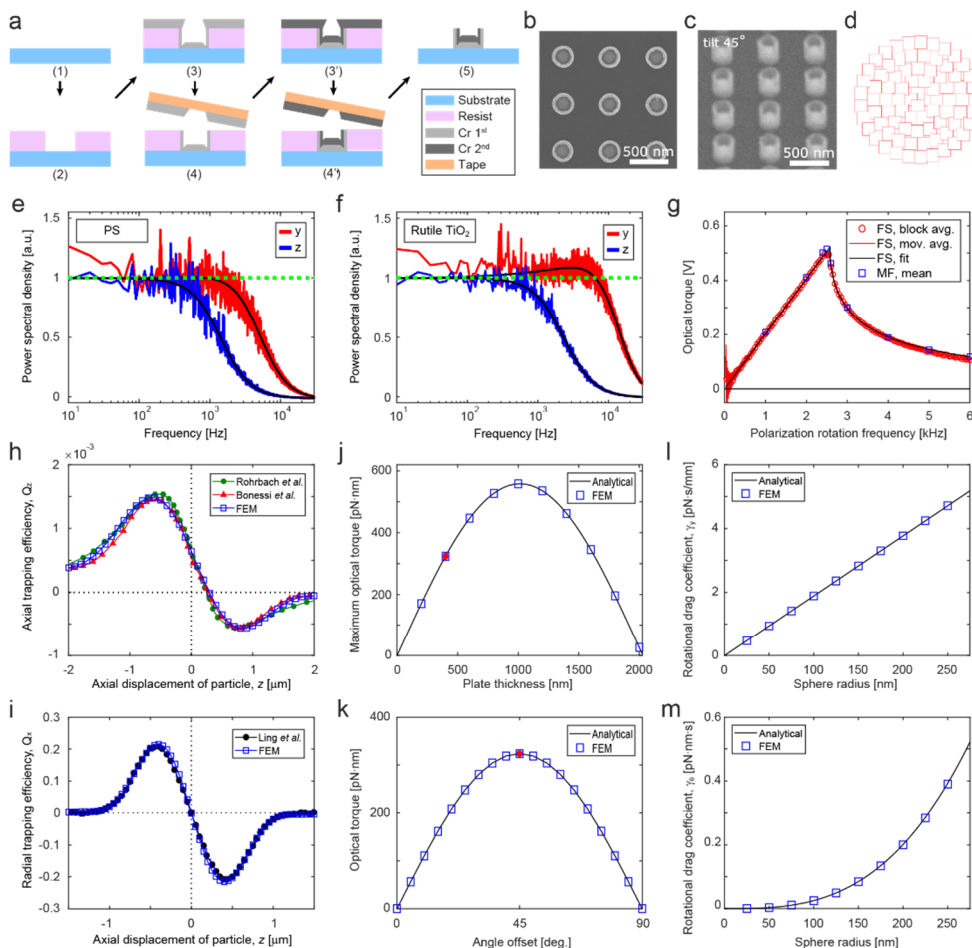


Figure S4.10. Improved methods for nanocylinder fabrication and trap calibration, and validation of FEM numerical models. (a-d) Our improvements in fabrication protocol, particularly in the etch mask and e-beam writing, for better control of the nanoscale geometry of rutile TiO₂ nanocylinders. (a) The fabrication steps for improved chromium (Cr) mask for rutile TiO₂ etching: (1) cleaning of a rutile TiO₂ substrate; (2) patterning of an e-beam resist layer (CSAR 62, ALLRESIST) on the substrate by e-beam lithography and resist development; (3) sputtering deposition (AC450, Alliance Concept) of the first Cr layer; (4) top Cr layer lift-off by attachment and subsequent removal of adhesive tape; (3'-4') sputtering and lift-off of the second Cr layer to permit a thicker Cr mask; (5) removal of e-beam resist by solvent (N-Methyl-2-pyrrolidone (NMP), GPR RECTAPUR® ($\geq 99.5\%$), VWR Chemicals). The resulting Cr mask has a very high base at center and a tall, thick surrounding wall. For the Cr mask shown here, the base has ~ 240 nm peak height and the surrounding wall is ~ 350 nm tall and ~ 40 nm thick. (b,c) The SEM micrographs of the Cr mask before etching, with (b) top-view and (c) 45° tilted view. (d) The improved e-beam writing pattern for disk-shaped Cr masks. This example is a disk pattern with $d = 100$ nm and beam step size of 10 nm. Each red square represents a position for an exposure of the e-beam. The e-beam writes in concentric rings from the center to the boundary, in a single sequence. (e,f) The effect of hydrodynamic memory on linear trap calibration of rutile TiO₂ nanocylinders. The OTW-measured (solid colored lines) and fitted (solid black lines) power spectral density (PSD) plots for linear trapping of (e) a PS sphere (batch P3, $d = 746$ nm) and (f) a rutile TiO₂ nanocylinder (batch T6, $d_{av} = 216$ nm, $h = 1102$ nm). The baseline amplitude (horizontal dashed green line) of each plot is normalized for a direct comparison. For the rutile TiO₂ cylinder in panel (f) only, the PSD plot from the radial trapping (along the y -axis) exhibits a resonance peak in the 1–10 kHz regime, resulting from the very high radial trapping

stiffness that accompanies the hydrodynamic memory effect (described by the hydrodynamically corrected PSD function ^{7, 11-13}). The PSD plots of the axial trapping of the rutile TiO₂ cylinder in panel (f) and the axial and radial trapping of the PS bead in panel (e) do not show any hydrodynamic memory effect due to smaller trap stiffness values (described by the conventional Lorentzian PSD function ¹¹). (g) Our improved, rapid calibration method for torque-speed curve measurements in angular trap calibration of rutile TiO₂ nanocylinders. The conventional multi-frequency (MF) method of torque-speed curve measurement involves repeated torque measurements at multiple different polarization rotation frequencies (PRF) ^{4, 5, 14-16}. In our frequency-sweep (FS) method, we sweep the PRF through a wide range within only a few seconds using a wavefunction generator (see **Methods** in the main text). In this example, we swept from 25 Hz to 7525 Hz in 6 s (i.e., 125 Hz/100 ms), and acquired the signal at a sampling frequency of 100 kHz. The measured signal can be converted to either block-averaged (red circles) or moving-averaged (red line) signal. The results are nearly identical and agree with the results from the MF method (blue squares; mean torque signal at steps of 1000 Hz across the measured PRF range and 100 Hz around the peak position). Also, a good fit (black line) to the theoretical torque-speed equation ¹⁵ is possible. (h-m) We validated our FEM models by comparing them with analytical and other numerical treatments of PS spheres. (h,i) For linear momentum transfer, the force curves for optically trapped PS spheres obtained from our FEM calculation agree well with other numerical results (corresponding data points are extracted from the literature figures) for both (h) axial (with $d = 200$ nm sphere ^{17, 18}) and (i) radial (with $d = 1$ μ m sphere ¹⁹) dimensions, when we use a beam with the same focal width as shown in the literature ¹⁷⁻¹⁹. (j,k) For angular momentum transfer, we use the ideal configurations that were used to derive **Eq. 4.1**, assuming a birefringent plate of 300 nm \times 300 nm cross-sectional area which is perpendicular to the beam propagation direction (**Supplementary Text S4.6.1**). We obtained FEM-calculated maximum torques as a function of either (j) the plate height h (with fixed offset angle $\theta = 45^\circ$ to show maximal torque values only) or (k) the offset angle θ (with fixed particle height $h = 400$ nm as an example). As anticipated by **Eq. 4.1**, our results show that the optimal plate height of ~ 1 μ m permits the maximal torque transfer as shown in panel (j). Also, for a fixed plate height ($h = 400$ nm), the maximal torque occurs at $\theta = 45^\circ$ and only smaller or zero torques are generated at other angles, as shown in panel (k). The red dots in (j) and (k) are the same data point. (l,m) For hydrodynamic drag in aqueous solution, we compare our FEM models with the well-known analytical equations of spheres for both (l) translational ($\gamma_s = 6\pi\eta r$; η is the dynamic viscosity of water and r is the radius of sphere) and (m) rotational drag coefficients ($\gamma_\theta = 8\pi\eta r^3$) ²⁰. The results of our FEM-based hydrodynamic calculations also agree excellently with the theory.

Advantages of improved Cr etch mask fabrication protocols

The previous Cr etch mask made by one-step Cr deposition by evaporation ²¹ is limited in the achievable maximum thickness of each mask, and the thickness at its edge is much smaller than that at its center. As a consequence, the edge of a mask erodes much faster than the center, resulting in a more tapered cylinder with longer etch time. The eroded edge also tends to be rough, so the cross section of etched cylinder is prone to be less circular. However, the improved Cr etch mask, with its reinforced edge and high base, ensures less tapered angles and a more perfect circular cross section even for extended etch times. Therefore, it is possible to fabricate tall, high aspect ratio, and small-taper-angle rutile TiO₂ cylinders that function as optimal force and torque transducers (e.g., cylinder batch T6, $h = 1102$ nm, $AR = 5.1$, taper angle 0.2° ; **Supplementary Fig. S4.4**, **Supplementary Table S4.1**).

We also improved the design pattern for writing circular disks with e-beam lithography. The new pattern consists of a single writing sequence and requires much less time compared to the conventional pattern, which approximates a disk shape with multiple trapezoidal writing sequences. As a finite overhead time exists for each writing sequence, the gain in writing time becomes more evident when patterning larger areas. The previous method also used single-sequence of writing per disk, consists of a single-pixel exposure with a defocused e-beam. The defocused e-beam is faster over large arrays of disks (~ 0.5 h to pattern a circular area with a 4 mm radius). However, e-beam

fluctuations can decrease the circularity of these disks. Our new method produces more circular disks and can cover the same area in ~ 1 h.

Advantages of improved torque-speed measurement method

Using the conventional multi-frequency (MF) method, it is preferable to have a large number of data points (e.g., 50 Hz step size) for a better fit to the theory and a more precise detection of the peak position (for demonstration purpose, much less number of data points are taken than usual in the data set shown in **Supplementary Fig. S4.10g**). However, for fast torque transducers like rutile TiO_2 nanocylinders, a smaller step size requires excessively long measurement times to switch between PRF values. The resulting torque-speed curves are prone to distortion by the long-term drift in the setup. Also, switching between many different frequencies is not practical, especially for setups with hardware that does not support automated PRF control. For example, in our setup, measurement of each torque signal costs ~ 1 min of overhead time due to the time required to manually switch the PRF and write the data to the hard disk. Hence, it requires at least ~ 1 h to acquire the data shown in **Supplementary Fig. S4.10g** using the MF method with 100 Hz steps. As our frequency-sweep (FS) method allows torque measurement over a wide range of PRF values in just a few seconds, it is effectively free from the long-term drift in the setup. Hence, this method offers enhanced reliability and flexibility in torque spectroscopy.

4.6.3. Supplementary Tables

Table S4.1. SEM-measured dimensions of rutile TiO₂ nanocylinders. The SEM-measured dimensions of rutile TiO₂ nanocylinder batches (T1–T8, U1–U6) are listed. The parameters describing the cylinder geometry include the height (H), the averaged diameter (D_{av}), aspect ratio ($AR = H/D_{av}$), and the taper angle (σ). The parameter D_{av} is obtained by averaging the SEM-measured sidewall profile as can be seen in **Supplementary Fig. S4.4c**, because the fabricated nanocylinder batches exhibit slight deviations from a perfectly straight sidewall. For the same reason, the taper angle is calculated from the slope of the linear fit to the averaged sidewall profile of each nanocylinder batch. Here, a positive (negative) taper angle means that the top flat surface (i.e., the surface protected by a Cr mask during plasma etching; designated by the yellow lines in **Supplementary Fig. S4.4a,b**) is smaller (larger) than the bottom flat surface (i.e., mechanically cleaved position) of a cylinder. The values are obtained by measuring $N = 5$ – 15 different individual cylinders per batch. For each parameter, the displayed statistical values are the mean, the standard deviation (SD), and the relative standard deviation (RSD = $SD/\text{mean} \times 100$).

Parameter	Unit	Trappable cylinders								Untrappable cylinders					
		T1	T2	T3	T4	T5	T6	T7	T8	U1	U2	U3	U4	U5	U6
H (mean)	nm	1071	816	578	766	830	1102	828	1115	664	1184	1062	1214	1048	1425
H (SD)	nm	6	4	7	10	10	14	4	15	10	13	1	3	3	6
H (RSD)	%	0.6	0.4	1.1	1.4	1.2	1.3	0.5	1.3	1.5	1.1	0.1	0.3	0.3	0.5
D_{av} (mean)	nm	166	199	205	214	215	216	229	256	259	259	299	293	326	354
D_{av} (SD)	nm	6	4	5	12	12	16	9	10	6	7	15	9	9	9
D_{av} (RSD)	%	3.6	2.1	2.5	5.7	5.7	7.2	4	4.1	2.4	2.6	4.9	3	2.7	2.6
AR (mean)		6.5	4.1	2.8	3.6	3.9	5.1	3.6	4.4	2.6	4.6	3.6	4.1	3.2	4.0
AR (SD)		0.2	0.1	0.1	0.2	0.2	0.4	0.1	0.2	0.1	0.1	0.2	0.1	0.1	0.1
AR (RSD)	%	3.9	2.3	2.9	6.0	5.8	7.2	3.8	4.8	3.1	2.4	4.9	2.9	2.6	2.5
σ (mean)	deg.	0.5	0.7	-1.6	0.2	-0.1	0.2	1.0	-0.2	4.8	0.4	0.5	2.7	0.6	3.9
N		6	6	15	8	10	6	8	5	5	5	5	5	5	6

Table S4.2. OTW-measured and FEM-calculated optical trapping parameters of the 3D-trappable rutile TiO₂ nanocylinders. The linear and angular optical trapping parameter values for all 3D-trappable rutile TiO₂ nanocylinder batches (T1–T8) are listed. Both experimental (mean, standard deviation (SD)) and numerically calculated (cal.) results are displayed. The linear trapping properties include the radial drag coefficient (γ_y), the radial trap stiffness (κ_y), and the radial trap relaxation time ($t_{c,y}$). Similarly, the angular trapping properties include the angular drag coefficient (γ_θ), the angular trap stiffness (κ_θ), and the angular trap relaxation time ($t_{c,\theta}$). Note that the drag coefficients are independent of trapping beam power, while trap stiffnesses and trap relaxation times are not. Also, the calculated stiffnesses (linear or angular) represent the mean of those that result from the two possible trapping orientations. Regarding the angular trapping, the averaged maximal torque (τ_o) and angular speed (f_o) at 100 mW beam power (scaled from the actually used ~92 mW for rapid interpretation) are also shown. The experimental values are obtained by measuring $N = 3$ –10 cylinders per batch.

Parameter	Unit	T1	T2	T3	T4	T5	T6	T7	T8
γ_y (mean)	pN·s/mm	6.0	4.4	2.3	3.7	4.8	4.9	6.4	5.8
γ_y (SD)	pN·s/mm	1.4	1.3	0.6	1.0	1.9	1.0	2.3	0.6
γ_y (cal.)	pN·s/mm	4.7	4.3	3.5	4.2	4.5	5.3	4.6	5.7
κ_y (mean)	pN/μm/mW	4.0	3.3	1.3	3.2	4.5	3.8	5.2	7.0
κ_y (SD)	pN/μm/mW	0.7	0.9	0.4	1.0	2.0	0.7	1.7	0.9
κ_y (cal.)	pN/μm/mW	7.8	8.6	5.7	8.7	9.5	11.0	9.2	9.0
$t_{c,y}$ (mean)	μs (at 100 mW)	15	13	18	12	11	13	12	8
$t_{c,y}$ (SD)	μs (at 100 mW)	5	5	7	5	6	3	6	1
$t_{c,y}$ (cal.)	μs (at 100 mW)	6	5	6	5	5	5	5	6
N (linear)		4	7	8	9	9	3	10	3
γ_θ (mean)	pN·nm·s	0.09	0.10	0.08	0.14	0.11	0.15	0.14	0.24
γ_θ (SD)	pN·nm·s	0.01	0.01	0.02	0.05	0.01	0.03	0.04	0.04
γ_θ (cal.)	pN·nm·s	0.09	0.10	0.08	0.11	0.12	0.16	0.13	0.23
κ_θ (mean)	pN·nm/rad/mW	67	41	51	94	97	67	95	168
κ_θ (SD)	pN·nm/rad/mW	13	4	8	25	40	9	27	20
κ_θ (cal.)	pN·nm/rad/mW	117	164	115	196	221	287	285	508
$t_{c,\theta}$ (mean)	μs (at 100 mW)	14	25	16	15	12	22	14	15
$t_{c,\theta}$ (SD)	μs (at 100 mW)	3	3	4	6	5	5	6	3
$t_{c,\theta}$ (cal.)	μs (at 100 mW)	7	6	7	6	5	5	5	4
τ_o	nN·nm (at 100 mW)	3.3	2.0	2.5	4.7	4.8	3.4	4.7	8.4
f_o	kHz (at 100 mW)	5.9	3.2	5.1	5.3	6.9	3.7	5.5	5.5
N (angular)		4	7	7	9	8	3	7	3

Table S4.3. Dimensions and linear optical trapping parameters of the PS spheres. The dimensions and linear optical trapping parameter values for all measured PS sphere batches (P1–P3) are listed. For sphere diameter, the displayed statistical values are the mean, the standard deviation (SD), and the relative standard deviation (RSD = SD/mean×100). These values are provided by the supplier of the spheres. For linear optical trapping parameters, both experimental (mean, standard deviation (SD)) and numerically calculated (cal.) results are displayed. The trapping properties include the radial drag coefficient (γ_y), the radial trap stiffness (κ_y), and the radial trap relaxation time ($t_{c,y}$). Note that the drag coefficients are independent of trapping beam power, while trap stiffnesses and trap relaxation times are not. The experimental values are obtained by measuring $N = 5-7$ different individual spheres per batch.

Parameter	Unit	P1	P2	P3
D (mean)	nm	370	505	746
D (SD)	nm	15	8	2
D (RSD)	%	4.1	1.6	0.3
γ_y (mean)	pN·s/mm	3.7	4.1	6.6
γ_y (SD)	pN·s/mm	0.3	0.4	0.5
γ_y (cal.)	pN·s/mm	3.3	4.4	6.6
κ_y (mean)	pN/ μ m/mW	0.9	1.5	2.7
κ_y (SD)	pN/ μ m/mW	0.1	0.2	0.2
κ_y (cal.)	pN/ μ m/mW	1.5	3.1	4.2
$t_{c,y}$ (mean)	μ s (at 100 mW)	39	27	25
$t_{c,y}$ (SD)	μ s (at 100 mW)	5	4	2
$t_{c,y}$ (cal.)	μ s (at 100 mW)	22	14	15
N		5	6	7

4.6.4. Supplementary References

1. Frieze, M. E. J., Nieminen, T. A., Heckenberg, N. R. & Rubinsztein-Dunlop, H. Optical alignment and spinning of laser-trapped microscopic particles. *Nature* **394**, 348-350 (1998).
2. Moothoo, D. N., Arlt, J., Conroy, R. S., Akerboom, F., Voit, A. & Dholakia, K. Beth's experiment using optical tweezers. *American Journal of Physics* **69**, 271-276 (2001).
3. Beth, R. A. Mechanical detection and measurement of the angular momentum of light. *Physical Review* **50**, 115-125 (1936).
4. Pedaci, F., Huang, Z., van Oene, M., Barland, S. & Dekker, N. H. Excitable particles in an optical torque wrench. *Nature Physics* **7**, 259-264 (2010).
5. La Porta, A. & Wang, M. D. Optical torque wrench: angular trapping, rotation, and torque detection of quartz microparticles. *Physical Review Letters* **92**, 190801 (2004).
6. Jahnel, M., Behrndt, M., Jannasch, A., Schäffer, E. & Grill, S. W. Measuring the complete force field of an optical trap. *Optics Letters* **36**, 1260-1262 (2011).
7. Jannasch, A., Demirörs, A. F., van Oostrum, P. D. J., van Blaaderen, A. & Schäffer, E. Nanonewton optical force trap employing anti-reflection coated, high-refractive-index titania microspheres. *Nature Photonics* **6**, 469-473 (2012).
8. Simpson, N. B., McGloin, D., Dholakia, K., Allen, L. & Padgett, M. J. Optical tweezers with increased axial trapping efficiency. *Journal of Modern Optics* **45**, 1943-1949 (1998).
9. Phillips, D. B. et al. Shape-induced force fields in optical trapping. *Nature Photonics* **8**, 400-405 (2014).
10. van Oene, M. M. et al. Quantifying the precision of single-molecule torque and twist measurements using Allan variance. *Biophysical Journal* **114**, 1970-1979 (2018).
11. Berg-Sørensen, K. & Flyvbjerg, H. Power spectrum analysis for optical tweezers. *Review of Scientific Instruments* **75**, 594-612 (2004).
12. Franosch, T. et al. Resonances arising from hydrodynamic memory in Brownian motion. *Nature* **478**, 85-88 (2011).
13. Jannasch, A., Mahamdeh, M. & Schäffer, E. Inertial effects of a small Brownian particle cause a colored power spectral density of thermal noise. *Physical Review Letters* **107**, 228301 (2011).
14. Gutiérrez-Medina, B., Andreasson, J. O. L., Greenleaf, W. J., LaPorta, A. & Block, S. M. An optical apparatus for rotation and trapping. In *Methods in Enzymology* (ed Walter, N. G.) **475**, 377-404 (Academic Press, 2010).
15. Inman, J., Forth, S. & Wang, M. D. Passive torque wrench and angular position detection using a single beam optical trap. *Optics Letters* **35**, 2949-2951 (2010).
16. Huang, Z., Pedaci, F., van Oene, M., Wiggin, M. J. & Dekker, N. H. Electron beam fabrication of birefringent microcylinders. *ACS Nano* **5**, 1418-1427 (2011).
17. Rohrbach, A. & Stelzer, E. H. K. Optical trapping of dielectric particles in arbitrary fields. *Journal of the Optical Society of America A* **18**, 839-853 (2001).
18. Bonessi, D., Bonin, K. & Walker, T. Optical forces on particles of arbitrary shape and size. *Journal of Optics A: Pure and Applied Optics* **9**, S228-S234 (2007).
19. Ling, L., Zhou, F., Huang, L. & Li, Z.-Y. Optical forces on arbitrary shaped particles in optical tweezers. *Journal of Applied Physics* **108**, 073110 (2010).
20. Leach, J. et al. Comparison of Faxen's correction for a microsphere translating or rotating near a surface. *Physical Review E* **79**, 026301 (2009).
21. Ha, S., Janissen, R., Ussembayev, Y. Y., van Oene, M. M., Solano, B. & Dekker, N. H. Tunable top-down fabrication and functional surface coating of single-crystal titanium dioxide nanostructures and nanoparticles. *Nanoscale* **8**, 10739-10748 (2016).

5

Quantifying the Precision of Single-Molecule Torque and Twist Measurements Using Allan Variance

Single-molecule manipulation techniques have provided unprecedented insights into the structure, function, interactions, and mechanical properties of biological macromolecules. Recently, the single-molecule toolbox has been expanded by techniques that enable measurements of rotation and torque, such as the optical torque wrench and several different implementations of magnetic (torque) tweezers. While systematic analyses of the position and force precision of single-molecule techniques have attracted considerable attention, their angle and torque precision have been treated in much less detail. Here, we propose the Allan deviation as a tool to systematically quantitate angle and torque precision in single-molecule measurements. We apply the Allan variance method to experimental data from our implementations of (electro-) magnetic torque tweezers and an optical torque wrench and find that both approaches can achieve a torque precision better than 1 pN·nm. The optical torque wrench, capable of measuring torque on (sub)-millisecond timescales, provides the best torque precision for measurement times $\lesssim 10$ s, after which drift becomes a limiting factor. For longer measurement times, the magnetic torque tweezers with their superior stability provide the best torque precision. Use of the Allan deviation enables critical assessments of the torque precision as a function of measurement time across different measurement modalities, and provides a tool to optimize measurement protocols for a given instrument and application.

This chapter has been published as: Maarten M. van Oene*, **Seungkyu Ha***, Tessa Jager, Mina Lee, Francesco Pedaci, Jan Lipfert, and Nynke H. Dekker, "Quantifying the Precision of Single-Molecule Torque and Twist Measurements Using Allan Variance", *Biophysical Journal* 114, pp. 1970–1979 (2018). (*equal contribution)

5.1. Introduction

Single-molecule manipulation techniques have provided unprecedented insights into the structure, function, interactions, and mechanical properties of biological macromolecules¹⁻⁷. Many single-molecule manipulation techniques, notably optical tweezers and atomic force microscopy, naturally operate in the space of (linear) extension and force. However, frequently biological macromolecules are subject to torsional strain, and the molecular motors that translocate along them must be able to progress amidst accumulated twist and torque. To quantify these phenomena, a number of techniques that enable measurements of rotation angle and torque^{8,9} have been developed recently. Examples of such techniques (reviewed in Ref. 9) include the rotor bead tracking assay¹⁰⁻¹⁵, optical torque tweezers¹⁶⁻²⁸, and various extensions of magnetic tweezers, comprising magnetic torque tweezers²⁹⁻³², freely-orbiting magnetic tweezers^{33,34}, and electromagnetic torque tweezers³⁵. While the field of force spectroscopy has benefited from systematic analyses of the position and force precision of single-molecule techniques³⁶⁻⁴⁴, torque and twist measuring techniques would be enriched by a better understanding of the achievable precision in angular detection and the determination of torque.

Here, we propose the Allan deviation (AD)³⁸⁻⁴⁹ as a criterion to systematically quantitate the angle and torque precision in single-molecule measurements. The AD allows us to critically assess the torque precision as a function of measurement time across different measurement modalities (e.g. magnetic versus optical torque tweezers) that rely on distinct physical principles. Being a real space quantity and having the same units as the observable of interest, it provides an intuitive and direct way to quantify and interpret precision³⁸⁻⁴⁴. In addition to enabling direct quantitative comparisons of different torque and twist measurement strategies, use of the AD in a systematic way provides an experimental user with a very convenient tool with which to optimize the measurement protocol for a given instrument and system. Here, we investigate the AD method using simulated traces and demonstrate its application to various implementations of (electro-) magnetic torque tweezers (eMTT and MTT) and an optical torque wrench (OTW). Using the AD analysis, we arrive at clear recommendations, e.g. for the optimal in-plane magnetic field strength in the eMTT and for choosing an optimal trapping laser power in the OTW.

5.2. Materials and Methods

5.2.1. Definition and properties of the Allan deviation

Given a time series of N observations of some quantity θ , recorded at a sampling frequency f_s over a total measurement time $t_{meas} = N/f_s$, the Allan variance (AV) of θ for the time interval τ is defined as^{42,43,45}:

$$\sigma_{\theta}^2(\tau) = \frac{1}{2}((\bar{\theta}_{i+1} - \bar{\theta}_i)^2), \quad \text{Equation 5.1}$$

where $\bar{\theta}_i$ is the mean of the i^{th} measurement interval of length τ . The angle bracket $\langle \dots \rangle$ denotes the arithmetic mean over all measurement intervals. In other words, the AV is one half of the averaged square distance between the means of neighboring intervals. From its definition, the value of the AV is always greater than zero; it can only be computed for time intervals $\tau \leq t_{\text{meas}}/2$; it is additive for independent signals, i.e., the AV is the sum of the individual AVs; and it is linear, i.e., a linear scaling of θ , $\theta' = \alpha \cdot \theta$, will simply scale the AV: $\sigma_{\theta'}^2(\tau) = \alpha^2 \cdot \sigma_{\theta}^2(\tau)$. The property of linearity is convenient since it allows for analysis of uncalibrated signals with the AV (e.g. one can analyze the voltage signal from a quadrant photodiode, position sensing detector, or photodiode without having to first convert to position or torque units). In addition, the linearity enables simple conversion from angle to torque signal (by multiplication with the rotational trap stiffness, κ_{θ} , in units of pN·nm/rad) before or after evaluation of the AV. The Allan deviation is defined as the square root of the Allan variance: $\sigma_{\theta}(\tau) = (\sigma_{\theta}^2)^{1/2}$. Since Allan deviation has the same units as the quantity under investigation, it may be more intuitive to report Allan deviations rather than Allan variances.

5.2.2. Computation of the Allan variance

In practice, the AV is estimated from a data set with a finite number of measurements using a discrete form of **Eq. 1**. In the simple form of the AV, the data is split in M bins of m data points each, and the value of each bin is the mean over its m data points. The mean-squared difference of consecutive bins estimates the AV:

$$\sigma_{\theta}^2(m\tau_s) = \frac{1}{2(M-1)} \sum_{i=1}^{M-1} (\bar{\theta}_{i+1} - \bar{\theta}_i)^2, \quad \text{Equation 5.2}$$

where τ_s is the sampling period and $\bar{\theta}_i$ is the mean of the i^{th} bin of length $m\tau_s$. The sampling period is taken to equal the integration time. For camera-based detection in the magnetic tweezers this assumes no dead time between frames, which is justified given the typical dead time ($\sim 10 \mu\text{s}$) relative to the integration time ($\sim 10 \text{ms}$). For photodiode-based detection in the OTW, the situation is quite different: while the effective integration time is very fast ($\sim 10 \text{ns}$), the photodiode is only read out at $\sim 100 \text{kHz}$. The inverse of this rate ($\sim 10 \mu\text{s}$) is analogous to a dead time, as no signal averaging occurs. Thus, in the OTW the dead time far exceeds the integration time. However, the application of **Eq. 5.2** remains valid in all situations considered in this work since the sampling period is much shorter than the characteristic time of the system (**Supplementary Text S5.6.1**). For each value of m , m frameshifts exist to compute the AV (**Fig. 5.1A**). The use of all of these frameshifts improves the estimate of the AV, and is known as the “overlapping” AV (**Eq. S5.3 in Supplementary Text S5.6.2**).

While the AV is defined for all values of m (up to the maximum $m = N/2$), the AVs for successive values of m are not independent and can be nearly identical, because most values in a bin of size m are identical to the values in a bin of size $m + 1$. For fitting of the AV data, it is therefore advantageous to calculate the octave-sampled AV by

choosing $m = 2^{\text{integer}}$, which ensures nearly independent differences^{46,47}. We compute the AV³⁹ using a publicly available Matlab function⁴⁹. All AV curves are fit using maximum likelihood estimation (MLE) using the shape factor by Lansdorp and Saleh⁴⁷ (**Eq. S5.4** in **Supplementary Text S5.6.3**).

5.2.3. Analytic expression for the Allan variance of a Brownian particle in a harmonic trap

We employ the analytical expression given by Lansdorp and Saleh^{47,48} for the AV of a particle undergoing Brownian motion in a harmonic well, and apply it to the case of rotational motion:

$$\sigma_{\theta}^2 = A \left(\frac{\tau_c}{\tau} \right)^2 \left(2 \frac{\tau}{\tau_c} + 4 \exp \left(-\frac{\tau}{\tau_c} \right) - \exp \left(-2 \frac{\tau}{\tau_c} \right) - 3 \right), \quad \text{Equation 5.3}$$

where $A = k_B T / \kappa_{\theta}$ and $\tau_c = \gamma_{\theta} / \kappa_{\theta}$. Here, γ_{θ} is the rotational friction coefficient and κ_{θ} is the trap stiffness of the rotational trap. Note that $k_B T / \kappa_{\theta} = \text{Var}(\theta)$ according to the equipartition theorem. We determine the friction coefficient γ_{θ} and the trap stiffness κ_{θ} by fitting the expression (**Eq. 5.3**) to our data using a maximum likelihood estimation algorithm⁴⁷. In the short time averaging limit, where diffusion is dominant, the AV reduces to:

$$\sigma_{\theta}^2 = \frac{2}{3} D \tau, \quad \text{Equation 5.4}$$

where D is the diffusion constant, which, according to the Einstein–Smoluchowski relation, equals $k_B T / \gamma_{\theta}$.

In most single-molecule experiments, the short time regime provides little information about the system under study, because the particle can barely respond to changes on these time scales, particularly for often relatively slow torque measurements. For long averaging times, the AV reaches the so-called thermal limit, where it reduces to:

$$\sigma_{\theta}^2 = 2 A \frac{\tau_c}{\tau} = 2 \frac{\text{Var}(\theta)}{n} = \frac{2 k_B T \gamma_{\theta}}{\kappa_{\theta}^2 \tau}, \quad \text{Equation 5.5}$$

where $n = \tau / \tau_c$ defines the number of independent observations. The averaging reduces the variance with the number of independent measurements n and, therefore, the AV decreases inversely proportional to τ , improving the angle precision. In between these two limits, the AV peaks at τ_{max} , with the best estimate of τ_{max} ($= 1.8926 \tau_c$) coming from the numerical solution of **Eq. 5.3** as opposed to the analytical solution of **Eqs. 5.4, 5.5** ($= \sqrt{3} \tau_c$).

Eqs. 5.3-5.5 can be converted from angle to torque AV by straightforward application of the property of linearity: in the harmonic approximation, torque Γ is proportional to angle θ ($\Gamma = -\kappa_{\theta} \theta$), and hence $\sigma_{\Gamma}^2 = \kappa_{\theta}^2 \cdot \sigma_{\theta}^2$. Thus, the thermal limit of the torque AV is given by:

$$\sigma_{\Gamma}^2 = \frac{2 k_B T \gamma_{\theta}}{\tau}. \quad \text{Equation 5.6}$$

In this limit, the AV for torque is independent of the trap stiffness κ_θ , suggesting that stiffness has no effect on the torque precision in the regime where the measurement precision is limited by thermal fluctuations³².

5.2.4. Stochastic simulations of rotational motion

To test our Allan deviation analysis and to illustrate the effects of various system parameters, we simulate stochastic time traces of rotational motion using numerical solutions to the corresponding overdamped Langevin equation (**Fig. 5.1**). To simulate the rotation angle as a function of time $\theta(t)$, we discretize time into time steps Δt . The angle at time step $i + 1$, θ_{i+1} , is given by the discretized overdamped Langevin equation as:

$$\theta_{i+1} = \theta_i + \left(\frac{\Gamma_{external} + \Gamma_{thermal}}{\gamma_\theta} \right) \Delta t, \quad \text{Equation 5.7}$$

where the right-hand side only involves quantities known at time step i ; γ_θ is the rotational friction coefficient (in units of pN·nm·s), $\Gamma_{external}$ is the external torque, and $\Gamma_{thermal} = N(0,1) \cdot (2k_B T \gamma_\theta / \Delta t)^{1/2}$, with the thermal energy, $k_B T \approx 4.1$ pN·nm at room temperature, and $N(0,1)$ is Gaussian distributed noise with zero mean and unit standard deviation. The Langevin dynamics simulations were implemented using custom Matlab routines (**Supplementary Text S5.6.4**).

5.2.5. Allan deviation measurements with magnetic tweezers

Torque application in magnetic tweezers relies on the alignment of superparamagnetic micron-sized beads or microspheres (referred to as 'beads' from here on after) with an externally applied magnetic field^{5, 29, 50}. Both MTT and eMTT employ a predominantly vertically oriented field generated by a cylindrical magnet, and a smaller field in the horizontal direction generated by a side magnet in the MTT³² (**Fig. 5.2A**) or by electromagnets in the eMTT³⁵ (**Fig. 5.3A**). The in-plane field generates a sufficiently weak angular trap to perform experiments on soft molecules, like DNA. Torque measurements in MTT and eMTT rely on tracking the rotational angle of the bead and observing changes in the equilibrium angle position of the bead inside the trap upon applying twist to a molecule of interest tethered between a surface and the magnetic bead. The torque is determined from the product of the angular shift and the trap stiffness, and hence the angle Allan deviation can be determined directly from the angular traces, while the torque Allan deviation requires a calibrated trap stiffness. Limitations in angular tracking will therefore also affect the torque precision.

Our MTT and eMTT measurements of the Allan deviation use custom-built instruments described in detail elsewhere^{32, 35}. In brief, they employ double-stranded DNA constructs bound to a flow cell surface via multiple digoxigenin-antidigoxigenin interactions and to superparamagnetic beads via multiple biotin-streptavidin interactions in PBS buffer. Bead sizes and DNA tether lengths are indicated in the main text and figure legends.

5.2.6. Allan deviation measurements with optical tweezers

The OTW is an extension of conventional optical tweezers that exploits the exchange of angular momentum between a nanofabricated, birefringent particle and a polarized trapping beam to apply and measure torque¹⁶⁻²⁸. Unlike the magnetic tweezers, which employ standard commercially available magnetic beads (whose magnetic anisotropy governs the achievable torque levels⁵⁰, and where a choice of diameters permits control over the drag coefficient), for the OTW no comparable particles exist. Instead, one typically custom fabricates birefringent dielectric particles using one of several fabrication routes (top-down, bottom-up), materials (quartz SiO₂ (0.009), vaterite CaCO₃ (0.1), calcite CaCO₃ (-0.16), rutile TiO₂ (0.26); optical birefringences specified in parentheses), shapes (spherical, cylindrical, etc.), and dimensions (with a size scale of a few μm being most prevalent)²³⁻²⁸. In our custom-built instrument²², we measure on cylindrically shaped rutile TiO₂ nanoparticles (diameter ~ 215 nm, height ~ 765 nm) fabricated in our cleanroom facility²⁶.

In the OTW, the optical tweezers trap a birefringent cylinder with its long axis aligned with the propagation direction of the light (**Fig. 5.4A**). The linear polarization of the trapping laser clamps the angular position of the rutile TiO₂ cylinder, and rotation of this polarization controls rotation of the particle about its long axis²⁶. The imbalance between left and right circularly polarized components in the output of the trap provides a direct measure for the exchange of angular momentum inside the trap, and hence a measure for the optical torque transferred to the particle. In the Allan deviation measurements, we fixed the direction of the linear polarization, and measured the fluctuations around this equilibrium position (**Supplementary Figs. S5.8A, S5.9A**). The power of the trapping laser is tuned using a half-wave plate and a polarizing beam splitter, in the range of 10–80 mW at the laser focus.

5.3. Results

The Allan deviation (AD) is the square root of the Allan variance, a type of variance that uses samples averaged over variable time intervals τ and that is computed from the difference between neighboring intervals (**Materials and Methods**). While other approaches to quantify precision exist (e.g., other variances, autocorrelation, or power spectrum analyses (**Supplementary Text S5.6.5, S5.6.6**)), we find AD to be a particularly convenient measure for several reasons: i) the AD at time τ provides a direct and intuitive measure of the precision expected for a measurement of a given duration; ii) being a real space quantity, the AD is immediately in the same units as the measured quantity of interest; iii) the AD is powerful in detecting low frequency, long time scale drifts⁴³, which are critical for single-molecule measurements of torque and twist; and iv) the AD can be straightforwardly computed from the raw experimental data, without the need to be calibrated *a priori*. In the following, we explore the use of AD to quantify the angle and torque precision of single-molecule measurements. First,

we present the results of stochastic simulations to introduce the concept of AD and validate our approach. We then use AD to compare the precision of three different single-molecule torque spectroscopy techniques: magnetic torque tweezers (MTT), electromagnetic torque tweezers (eMTT), and an optical torque wrench (OTW).

5.3.1. Allan deviation analysis of simulated traces

To explore the effects of the various system parameters on the AD, we simulated traces of the stochastic rotational motion of a bead subject to Brownian fluctuations while held in a harmonic trap (**Fig. 5.1B-D** and **Supplementary Fig. S5.1**). The simulated rotational motion (about an axis through the bead's center of mass) reveals the effects of varying rotational trap stiffness κ_θ and rotational drag coefficient γ_θ on the angular time trace (**Fig. 5.1B**) and on the angle AD (**Fig. 5.1C**) and torque AD (**Fig. 5.1D**). In the green data set, $\gamma_\theta = 10$ pN·nm·s and $\kappa_\theta = 1000$ pN·nm/rad, such that the characteristic time is $\tau_c = \gamma_\theta/\kappa_\theta = 10$ ms. To compare the effect of different drag coefficients, we simulate the red data set with the same stiffness but a ten-fold higher drag coefficient, $\gamma_\theta = 100$ pN·nm·s. To compare the effect of different stiffnesses, we generate the blue data set with the same drag coefficient as the green data set but ten-fold lower trap stiffness, $\kappa_\theta = 100$ pN·nm/rad. All other parameters are identical for the three simulated traces.

The simulated angle traces provide an instructive example of how the system parameters affect the observed behavior. The widths of the histograms (**Fig. 5.1B**) – and thus the amplitude of the angular fluctuations – are indifferent to changes in drag coefficient (compare green and red datasets), but are affected by changes in stiffness (compare green and blue datasets); a decrease in stiffness causes increased angular fluctuations, as expected from the equipartition theorem. Another feature visible in the angle traces is the time scale over which the angular fluctuations occur. The fluctuations in the green data appear “denser” on the time axis, compared to the red and blue data, due to the fact that the characteristic time τ_c for the green dataset (10 ms) is smaller than for the red and blue datasets (100 ms).

The ADs (**Fig. 5.1C,D**) for our simulated traces all display the expected trend of an initial rise proportional to $\tau^{1/2}$ and a transition to a decrease proportional to $\tau^{-1/2}$ for larger τ ⁴³. Changing the drag coefficient causes a shift of the curve on the time axis in both angle and torque Allan deviations (green and red datasets). This shift indicates that a higher drag coefficient is linked to slower dynamics, consistent with the higher characteristic time τ_c . For the angle AD (**Fig. 5.1C**), the change in stiffness initially has no effect: the curves overlap in the diffusion limit (green and blue datasets, **Eq. 5.4**). However, at longer time scales, a higher stiffness results in an improved angular precision (**Eq. 5.5**). In contrast, different stiffnesses do not alter the torque precision for large τ (**Fig. 5.1D**), since in the thermal limit, the torque precision is independent of the trap stiffness κ_θ (**Eq. 5.6**). The analytical expression for the Allan variance (**Eq. 5.3**) provides an excellent fit to the data, and we recover the values for κ_θ and γ_θ input into

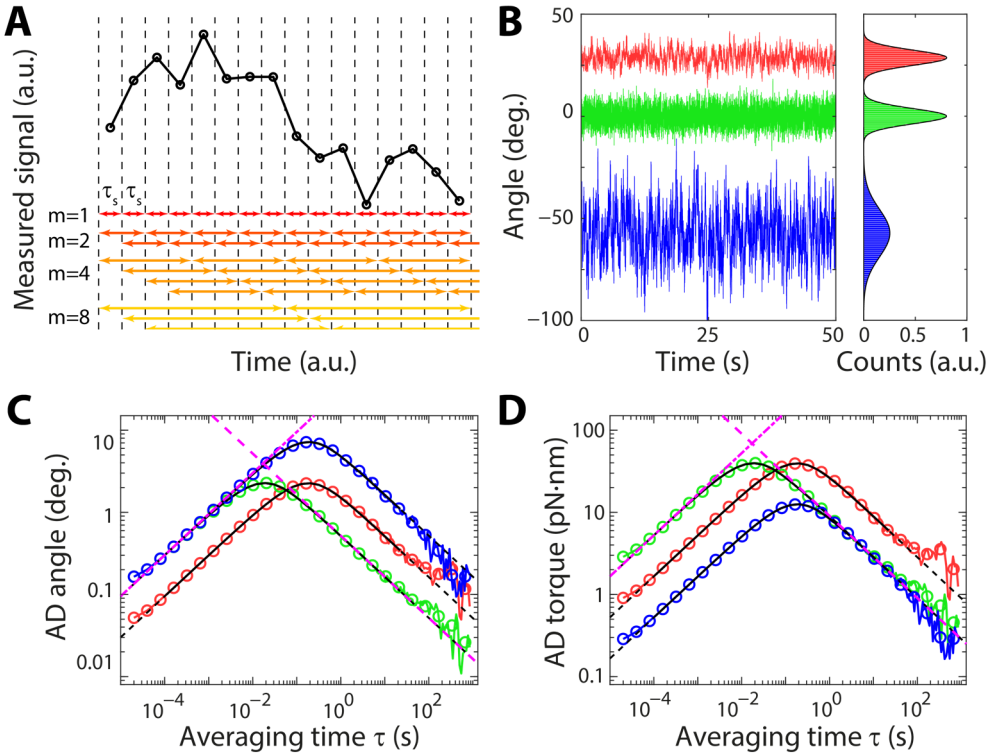


Figure 5.1. Allan deviation of simulated traces. **A)** Illustration of the octave-sampled overlapping Allan deviation. The example trace (black) contains 16 data points. Each data point is recorded during the sampling period τ_s . The data are split into bins of m data points. In octave-sampled data, $m = 2^{\text{integer}}$ (going from red to yellow, $m = 1, 2, 4, 8$). Splitting in bins is possible in m different frame shifts. For $m = 8$, only three frame shifts are displayed for clarity. **B)** Simulated angular traces ≈ 1700 s each sampled at 50 kHz (corresponding to 8.5×10^7 data points), for rotational Brownian motion of particles in harmonic traps. The left panel shows a zoom-in on the first 50 s of the traces, and the right panel shows the histograms for the full traces. The traces are offset vertically for clarity. The red, green, and blue traces are simulations with drag coefficient $\gamma_\theta = 100, 10, \text{ and } 10$ pN·nm·s, and trap stiffness $\kappa_\theta = 1000, 1000, \text{ and } 100$ pN·nm/rad, respectively. **C,D)** Angle and torque Allan deviation (AD) for the traces in **B)**. Colored lines (circles) reflect the normal AD and octave-sampled overlapping AD, respectively. The results of the fits are indicated by solid black lines and their extrapolations as dashed black lines (Eq. 5.3). The fitted parameters are $\gamma_\theta = 99.4 \pm 0.1, 9.9 \pm 0.01, \text{ and } 10.0 \pm 0.01$ pN·nm·s and $\kappa_\theta = 1009.6 \pm 36.6, 998.9 \pm 9.7, \text{ and } 99.6 \pm 2.9$ pN·nm/rad for the red, green, and blue data, respectively, from $N = 5$ independent simulated traces for each condition. The dash-dotted and dashed magenta lines are the diffusion and thermal limits, shown for the green datasets only.

the simulations, confirming the validity of the method (**Fig. 5.1C,D**, where the range of fitted data, indicated by the black solid lines, is constrained at the shortest and longest integration time limits to avoid the influence of noise not taken into consideration in **Eq. 5.3**).

5.3.2. Angle and torque precision in the MTT

The MTT employ a cylindrical magnet to generate a predominantly vertically oriented field and a side magnet to apply an additional, smaller field in the horizontal direction. MTT measure torque by detecting changes in the equilibrium position of the bead-

rotation angle about the tether axis upon over- and underwinding nucleic acid tethers³⁰⁻³² (**Materials and Methods** and **Supplementary Fig. S5.2A-C**). Here, we analyze traces of angular fluctuations recorded in our MTT implementation (**Fig. 5.2A**) using a 2.8 μm diameter magnetic bead and a 1 μm diameter non-magnetic fiducial marker bead to track the rotation angle about the tether axis from analysis of the camera images⁵¹ (**Fig. 5.2A**, inset). We focus on a representative data set consisting of 32 angle traces, recorded while over- and underwinding a 7.9 kbp DNA molecule tethered between the magnetic bead and the flow cell surface and held at a stretching force of ~ 2 pN (**Supplementary Fig. S5.2C**). Upon over- and underwinding the DNA by integer numbers of turns, systematic changes of the equilibrium angle position are visible (**Supplementary Fig. S5.2C**, middle panel, left axis). These can be related to the changes in the torque exerted by the molecule (**Supplementary Fig. S5.2C**, middle panel, right axis) by multiplying with the mean trap stiffness (deduced from the fits to AD curves, as detailed below; and equivalent to deducing the trap stiffness from the standard deviation of the angular fluctuations, **Supplementary Fig. S5.2C**, top panel). In addition, we observe that tether extension decreases rapidly past the buckling point of the DNA molecule for positive turns (corresponding to overwinding), but stays approximately constant for negative turns (corresponding to underwinding), due to torque-induced DNA melting^{32, 52} (**Supplementary Fig. S5.2C**, bottom panel).

Applying our AD analysis to the angle traces recorded in the MTT at different numbers of applied turns reveals some variability, but indicates that we generally reach an angle precision of $\sim 1^\circ$ for a 50 s measurement (**Fig. 5.2B**). From fits of the analytical expression (**Eq. 5.3**) to the angle AV data, we obtain the trap stiffness for each trace (**Fig. 5.2D**), revealing a $\sim 13\%$ variation from trace to trace, without any systematic changes throughout the measurement (**Supplementary Fig. S5.2D**). This yields a mean trap stiffness of 339 ± 45 pN·nm/rad, in excellent agreement with the value obtained from directly computing the standard deviation of the angular fluctuations (330 ± 46 pN·nm/rad). Multiplying each angle AD curve by its fitted value of the trap stiffness, we convert the angle to a torque signal (**Fig. 5.2C**). AD analysis of the torque signal indicates that the torque precision in the MTT follows the thermal limit (**Fig. 5.2C**, dashed magenta line) for measurement times longer than ~ 2 s and reaches ~ 5 pN·nm after 50 s (**Fig. 5.2C**). These results are consistent with our previous torque precision estimate for this setup³² of 1–3 pN·nm for a 300 s measurement. In addition, we obtain values for the drag coefficient from the AV fits that exhibit systematic changes with DNA tether extensions, increasing by ~ 70 – 80% upon decreasing the extension from 2.4 μm to 0.7 μm (**Fig. 5.2E**). Both the observed value for the drag coefficients and the dependence on DNA extension are in reasonable agreement with the predictions of a model (**Fig. 5.2E**, solid black line) that describes the rotation of a 2.8 μm diameter bead along a circular trajectory, taking into account the increase in friction coefficient due to the proximity of the flow cell surface^{53, 54} (see **Eq. S5.10** in **Supplementary Text S5.6.7**). The observed dependence of the friction coefficient on DNA tether extension highlights the ability of our AD analysis to detect subtle changes in measurement

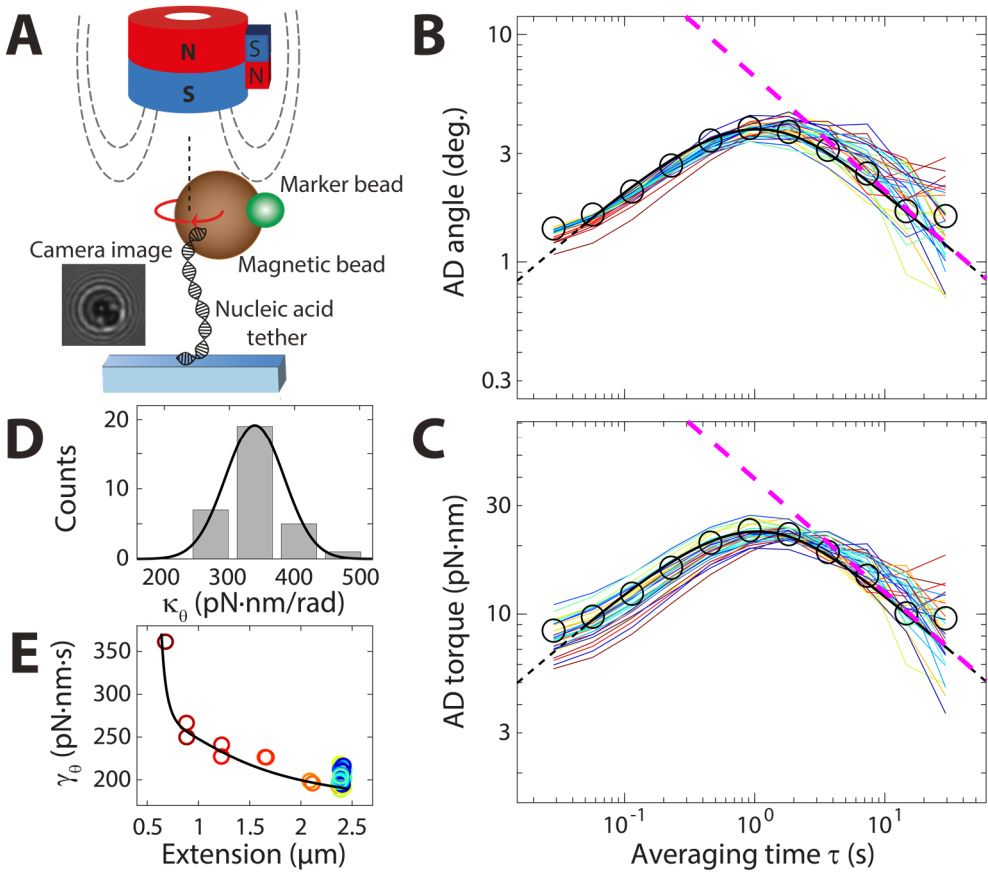


Figure 5.2. Angle and torque precision in the magnetic torque tweezers (MTT). **A)** Schematic of the “classical” MTT implementation³². Angle tracking is achieved by attaching a smaller (1 μm diameter) non-magnetic marker bead (green) to a larger (2.8 μm diameter) magnetic bead (brown) and tracking the rotation of the bead pair from CCD images (inset). The magnetic bead is tethered to a glass slide (blue) by a single DNA molecule (black), held and manipulated in a weak rotational trap set up by a vertically aligned permanent magnets with a side magnet added (on top). The axis of bead rotation is indicated by the vertical dashed black line. **B)** Octave-sampled overlapping Allan deviation (AD) of 32 angle traces of 100 s each sampled at 35 Hz (corresponding to 3.5×10^3 data points), recorded in a torque measurement on a single 7.9 kbp DNA molecule (each trace is shown as a distinctly colored solid line, denoting the number of applied turns). The octave-sampled points for a single trace are shown as black circles. The fit of the analytical expression for the AV (Eq. 3) is shown as a solid black line and its extrapolation as a dashed black line. The thermal limit is indicated as a dashed magenta line. **C)** Torque AD of the same traces as **B)** obtained by multiplication with the corresponding trap stiffnesses (color-coding is as in **B)**). Similar to **B)**, octave-sampled points for one trace are shown as black circles and the fit to Eq. 3 is shown as a solid black line, and its extrapolation is shown as a dashed black line. The thermal limit is indicated as a dashed magenta line. **D)** The values for the trap stiffness κ_θ determined from the fits for all traces in **B)**. The data are approximately Gaussian distributed (solid black line) with a standard deviation of ~ 45 pN·nm/rad. **E)** Rotational friction coefficients γ_θ (distinctly colored circles) determined from the AV fits for all traces in **B)** shown as a function of the height of the bead above the flow cell surface. The color-coding denotes the number of applied turns. The solid black line reflects a prediction for the rotational friction coefficient of a 2.8 μm diameter bead rotating on a circular trajectory, taking into account corrections due to the presence of the surface.

parameters and demonstrates the importance of taking into account surface proximity effects when evaluating friction coefficients in single-molecule measurements⁵⁵.

5.3.3. Angle and torque precision in the eMTT at different fields

eMTT (**Fig. 5.3A**) are similar to MTT, with the main difference that in the eMTT electromagnets (implemented as two pairs of Helmholtz coils) generate the field in the horizontal direction. eMTT have the advantage over MTT that the horizontal field component is readily tunable by altering the current in the Helmholtz coils³⁵. The ability to tune the trap stiffness, however, raises the question what stiffness, if any, is optimal for a given torque measurement application. To explore the effects of trap stiffness and bead size, we measured angular fluctuations and analyzed the ADs of several, differently-sized, DNA-tethered beads in the eMTT (**Supplementary Figs. S5.3-S5.5**); for each bead size, measurements were carried out at different applied currents in the Helmholtz coils, corresponding to different applied fields in the horizontal direction. We present the results of a single 0.7 μm diameter bead trapped at different magnetic field strengths in **Fig. 5.3**.

From the AD of the angle signal in the eMTT, it is apparent that higher fields, corresponding to higher trap stiffnesses, give rise to a better angle precision (**Fig. 5.3B**). For the 0.7 μm diameter beads, the measurements reach $\sim 1^\circ$ precision in 3 s at the highest field strength of 16 mT (**Fig. 5.3B**, lightest brown). This is much faster than what was observed in the MTT (~ 50 s, **Fig. 5.2B**), despite the lower trap stiffness employed in the eMTT, and results from our use of much smaller beads in the eMTT measurement. Converting the angle AD to torque AD by multiplication with the trap stiffness (itself deduced by fitting the corresponding angle AD curve), we find that the torque precision measurements are independent of trap stiffness in the thermal limit, i.e. at times longer than ~ 1 s (**Fig. 5.3C**), as is expected from **Eq. 5.6**. The torque AD is identical for all employed trap stiffnesses for times between 1 and 100 s, and already reaches a torque precision of ~ 5 pN·nm after 1 s, again much faster than in the MTT (~ 50 s, **Fig. 5.2C**) due to the smaller beads used here. The torque precision reaches ~ 0.5 pN·nm for 100 s measurements (**Fig. 5.3C**). The angle ADs are well described by the analytical expression in **Eq. 5.3**, yielding fitted drag coefficients γ_θ (**Fig. 5.3D**) that are independent of the magnetic field, as expected, and fitted trap stiffnesses κ_θ (**Fig. 5.3E**) that increase monotonically with the magnetic field. In the field range used in our implementation of the eMTT (1–16 mT), the dependence of κ_θ on field can be reasonably approximated as linear³⁵ (**Fig. 5.3E**, dashed black line).

In these eMTT measurements, we start to see deviations from the thermal limit behavior ($\propto \tau^{-1/2}$) after ~ 100 s, and the torque AD signals for different field strengths begin to differ. In general, for times longer than ~ 100 s, the torque AD is higher for higher field strengths, due to pronounced drifts apparent as increases in the torque AD with time for long times (**Fig. 5.3C**, see traces at 4 and 8 mT). The drifts are very likely due to heating of the coils when running relatively high currents to achieve high fields for extended periods of time. Our present implementation of the eMTT requires ~ 16 A to achieve ~ 16 mT field and is air-cooled only³⁵. The heating is most dramatically visible in the trace at 16 mT, which had to be terminated after ~ 280 s (**Supplementary**

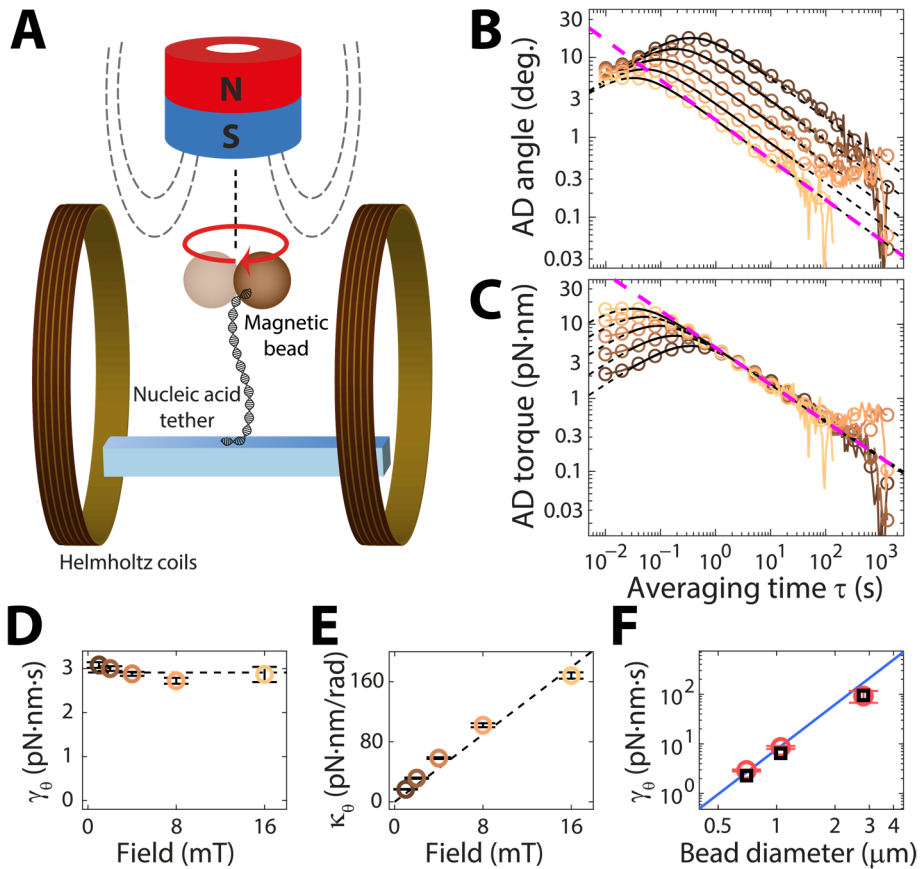


Figure 5.3. Angle and torque precision in the electromagnetic torque tweezers (eMTT). **A)** Schematic of the eMTT setup³⁵. A magnetic bead (brown) is tethered to a glass slide (blue) by a single 3.4 kbp DNA molecule (black). The bead is lifted off from the surface by a cylindrical magnet (on top). Four coils (only two are shown here) generate an in-plane magnetic field to orient the bead. Here, the angular orientation of the magnetic bead is deduced from its spatial position within a circular annulus whose radius is set by the distance between the tether attachment point and the pole of the magnetic bead³⁵. The axis of bead rotation is indicated by the vertical dashed black line. **B)** Angle Allan deviation (AD) of angle traces ≈ 2600 s each (except at 16 mT; 280 s) sampled at 100 Hz (corresponding to 2.6×10^5 data points), recorded on a single DNA tethered bead at 1, 2, 4, 8, and 16 mT (going from dark brown to light brown). Colored lines (circles) reflect the normal AD and octave-sampled overlapping AD, respectively. The octave-sampled data are used to fit (solid black lines) the data to the analytical expression (Eq. 5.3), and their extrapolations are shown as dashed black lines. The dashed magenta line indicates the thermal limit for the stiffest trap. **C)** Torque AD of the same traces as **B)** obtained by multiplication with the corresponding trap stiffnesses. The color-coding is the same as in **B)**. The dashed magenta line indicates the thermal limit. **D,E)** The values of the rotational drag coefficient γ_θ and the rotational trap stiffness κ_θ obtained from the fits in **B)**. The data points and their corresponding error bars denote the average and standard deviation, respectively, from $N = 5$ independent measurements. In **D)**, the dashed black line is a constant-value fit to the drag coefficients. In **E)**, the dashed black line is a linear fit to the data through the origin. **F)** Drag coefficients from AV fits for three different bead sizes ($d = 0.7, 1.05,$ and $2.8 \mu\text{m}$; **Supplementary Figs. S5.3-S5.5**). Red circles and error bars are the drag coefficients (mean \pm STD) determined from AV fits for differently sized beads (**Supplementary Figs. S5.3G-S5.5G**) averaged over measurements at different field strengths. Black squares are the predictions from Eq. S5.10. The solid blue line is a fit of the scaling relation $\gamma_\theta \sim d^3$.

Fig. S5.3A) as the coils reached a temperature of 60 °C, at which point they are shut

down by an automatic safety switch. A clear recommendation that emerges from the AD analysis is, therefore, to run at low field strengths and thus trap stiffnesses in the eMTT for optimal torque measurements: in the absence of drift, higher trap stiffnesses do not confer any disadvantages in the torque precision; yet the high currents required for high trap stiffnesses tend to cause significant drifts due to heating and thus deterioration of the torque precision for times longer than ~ 100 s. In contrast, for low currents and trap stiffnesses, we observe very low levels of drifts even for (very) long measurements, and reach, e.g., a best precision of ~ 0.1 pN·nm for ~ 1000 s measurements at ≤ 2 mT.

5.3.4. Angle and torque precision in eMTT for different bead sizes

In addition, in the eMTT experiments we probe the effect of different drag coefficients by comparing different bead sizes at roughly constant trap stiffness (**Supplementary Fig. S5.6**). Similar to the simulations (**Fig. 5.1C,D**), a higher drag coefficient shifts the AD curve to longer time scales. At intermediate averaging times $\tau \sim 10$ – 100 s, the smaller the bead, the better the angle and torque precision, as expected from the corresponding thermal limits (**Eqs. 5.5, 5.6**, respectively). The rotational drag coefficients obtained from the AV fits (**Fig. 5.3F**, red circles) are in good agreement with predictions of the model (**Fig. 5.3F**, black squares) that take into account the bead and tether geometry and surface effects (**Eq. S5.10**), and roughly follow a $\gamma_{\theta} \sim d^3$ scaling, where d is bead diameter (**Fig. 5.3F**, solid blue line). The bead size analysis confirms that a decrease in drag coefficient improves the precision in both angle and torque.

As an independent test of the torque precision achieved in the eMTT, we analyzed a high-precision DNA torque measurement that employed $1 \mu\text{m}$ diameter beads and a measurement time of 200 s per measurement point (**Supplementary Fig. S5.7A**). The torque AD analysis (**Supplementary Fig. S5.4F**) suggests that this measurement should achieve a torque precision of ~ 0.5 – 0.9 pN·nm at ~ 200 s. We analyzed the deviations of the measured torque values from a strictly linear behavior in the elastic response regime (**Supplementary Fig. S5.7B**) and the deviations from constant torque in the DNA melting regime (**Supplementary Fig. S5.7C**). The deviations are approximately Gaussian distributed with a standard deviation of 0.9 and 0.6 pN·nm for the two regimes respectively, in excellent overall agreement with the expected precision from the AD analysis.

5.3.5. Angle and torque measurements in the OTW

In the optical tweezers measurements, we keep the linear polarization of the trapping beam fixed and measure the torque transferred from the laser beam to a trapped, birefringent cylinder undergoing thermal fluctuations (**Materials and Methods, Fig. 5.4A**). The cylinders are fabricated out of rutile TiO_2 , selected over other materials (e.g. quartz SiO_2) for its extraordinarily high birefringence. While the OTW directly measures angular momentum transfer, and thus torque, the torque traces are recorded in voltage. The corresponding AD can be converted to either the angle AD in degrees

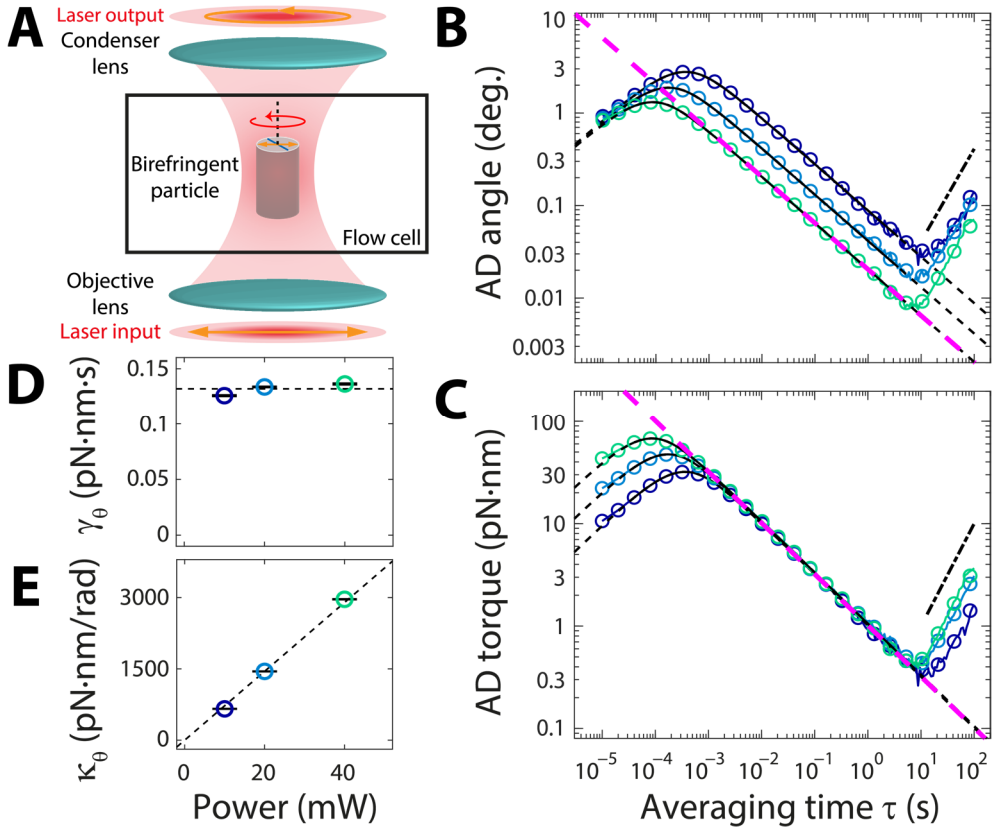


Figure 5.4. Angle and torque precision in the optical torque wrench (OTW). **A)** Schematic of the OTW setup²². The objective lens focuses a linearly polarized laser beam input (red), and traps a birefringent cylinder (gray) near the focus within a flow cell. Manipulation of the linear polarization allows us to control the angular position of the particle. At the output of the trap, the laser light is collected by a condenser lens. The polarization state of the output reports on the torque transferred from beam to particle. The axis of cylinder rotation is indicated by the vertical dashed black line. **B)** Angle Allan deviation (AD) obtained from **C)** by division with the corresponding trap stiffnesses. Colored lines (circles) reflect the normal AD and octave-sampled overlapping AD, respectively. The color-coding is the same as in **C)**. The dashed magenta line indicates the thermal limit for the stiffest trap. **C)** Torque AD of torque traces 200 s each sampled at 100 kHz (corresponding to 2.0×10^7 data points), recorded on a single rutile TiO_2 cylinder at 10, 20, and 40 mW (going from dark blue to light green). The octave-sampled data are used to fit (solid black lines) the data to the analytical expression (Eq. 5.3, multiplied by κ_θ^2), and their extrapolations are shown as dashed black lines. The fits only provide two independent parameters, γ_θ and κ_θ , so the system was precalibrated²² to obtain the detector sensitivity in units of pN·nm/mV. The dashed magenta line indicates the thermal limit. The dash-dotted black line has slope +1, corresponding to linear drift. **D), E)** The values of the rotational drag coefficient γ_θ and the rotational trap stiffness κ_θ obtained from the fits in **C)**. The data points and their corresponding error bars denote the average and standard deviation, respectively, from $N = 5$ independent measurements. In **D)**, the dashed black line is a constant-value fit to the drag coefficients. In **E)**, the dashed black line is a linear fit to the data through the origin.

(Fig. 5.4B) or the torque AD in pN·nm (Fig. 5.4C) using parameters obtained through a separate calibration process²². We also fit the torque AD (Eq. 5.3, multiplied by κ_θ^2) to obtain values for the parameters κ_θ and γ_θ . The drag coefficient γ_θ is nearly independent of laser power (Fig. 5.4D) and averages to 0.13 ± 0.01 pN·nm·s, in good agreement with

a theoretical value of $\sim 0.12 \text{ pN}\cdot\text{nm}\cdot\text{s}$ ⁵⁶. The angular trap stiffness κ_θ increases linearly with the laser power (**Fig. 5.4E**), i.e. quadratically with the electric field amplitude⁹. The Allan deviations for the OTW data (**Fig. 5.4B,C**) report on the precision of this experimental apparatus. As in the eMTT, we observe that angular precision improves (e.g. from $\sim 0.03^\circ$ to $\sim 0.007^\circ$ at $\sim 10 \text{ s}$ (**Fig. 5.4B**) with increased stiffness (achieved by increasing laser power from 10 to 40 mW). At the highest laser power, the measurements reach an angular precision of $\sim 1^\circ$ after only 0.3 ms; a much shorter timescale than in the magnetic tweezers measurements that results from the order(s)-of-magnitude higher trap stiffness and lower drag coefficient in the optical tweezers (compare panels **D, E** in **Figs. 5.2-5.4**). For the torque AD (**Fig. 5.4C**), all curves converge to the thermal limit. Similar dependencies for laser powers up to 80 mW were observed in a separate data set (**Supplementary Fig. S5.9**).

The best torque precision in the OTW achieved is $\sim 0.3 \text{ pN}\cdot\text{nm}$, comparable to $\sim 0.1 \text{ pN}\cdot\text{nm}$ precision achieved in the eMTT measurements. This requires the optimized environmental conditions reflected in **Fig. 5.4** and **Supplementary Fig. S5.8** (see, for comparison, **Supplementary Fig. S5.9** where air currents induced earlier onset of drift) and is achieved after an averaging time of $\sim 10 \text{ s}$ at a laser power of 10 mW (**Fig. 5.4C**). On longer timescales, we find that drift in the OTW becomes dominant and deteriorates the precision. Similar dominance of drift only appears after $\sim 100 \text{ s}$ in the eMTT at high Helmholtz fields ($\geq 4 \text{ mT}$). The earlier onset of drift in the OTW compared to the eMTT derives from the increased number of optical and electronic components present, coupled to laser power-dependent heating (observable from $\sim 10 \text{ s}$ onwards in **Fig. 5.4B,C**). These clear differences observed in the noise highlight the ability of our AD analysis to detect and compare noise components among different setups and environmental conditions.

5.4. Discussion

Examination of the AD provides insights into the achievable precision and optimal measurement duration and parameters. For a hypothetical measurement without drift, the AD can become arbitrarily small, provided the trace is averaged long enough, as the AD decreases in the thermal limit as $\tau^{-1/2}$. This would imply that the precision achievable experimentally could be arbitrarily high. In practice, of course, noise other than the white noise deriving from thermal fluctuations will kick in and limit further improvements in precision. Given the additive nature of the AD (**Eq. 5.2**), at a certain averaging time τ , drift will start to dominate over the thermal limit; on longer timescales, the precision will no longer improve with averaging, but rather worsen. The resulting minimum in the AD then designates the best achievable precision and hence the optimum measurement time. Different sources of drift will exhibit distinct signatures in the AD. For example, for linear drift, the AD should increase as τ^1 (**Supplementary Text S5.6.6**), as we observe for the OTW traces (**Fig. 5.4B,C**, $\tau = 10-$

100 s). If the dominant source of noise has a $1/f$ character, then the AD scales as τ^0 (i.e. becomes constant; **Supplementary Text S5.6.6**), as we observe around 2 s in the AD plots for the OTW dataset presented in **Supplementary Fig. S5.9E,F**.

In this work, we have introduced the use of the AD to evaluate the performance of several instruments designed to measure torque on individual (biological) molecules. In both of the magnetic tweezers measurements, drift does not appear to significantly limit the measurements, even for very long measurement times (**Fig. 5.3B,C**, $\tau = 100\text{--}1000$ s), provided that low enough Helmholtz fields (≤ 2 mT) are used to avoid drifts through heating of the coils in the eMTT configuration. It might be possible to avoid this limitation in future implementations, e.g. by configuring water-cooled coils. Nonetheless, even the current instrument enables measurements with a torque precision better than 1 pN·nm (**Fig. 5.3C** and **Supplementary Figs. S5.3F-S5.5F, S5.7**). We achieved a similar torque precision (0.3 pN·nm in 10 s, **Fig. 5.4C**; for direct comparison with the eMTT, see **Supplementary Fig. S5.10**) in the OTW under the best conditions (low laser power and blocking of air current). Potentially, the precision of the OTW can be enhanced by further improvements to the instrument's long-term stability.

A general lesson from our analysis is that to optimize torque and/or angle precision the drag coefficient should be minimized, in particular by using smaller particles⁸. The eMTT data sets clearly demonstrate the improvements in precision obtained through using smaller beads; recent approaches to angle and torque measurements using gold nanoparticles push this development even further¹⁵. Furthermore, once a particle size has been selected, it is generally advisable to maximize the trap stiffness for improved angle (but not torque) precision given measurement times in which precision is thermally limited. However, there are important caveats to this general advice: first, smaller particles usually result in reduced stiffness and achievable torque, because they contain less volume for torque exchange (lower magnetic content in magnetic beads and a shorter light path in birefringent particles); second, increasing the trap stiffness can result in increased drift due to the practical limitations (e.g., heating from increased current in eMTT or laser power in OTW), deteriorating the precision for longer measurement timescales; third, the use of ever smaller particles may push the limits of the detection systems (e.g., pixel size for camera- and diode sensitivity for photodiode-based signal acquisition); fourth, maximization of the trap stiffness and minimization of the drag coefficient reduce the characteristic time τ_c , which demands for faster acquisition systems, as most calibration methods (and particularly AD analysis, see **Supplementary Text S5.6.1**), require measurements on timescales shorter than τ_c ; and finally, the timescale of dynamics in the system under investigation and the quantity of interest, angle or torque, ultimately determine the optimal drag coefficient and stiffness of operation.

The AD provides a direct and quantitative measure for the precision in single-molecule experiments. It can therefore be employed as a tool for optimizing experimental assays: it can be used to systematically track down sources of drift and

other forms of noise and to determine the optimal measurement time at the desired precision. We foresee that usage of the AD analysis will instruct researchers about the optimal measurement strategy, and thus will facilitate new breakthroughs in the field of single-molecule torque spectroscopy.

5.5. References

1. Bustamante, C., Bryant, Z. & Smith, S. B. Ten years of tension: single-molecule DNA mechanics. *Nature* **421**, 423-427 (2003).
2. Strick, T. R. et al. Stretching of macromolecules and proteins. *Reports on Progress in Physics* **66**, 1-45 (2003).
3. Neuman, K. C. & Nagy, A. Single-molecule force spectroscopy: optical tweezers, magnetic tweezers and atomic force microscopy. *Nature Methods* **5**, 491-505 (2008).
4. Puchner, E. M. & Gaub, H. E. Force and function: probing proteins with AFM-based force spectroscopy. *Current Opinion in Structural Biology* **19**, 605-614 (2009).
5. Vilfan, I. D., Lipfert, J., Koster, D. A., Lemay, S. G. & Dekker, N. H. Magnetic tweezers for single-molecule experiments. In *Handbook of Single-Molecule Biophysics* (ed Hinterdorfer, P., van Oijen, A.) 371-395 (Springer, 2009).
6. Dulin, D., Lipfert, J., Moolman, M. C. & Dekker, N. H. Studying genomic processes at the single-molecule level: introducing the tools and applications. *Nature Reviews. Genetics* **14**, 9-22 (2013).
7. Robinson, A. & van Oijen, A. M. Bacterial replication, transcription and translation: mechanistic insights from single-molecule biochemical studies. *Nature Reviews. Microbiology* **11**, 303-315 (2013).
8. Bryant, Z., Oberstrass, F. C. & Basu, A. Recent developments in single-molecule DNA mechanics. *Current Opinion in Structural Biology* **22**, 304-312 (2012).
9. Lipfert, J., van Oene, M. M., Lee, M., Pedaci, F. & Dekker, N. H. Torque spectroscopy for the study of rotary motion in biological systems. *Chemical Reviews* **115**, 1449-1474 (2015).
10. Bryant, Z., Stone, M. D., Gore, J., Smith, S. B., Cozzarelli, N. R. & Bustamante, C. Structural transitions and elasticity from torque measurements on DNA. *Nature* **424**, 338-341 (2003).
11. Gore, J., Bryant, Z., Stone, M. D., Nollmann, M., Cozzarelli, N. R. & Bustamante, C. Mechanochemical analysis of DNA gyrase using rotor bead tracking. *Nature* **439**, 100-104 (2006).
12. Gore, J., Bryant, Z., Nollmann, M., Le, M. U., Cozzarelli, N. R. & Bustamante, C. DNA overwinds when stretched. *Nature* **442**, 836-839 (2006).
13. Oberstrass, F. C., Fernandes, L. E. & Bryant, Z. Torque measurements reveal sequence-specific cooperative transitions in supercoiled DNA. *Proceedings of the National Academy of Sciences* **109**, 6106-6111 (2012).
14. Oberstrass, F. C., Fernandes, L. E., Lebel, P. & Bryant, Z. Torque spectroscopy of DNA: base-pair stability, boundary effects, backbending, and breathing dynamics. *Physical Review Letters* **110**, 178103 (2013).
15. Lebel, P., Basu, A., Oberstrass, F. C., Tretter, E. M. & Bryant, Z. Gold rotor bead tracking for high-speed measurements of DNA twist, torque and extension. *Nature Methods* **11**, 456-462 (2014).
16. Friese, M. E. J., Nieminen, T. A., Heckenberg, N. R. & Rubinsztein-Dunlop, H. Optical alignment and spinning of laser-trapped microscopic particles. *Nature* **394**, 348-350 (1998).
17. Oroszi, L., Galajda, P., Kirei, H., Bottka, S. & Ormos, P. Direct measurement of torque in an optical trap and its application to double-strand DNA. *Physical Review Letters* **97**, 058301 (2006).
18. La Porta, A. & Wang, M. D. Optical torque wrench: angular trapping, rotation, and torque detection of quartz microparticles. *Physical Review Letters* **92**, 190801 (2004).
19. Forth, S., Deufel, C., Sheinin, M. Y., Daniels, B., Sethna, J. P. & Wang, M. D. Abrupt buckling transition observed during the plectoneme formation of individual DNA molecules. *Physical Review Letters* **100**, 148301 (2008).
20. Inman, J., Forth, S. & Wang, M. D. Passive torque wrench and angular position detection using a single-beam optical trap. *Optics Letters* **35**, 2949-2951 (2010).
21. Pedaci, F., Huang, Z. X., van Oene, M., Barland, S. & Dekker, N. H. Excitable particles in an optical torque wrench. *Nature Physics* **7**, 259-264 (2011).
22. Pedaci, F., Huang, Z., van Oene, M. & Dekker, N. H. Calibration of the optical torque wrench. *Optics Express* **20**, 3787-3802 (2012).
23. Deufel, C., Forth, S., Simmons, C. R., Deigosha, S. & Wang, M. D. Nanofabricated quartz cylinders for angular trapping: DNA supercoiling torque detection. *Nature Methods* **4**, 223-225 (2007).
24. Gutiérrez-Medina, B., Andreasson, J. O., Greenleaf, W. J., La Porta, A. & Block, S. M. An optical apparatus for rotation and trapping. *Methods in Enzymology* **475**, 377-404 (2010).

25. Huang, Z., Pedaci, F., van Oene, M., Wiggin, M. J. & Dekker, N. H. Electron beam fabrication of birefringent microcylinders. *ACS Nano* **5**, 1418-1427 (2011).
26. Ha, S., Janissen, R., Ussembayev, Y. Y., van Oene, M. M., Solano, B. & Dekker, N. H. Tunable top-down fabrication and functional surface coating of single-crystal titanium dioxide nanostructures and nanoparticles. *Nanoscale* **8**, 10739-10748 (2016).
27. Parkin, S. J. et al. Highly birefringent vaterite microspheres: production, characterization and applications for optical micromanipulation. *Optics Express* **17**, 21944-21955 (2009).
28. Ramaiya, A., Roy, B., Bugiel, M. & Schäffer, E. Kinesin rotates unidirectionally and generates torque while walking on microtubules. *Proceedings of the National Academy of Sciences* **114**, 10894 (2017).
29. Mosconi, F., Allemand, J. F. & Croquette, V. Soft magnetic tweezers: a proof of principle. *Review of Scientific Instruments* **82**, 034302 (2011).
30. Celedon, A. et al. Magnetic tweezers measurement of single molecule torque. *Nano Letters* **9**, 1720-1725 (2009).
31. Kauert, D. J., Kurth, T., Liedl, T. & Seidel, R. Direct mechanical measurements reveal the material properties of three-dimensional DNA origami. *Nano Letters* **11**, 5558-5563 (2011).
32. Lipfert, J., Kerssemakers, J. W., Jager, T. & Dekker, N. H. Magnetic torque tweezers: measuring torsional stiffness in DNA and RecA-DNA filaments. *Nature Methods* **7**, 977-980 (2010).
33. Lipfert, J., Wiggin, M., Kerssemakers, J. W., Pedaci, F. & Dekker, N. H. Freely orbiting magnetic tweezers to directly monitor changes in the twist of nucleic acids. *Nature Communications* **2**, 439 (2011).
34. Lipfert, J., Wiggin, M., Kerssemakers, J. W., Pedaci, F. & Dekker, N. H. Corrigendum: Freely orbiting magnetic tweezers to directly monitor changes in the twist of nucleic acids. *Nature Communications* **6**, 7192 (2015).
35. Janssen, X. J., Lipfert, J., Jager, T., Daudey, R., Beekman, J. & Dekker, N. H. Electromagnetic torque tweezers: a versatile approach for measurement of single-molecule twist and torque. *Nano Letters* **12**, 3634-3639 (2012).
36. Moffitt, J. R., Chemla, Y. R., Smith, S. B. & Bustamante, C. Recent advances in optical tweezers. *Annual Review of Biochemistry* **77**, 205-228 (2008).
37. Capitanio, M. & Pavone, F. S. Interrogating biology with force: single molecule high-resolution measurements with optical tweezers. *Biophysical Journal* **105**, 1293-1303 (2013).
38. Perkins, T. T. Ångström-precision optical traps and applications. *Annual Review of Biophysics* **43**, 279-302 (2014).
39. Andersson, M., Czerwinski, F. & Oddershede, L. B. Optimizing active and passive calibration of optical tweezers. *Journal of Optics* **13**, 044020 (2011).
40. Huhle, A. et al. Camera-based three-dimensional real-time particle tracking at kHz rates and Ångström accuracy. *Nature Communications* **6**, 5885 (2015).
41. Dulin, D., Cui, T. J., Cnossen, J., Docter, M. W., Lipfert, J. & Dekker, N. H. High spatiotemporal-resolution magnetic tweezers: calibration and applications for DNA dynamics. *Biophysical Journal* **109**, 2113-2125 (2015).
42. Gibson, G. M., Leach, J., Keen, S., Wright, A. J. & Padgett, M. J. Measuring the accuracy of particle position and force in optical tweezers using high-speed video microscopy. *Optics Express* **16**, 14561-14570 (2008).
43. Czerwinski, F., Richardson, A. C. & Oddershede, L. B. Quantifying noise in optical tweezers by Allan variance. *Optics Express* **17**, 13255-13269 (2009).
44. Mahamdeh, M. & Schäffer, E. Optical tweezers with millikelvin precision of temperature-controlled objectives and base-pair resolution. *Optics Express* **17**, 17190-17199 (2009).
45. Allan, D. W. Statistics of atomic frequency standards. *Proceedings of the IEEE* **54**, 221-230 (1966).
46. Allan, D. W., Weiss, M. A. & Jespersen, J. L. A frequency-domain view of time-domain characterization of clocks and time and frequency distribution systems. *In Proceedings of the 45th Annual Symposium on Frequency Control*, 667-678 (1991).
47. Lansdorp, B. M. & Saleh, O. A. Power spectrum and Allan variance methods for calibrating single-molecule video-tracking instruments. *Review of Scientific Instruments* **83**, 025115 (2012).
48. Lansdorp, B. M. & Saleh, O. A. Erratum: "Power spectrum and Allan variance methods for calibrating single-molecule video-tracking instruments" [Review of Scientific Instruments 83, 025115 (2012)]. *Review of Scientific Instruments* **85**, 019901 (2014).
49. Czerwinski, F. Allan v3.0. <http://mathworks.com/matlabcentral/fileexchange/26659-allan-v3-0> (2010).
50. van Oene, M. M. et al. Biological magnetometry: torque on superparamagnetic beads in magnetic fields. *Physical Review Letters* **114**, 218301 (2015).
51. Lipfert, J., Kerssemakers, J. J., Rojer, M. & Dekker, N. H. A method to track rotational motion for use in single-molecule biophysics. *Review of Scientific Instruments* **82**, 103707 (2011).
52. Strick, T. R., Croquette, V. & Bensimon, D. Homologous pairing in stretched supercoiled DNA. *Proceedings of the National Academy of Sciences* **95**, 10579-10583 (1998).

53. Leach, J. et al. Comparison of Faxen's correction for a microsphere translating or rotating near a surface. *Physical Review E* **79**, 026301 (2009).
54. Faxen, H. Der widerstand gegen die bewegung einer starren kugel in einer zähen flüssigkeit, die zwischen zwei parallelen ebenen wänden eingeschlossen ist. *Annalen der Physik* **68**, 89-119 (1922).
55. Lobo, S., Escauriaza, C. & Celedon, A. Measurement of surface effects on the rotational diffusion of a colloidal particle. *Langmuir* **27**, 2142-2145 (2011).
56. Ortega, A. & García de la Torre, J. Hydrodynamic properties of rodlike and disklike particles in dilute solution. *The Journal of Chemical Physics* **119**, 9914-9919 (2003).

5.6. Supplementary Information

5.6.1. Comparison of magnetic tweezers and optical tweezers in applying Allan variance

The Allan variance is mathematically a two-sample variance with no dead time, where sampling interval T is the same as averaging time τ ($T = \tau$) (for details, see **Supplementary Text S5.6.5**):

$$\sigma_{\theta}^2(M, T, \tau) = \sigma_{\theta}^2(2, \tau, \tau) = \sigma_{AV, \theta}^2(\tau). \quad \text{Equation S5.1}$$

For the magnetic tweezers (or other using video microscopy-based technique), there is negligible dead time between successive frames of a camera so that each measurement is a physical average of the signal during T ($T \approx \tau$), as described by the above equation. In the optical tweezers, detection occurs via photodiodes that have very fast response times. In this context, such a short response time can be considered as negligible integration time. Unless a specific configuration is employed in either acquisition hardware or software, no signal averaging (i.e., integration) occurs during the sampling interval T . Hence, the inverse of sampling frequency is equivalent to the dead time. Thus, in photodiodes the dead time far exceeds the integration time.

Nonetheless, the application of AV for photodiode-based detection remains valid provided that the sampling period T is much shorter than the characteristic time τ_c of the system. For such a case, a trapped particle essentially moves in a straight line between consecutive data points. For such a straight line, the average position calculated using the integral (corresponding to measurements that include averaging signal over T) is identical to the average of the two end points of the line (corresponding to measurements that consist of two sampled signal values without averaging over T). In other words, while optical tweezers measurements do not fulfill the zero-dead-time assumption ($T = \tau$) in a strict sense since physically $T \gg \tau$, effectively the measured signal is identical to that acquired over $T = \tau$ condition, provided that $T \ll \tau_c$. Hence, OTW and MT data can be interpreted with the same Allan variance equation. To our understanding, this forms the basis for the previous application of Allan variance analysis to linear optical tweezers data (e.g. Refs. 1-4). The importance of fulfilling the condition $T \ll \tau_c$ in optical tweezers measurements is demonstrated in one of these literatures (Figure 4a of Ref. 1), where it is shown that measured Allan variance curves

show improved agreement with theoretical predictions when the data acquisition frequency f_s is sufficiently high ($T = f_s^{-1} \ll \tau_c$).

5.6.2. The effect of noise correlation in Allan variance

The Allan variance is calculated from the difference between neighboring samples $\bar{\theta}_i$, which are averages over a time interval $m\tau_s$ (Eq. 5.2 of the main text). For a single value of m , i.e., a single integration time, the differences are not all independent (S5.6.2.1). The number of independent differences is important, because it determines the noise on the Allan variance. Also, for different values of m , not all of the calculated Allan variance values are independent (S5.6.2.2). The independence of the Allan variance at different values of m is important, because it is a requirement in some fitting algorithms. Here, we elaborate on the independence between the difference terms of Allan variance, and discuss its implications for fitting Allan variance data.

5.6.2.1. Independence of the difference between consecutive samples at a single integration time

For a data set with a finite number of elements, the “simple” Allan variance can be estimated from its discrete form (Eq. 5.2 of the main text):

$$\sigma_{\bar{\theta}}^2(m\tau_s) = \frac{1}{2(M-1)} \sum_{i=1}^{M-1} (\bar{\theta}_{i+1} - \bar{\theta}_i)^2, \quad \text{Equation S5.2}$$

where τ_s is the sampling period taken to be equal to the integration time (e.g., the dead time between frames is assumed to be zero in case of camera-based detection), m is the number of data points in a bin, M is the number of bins, and sample $\bar{\theta}_i$ is the mean of the i^{th} bin of length $m\tau_s$. The term $(\bar{\theta}_{i+1} - \bar{\theta}_i)$ will be referred to as the difference term. Each measurement $\bar{\theta}_i$, except for the first and last (i.e., $\bar{\theta}_1$ and $\bar{\theta}_M$), occurs twice in the difference term: once in conjunction with its preceding bin and once in conjunction with its successive bin. Therefore the $(M-1)$ difference terms are not all independent of each other⁵.

The use of a fully “overlapping” Allan variance (Fig. 5.1A) can improve the estimate of the Allan variance even further:

$$\sigma_{\bar{\theta}}^2(m\tau_s) = \frac{1}{2(N+1-2m)} \sum_{j=1}^{N+1-2m} (\bar{\theta}_{j+m} - \bar{\theta}_j)^2, \quad \text{Equation S5.3}$$

where $N = M \cdot m$ is the total number data points, j is the position of the first data point of a bin with m data points, and $\bar{\theta}_j$ is the average over a bin of length $m\tau_s$ with the first data point located at j . Here, the term $(\bar{\theta}_{j+m} - \bar{\theta}_j)$ will be referred to as the difference term. Again, each measurement $\bar{\theta}_j$ occurs twice, except for the first and last successive m measurements (i.e., $\bar{\theta}_1, \bar{\theta}_2, \bar{\theta}_3, \dots, \bar{\theta}_m$ and $\bar{\theta}_{N+1-2m+1}, \bar{\theta}_{N+1-2m+2}, \bar{\theta}_{N+1-2m+3}, \dots$

$\bar{\theta}_{N+1-2m+m}$). In addition, $\bar{\theta}_j$ also has overlapping data points with the successive $(m-1)$ measurements (i.e., $\bar{\theta}_{j+1}, \bar{\theta}_{j+2}, \bar{\theta}_{j+3}, \dots, \bar{\theta}_{j+(m-1)}$). Therefore the $(N+1-2m)$ difference terms are not all independent of each other.

The degree of dependence of the difference terms should be taken into consideration when computing the noise in the estimate of the Allan variance. In both the “simple” and “overlapping” Allan variance, the $(M-1)$ and $(N+1-2m)$ differences are normally distributed with zero mean ⁶, and the squared differences are gamma distributed, hence the estimate of the Allan variance is gamma distributed ⁶. The shape parameter of this gamma distribution is equal to half the number of degrees of freedom. Due to the aforementioned dependence of the difference terms, the number of degrees of freedom lies below the number of difference terms. It is important to know the number of degrees of freedom, as fitting algorithms such as maximum likelihood estimation account for the noise distribution of the calculated Allan variance, which involves the number of degrees of freedom. In their paper, Lansdorp and Saleh estimate the number of degrees of freedom and recommend a shape factor for the gamma distribution (**Supplementary Text S5.6.3**), which works reasonably well for fitting of both “simple” and “overlapping” Allan variances ⁶.

5.6.2.2. Independence of the Allan variance at different integration times

Most fitting algorithms assume the noise of separate points, here the points at different integration times $m\tau_s$, to be independent. For different integration times, in particular for successive values of m , the Allan variances are calculated from different bin sizes; however, the difference terms of which the Allan variances are comprised can be nearly identical, because most values in a bin of size m are identical to the values in a bin of size $m+1$. Therefore, calculating the Allan variance for all values of m is redundant; calculating the octave-sampled Allan variance for $m = 2^{\text{integer}}$ is sufficient and ensures nearly independent Allan variance values ⁷. Moreover, the octave-sampling has an advantage in computational efficiency over using all values of m . In our benchmark test, it is 108 ± 3 , 852 ± 31 , and 6620 ± 327 times shorter in computation time, for the input data sizes of 3×10^3 , 3×10^4 , and 3×10^5 elements (**Supplementary Fig. S5.11**). As an example, for 3×10^5 elements, only ~ 1 s was required to compute the octave-sampled AV while ~ 2 h was required when using all values of m . The benchmark test was repeated three times with a desktop PC equipped with Intel® Core™ i5-2400 (3.10 GHz) processor and 16 GBytes DDR3 (PC3-12800) memory.

5.6.3. The shape factor used for MLE fitting of Allan variance data

The shape factor η_{AV} (**Eq. S5.4**) used in the maximum likelihood estimation (MLE) fitting of Allan variance data in our manuscript provides information about the extent to which the weighting is different between data points. We employ the following form:

$$\eta_{AV}(m) = \frac{1}{2} \left(\frac{N}{m} - 1 \right), \quad \text{Equation S5.4}$$

where N is the number of total data points and m is the bin size for the octave-sampled Allan variance, in powers of 2 (i.e., $m = 1, 2, 4, 8, \dots$ up to $\leq N/2$)⁶.

5.6.4. Matlab routine for angular Langevin dynamics simulation

The Matlab code (tested in Matlab version R2017b) listed below is used to generate simulated angular fluctuation datasets in **Fig. 5.1** and **Supplementary Fig. S5.1**. It simulates a particle trapped in a harmonic potential while subject to overdamped angular motion (**Eq. 5.7** of the main text; also refer Equations S30-S32 of Ref. 8). The equation of motion (and hence the Matlab code) are very similar to the case of linear trapping (Supplemental materials of Ref. 9), except that the units of the physical quantities differ. After execution of this code, the 'theta' array contains the angular position as a function of 'time' array as shown in **Fig. 5.1B** and **Supplementary Fig. S5.1A**. This simulated raw data can be used to calculate Allan deviation and other plots such as ACF and PSD.

```

%%%%%%%%%%%%%%%%%%%%%%%%%%%%%%%%%%%%%%%%%%%%%%%%%%%%%%%%%%%%%%%%%%%%%%%% Angular Langevin dynamics simulation in Matlab %%%%%%%%%%%%%%%%%%%%%%%%%%%%%%%%%%%%%%%%%%%%%%%%%%%%%%%%%%%%%%%%%%%%%%%%%
gamma = 10; % pN*nm*s, rotational drag coefficient
kappa = 1000; % pN*nm/rad, angular stiffness
kT = 4.1; % pN*nm, thermal energy at room
temperature
dt = 20e-6; % s, sampling period
N = 2^20; % number of data points
Nloop = N - 1; % number of loops
time = (0:Nloop)*dt; % s, time array
rv = randn([1,Nloop]); % random variable (mean = 0, std = 1)
tau_thermal = rv*...
    sqrt(2*kT*gamma/dt); % pN*nm, torque from thermal noise
theta(1) = 0; % rad, initial angular position
for i = 1:Nloop
    tau_external(i) = -kappa*theta(i); % pN*nm, external torque
    dtheta = ((tau_external(i) + ...
        tau_thermal(i))/gamma)*dt; % rad, change in angular position
    theta(i+1) = theta(i) + dtheta; % rad, angular position in the next step
end
%%%%%%%%%%%%%%%%%%%%%%%%%%%%%%%%%%%%%%%%%%%%%%%%%%%%%%%%%%%%%%%%%%%%%%%%

```

5.6.5. Comparison of Allan variance to other variances

The Allan variance is a special case of the M -sample variance. This M -sample variance includes several other variances as special cases (including the commonly employed “normal” variance) and is expressed as¹⁰:

$$\sigma_{\theta}^2(M, T, \tau) = \frac{1}{M-1} \sum_{i=1}^M \left(\bar{\theta}_i - \frac{1}{M} \sum_{j=1}^M \bar{\theta}_j \right)^2, \quad \text{Equation S5.5}$$

where M is the number of samples, T is the time between samples, τ is the time over which each sample is averaged, $\bar{\theta}_i$ is the i^{th} measured sample averaged over τ , and

$\frac{1}{M} \sum_{j=1}^M \bar{\theta}_j$ is the mean over all M samples. In most interpretations of the “normal” variance, the measurements are considered instantaneous ($\tau \rightarrow 0$, often $\tau \ll \tau_c$ is sufficient); the “normal” variance is $\sigma_{\theta}^2(M, T, 0)$ or, written as an infinite time average, $\sigma_{\theta}^2 = \langle (\theta_i - \bar{\theta})^2 \rangle$. For a white noise process, this variance is independent of the number of measurements M , so more measurements do not improve the precision of θ . If the time between measurements T equals the averaging time τ , the variance $\sigma_{\theta}^2(M, \tau, \tau)$ decreases for extended averaging time, thereby improving the precision. For example, the variance for Brownian motion in a harmonic potential is expressed as ¹¹⁻¹³:

$$\sigma_{\theta}^2(M, \tau, \tau) = A \left(\frac{\tau_c}{\tau} \right)^2 \left(2 \frac{\tau}{\tau_c} + 2 \exp \left(-\frac{\tau}{\tau_c} \right) - 2 \right), \quad \text{Equation S5.6}$$

where $A = k_B T / \kappa_{\theta}$ and $\tau_c = \gamma_{\theta} / \kappa_{\theta}$. This equation resembles the equation for the Allan variance (Eq. 5.3 of the main text), and in the long-time limit, $\tau \gg \tau_c$, it approaches the same thermal limit. In the short time limit, $\tau \ll \tau_c$, it converges to the “normal” variance, $\sigma_{\theta}^2 = k_B T / \kappa_{\theta}$. The minimum number of samples to calculate the M -sample variance is two, and the corresponding variance $\sigma_{\theta}^2(2, T, 0)$ can be written as $\sigma_{\theta}^2(2, T, 0) = \frac{1}{2}(\theta_2 - \theta_1)^2$ or, as an infinite time average, $\sigma_{\theta}^2 = \frac{1}{2} \langle (\theta_{i+1} - \theta_i)^2 \rangle$. This variance uses the difference between neighboring measurements, instead of the difference from the mean. Therefore, the two-sample variance is very useful in removing drift and other low frequency noise. The Allan variance is a two-sample variance with no dead time, i.e., $\sigma_{AV, \theta}^2(\tau) = \sigma_{\theta}^2(2, \tau, \tau)$ ¹⁰. The reduced sensitivity to drift at short time scales and the increase in precision (for white noise processes) at long time scales make the Allan variance a very useful tool in characterizing our single-molecule torque spectroscopy instruments.

5.6.6. Comparison of Allan variance to power spectrum analysis

An alternative to the variances in the time domain is provided by the power spectral density in the frequency domain. The power spectrum describes to what extent different frequencies contribute to the variance. A power spectrum can be converted to the corresponding Allan variance using a transfer function $H(f)$ ¹⁰:

$$H(f) = \frac{2 \sin^4(\pi \tau f)}{(\pi \tau f)^2}, \quad \text{Equation S5.7}$$

$$\sigma_{AV}^2(\tau) = \int_0^{\infty} S(f) H(f) df, \quad \text{Equation S5.8}$$

where $S(f)$ is the one-sided power spectrum. Conversely, the Allan variance $\sigma_{AV}^2(\tau)$ can be converted into a power spectrum $S(f)$ by plotting $2\tau \sigma_{AV}^2(\tau)$ as a function of $\pi\tau = f^{-1}$ ³. Some typical types of noise, like white noise, flicker noise, and Brownian noise are characterized by a frequency dependence with integer exponent, here f^0 , f^{-1} , and f^{-2} , respectively. These three have corresponding time dependencies for the Allan variance,

τ^{-1} , τ^0 , and τ^1 , respectively ¹⁰. As a remark, linear drift scales as τ^2 , but the corresponding power spectrum does not scale as f^{-3} ¹⁰. The one-sided power spectrum for Brownian motion in a harmonic potential is given by:

$$S(f) = \frac{A}{1 + (f/f_c)^2}, \quad \text{Equation S5.9}$$

where $A = 4\tau_c k_B T / \kappa$ and $f_c = \kappa / 2\pi\gamma$. In the high frequency limit $f \gg f_c$, $S(f)$ is proportional to f^{-2} . This Brownian noise corresponds to the diffusion limit in the Allan variance $\propto \tau^1$ (Eq. 5.4 of the main text). In the low frequency limit $f \ll f_c$, $S(f)$ is proportional to f^0 . This white noise is linked to the thermal limit in the Allan variance $\propto \tau^{-1}$ (Eq. 5.5 of the main text). If the frequency bandwidth $\Delta f \ll f_c$, the area under the power spectrum from 0 Hz to Δf approximates the angular precision by the variance $\sigma^2 = A \cdot \Delta f$ ¹⁴. The Allan variance, however, provides a much more convenient measure for the precision, especially if drift and low frequency noise become apparent.

5.6.7. Rotational drag coefficient of a bead on a circular trajectory

A sphere of radius R_{bead} , rotating about an axis at a radial distance of R_{circle} from its center, at a distance D from the surface, immersed in a fluidic medium of viscosity η , has a rotational friction coefficient (Equation 18 of Refs. 15, 16):

$$\gamma_\theta \approx \frac{\gamma_{rotational}}{1 - \left(\frac{1}{8}\right)\left(\frac{R_{bead}}{D}\right)^3} + \frac{\gamma_{translational} R_{circle}^2}{1 - \left(\frac{9}{16}\right)\left(\frac{R_{bead}}{D}\right) + \left(\frac{1}{8}\right)\left(\frac{R_{bead}}{D}\right)^3}, \quad \text{Equation S5.10}$$

where $\gamma_{rotational} = 8\pi\eta R_{bead}^3$ and $\gamma_{translational} = 6\pi\eta R_{bead}$.

5.6.8. Supplementary Figures

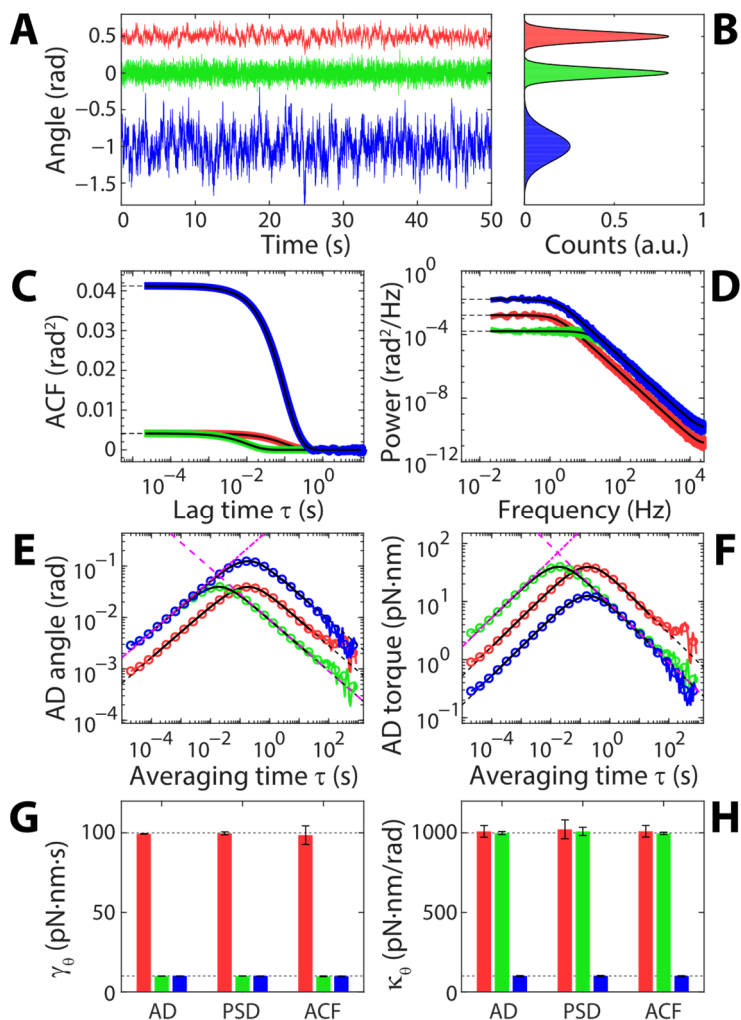


Figure S5.1. Additional analysis of the simulated traces in Fig. 5.1 of the main text. **A)** Simulated angle traces of ~ 1700 s each sampled at 50 kHz (corresponding to 8.5×10^7 data points) for the Brownian motion of a particle in a harmonic trap. A zoom-in on the first 50 s of each trace is shown. The traces are offset vertically for clarity. The red, green, and blue traces (from top to bottom) are simulations with drag coefficients $\gamma_\theta = 100, 10,$ and 10 pN·nm·s, and trap stiffnesses $\kappa_\theta = 1000, 1000,$ and 100 pN·nm/rad, respectively. Same data as in Fig. 5.1B. **B)** Histograms for the full traces. The solid black lines are Gaussian fits to the histograms. **C)** Autocorrelation function analysis (ACF) of the full traces. Black lines are fits to the data, $ACF \propto \exp(-\tau/\tau_c)$, with their extrapolations shown as dashed black lines. **D)** Power spectral density (PSD) analysis of the full traces. Black lines are fits to the data (Eq. S5.9). **E)** Angle Allan deviation (AD). Colored lines (circles) reflect the normal AD (octave-sampled overlapping AD). Same data as in Fig. 5.1C. The solid black lines are fits to the data (Eq. 5.3). The dash-dotted and dashed magenta lines are the diffusion and thermal limits, shown for the green trace only. **F)** Torque AD. Same data as in Fig. 5.1D. **G,H)** Rotational drag coefficient γ_θ and trap stiffness κ_θ obtained from the AD, PSD, and ACF fits. The bar heights and error bars denote the average and standard deviation, respectively, from $N = 5$ independent simulated traces. The dashed black lines indicate the parameter values used in the simulations.

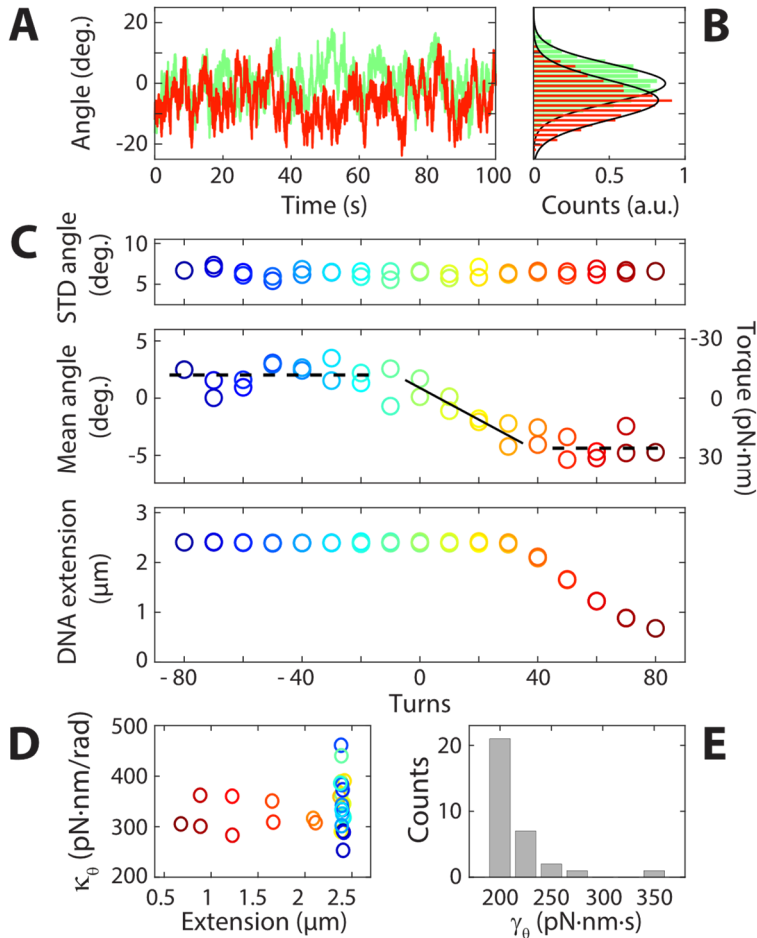


Figure S5.2. Torque measurements in the MTT. Data shown are for a 2.8 μm diameter magnetic bead tethered to a surface by a 7.9 kbp DNA molecule at a stretching force of ~ 2 pN in PBS buffer, using the same data as in Fig. 5.2 of the main text. **A)** Angle traces of 100 s each at 0 (light green) and 50 turns (red). **B)** Histograms of the full traces. The solid black lines are Gaussian fits to the histograms. A shift in the mean angle position upon overwinding the molecule is readily apparent and provides the basis for the single-molecule torque measurement. **C)** Systematic analysis of angle traces as a function of the number of applied turns, such as the ones shown in **A,B)**, reveals systematic shifts in the mean angle (middle panel), while the standard deviations of the fluctuations remain constant (top panel). The data points are color-coded as a function of the number of applied turns. The average trap stiffness (~ 339 pN-nm/rad) of the rotational trap is determined from Allan variance fits, enabling a direct conversion of the mean angle to torque (middle panel, right axis). The bottom panel shows the tether extension as a function of the applied number of turns obtained in the same measurement. The tether extension decreases linearly with the number of applied turns beyond ~ 35 turns, as the molecule buckles and is plectonemically supercoiled in this regime. Note the corresponding plateau in the torque signal (~ 24 pN-nm) for > 35 turns (the dashed black line in this regime is a constant-value fit). Around zero turns, the molecule opposed the applied torque elastically, resulting in an approximately constant extension of the molecule and a linear dependence of the torque on applied turns (the solid black line in this regime is a linear fit). Upon underwinding (corresponding to negative turns), the DNA extension remains approximately constant and the torque exhibits a plateau at the critical melting torque ~ -11 pN-nm (the dashed black line in this regime is a constant-value fit). **D)** Trap stiffness determined from Allan variance fits (same data as in Fig. 5.2D), shown as a function of DNA extension. Color-coding is as in **C)**. **E)** Histogram of the friction coefficient determined from the Allan variance fits (same data as in Fig. 5.2E).

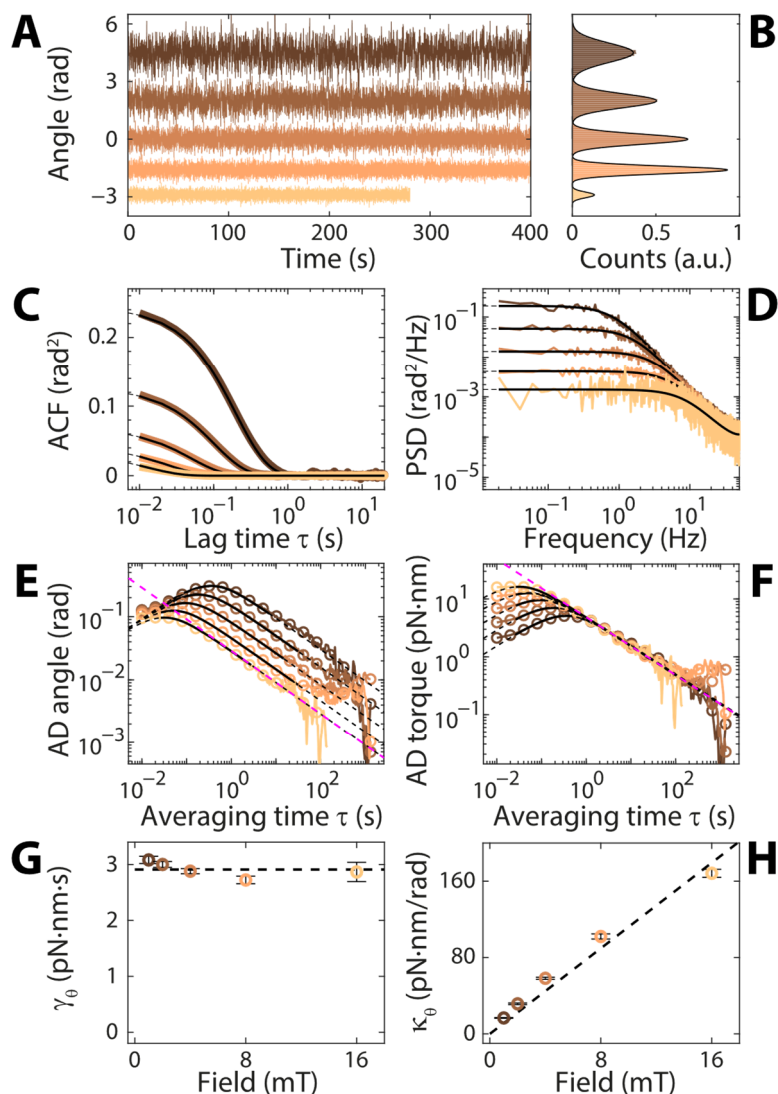


Figure S5.3. Additional analysis of the eMTT data for 0.7 μm diameter beads. Data and color-coding (increasing magnetic field strengths of 1, 2, 4, 8, and 16 mT, going from dark brown to light brown) as in Fig. 5.3 of the main text. **A)** Zoom-in on the first 400 s (at 16 mT, 280 s) of the angle traces of ~ 2600 s each sampled at 100 Hz (corresponding to 2.6×10^5 data points). The traces are offset vertically for clarity. **B)** Histograms over the full traces. The solid black lines are Gaussian fits to the histograms. **C)** Autocorrelation function analysis. The solid black lines are fits to the data, and their extrapolations are shown as dashed black lines. **D)** Power spectrum analysis. **E)** Angle Allan deviation (AD). Colored lines (circles) reflect the normal AD (octave-sampled overlapping AD). Same data as in Fig. 5.3B. The dashed magenta line indicates the thermal limit for the stiffest trap. The fitted parameters are displayed in G,H. **F)** Torque AD. Same data as in Fig. 5.3C. The dashed magenta line corresponds to the thermal limit. **G)** Rotational drag coefficient γ_θ obtained from the AD fits in E) versus magnetic field strength. The dashed black line is a constant-value fit to the data. Same data as in Fig. 5.3D. The data points and their corresponding error bars denote the average and standard deviation, respectively, from $N = 5$ independent measurements. **H)** Rotational trap stiffness κ_θ obtained from the AD fits in E) versus magnetic field strength. The solid black line is a linear fit to the data. Same data as in Fig. 5.3E.

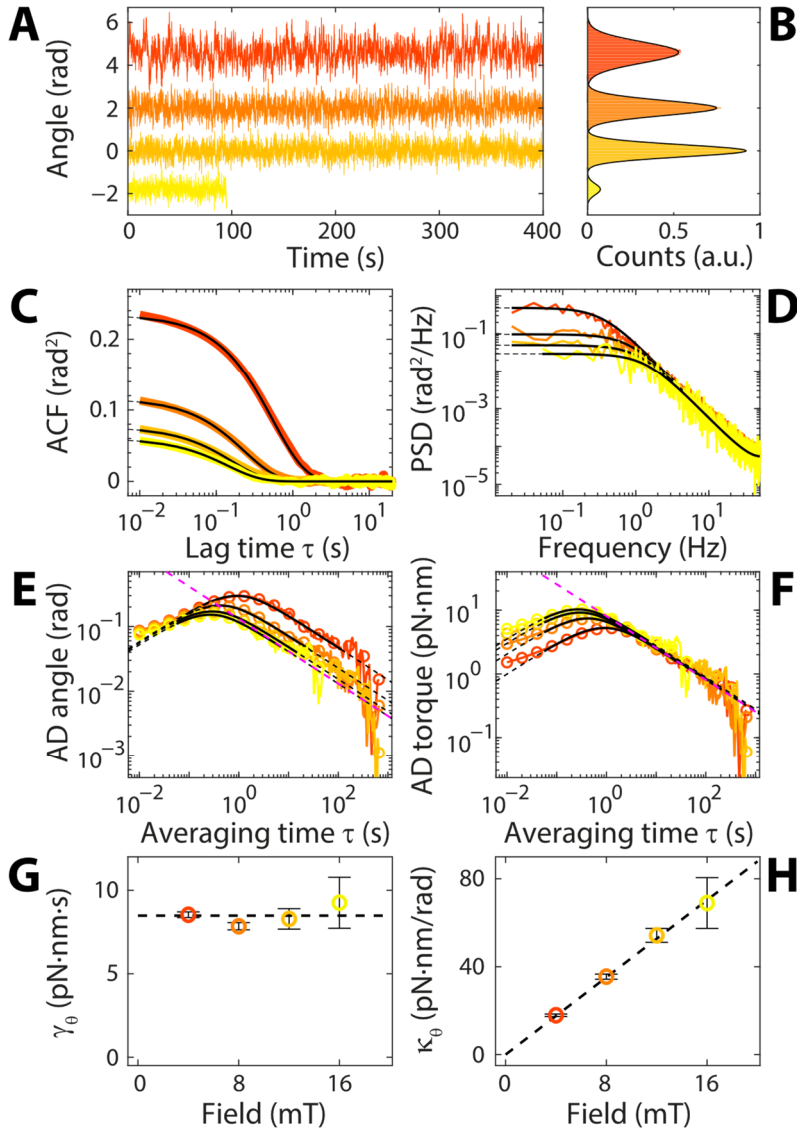


Figure S5.4. MyOne (1.05 μm diameter) beads trapped at different field strengths using eMTT. The color-coding indicates increasing magnetic field strength (4, 8, 12, and 16 mT, going from red to yellow). **A)** Zoom-in on the first 400 s (at 16 mT, 95 s) of the angle traces of ~ 1300 s each sampled at 100 Hz (corresponding to 1.3×10^5 data points). The traces are offset vertically for clarity. **B)** Histograms over the full traces. The solid black lines are Gaussian fits to the histograms. **C)** Autocorrelation function analysis. The solid black lines are fits to the data, and their extrapolations are shown as dashed black lines. **D)** Power spectrum analysis. **E)** Angle Allan deviation (AD). Colored lines (circles) reflect the normal AD (octave-sampled overlapping AD). The dashed magenta line indicates the thermal limit for the stiffest trap. The fitted parameters are displayed in **G,H**. **F)** Torque AD. The dashed magenta line corresponds to the thermal limit. **G)** Rotational drag coefficient γ_θ obtained from the AD fits in **E** versus magnetic field strength. The dashed black line is a constant-value fit to the data. The data points and their corresponding error bars denote the average and standard deviation, respectively, from $N = 5$ independent measurements. **H)** Rotational trap stiffness κ_θ obtained from the AD fits in **E** versus magnetic field strength. The dashed black line is a linear fit to the data.

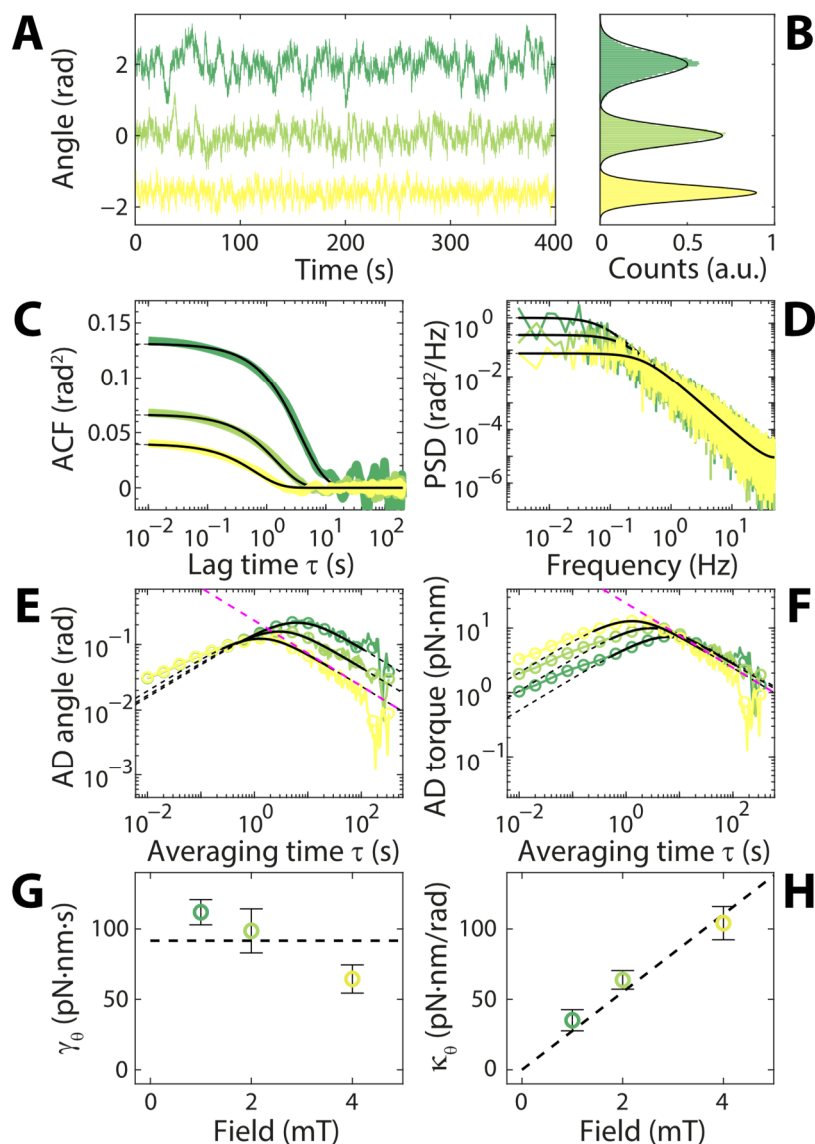


Figure S5.5. M270 (2.8 μm diameter) beads trapped at different field strengths using eMTT. The color-coding indicates increasing magnetic field strength (1, 2, and 4 mT, going from green to light yellow). **A)** Zoom-in on the first 400 s of the angle traces of ~ 650 s each sampled at 100 Hz (corresponding to 6.5×10^4 data points). The traces are offset vertically for clarity. **B)** Histograms over the full traces. The solid black lines are Gaussian fits to the histograms. **C)** Autocorrelation function analysis. The solid black lines are fits to the data, and their extrapolations are shown as dashed black lines. **D)** Power spectrum analysis. **E)** Angle Allan deviation (AD). Colored lines (circles) reflect the normal AD (octave-sampled overlapping AD). The dashed magenta line indicates the thermal limit for the stiffest trap. The fitted parameters are displayed in **G,H**. **F)** Torque AD. The dashed magenta line corresponds to the thermal limit. **G)** Rotational drag coefficient γ_θ obtained from the AD fits in **E)** versus magnetic field strength. The dashed black line is a constant-value fit to the data. The data points and their corresponding error bars denote the average and standard deviation, respectively, from $N = 3$ independent measurements. **H)** Rotational trap stiffness κ_θ obtained from the AD fits in **E)** versus magnetic field strength. The dashed black line is a linear fit to the data.

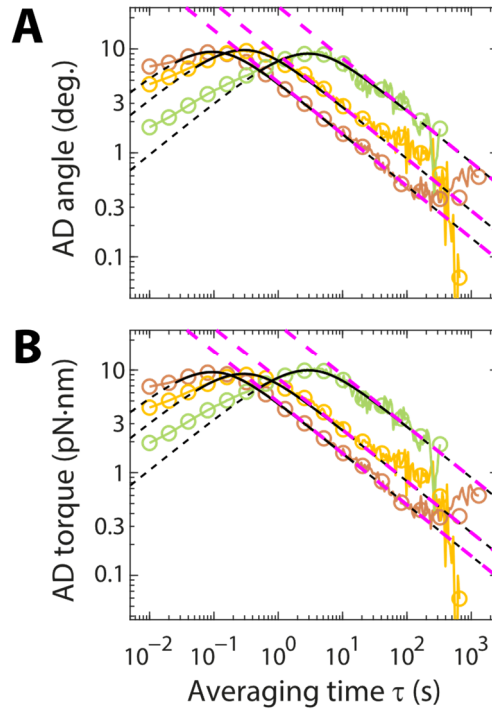


Figure S5.6. Angle and torque Allan deviation for different bead sizes in the eMTT. The traces were selected from **Supplementary Figs. S5.3-S5.5** in order to obtain similar trap stiffnesses (~ 60 pN·nm/rad). We record the fluctuations of a MagSense bead ($d = 0.7 \mu\text{m}$) at 4 mT (brown, $\kappa_\theta = 58$ pN·nm/rad), a MyOne bead ($d = 1.05 \mu\text{m}$) at 12 mT (orange, $\kappa_\theta = 54$ pN·nm/rad), and a M270 bead ($d = 2.8 \mu\text{m}$) at 2 mT (light green, $\kappa_\theta = 64$ pN·nm/rad). **A)** Angle Allan deviation. **B)** Torque Allan deviation. The solid black lines are fits to the data, and their extrapolations are shown as dashed black lines in **A,B**). The dashed magenta lines indicate the thermal limits.

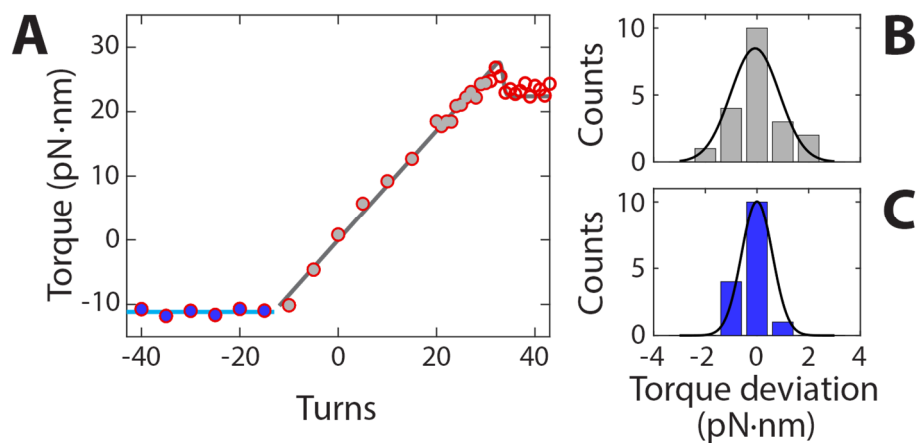


Figure S5.7. High-precision torque measurements in the eMTT and estimates of torque precision. A) Torque versus applied turns measurement for a 7.9 kbp DNA molecules in high-salt buffer (TE buffer with 550 mM NaCl) using 1.05 μm diameter MyOne beads at a stretching force of 3.5 pN, with an angular trap stiffness of ~ 50 pN·nm/rad). Data are taken from Figure 5d of Ref. 17. The experimental torque measurements are shown as red circles. Each data point corresponds to a measurement of 200 s. The solid dark gray line is a fit of a model of DNA elasticity (17). Data points in the elastic response regime of DNA (denoted in gray) are characterized by a linear torque versus turns dependence. At a negative torque of ~ -11 pN·nm, DNA undergoes torque-induced melting (blue data points). **B)** Deviation of the experimental data in the linear response regime from the best linear fit (gray data points fitted by solid dark gray line in **A**). The solid black line shows a Gaussian fit to the data, yielding a standard deviation of 0.9 pN·nm. **C)** Deviations of the experimental data in the torque-induced DNA melting regime from the best fit constant (blue data points fitted by solid light blue line in **A**). The solid black line shows a Gaussian fit with a standard deviation of 0.6 pN·nm.

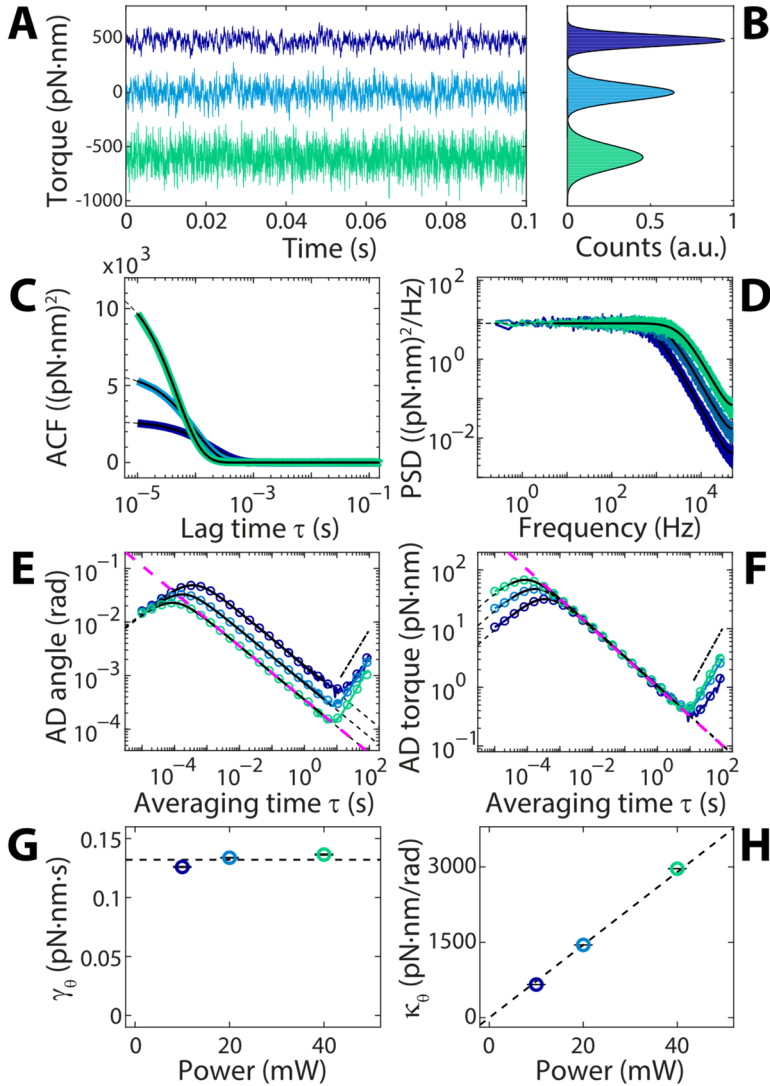


Figure S5.8. Additional analysis of the OTW data in Fig. 5.4 of the main text. The color-coding is the same as in the main text (10, 20, and 40 mW, going from dark blue to light green). **A)** Zoom-in on the first 0.1 s of the torque traces of 200 s each sampled at 100 kHz (corresponding to 2.0×10^7 data points). The traces are offset vertically for clarity. **B)** Histograms over the full traces. The solid black lines are Gaussian fits to the histograms. **C)** Autocorrelation function analysis. The solid black lines are fits to the data, and their extrapolations are shown as dashed black lines. **D)** Power spectrum analysis. **E)** Angle Allan deviation (AD). Colored lines (circles) reflect the normal AD (octave-sampled overlapping AD). Same data as in Fig. 5.4B. The dashed magenta line indicates the thermal limit for the stiffest trap. **F)** Torque AD. Same data as in Fig. 5.4C. The dashed magenta line corresponds to the thermal limit. The dash-dotted black line has slope +1, corresponding to linear drift. The fitted parameters are displayed in **G,H**. **G)** Rotational drag coefficient γ_θ obtained from the torque AD fits in **F)** versus laser power. The dashed black line is a constant-value fit to the data. Same data as in Fig. 5.4D. The data points and their corresponding error bars denote the average and standard deviation, respectively, from $N = 5$ independent measurements. **H)** Rotational trap stiffness κ_θ obtained from the AD fits in **F)** versus laser power. The dashed black line is a linear fit to the data. Same data as in Fig. 5.4E.

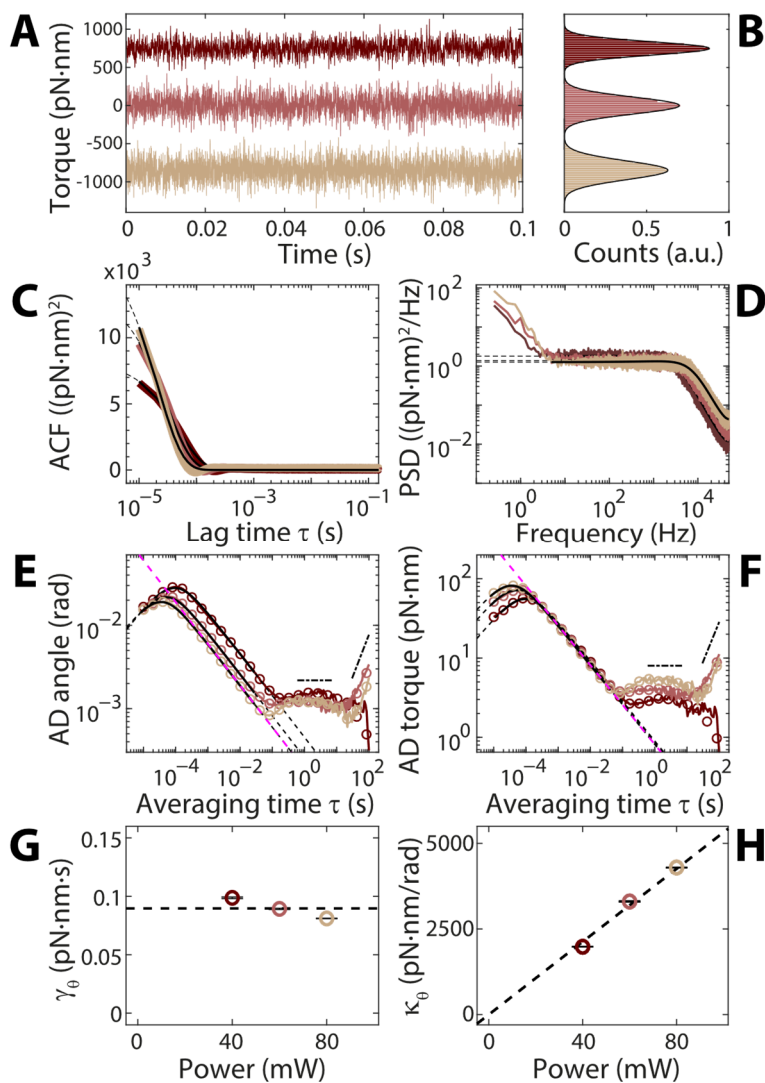


Figure S5.9. OTW data acquired under less favourable environmental conditions. The color-coding is as follows: 40, 60, and 80 mW, going from dark red-brown to light brown. **A)** Zoom-in on the first 0.1 s of the torque traces of 200 s each sampled at 100 kHz (corresponding to 2.0×10^7 data points). The traces are offset vertically for clarity. **B)** Histograms over the full traces. The solid black lines are Gaussian fits to the histograms. **C)** Autocorrelation function analysis. The solid black lines are fits to the data, and their extrapolations are shown as dashed black lines. **D)** Power spectrum analysis. **E)** Angle Allan deviation (AD). Colored lines (circles) reflect the normal AD (octave-sampled overlapping AD). The dashed magenta line indicates the thermal limit for the stiffest trap. **F)** Torque AD. The dashed magenta line corresponds to the thermal limit. Note the additional noise component (in contrast to **Fig. 5.4B,C** and **Supplementary Fig. S5.8E,F**) in the range 0.1–20 s, which we attribute to excess air currents present in the setup at the time of acquisition. The dash-dotted black lines have slope +1 or 0, corresponding to linear drift or $1/f$ noise, respectively. The fitted parameters are displayed in **G,H**. **G)** Rotational drag coefficient γ_θ obtained from the torque AD fits in **F)** versus laser power. The dashed black line is a constant-value fit to the data. The data points and their corresponding error bars denote the average and standard deviation, respectively, from $N = 5$ independent measurements. **H)** Rotational trap stiffness κ_θ obtained from the AD fits in **F)** versus laser power. The dashed black line is a linear fit to the data.

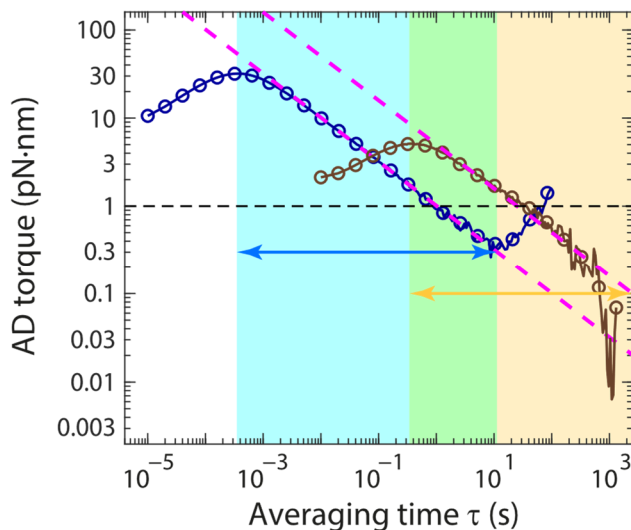


Figure S5.10. Comparison of the best achievable torque Allan deviation in the eMTT and OTW. The traces were selected from Figs. 5.3C, 5.4C to compare the best achievable torque precisions. We record the fluctuations of a MagSense bead ($d = 0.7 \mu\text{m}$) at 1 mT (dark brown) in eMTT, and a TiO_2 cylinder at 10 mW in OTW (dark blue). Colored lines (circles) reflect the normal AD (octave-sampled overlapping AD). The dashed magenta lines indicate the thermal limits. The color shading and the corresponding double-sided arrows indicate the averaging times (ranging from the timescale at which the Allan deviation peaks to that at which unwanted noise starts to dominate) over which the eMTT (light yellow) and the OTW (light blue) permit meaningful torque measurement. The range of averaging times in which the instruments' torque precision overlaps is shown in light green. The dashed black line corresponds to a torque precision of 1 pN·nm.

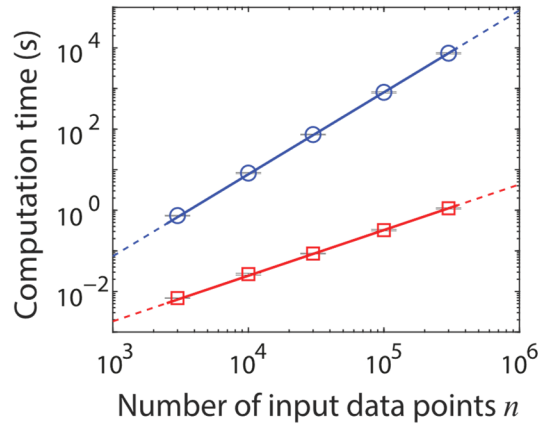


Figure S5.11. Comparison of efficiency in overlapping Allan variance computation. The overlapping Allan variance computation times as a function of the number of input data points n . The blue circles and red squares reflect the use of all available integration times ($m\tau_s$; $m = \text{integer}$) and octave-sampled integration times ($m\tau_s$; $m = 2^{\text{integer}}$), respectively. The solid colored lines are power-law fits to the data, $\text{computation time} \propto n^\alpha$ ($\alpha = 2.0$ and 1.1 for blue circles and red rectangles, respectively), with their extrapolations shown as dashed colored lines. The data points and their corresponding error bars denote the average and standard deviation, respectively, for $N = 3$ computations.

5.6.9. Supplementary References

1. Czerwinski, F., Richardson, A. C. & Oddershede, L. B. Quantifying noise in optical tweezers by Allan variance. *Optics Express* **17**, 13255-13269 (2009).
2. Mahamdeh, M. & Schäffer, E. Optical tweezers with millikelvin precision of temperature-controlled objectives and base-pair resolution. *Optics Express* **17**, 17190-17199 (2009).
3. Andersson, M., Czerwinski, F. & Oddershede, L. B. Optimizing active and passive calibration of optical tweezers. *Journal of Optics* **13**, 044020 (2011).
4. Perkins, T. T. Ångström-precision optical traps and applications. *Annual Review of Biophysics* **43**, 279-302 (2014).
5. Howe, D. A., Allan, D. U. & Barnes, J. A. Properties of signal sources and measurement methods. *In Proceedings of the 35th Annual Symposium on Frequency Control (IEEE)*, A1-A47 (1981).
6. Lansdorp, B. M. & Saleh, O. A. Power spectrum and Allan variance methods for calibrating single-molecule video-tracking instruments. *Review of Scientific Instruments* **83**, 025115 (2012).
7. Allan, D. W., Weiss, M. A. & Jespersen, J. L. A frequency-domain view of time-domain characterization of clocks and time and frequency distribution systems. *In Proceedings of the 45th Annual Symposium on Frequency Control (IEEE)*, 667-678 (1991).
8. van Oene, M. M. et al. Biological Magnetometry: Torque on superparamagnetic beads in magnetic fields. *Physical Review Letters* **114**, 218301 (2015).
9. Volpe, G. & Volpe, G. Simulation of a Brownian particle in an optical trap. *American Journal of Physics* **81**, 224-230 (2013).
10. Rutman, J. Characterization of phase and frequency instabilities in precision frequency sources: Fifteen years of progress. *Proceedings of the IEEE* **66**, 1048-1075 (1978).
11. Wong, W. P. & Halvorsen, K. The effect of integration time on fluctuation measurements: calibrating an optical trap in the presence of motion blur. *Optics Express* **14**, 12517-12531 (2006).
12. Lebel, P., Basu, A., Oberstrass, F. C., Tretter, E. M. & Bryant, Z. Gold rotor bead tracking for high-speed measurements of DNA twist, torque and extension. *Nature Methods* **11**, 456 (2014).
13. Yasuda, R., Miyata, H. & Kinoshita, K. Direct measurement of the torsional rigidity of single actin filaments. *Journal of Molecular Biology* **263**, 227-236 (1996).
14. Neuman, K. C. & Nagy, A. Single-molecule force spectroscopy: optical tweezers, magnetic tweezers and atomic force microscopy. *Nature Methods* **5**, 491 (2008).
15. Lipfert, J., Wiggin, M., Kerssemakers, J. W. J., Pedaci, F. & Dekker, N. H. Freely orbiting magnetic tweezers to directly monitor changes in the twist of nucleic acids. *Nature Communications* **2**, 439 (2011).
16. Lipfert, J., Wiggin, M., Kerssemakers, J. W. J., Pedaci, F. & Dekker, N. H. Corrigendum: Freely orbiting magnetic tweezers to directly monitor changes in the twist of nucleic acids. *Nature Communications* **6**, 7192 (2015).
17. Janssen, X. J. A., Lipfert, J., Jager, T., Daudey, R., Beekman, J. & Dekker, N. H. Electromagnetic torque tweezers: a versatile approach for measurement of single-molecule twist and torque. *Nano Letters* **12**, 3634-3639 (2012).

6

Stretched and Oriented DNA Arrays Embedded in Microfluidic Device for Multiplexing Protein-DNA Investigation

The stretched and oriented DNA arrays (SODA) is a platform for the characterization of protein-DNA interactions at the single-molecule level. Stretched single DNA molecules, arranged in a dense array by specifically binding to thin gold nanostructures fabricated onto a glass coverslip, enable simultaneous observation of protein-DNA interaction dynamics from hundreds of DNA strands using total internal reflection fluorescence microscopy. Providing high-throughput measurements and straightforward visualization of fluorescently labeled proteins and DNA molecules, SODA is a promising tool for addressing multiple types of questions in molecular biology. Such questions include the dynamics of DNA binding proteins, mechanisms of target DNA sequence searching, processivity of enzymes in a crowded environment, and many more. We present our development of prototype SODA microfluidic devices, focusing on the aspects of fabrication and surface functionalization. Moreover, its potential for biophysics research is demonstrated by observing the behavior of DNA-binding proteins.

The work presented in this chapter is a collaboration among the following authors: **Seungkyu Ha**, Eugen Ostrofet, Richard Janissen, Humberto Sanchez, Bojk Berghuis, Theo van Laar, Andrea Martorana, Jacob W. J. Kerssemakers, Belen Solano, Claire Wyman, and Nynke H. Dekker.

6.1. Introduction

Single-molecule approaches in biophysics allow observation and quantification of the heterogeneity of biomolecular behavior, without obscuring it by ensemble averaging in conventional bulk experiments ^{1, 2}. The advancements of single-molecule instrumentation have continuously contributed to a better characterization of biological processes ³⁻¹⁰. Particularly, they have brought a large impact on understanding the interactions between nucleic acids and genome processing machines, such as polymerases ^{11, 12}, helicases ^{13, 14}, and ribosomes ^{15, 16}. One of the key enabling factors for these findings has been the pursuit of higher spatiotemporal resolution in single-molecule techniques, which either probe the mechanical properties of, or directly image, biological molecules, complexes, or cells. The former aspect includes force spectroscopy (optical tweezers, magnetic tweezers, and atomic force microscopy) ^{3, 7} and torque spectroscopy (optical torque wrench and (electro)magnetic torque tweezers) ^{8, 9}, while the latter aspect includes conventional (fluorescence) microscopy ¹⁷, fluorescence resonance energy transfer (FRET) ¹⁸, super-resolution microscopy ¹⁹, and cryo-electron microscopy ²⁰.

However, developments of more specialized tools remain desirable, particularly for the investigations of genome processing proteins, which exhibit highly complex and heterogeneous behavior depending on the sequence of nucleic acids under interaction, presence of roadblocks, or physiological buffer conditions. The requirements for such further developments include: i) possibility to simultaneously measure a large number of protein-DNA complexes in a multiplexed manner, to obtain statistically relevant datasets; ii) ability to directly determine the locations of proteins and nucleic acids under interaction in real time, to enable straightforward and unbiased acquisition of information on their dynamics.

Considering the first requirement, the multiplexing capability is inherent for the most of imaging-based single-molecule techniques, but not for the force/torque-based ones. For single-molecule instrumentation with force/torque controllability, conventional techniques such as optical tweezers and atomic force microscopy are still largely limited in their multiplexing capability (only 1–10 biomolecules are simultaneously trackable), although these techniques possess a capacity to precisely assess minuscule force and torque on biomolecules. On the other hand, multiplexing capability is pioneered by magnetic tweezers ²¹⁻²⁴ and magnetic torque tweezers ²⁵. In addition to these magnetism-based approaches, other multiplexing single-molecule force spectroscopy techniques that rely on different physical mechanisms have been developed recently. For example, acoustic standing waves and centrifugal forces are utilized in acoustic force spectroscopy ^{26, 27} and centrifugal force microscopy ^{28, 29}, respectively.

However, the abovementioned high-throughput single-molecule techniques based on force and torque indirectly probe the protein-nucleic acid interactions, in

principle by processing camera-acquired images of biomolecule-tethered microspheres. Therefore, in general, they do not directly visualize proteins and nucleic acid molecules in motion, which is the abovementioned second requirement. Meanwhile, the capability of visualization in real time is straightforwardly implementable in imaging-based techniques, specifically fluorescence microscopy¹⁷. Moreover, the fluorescence microscopy-based techniques can exploit the well-developed library of fluorescent tags for biomolecules³⁰. The use of diverse fluorescent tags renders different biomolecules directly distinguishable on fluorescence microscopy imaging, and have proven their ability to investigate diverse biological processes, e.g., mechanics of nucleic acid molecules^{31, 32}, assembly dynamics and functions of multi-protein complexes^{13, 33}, and DNA sequence-specific enzymatic activities^{34, 35}. Although such direct visualization is also possible with hi-speed atomic force microscopy³⁶, its observation is largely limited to only small areas and it lacks the specificity equivalent to the use of fluorescent tags.

A single-molecule technique designated as DNA nanocurtains³⁷⁻⁴⁰ most elegantly combines both capabilities of multiplexing and real-time fluorescence imaging, without the necessity of highly specific and complicated instrumentation. It utilizes supported lipid bilayer (SLB) coated on a glass coverslip for surface passivation and DNA anchorage. The diffusive nature of lipids within an SLB is utilized to position the DNA molecules, by attaching them to lipids and then using weak buffer flow to push them to a nanofabricated barrier array present on the coverslip. The anchored DNA molecules can be flow-stretched by strong buffer flow and brought to the vicinity of the coverslip surface, permitting observation with total internal reflection fluorescence (TIRF) microscopy at a high signal-to-noise ratio. In this way, the interaction of fluorophore-labeled proteins with DNA strands can be tracked in real time. The use of nanofabricated barriers allows to form a dense, regular array of DNA strands, with controlled spacings between them. Therefore, DNA nanocurtains offer substantial advantages in the aspects of multiplexing and data analysis when compared to other similar techniques employing random surface attachment of DNA⁴¹ or DNA-coupled microspheres¹¹ on a coverslip surface.

In spite of the fact that the DNA nanocurtains do not directly report on force and/or torque on biomolecules, their high-throughput direct visualization functionality has been successfully employed to address diverse important questions in the field of genome processing. Such examples include mechanisms of homologous recombination⁴², protein interaction with DNA-bound roadblocks⁴³, DNA target search by proteins^{35, 44}, chromosome organization⁴⁵, and nucleosome deposition on DNA⁴⁶.

We report our preliminary results on the development of a DNA nanocurtain platform for which we designate with a more descriptive term, i.e., stretched and oriented DNA arrays (SODA). The goal of this development is to set up a more advanced DNA nanocurtain platform that is optimized for single-molecule studies of highly complicated protein-DNA complexes, e.g., eukaryotic replisome^{13, 33} in crowded environments. Taking into account this specific aim, the prototype design of our SODA

device is inspired by the parallel array of double-tethered isolated (PARDI) curtains³⁹. Among variety of existing DNA nanocurtain configurations³⁹, PARDI allows placement of non-overlapping single DNA molecules with predetermined lateral distances between them. Therefore, the dynamics of proteins bound on a single DNA strand is not biased by the interactions with other DNA strands at close proximity⁴⁴. Additionally, we design our microfluidic channels to maximize the use of a coverslip area and minimize the required volume of biomaterials. Here, we mainly describe our design, fabrication, and surface functionalization of SODA devices. Notably, we introduce a modified SODA device that can be combined with magnetic tweezers. In addition, we demonstrate the utilization of our SODA platform by observing interactions between DNA strands and Rad51 proteins that have been widely investigated due to their capability of nucleoprotein filament formation and importance in DNA repair mechanism^{42, 47-52}.

6.2. Results and discussion

6.2.1. Fabrication of nanoscale gold barrier and anchor array on glass coverslip

Single DNA molecules (either single-stranded or double-stranded) can be specifically immobilized in a SODA device to thin (~30 nm-thick) gold nanostructures fabricated on standard microscope glass coverslips (~170 μm -thick). As the feature size of such gold structures is at the submicron scale (with the aim to support only single DNA strands at precisely defined positions), electron-beam (e-beam) lithography is utilized for their fabrication (**Fig. 6.1a**). In a SODA device, each DNA molecule can be immobilized by either one^{53, 54} or both^{44, 55} of its extremities, and these singly-tethered and doubly-tethered configurations exhibit their own particular advantages³⁹.

In common for both DNA-tethering configurations, one extremity of each DNA molecule is bound to one of the lipid molecules that consist the SLB on a coverslip *via* streptavidin-biotin coupling, thereby permitting two-dimensional diffusion of DNA molecules on the coverslip surface. Upon application of weak directional flow of buffer, DNA molecules move along the flow direction by hydrodynamic drag force until such movement is blocked by the physical confinement from the gold barriers (**Fig. 6.1b**, left side). The V-shape of the barriers is intended to precisely guide DNA molecules to its apex⁵⁴, while the barrier size can be optimized to host only one DNA molecule per barrier (the results of such optimization can be found in section 6.2.4.). In the case of singly-tethered DNA molecules, stretching of DNA can be achieved by continuously maintaining a buffer flow which is fast enough to apply a sufficiently high hydrodynamic drag force for such stretching. This singly-tethered configuration offers the following experimental advantages: i) it provides a convenient means to validate the proper, specific binding of both proteins and DNA strands by pausing and flowing

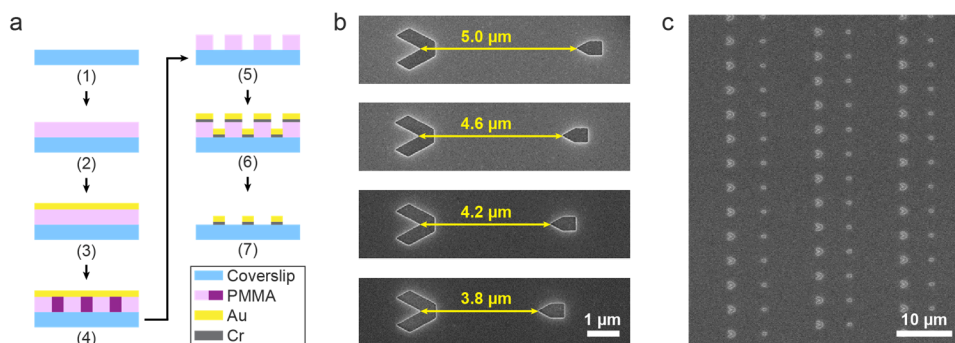


Figure 6.1. Fabrication of nanoscale gold barrier and anchor arrays on glass coverslip. (a) Fabrication steps: (1) cleaning glass coverslip; (2) spin-coating positive e-beam resist (PMMA); (3) sputtering thin gold (Au) layer for discharging; (4) e-beam patterning (unexposed and exposed PMMA regions are designated by pink and violet, respectively); (5) removal of Au layer and development of exposed PMMA (only the exposed parts are dissolved in developer solution); (6) e-beam evaporation-based deposition of chromium (Cr) adhesion layer followed by Au layer; (7) desired Au nanostructures remain after lift-off of resist layer. (b) The distance between Au barrier (alphabet V-shape at left) and anchor (pentagon-shape at right) is controlled to vary the tension applied on doubly-tethered DNA molecules. (c) Large array of Au barrier-anchor pairs. SEM images in panels (b,c) are taken at step (6) of panel (a).

the buffer ³⁹, ii) the dynamic control of DNA tension is possible through the adjustment of buffer flow speed.

To achieve the doubly-tethered configuration, the other extremity at downstream side of each flow-stretched DNA is bound to a pentagon-shaped gold anchor (**Fig. 6.1b**, right side) using specific chemical interactions, e.g., antigen-antibody binding of digoxigenin and digoxigenin antibodies ⁵³ (details of this procedure can be found in section **6.2.3.**). The pentagonal shape features a sharp edge that points to upstream to prevent unnecessary accumulation of biomolecules upon buffer flow ⁵⁵. Properly doubly-tethered DNA molecules can remain stretched without buffer flow. This implies several experimental advantages for studying protein-DNA interactions: i) the precision of spatial measurement can be enhanced as no additional fluctuations are introduced by buffer flow ⁴⁷, ii) the backward and forward movements of protein diffusing along DNA will not be biased by the unidirectional buffer flow ⁵⁶, iii) the consumed volume of biomaterials can be significantly reduced for each experiment, and iv) although the tension applied on each DNA molecule cannot be adjusted in real time, it can be still controlled in a static manner by a combination of barrier distance (**Fig. 6.1b**) and flow rate. For example, assuming 16 kbp double-stranded DNA (~5.4 μm contour length) with persistence length of ~50 nm, the DNA extensions of 3.8 μm, 4.2 μm, 4.6 μm, and 5.0 μm correspond to ~0.2 pN, ~0.4 pN, ~0.9 pN, and ~3.1 pN, respectively (according to the worm-like chain model ⁵⁷). Overall, our optimized nanofabrication protocol for producing gold nanostructures is highly reproducible (**Supplementary Fig. S6.1, S6.2**) and allows generating a large regular array of such structures reliably on a desired region of a coverslip (**Fig. 6.1c**).

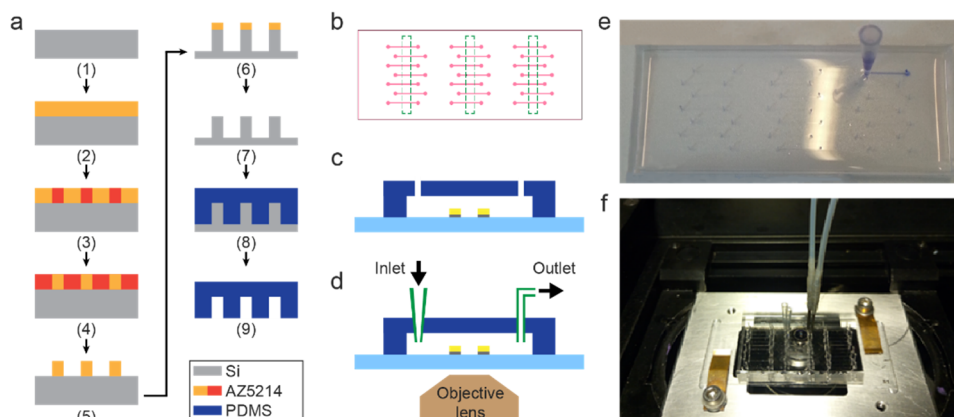


Figure 6.2. Fabrication of PDMS-based microfluidic device. (a) Fabrication steps for PDMS microfluidic channels: (1) cleaning Si substrate (gray) and coating adhesion promoter; (2) deposition of AZ5214 photoresist (light orange, insoluble in developer solution); (3) photoresist exposure by direct laser writing (dark orange, soluble in developer solution); (4) image reversal by post-exposure bake and flood exposure; (5) development of photoresist; (6) deep etching by Bosch process; (7) removal of remaining photoresist by O₂ plasma cleaning; (8) PDMS pouring, degassing, and curing on the prepared Si mold; (9) detachment of cured PDMS block from Si mold. (b) Microfluidic channel design (pink) used for laser writing in step (3) of panel (a). The region containing Au nanostructures is overlaid (dashed green squares). (c) The fabricated PDMS block (panel (a)) is punched at inlet/outlet positions, and then assembled with the coverslip with Au nanostructures, after corona discharge treatment of both PDMS block and coverslip (Fig. 6.1a). The color coding of the materials is the same as Fig. 6.1a and Fig. 6.2a. (d) The inlet/outlet tubes are connected to the punched holes and then the assembled device is loaded onto a TIRF microscope. (e) An assembled device imaged before loading onto a microscope. Tight assembly is demonstrated by flowing a solution containing blue pigment into a fluidic channel at top-right corner of a device. (f) A device loaded onto a TIRF microscope by two clamping springs, with plastic pipette tips as inlet (at left side) and steel needles connected to plastic tubes as outlet (at right side). The outlet tubes are connected to syringe pumps for controlled buffer flow speed.

6.2.2. Fabrication of PDMS-based microfluidic device

To carry out bioassay experiments, microfluidic devices offer convenient means for maintaining physiological environment with convenient buffer exchange. In our microfluidic channel design, a glass coverslip with gold nanostructures (Fig. 6.1) forms the bottom surface, while top and side surfaces are provided by a micro-patterned poly(dimethylsiloxane) (PDMS) block (Fig. 6.2). The use of a PDMS block offers a reliable route to replicate custom-designed, disposable microfluidic channels⁵⁸. Also, due to the high elasticity of PDMS and the ease of producing thick layers (~5 mm-thick in our device), it is straightforward to connect inlet and outlet tubing with tight sealing for the supply of physiological buffers and biomolecules. A proven route for reliable PDMS block fabrication is to replicate PDMS blocks by using a silicon (Si) mold⁵⁹.

The Si mold functions as a template for casting PDMS microfluidic channels, and it is fabricated by well-established microfabrication techniques involving lithography and etching. This methodology allows channel widths ranging from a few microns to a few hundred microns, while the channel lengths span from millimeters to centimeters. Therefore, unlike the submicron gold nanostructure patterns that require

e-beam lithography, photolithography with $\sim 1\ \mu\text{m}$ resolution is sufficient to fabricate the Si molds for microfluidic channels and also more practical with respect to the time required for a large-area patterning of photoresist (4-inch Si wafer). To allow for more flexibility in the channel design and implementation speed, we utilize direct laser writing (DLW) for Si mold fabrication (**Fig. 6.2a**). Compared to the conventional photolithography based on chromium-patterned photomasks (which are expensive and time-consuming to prepare), the use of the DLW maskless photolithography technique allows us to rapidly modify the dimensions of microfluidic channels on demand. Hence, DLW is suitable for rapid prototyping in research environments, as is the e-beam lithography utilized for gold nanostructure patterning.

To obtain our designed microfluidic channel heights of $\sim 40\ \mu\text{m}$, deep and straight etching is required for Si molds. For such deep etching, conventional dry or wet etching techniques are not suitable due to the difficulty to obtain the necessary straight sidewall profiles for the microfluidic channel mold. Hence, we employed the Bosch deep reactive ion etching process, which is a specialized dry etching technique that allows to obtain deep and straight sidewalls⁵⁹. By optimizing the etching conditions, we could reproducibly obtain the desired channel heights of $\sim 40\ \mu\text{m}$. Together with the channel width of $200\ \mu\text{m}$, channel length of 8 mm, and circular inlet/outlet ports with diameters of 1 mm each, only a minute volume of buffer ($\sim 1\ \mu\text{L}$) is required to entirely fill each microfluidic channel.

To permit the testing of many different experimental conditions within a single device, we design the Si molds to contain multiple microfluidic channels within the available area of a coverslip (**Fig. 6.2b**) (depending on the channel dimensions, we include 20–50 channels per coverslip within an area of $24\ \text{mm} \times 60\ \text{mm}$). The positions of the laser-written channels are designed to align with the e-beam-written gold nanostructures upon flow cell assembly. Therefore, the gold nanostructures are centered within the bottom area of each channel (i.e., the regions within green dashed squares in **Fig. 6.2b**).

After pouring and curing PDMS on the Si molds, the final PDMS block can be detached from the molds and cut into blocks of desired sizes. Then, immediately after corona discharge treatment, both the coverslip with nanofabricated gold nanostructures and the PDMS block with microfabricated channels are firmly assembled together to complete the microfluidic device (**Fig. 6.2c**). The prior surface treatment with corona discharge is necessary to enhance the bonding strength between the PDMS block and coverslip⁶⁰, as channels should remain tightly sealed regardless of the pressure required for buffer flow (**Fig. 6.2d**). Sufficiently tight sealing is reproducibly achieved in the assembled devices, as exemplified by flowing a blue-colored solution through the microchannel shown in **Fig. 6.2e**. The photo in **Fig. 6.2f** shows an actual device loaded onto a TIRF microscope, similar to the schematic in **Fig. 6.2d**.

We also developed a magnetic tweezers-compatible (MTC)-SODA device (**Supplementary Fig. S6.3**), aiming for utilization in hybrid setups in which TIRF

microscopy is combined with magnetic tweezers^{31, 61, 62}. Such hybrid setups are of interest for single-molecule studies as they allow integration of the functionalities of DNA nanocurtains with those of the magnetic tweezers, which can apply controlled force without relying on buffer flow. In MTC-SODA devices, the central area of the PDMS block is recessed to a thickness between 100 μm and 200 μm , comparable to the typical thickness of spacer layers in fluidic chambers utilized in magnetic tweezers. The surrounding part of the PDMS block, however, is maintained at a thickness of ~ 5 mm to properly support inlet/outlet tubing. Thus, the MTC-SODA device enables the physical approach of a magnet into the vicinity of microfluidic channels for the application of a sufficiently intense magnetic field gradient to manipulate magnetic particles conjugated to biomolecules within microfluidic channels.

This MTC-SODA configuration can furthermore permit both vertical and horizontal application of magnetic force on biomolecules⁶². Since the physical confinement of gold nanobarriers can trap DNA molecules with respect to the horizontal force only, it is required to employ a modified tethering protocol to allow for the application of a desired level of magnetic force in non-horizontal directions as well. We predict that DNA molecules can be firmly fixed to only the gold barriers through specific chemical interactions (i.e., using the same strategy for tethering to gold anchors), once after they are positioned at the barriers by the physical confinement. The magnetic tweezers-compatibility has been proven by proof-of-concept experiments in which single DNA molecules are tethered between magnetic microspheres and glass surface (using the tethering protocol in Ref. 63) and successfully stretched by magnetic pulling forces within MTC-SODA devices.

6.2.3. Chemical functionalization of glass coverslip and gold nanostructures

An assembled SODA device loaded on a TIRF microscope (**Fig. 6.2**) is ready for the following steps of surface functionalization and biological experiments (**Fig. 6.3a**). The key principle of DNA-positioning is to make DNA diffusive on the coverslip surface (as mentioned in section 6.2.1.), by forming an SLB on coverslip^{64, 65} and attaching the DNA molecules to lipids. The successful formation of an SLB on glass coverslip (SiO_2) surface was demonstrated by quartz crystal microbalance (QCM)^{64, 66, 67} measurement (**Fig. 6.3b**), in which the decrease of frequency indicates the increase in total mass adhered on the glass-coated sensor surface. The frequency decreases due to the adsorption of unilamellar lipid vesicles onto the glass surface until a critical concentration is reached at which lipid vesicles start to disintegrate and fuse together into a lipid bilayer. The release of liquid inside those vesicles increases frequency. The completion of an SLB can be detected from the saturated, nearly flat frequency signal. We also confirmed the formation of uniform SLB by using fluorophore-labeled lipid molecules subject to the fluorescence recovery after photobleaching (FRAP) technique⁶⁸. In the FRAP test, a small region of a labeled SLB is photobleached by a fast light pulse (the black spot visible

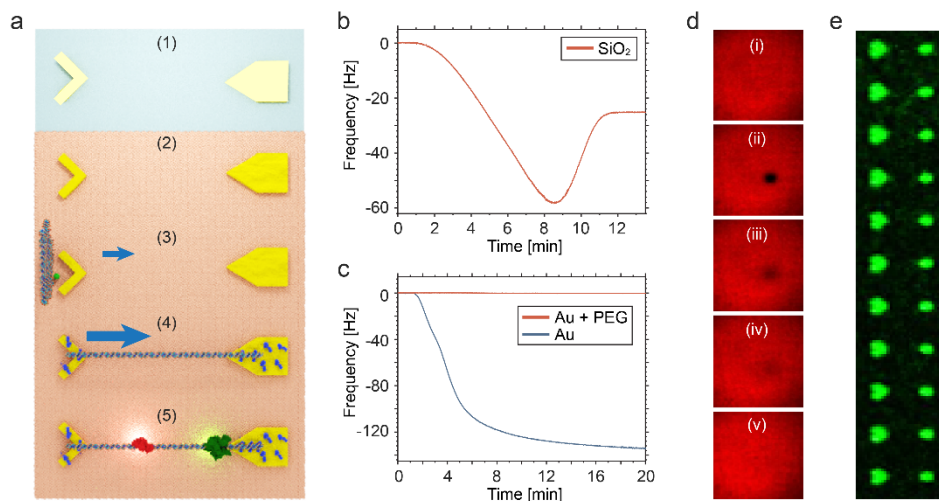


Figure 6.3. Surface functionalization of glass coverslip and gold nanostructures. (a) Schematic of the steps in functionalization employed: (1) Au nanostructure (light yellow) fabrication on glass coverslip (blue), as depicted in **Fig. 6.1a**; (2) coating of Au with PEG linker molecules containing a thiol (SH) functional group (dark yellow), and then coating of the coverslip (SiO_2) with SLB (brown); (3) positioning single DNA molecules at Au barriers by weak flow (short arrow) using the fact that DNA molecules are linked to lipid molecules and diffusive; (4) stretching DNA molecules by strong flow (long arrow), and to obtain doubly-tethered molecules, linking to Au anchors using antibodies (blue molecules) selectively bound on Au through the linker molecules attached in step (2); (5) loading of labeled proteins (red and green) onto DNA for inspection by TIRF microscopy. (b) Measured QCM curve demonstrating stable SLB formation on the coverslip (SiO_2), as depicted in step (2) of panel (a). (c) Measured QCM curves demonstrating that a PEGylated Au surface does not allow adhesion of lipid vesicles unlike the non-coated Au surface. Here, we perform a FRAP experiment with fluorescently labeled lipid molecules (red): (i) the coverslip surface is uniformly covered by SLB; (ii) a pulse of intense light irradiation creates the dark spot as a result of photobleaching; (iii-iv) the dark spot gradually disappears over time as non-bleached lipid molecules diffuse into the area; (v) the dark spot completely disappears and the image resembles that of frame (i). (e) Fluorescence microscopy image proving the selective functionalization of Au nanostructures with respect to glass. Only Au structures are visible as they are selectively coated by fluorescently labeled SH-PEG molecules. The bright spots at left are Au barriers while the bright spots at right are Au anchors.

at frame (ii) in **Fig. 6.3d**). The bleached lipids and non-bleached lipids are intermixed by two-dimensional diffusion within the SLB, and hence the bleached spot gradually disappears. Eventually, the fluorescence intensity becomes uniform again (frame (v) in **Fig. 6.3d**). This result clearly proves that the formed SLB is homogeneous and diffusive (**Fig. 6.3d**, **Supplementary Fig. S6.4**). Moreover, our SLB-coated surfaces substantially reduce the nonspecific binding of proteins^{39, 69} compared to non-coated bare glass coverslips (**Supplementary Fig. S6.5**). This is crucial in proper observation of protein-DNA interactions by excluding undesired aspecific surface adhesion of fluorophore-labeled proteins in the regions of interest.

By coating the gold nanostructures with a layer of biocompatible poly(ethylene glycol) (PEG) prior to SLB formation, we successfully prevent undesired liposome adsorption on the gold structures. This is demonstrated by our QCM-measurements on

differently treated gold-coated sensor surfaces. The PEGylated gold surface prevents the adhesion of lipid vesicles (as indicated by the nearly flat signal), while the bare gold surface is susceptible to lipid adhesion (**Fig. 6.3c**). We also observed that the thiolated PEG (SH-PEG) molecules are predominantly bound to the gold surface, demonstrating a high selectivity over glass surface (**Fig. 6.3e, Supplementary Fig. S6.6**). This allows for the formation of intact SLB on the glass surface, which shows FRAP results similar to those from SLB formed on coverslips without gold structures. Although gold nanostructures behave as an effective diffusion barrier even at the absence of a specific surface coating (e.g., PEGylation in our case)⁷⁰, the possibility to maintain gold surfaces free from lipids is desirable to increase the efficiency of DNA attachment to the gold nanostructures.

6.2.4. Optimization of gold nanobarrier size for loading of single DNA molecules

The ability to load one and only one individual DNA molecule per each gold nanobarrier is desirable to observe protein-DNA interaction under a controlled manner, excluding any undesirable interference with other DNA molecules in the vicinity. Also, non-overlapping DNA molecules facilitate a robust and automated image processing routine, crucial for high throughput data analysis of hundreds to thousands of molecules per experiment. To achieve these goals, we further optimized the geometry of the gold barriers. We fabricated the gold barriers with lengths (L) ranging from 200 nm and 600 nm, with 100 nm increments (**Fig. 6.4a**), in a SODA device. As aforementioned (section 6.2.1.), the use of singly-tethered DNA scheme provides the ability to distinguish whether DNA molecules are specifically anchored to gold barrier or aspecifically bound to fluidic channel surface. Hence, for a more precise counting of DNA molecules confined to each gold nanobarrier, we used the singly-tethered scheme in the process of optimizing the barrier size. In step (3) in **Fig. 6.3a**, we load fluorophore-labeled DNA molecules and anchor them to gold nanobarriers (**Fig. 6.3b**). Therefore, only DNA molecules are visible in fluorescence microscopy (**Fig. 6.4c**).

The local fluorescence intensity around each barrier (e.g., orange box in **Fig. 6.4c**) is in principle proportional to the number of DNA molecules confined per barrier⁵⁴. Based on this, we are able to estimate the number of DNA molecules trapped within each gold barrier (**Fig. 6.4d**), under our chosen experimental conditions (i.e., constant DNA concentration and flow rate of the buffer used for loading DNA). Using the smallest barriers ($L = 200$ nm), it is possible to support only single DNA molecules as desired (**Fig. 6.4c,d, Supplementary Fig. S6.7**). However, these small barriers are less practical for high throughput measurements, as most of them (~95%) do not trap any DNA molecule at all (**Fig. 6.4c,d, Supplementary Fig. S6.7**). For larger barrier size of $L = 300$ nm, the rate of trapping DNA becomes higher, but the probabilities to trap two or more DNA strands also increase. Considering this trade-off relationship between the trapping rate and the probability to confine only one DNA strand, we decide to use $L = 400$ nm barrier size in practice. This size offers a sufficient DNA trapping rate (~50%), together

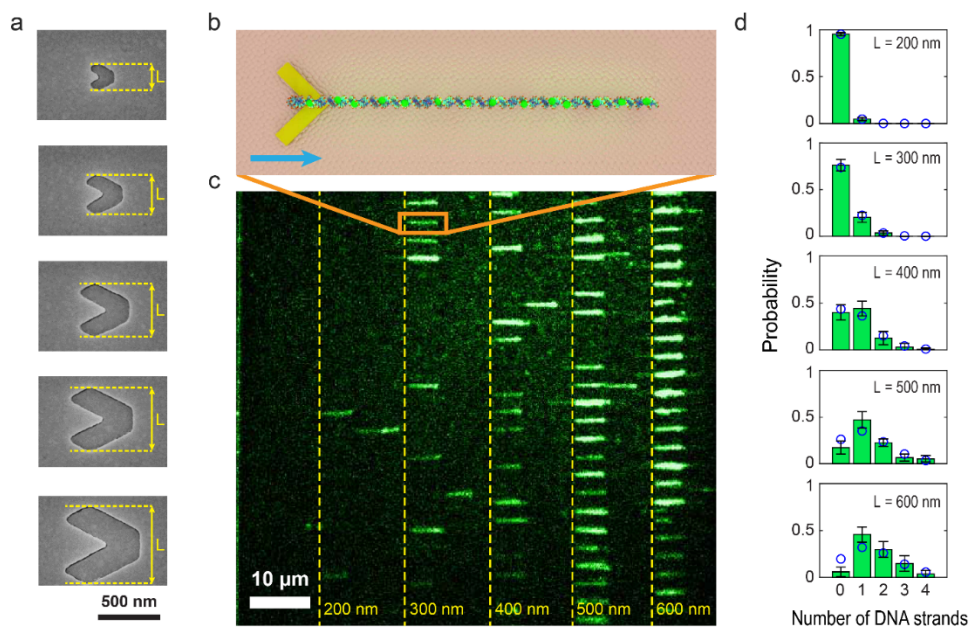


Figure 6.4. Optimization of gold nanobarrier size for loading of single DNA molecules. (a) SEM micrographs of gold nanobarriers with varying sizes ($L = 200\text{--}600$ nm), taken just before lift-off (at step (6) of Fig. 6.1a). (b) Illustration showing a single DNA molecule hold by a gold nanobarrier under flow stretching (buffer flow direction is indicated by the blue arrow). The DNA strand is fluorescently labeled by intercalating dye (green). (c) Fluorescence microscopy image of labeled DNA molecules confined in an array by gold nanobarriers, under flow stretching. The region in an orange square is assumed to confine only one DNA molecule, as depicted in panel (b). The direction of buffer flow is the same as indicated by the arrow in panel (b). The gold nanostructure pattern is designed to contain five columns of gold barriers within one field of view of the microscope used in this test. Each column is indicated by a vertical yellow dashed line with the size of barriers (L) in yellow letters. (d) Histograms showing the probabilities of having specific number of single DNA molecules per each gold barrier, as a function of barrier size. The number of DNA strands are estimated from fluorescence intensity of labeled DNA molecules, measured within regions large enough to include the whole length of DNA (as like the orange square in panel (c)). For each gold nanobarrier dimension, $N = 168$ regions were analyzed. The blue circles are the results of fitting to the Poisson distribution.

with a high probability of single DNA confinement ($\sim 73\%$) (Fig. 6.4c,d, Supplementary Fig. S6.7). For this size, the fit to the Poisson distribution also results in the mean value which is the closest to one (i.e., single DNA confinement is the most probable) among all the tested barrier sizes (Fig. 6.4d, Supplementary Fig. S6.7).

6.2.5. Protein-DNA interaction observed by SODA microfluidic devices

With the optimized gold barrier size (Fig. 6.4), we fabricated SODA devices to demonstrate their capability of properly observing protein-DNA bioassays and to develop automatized data analysis routines (Fig. 6.5). For these purposes, we chose to test the DNA binding protein Rad51 because it has been widely studied and its

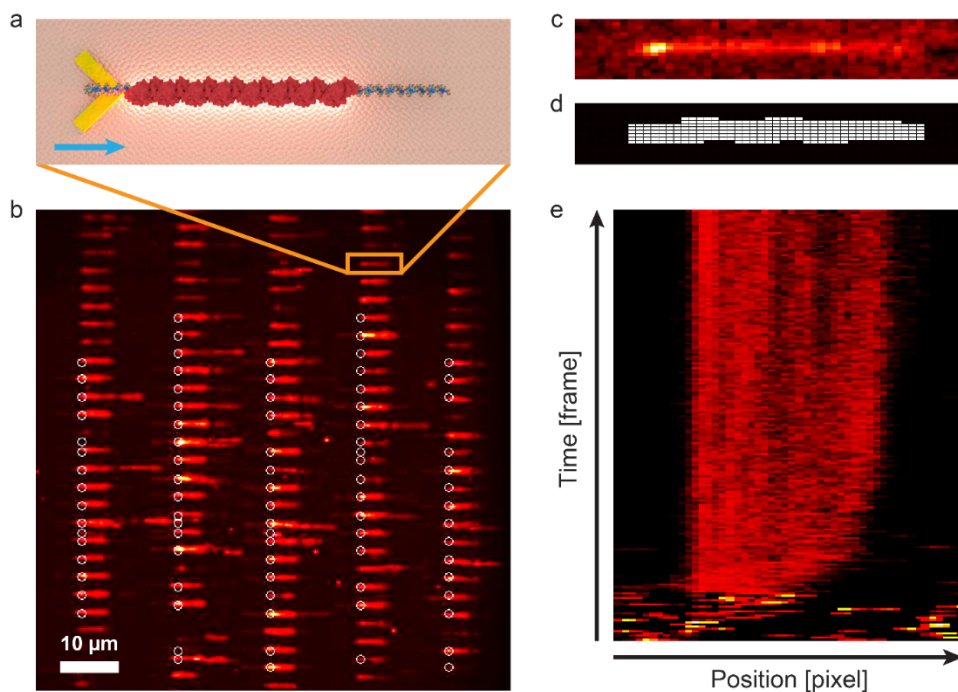


Figure 6.5. Protein-DNA interaction observed by SODA microfluidic devices. (a) Illustration showing a single DNA molecule held by a gold nanobarrier, loaded with Rad51 proteins, under flow stretching (buffer flow direction is indicated by the blue arrow). (b) Fluorescence microscopy image of labeled Rad51 molecules confined in an array by gold nanobarriers, under flow stretching (DNA strands are not labeled here). The region in an orange square is assumed to have only one DNA molecule, as depicted in panel (a). (c) A zoom-in image of panel (b), showing only a single DNA strand. (d) An example of image analysis based on fluorescence intensity, in which the image binarization with a certain intensity threshold reports the position of Rad51 molecules (white pixels) distinguished from the neighboring background (black pixels) that is noisy in the raw image. (e) An example of kymograph showing the time evolution of Rad51 binding to a single DNA strand (the large fluctuation shown at earlier time frames is due to a disturbance in buffer flow). In panels (b-e), the buffer flow direction is the same as depicted in panel (a).

nucleoprotein filament formation upon DNA-binding is well known^{42, 47-52}. Furthermore, although it is a key enzyme in eukaryotic homologous recombination process, its working mechanism is not fully understood yet⁷¹. In this pilot experiment, we labeled the Rad51 proteins with Alexa Fluor 488 dyes⁴⁸ (while DNA molecules are not labeled) to detect nucleoprotein filament formation in real time (Fig. 6.5a). Similar to our experiments with DNA only (in section 6.2.4.), we employed the singly-tethered DNA configuration to be able to clearly distinguish between specifically and non-specifically bound proteins.

The location of each nucleoprotein filament was detected from the fluorescence images (Fig. 6.5b) and quantified with home-made software routines (Fig. 6.5c,d). In this context, kymographs can be generated to visualize the evolution of protein-DNA interactions over time (Fig. 6.5e). In our experimental setting, ~100 protein-DNA complexes could be measured and tracked simultaneously within one

field of view of the employed TIRF microscopy. This is order(s)-of-magnitude higher throughput compared to other single-molecule techniques that i) are relying on the fluorescence detection of randomly attached DNA molecules on surface (**Supplementary Fig. S6.8**), and ii) are not based on fluorescence such as optical tweezers and atomic force microscopy. If necessary, it would be possible to exhibit even higher throughput, e.g., by employing a wider field of view and/or a more densely packed gold nanostructure array.

6.3. Conclusions

We have demonstrated that our designed, fabricated, and functionalized SODA microfluidic devices are capable of providing a reliable high-throughput platform to study protein-DNA interactions. In the aspect of device fabrication, the use of maskless lithography from nano- to micron-scale offers high flexibility in device design (i.e., the use of e-beam lithography for submicron-scale gold nanostructures and DLW for micron-scale microfluidic channels). In addition, using custom-made PDMS-based fluidic channels, multiple parallel experiments on a single fluidic device are possible with minimal necessity for volumes of biomaterial ($\sim 1 \mu\text{L}$ per channel). A variation in the fabrication of PDMS block further allows the combined use with magnetic tweezers, which could result in a more powerful high-throughput single-molecule platform that combines the functionalities of direct single-molecule visualization with dynamic and precise single-molecule manipulation by force control. Our surface functionalization protocol features uniform SLB coating that has highly selective adherence to glass over gold, which minimizes non-specific surface adhesion of proteins. Hence, the coating allows highly specific confinement and binding of DNA strands to only pre-defined gold nanostructures, together with efficient surface passivation. The optimized gold barrier geometry balances between the DNA trapping efficiency and single DNA loading probability, permitting high-throughput measurement of single DNA molecules, together with an automatized image analysis. Moreover, our proof-of-concept experiments and data analysis on the nucleoprotein filament formation dynamics by Rad51 and DNA demonstrated its successful integration of the abovementioned features into a single microfluidic device with high-throughput capability. Altogether, the SODA device is expected to be actively utilized in the investigation of diverse highly complex protein-DNA interaction dynamics, e.g., mechanisms of eukaryotic DNA replication machinery.

6.4. Materials and Methods

6.4.1. Fabrication of SODA devices

6.4.1.1. Nanofabrication of gold nanostructures

We use borosilicate microscope coverslips with area of 24 mm × 60 mm and thickness of ~170 μm (#1.5, Menzel-Gläser, Thermo Fisher Scientific) as the substrates for gold nanostructure fabrication. We clean the substrates in a custom-made Teflon holder by successive sonication in acetone (A), isopropyl alcohol (IPA), and deionized (DI) water for 5 min each at room temperature, followed by a brief N₂ blow drying and spin-drying at 2000 rpm for 3 min (step (1) in **Fig. 6.1a**).

We spin-coat a ~250 nm-thick positive e-beam resist layer of poly(methyl methacrylate) (PMMA 950k A4, MicroChem) at 500 rpm for 5 s and then 3000 rpm for 55 s. After spin-coating, any resist contamination at the backside of the coverslips should be removed by micro-fiber swabs (MiraSWAB, Foamtec International) soaked with IPA, to prevent any undesired backscattering of e-beam from these transparent substrates that substantially degrades the quality of e-beam written patterns. We bake the resist-coated and backside-cleaned substrates on a hot plate at 175 °C for 30 min (step (2) in **Fig. 6.1a**). On top of the cured resist layer, we deposit a ~30 nm-thick gold layer in a sputter coater (EM-ACE600, Leica), to prevent charge accumulation on these nonconductive substrates that substantially deviates e-beam and hence distorts e-beam written patterns (step (3) in **Fig. 6.1a**). We write patterns for gold nanostructures by e-beam lithography (EBPG 5200 or EBPG 5000+, Vistec) (step (4) in **Fig. 6.1a**).

In prior to the development, to enable the access of developer solution to the e-beam written PMMA layer, the top gold layer should be removed by dipping the substrates in gold etchant solution (TFA, Transene Inc.) for 1 min with gentle agitation. Then the substrates are thoroughly washed with ample amount of DI water, followed by a brief N₂ blow drying and spin-drying at 2000 rpm for 3 min. The development on the exposed PMMA layer is conducted by soaking the substrates in 1:3 mixture of methyl isobutyl ketone (MIBK) and IPA for 60 s, followed by soaking in IPA for 30 s. During development, gentle agitation is required for homogeneous development over the whole coverslip surface. Then the substrates are briefly dried by N₂ blow and then spin-dried at 2000 rpm for 3 min. The developed substrates are baked at 100 °C for 2 min, to remove residual solvents and moisture inside the patterned holes. To remove any remaining resist within the patterned holes that might degrade the adhesion of metals to the glass coverslip (**Supplementary Fig. S6.2**), it is necessary to perform descum process in which the developed PMMA layer is slightly etched by a plasma asher (TePla300, PVA TePla; etching with 17 sccm O₂ flow at 100 W RF power for 3 min results in ~10 nm etch of 950k A4 PMMA) (step (5) in **Fig. 6.1a**).

After deposition of 5 nm-thick chromium (Cr) layer as an adhesion promoter between gold (Au) and glass coverslip, 30 nm-thick Au layer is deposited by e-beam

evaporation (Temescal FC-2000, Ferrotec; using deposition rates of 0.05 nm/s for Cr and 0.1 nm/s for Au) (step (6) in **Fig. 6.1a**). For lift-off, the substrates are soaked in an 80 °C-heated resist stripper solution (PRS-3000, J.T.Baker) for 1 h. The resist removal can be assisted by the simultaneous use of a magnetic stirrer and/or the intermittent use of a glass pipette to induce a strong flow in the hot solution. The substrates are thoroughly washed in ample amount of DI water, spin-dried at 2000 rpm for 3 min, and finally cleaned with O₂ plasma (TePla300, PVA TePla; cleaning with 17 sccm O₂ flow at 300 W RF power for 5 min) (step (7) in **Fig. 6.1a**). The fabricated gold nanostructures are inspected by both optical microscope (Olympus) and scanning electron microscope (S4800 FESEM, Hitachi).

6.4.1.2. Microfabrication of Si mold for PDMS block

We use 4-inch Si wafers with thickness of 500–1000 μm (University Wafer) as the substrates to fabricate Si molds for templating PDMS blocks. We clean the wafers in a custom-made Teflon holder by successive sonication in acetone (A), isopropyl alcohol (IPA), and deionized (DI) water for 5 min each at room temperature, followed by a brief N₂ blow drying and spin-drying at 2000 rpm for 3 min. We spin-coat a layer of hexamethyldisilazane (HMDS, MicroChemicals) as an adhesion promoter at 500 rpm for 5 s and then 2000 rpm for 55 s. We bake the HMDS layer on a hot plate at 200 °C for 2 min (step (1) in **Fig. 6.2a**).

We spin-coat a ~1.7 μm-thick AZ5214 photoresist (MicroChemicals) at 500 rpm for 5 s and then 3000 rpm for 55 s, followed by baking the resist in an oven at 90 °C for 15 min (step (2) in **Fig. 6.2a**). Microfluidic channel patterns are written on the baked photoresist layer using a DLW (ML-2, Durham Magneto Optics Ltd.) with a 405 nm-wavelength laser beam at a dose of 18 mJ/cm² (step (3) in **Fig. 6.2a**). Then post-exposure bake is performed in an oven at 120 °C for 50 s, to render the exposed region insoluble in development (at this stage, the micro-patterns written by the laser beam become visible by bare eyes). Then, all non-exposed regions become soluble in development by performing a flood exposure with a 320–365 nm-wavelength lamp at ~10 mW/cm² intensity for 15 s (i.e., at a dose of 150 mJ/cm²) by using a mask aligner (EVG 620, EV Group) (step (4) in **Fig. 6.2a**). The development of photoresist is conducted by soaking the substrates in MF321 developer (Shipley) for 90 s with constant agitation and then DI water for 90 s. Then the wafers are washed by using a DI water gun and then spin-dried at 2000 rpm for 3 min (step (5) in **Fig. 6.2a**).

The developed wafers are deep-etched by Bosch plasma etching process based on sulfur hexafluoride (SF₆) and octafluorocyclobutane (C₄F₈) gases which results in ~40 μm-deep straight etched sidewalls with rapid etch rates of 2–3 μm/min (AMS 100 I-Speeder, Adixen, or PlasmaPro 100 Estrelas, Oxford Instruments) (step (6) in **Fig. 6.2a**). The remaining photoresist on top of micro-patterned structures is removed by performing an intense O₂ plasma cleaning process for 5–10 min within the same plasma etcher used for Bosch etching (step (7) in **Fig. 6.2a**).

6.4.1.3. Fabrication of PDMS microfluidic device

We use PDMS (Sylgard 184, Dow Corning) prepared by manually mixing the base and curing agent in a 10:1 ratio by weight for at least 1 min. The mixed PDMS is degassed by performing centrifuge at 3000 rcf for 3 min (Centrifuge 5702, Eppendorf). Before centrifuge, the PDMS mixture looks opaque due to the embedded air bubbles, but it becomes transparent after centrifuge. The degassed PDMS mixture is poured onto a Si mold. Here, either aluminum foil or a custom-made plastic block is used as a frame to confine the fluidic PDMS mixture within the Si mold. Then the PDMS is further degassed in a vacuum chamber for ~1 h. A large number of bubbles are visible on the surface of PDMS layer at the early stage of vacuum treatment, but they gradually decrease over time. Taking out of the vacuum chamber, we immediately transfer the PDMS on Si mold into a convection oven at 80 °C to cure PDMS for 1–2 h (step (8) in **Fig. 6.2a**). For an MTC-SODA device (**Supplementary Fig. S6.3**), we only briefly cure the PDMS sample at 80 °C for ~10 min, and then place a smaller borosilicate microscope coverslip with area of 22 mm × 22 mm and thickness of ~150 μm (#1, Menzel-Gläser, Thermo Fisher Scientific) at the top of the PDMS layer. As the PDMS layer is not fully cured yet, its plasticity allows to form a thin layer of PDMS at center by gently pressing with a Teflon block. Afterwards, the sample is transferred back into the oven at 80 °C to finish the curing process for 1–2 h. The rest of the process is the same as the normal SODA device as described below, but a more careful treatment is necessary for the thin layer of PDMS and embedded coverslip at center.

After cooling down to room temperature, the cured PDMS layer is peeled off from the Si mold and cut into a desired size by using a razor blade (step (9) in **Fig. 6.2a**). The inlet/outlet holes are generated by punching holes with biopsy punches (Uni-Core, Harris) (a 0.75 mm-diameter punch for inlets to connect plastic pipette tips and a 0.5 mm-diameter punch for outlets to insert metal needles that are connected to plastic tubes and then syringe pumps). During this process, the side of PDMS that will consist microfluidic channels should be protected from contamination. This side of PDMS and the surface of a glass coverslip with gold nanostructures are both uniformly treated with a handheld corona discharger (BD-20ACV, Electro-Technic Products) for ~10 s, to render their surfaces highly hydrophilic to promote adhesion. After positioning the PDMS block on top of the coverslip, gently press for a few seconds to form a firm bonding between them. The microfluidic device is finalized by briefly curing in a convection oven at 80 °C for 1 min (**Fig. 6.2c**). The used Si molds are being protected by a PDMS-coating during storage, by pouring and curing PDMS as described above.

6.4.2. Surface coatings and bioassay for experiments with SODA devices

6.4.2.1. Surface functionalization

The SLB is formed on a glass coverslip by depositing liposomes consisting of 1,2-dioleoyl-sn-glycero-3-phosphocholine (DOPC) and biotin-labeled 1,2-dioleoyl-sn-glycero-3-phosphoethanolamine (DOPE) (Avanti Polar Lipids Inc.) in a molar ratio of

99.5:0.5. For fluorescence imaging of SLB for FRAP experiments, rhodamine-conjugated DOPC lipids were used (**Fig. 6.3d**). The gold nanostructures fabricated on glass coverslips are coated by PEG molecules (SH-mPEG, Rapp Polymere GmbH). For fluorescence microscopy imaging of gold structures, FITC-labeled PEG molecules (SH-PEG-FITC, Rapp Polymere GmbH) are utilized (**Fig. 6.3e**). Prior to the application to gold nanostructure-patterned coverslips, these coatings were demonstrated on gold- or silica-coated crystal sensors by using QCM measurement (Q-Sense E4, Biolin Scientific) (**Fig. 6.3b,c**).

6.4.2.2. Bioassay preparation

To construct double stranded DNA, we use a linear 20.2 kbp DNA amplicon from the plasmid pIA1218 (kindly provided by Prof. dr. Irina Artsimovitch, Ohio State University), ligated to biotin and digoxigenin enriched ~600 bp DNA handles, as previously described^{12, 51, 72}. For visualization in a fluorescence microscope, DNA strands are stained by YOYO-1 intercalation dyes (Invitrogen) (**Fig. 6.4**). The Rad51 proteins are prepared and fluorescently labeled with Alexa Fluor 488 dyes as previously described⁴⁸ (**Fig. 6.5**).

6.4.2.3. Experiments with SODA devices

In our experiments with SODA devices, we use three different buffers (**A**: 10 mM HEPES, 150 mM NaCl, pH 7.4; **B**: 10 mM HEPES, 150 mM NaCl, 2 mM CaCl₂, pH 7.4; **C**: 10 mM HEPES, 10 mM NaCl, pH 7.4). First, we wash the microfluidic channels with 6 μ L of buffer **A**. Then, we flow 4 μ L solution with liposomes (25 μ g/mL in buffer **B**, formed by mixture of DOPC and biotin-DOPE as described above) twice to form an SLB. The channels are washed three times with buffer **A**, 4 μ L each. Then 3 μ L of streptavidin solution (10 μ g/mL in buffer **A**) is used to attach streptavidin molecules onto the biotin-conjugated lipid molecules in the SLB. The channels are washed again with 4 μ L buffer **A** and then 6 μ L buffer **C**, followed by incubation with a 3.5 μ L of DNA solution (biotin-DNA-digoxigenin as described above; 0.5 ng/ μ L in buffer **A**) (YOYO-1 labeled DNA molecules are used instead for the experiments shown in **Fig. 6.4**). The DNA strands are fixed to the streptavidin-bound lipid molecules through their biotin handles and become diffusive within the SLB. The trapping at gold nanobarriers and flow stretching of DNA molecules are performed with buffer **C**, with a controlled flow rate by using a syringe pump. For the nucleoprotein filament formation with Rad51 shown in **Fig. 6.5**, Rad51 proteins (1 μ M) were added to the binding buffer (Tris-HCl at pH 7.5, 60 mM KCl, 2 mM CaCl₂, 1 mM DTT (dithiothreitol), and 1 mM ATP).

6.5. References

1. Tinoco, I. & Gonzalez, R. L. Biological mechanisms, one molecule at a time. *Genes & Development* **25**, 1205-1231 (2011).
2. Miller, H., Zhou, Z., Shepherd, J., Wollman, A. J. M. & Leake, M. C. Single-molecule techniques in biophysics: a review of the progress in methods and applications. *Reports on Progress in Physics* **81**, 024601 (2018).
3. Neuman, K. C. & Nagy, A. Single-molecule force spectroscopy: optical tweezers, magnetic tweezers and atomic force microscopy. *Nature Methods* **5**, 491 (2008).
4. Bustamante, C., Cheng, W. & Mejia, Y. X. Revisiting the central dogma one molecule at a time. *Cell* **144**, 480-497 (2011).
5. Fazal, F. M. & Block, S. M. Optical tweezers study life under tension. *Nature Photonics* **5**, 318 (2011).
6. Dulin, D., Lipfert, J., Moolman, M. C. & Dekker, N. H. Studying genomic processes at the single-molecule level: introducing the tools and applications. *Nature Reviews. Genetics* **14**, 9 (2012).
7. Capitanio, M. & Pavone, Francesco S. Interrogating biology with force: single molecule high-resolution measurements with optical tweezers. *Biophysical Journal* **105**, 1293-1303 (2013).
8. Forth, S., Sheinin, M. Y., Inman, J. & Wang, M. D. Torque measurement at the single-molecule level. *Annual Review of Biophysics* **42**, 583-604 (2013).
9. Lipfert, J., van Oene, M. M., Lee, M., Pedaci, F. & Dekker, N. H. Torque spectroscopy for the study of rotary motion in biological systems. *Chemical Reviews* **115**, 1449-1474 (2015).
10. Monachino, E., Spenkelink, L. M. & van Oijen, A. M. Watching cellular machinery in action, one molecule at a time. *The Journal of Cell Biology* **216**, 41 (2017).
11. Lewis, J. S. et al. Single-molecule visualization of *Saccharomyces cerevisiae* leading-strand synthesis reveals dynamic interaction between MTC and the replisome. *Proceedings of the National Academy of Sciences* **114**, 10630 (2017).
12. Janissen, R. et al. Global DNA compaction in stationary-phase bacteria does not affect transcription. *Cell* **174**, 1188-1199.e14 (2018).
13. Ticaú, S., Friedman, Larry J., Ivica, Nikola A., Gelles, J. & Bell, Stephen P. Single-molecule studies of origin licensing reveal mechanisms ensuring bidirectional helicase loading. *Cell* **161**, 513-525 (2015).
14. Dulin, D., Yu, Z., Cui, T. J., Berghuis, B. A., Depken, M. & Dekker, N. H. Real-time observation of replicative helicase assembly onto single-stranded DNA. *bioRxiv* (2016).
15. Uemura, S., Aitken, C. E., Korlach, J., Flusberg, B. A., Turner, S. W. & Puglisi, J. D. Real-time tRNA transit on single translating ribosomes at codon resolution. *Nature* **464**, 1012 (2010).
16. Petrov, A., Chen, J., O'Leary, S., Tsai, A. & Puglisi, J. D. Single-molecule analysis of translational dynamics. *Cold Spring Harbor Perspectives in Biology* **4**, (2012).
17. Shashkova, S. & Leake, Mark C. Single-molecule fluorescence microscopy review: shedding new light on old problems. *Bioscience Reports* **37**, (2017).
18. Roy, R., Hohng, S. & Ha, T. A practical guide to single-molecule FRET. *Nature Methods* **5**, 507 (2008).
19. Whelan, D. R. & Bell, T. D. M. Super-resolution single-molecule localization microscopy: tricks of the trade. *The Journal of Physical Chemistry Letters* **6**, 374-382 (2015).
20. Xu, J., Zhao, L., Xu, Y., Zhao, W., Sung, P. & Wang, H.-W. Cryo-EM structures of human RAD51 recombinase filaments during catalysis of DNA-strand exchange. *Nature Structural & Molecular Biology* **24**, 40 (2016).
21. De Vlaminck, I. & Dekker, C. Recent advances in magnetic tweezers. *Annual Review of Biophysics* **41**, 453-472 (2012).
22. Berghuis, B. A., Köber, M., van Laar, T. & Dekker, N. H. High-throughput, high-force probing of DNA-protein interactions with magnetic tweezers. *Methods* **105**, 90-98 (2016).
23. Manosas, M., Camunas-Soler, J., Croquette, V. & Ritort, F. Single molecule high-throughput footprinting of small and large DNA ligands. *Nature Communications* **8**, 304 (2017).
24. Dulin, D. et al. Signatures of nucleotide analog incorporation by an RNA-dependent RNA polymerase revealed using high-throughput magnetic tweezers. *Cell Reports* **21**, 1063-1076 (2017).
25. Kriegel, F., Ermann, N., Forbes, R., Dulin, D., Dekker, N. H. & Lipfert, J. Probing the salt dependence of the torsional stiffness of DNA by multiplexed magnetic torque tweezers. *Nucleic Acids Research* **45**, 5920-5929 (2017).
26. Sitters, G., Kamsma, D., Thalhammer, G., Ritsch-Marte, M., Peterman, E. J. G. & Wuite, G. J. L. Acoustic force spectroscopy. *Nature Methods* **12**, 47 (2014).
27. Kamsma, D. & Wuite, G. J. L. Single-molecule measurements using acoustic force spectroscopy (AFS). In *Single Molecule Analysis: Methods and Protocols* (ed Peterman, E. J. G.) 341-351 (Springer New York, 2018).
28. Halvorsen, K. & Wong, W. P. Massively parallel single-molecule manipulation using centrifugal force. *Biophysical Journal* **98**, L53-L55 (2010).

29. Yang, D., Ward, A., Halvorsen, K. & Wong, W. P. Multiplexed single-molecule force spectroscopy using a centrifuge. *Nature Communications* **7**, 11026 (2016).
30. Terai, T. & Nagano, T. Small-molecule fluorophores and fluorescent probes for bioimaging. *Pflügers Archiv - European Journal of Physiology* **465**, 347-359 (2013).
31. van Loenhout, M. T. J., de Grunt, M. V. & Dekker, C. Dynamics of DNA supercoils. *Science* **338**, 94 (2012).
32. Ganji, M. et al. Real-time imaging of DNA loop extrusion by condensin. *Science* **360**, 102-105 (2018).
33. Duzdevich, D., Warner, Megan D., Ticau, S., Ivica, Nikola A., Bell, Stephen P. & Greene, Eric C. The dynamics of eukaryotic replication initiation: origin specificity, licensing, and firing at the single-molecule level. *Molecular Cell* **58**, 483-494 (2015).
34. van Oijen, A. M., Blainey, P. C., Crampton, D. J., Richardson, C. C., Ellenberger, T. & Xie, X. S. Single-molecule kinetics of λ exonuclease reveal base dependence and dynamic disorder. *Science* **301**, 1235 (2003).
35. Sternberg, S. H., Redding, S., Jinek, M., Greene, E. C. & Doudna, J. A. DNA interrogation by the CRISPR RNA-guided endonuclease Cas9. *Nature* **507**, 62 (2014).
36. Ando, T., Uchihashi, T. & Kodera, N. High-Speed AFM and applications to biomolecular systems. *Annual Review of Biophysics* **42**, 393-414 (2013).
37. Finkelstein, I. J. & Greene, E. C. Supported lipid bilayers and DNA curtains for high-throughput single-molecule studies. In *DNA Recombination: Methods and Protocols* (ed Tsubouchi, H.) 447-461 (Humana Press, 2011).
38. Robison, A. D. & Finkelstein, I. J. High-throughput single-molecule studies of protein-DNA interactions. *FEBS Letters* **588**, 3539-3546 (2014).
39. Collins, B. E., Ye, L. F., Duzdevich, D. & Greene, E. C. Chapter 12 - DNA curtains: novel tools for imaging protein-nucleic acid interactions at the single-molecule level. In *Methods in Cell Biology* (ed Waters, J. C., Wittman, T.) **123**, 217-234 (Academic Press, 2014).
40. Zhao, Y., Jiang, Y. & Qi, Z. Visualizing biological reaction intermediates with DNA curtains. *Journal of Physics D: Applied Physics* **50**, 153001 (2017).
41. Ganji, M., Kim, S. H., van der Torre, J., Abbondanzieri, E. & Dekker, C. Intercalation-based single-molecule fluorescence assay to study DNA supercoil dynamics. *Nano Letters* **16**, 4699-4707 (2016).
42. Lee, J. Y. et al. Base triplet stepping by the Rad51/RecA family of recombinases. *Science* **349**, 977 (2015).
43. Finkelstein, I. J. & Greene, E. C. Molecular traffic jams on DNA. *Annual Review of Biophysics* **42**, 241-263 (2013).
44. Wang, F., Redding, S., Finkelstein, I. J., Gorman, J., Reichman, D. R. & Greene, E. C. The promoter-search mechanism of *Escherichia coli* RNA polymerase is dominated by three-dimensional diffusion. *Nature Structural & Molecular Biology* **20**, 174 (2013).
45. Terakawa, T., Bisht, S., Eeftens, J. M., Dekker, C., Haering, C. H. & Greene, E. C. The condensin complex is a mechanochemical motor that translocates along DNA. *Science* **358**, 672-676 (2017).
46. Visnapuu, M.-L. & Greene, E. C. Single-molecule imaging of DNA curtains reveals intrinsic energy landscapes for nucleosome deposition. *Nature Structural & Molecular Biology* **16**, 1056 (2009).
47. Granéli, A., Yeykal, C. C., Robertson, R. B. & Greene, E. C. Long-distance lateral diffusion of human Rad51 on double-stranded DNA. *Proceedings of the National Academy of Sciences* **103**, 1221 (2006).
48. Modesti, M. et al. Fluorescent Human RAD51 reveals multiple nucleation sites and filament segments tightly associated along a single DNA molecule. *Structure* **15**, 599-609 (2007).
49. van Mameren, J., Modesti, M., Kanaar, R., Wyman, C., Peterman, E. J. G. & Wuite, G. J. L. Counting RAD51 proteins disassembling from nucleoprotein filaments under tension. *Nature* **457**, 745 (2008).
50. Gross, P., Farge, G., Peterman, E. J. G. & Wuite, G. J. L. Chapter 17 - combining optical tweezers, single-molecule fluorescence microscopy, and microfluidics for studies of DNA-protein interactions. In *Methods in Enzymology* (ed Walter, N. G.) **475**, 427-453 (Academic Press, 2010).
51. Lee, M., Lipfert, J., Sanchez, H., Wyman, C. & Dekker, N. H. Structural and torsional properties of the RAD51-dsDNA nucleoprotein filament. *Nucleic Acids Research* **41**, 7023-7030 (2013).
52. Gibb, B., Ye, L. F., Kwon, Y., Niu, H., Sung, P. & Greene, E. C. Protein dynamics during presynaptic-complex assembly on individual single-stranded DNA molecules. *Nature Structural & Molecular Biology* **21**, 893 (2014).
53. Fazio, T., Visnapuu, M.-L., Wind, S. & Greene, E. C. DNA curtains and nanoscale curtain rods: high-throughput tools for single molecule imaging. *Langmuir* **24**, 10524-10531 (2008).
54. Visnapuu, M.-L., Fazio, T., Wind, S. & Greene, E. C. Parallel arrays of geometric nanowells for assembling curtains of DNA with controlled lateral dispersion. *Langmuir* **24**, 11293-11299 (2008).
55. Gorman, J., Fazio, T., Wang, F., Wind, S. & Greene, E. C. Nanofabricated racks of aligned and anchored DNA substrates for single-molecule imaging. *Langmuir* **26**, 1372-1379 (2010).
56. Monico, C., Capitano, M., Belcastro, G., Vanzi, F. & Pavone, S. F. Optical methods to study protein-DNA interactions in vitro and in living cells at the single-molecule level. *International Journal of Molecular Sciences* **14**, 3961-3992 (2013).

57. Bouchiat, C., Wang, M. D., Allemand, J. F., Strick, T., Block, S. M. & Croquette, V. Estimating the persistence length of a worm-like chain molecule from force-extension measurements. *Biophysical Journal* **76**, 409-413 (1999).
58. Sia, S. K. & Whitesides, G. M. Microfluidic devices fabricated in poly(dimethylsiloxane) for biological studies. *Electrophoresis* **24**, 3563-3576 (2003).
59. Moolman, M. C., Huang, Z., Krishnan, S. T., Kerssemakers, J. W. J. & Dekker, N. H. Electron beam fabrication of a microfluidic device for studying submicron-scale bacteria. *Journal of Nanobiotechnology* **11**, 12 (2013).
60. Haubert, K., Drier, T. & Beebe, D. PDMS bonding by means of a portable, low-cost corona system. *Lab on a Chip* **6**, 1548-1549 (2006).
61. Xin, Q. et al. Magnetic tweezers for the mechanical research of DNA at the single molecule level. *Analytical Methods* **9**, 5720-5730 (2017).
62. Madariaga-Marcos, J., Hormeño, S., Pastrana, C. L., Fisher, G. L. M., Dillingham, M. S. & Moreno-Herrero, F. Force determination in lateral magnetic tweezers combined with TIRF microscopy. *Nanoscale* **10**, 4579-4590 (2018).
63. Janissen, R., Berghuis, B. A., Dulin, D., Wink, M., van Laar, T. & Dekker, N. H. Invincible DNA tethers: covalent DNA anchoring for enhanced temporal and force stability in magnetic tweezers experiments. *Nucleic Acids Research* **42**, e137-e137 (2014).
64. Lind, T. K. & Cárdenas, M. Understanding the formation of supported lipid bilayers via vesicle fusion – A case that exemplifies the need for the complementary method approach (Review). *Biointerphases* **11**, 020801 (2016).
65. Vafaei, S., Tabaei, S. R. & Cho, N.-J. Optimizing the performance of supported lipid bilayers as cell culture platforms based on extracellular matrix functionalization. *ACS Omega* **2**, 2395-2404 (2017).
66. Dixon, M. C. Quartz crystal microbalance with dissipation monitoring: enabling real-time characterization of biological materials and their interactions. *Journal of Biomolecular Techniques: JBT* **19**, 151-158 (2008).
67. van der Meulen, S. A. J., Dubacheva, G. V., Dogterom, M., Richter, R. P. & Leunissen, M. E. Quartz crystal microbalance with dissipation monitoring and spectroscopic ellipsometry measurements of the phospholipid bilayer anchoring stability and kinetics of hydrophobically modified DNA oligonucleotides. *Langmuir* **30**, 6525-6533 (2014).
68. Day, C. A., Kraft, L. J., Kang, M. & Kenworthy, A. K. Analysis of protein and lipid dynamics using confocal fluorescence recovery after photobleaching (FRAP). *Current Protocols in Cytometry* **62**, 2.19.11-12.19.29 (2012).
69. Persson, F., Fritzsche, J., Mir, K. U., Modesti, M., Westerlund, F. & Tegenfeldt, J. O. Lipid-based passivation in nanofluidics. *Nano Letters* **12**, 2260-2265 (2012).
70. Groves, J. T. & Boxer, S. G. Micropattern formation in supported lipid membranes. *Accounts of Chemical Research* **35**, 149-157 (2002).
71. Willis, N. A., Panday, A., Duffey, E. E. & Scully, R. Rad51 recruitment and exclusion of non-homologous end joining during homologous recombination at a Tus/Ter mammalian replication fork barrier. *PLOS Genetics* **14**, e1007486 (2018).
72. Ha, S., Janissen, R., Ussembayev, Y. Y., van Oene, M. M., Solano, B. & Dekker, N. H. Tunable top-down fabrication and functional surface coating of single-crystal titanium dioxide nanostructures and nanoparticles. *Nanoscale* **8**, 10739-10748 (2016).

6.6. Supplementary Information

6.6.1. Supplementary Figures

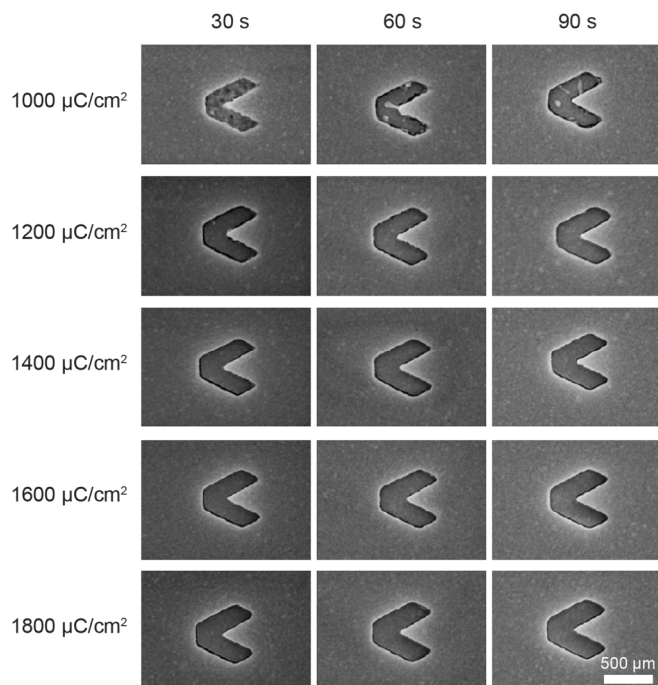


Figure S6.1. Optimization of e-beam writing dose and development time. Scanning electron microscopy (SEM) images of gold nanobarrriers fabricated with varying e-beam writing dose (step (4) in **Fig. 6.1a**) and development time (step (5) in **Fig. 6.1a**). The development is not complete for all tested times (30–90 s) at the lowest dose 1000 $\mu\text{C}/\text{cm}^2$ (as can be seen from the undeveloped parts of resist within each pattern area). For a slightly higher dose (1200 $\mu\text{C}/\text{cm}^2$), development becomes complete only for longer developing times (60–90 s). In the case of much higher doses (1400–1800 $\mu\text{C}/\text{cm}^2$), development is always complete in the tested range of developing times (30–90 s). However, too high doses (1800 $\mu\text{C}/\text{cm}^2$) imply much longer e-beam writing times, whereas too short development times (30 s) might result in incomplete development for very small patterns. Hence, for reproducible gold nanostructure fabrication, optimal conditions are determined as 1400–1600 $\mu\text{C}/\text{cm}^2$ and 60–90 s.

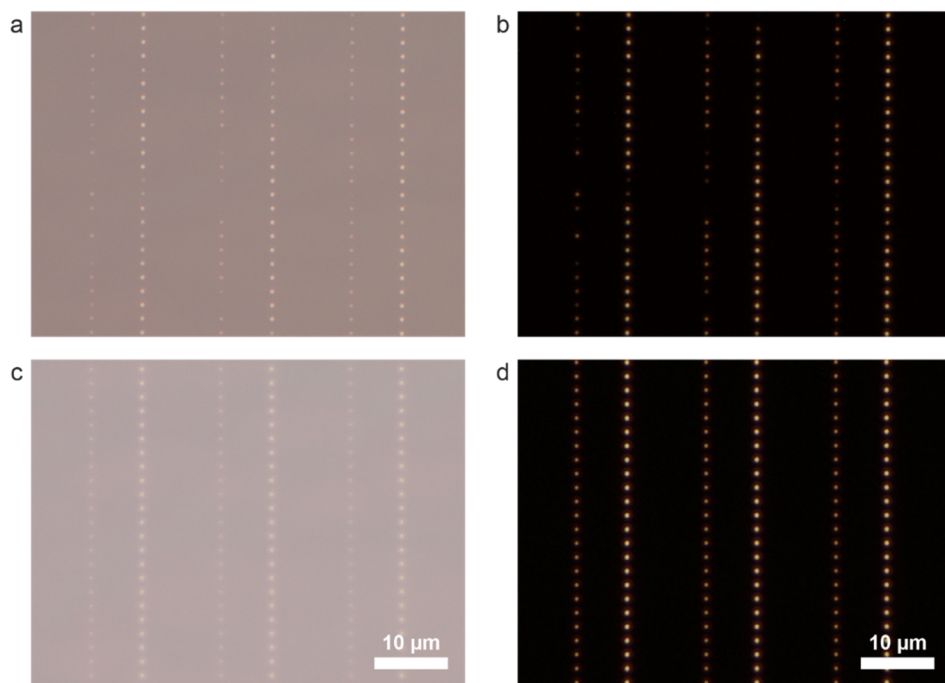


Figure S6.2. The necessity of descum step in gold nanostructure fabrication. Microscopy images of the gold nanostructures fabricated **(a,b)** without a descum step and **(c,d)** with a descum step. Both bright field images **(a,c)** and dark field images **(b,d)** are shown for each sample, with the dark field images more clearly indicating the location and size of each nanostructure. Based on the relative size difference, the gold barriers (smaller spots) and anchors (larger spots) are distinguishable. It is apparent that many gold nanostructures are incomplete or missing in the absence of the descum step. All images are recorded following lift-off (i.e., step (7) in **Fig. 6.1a**).

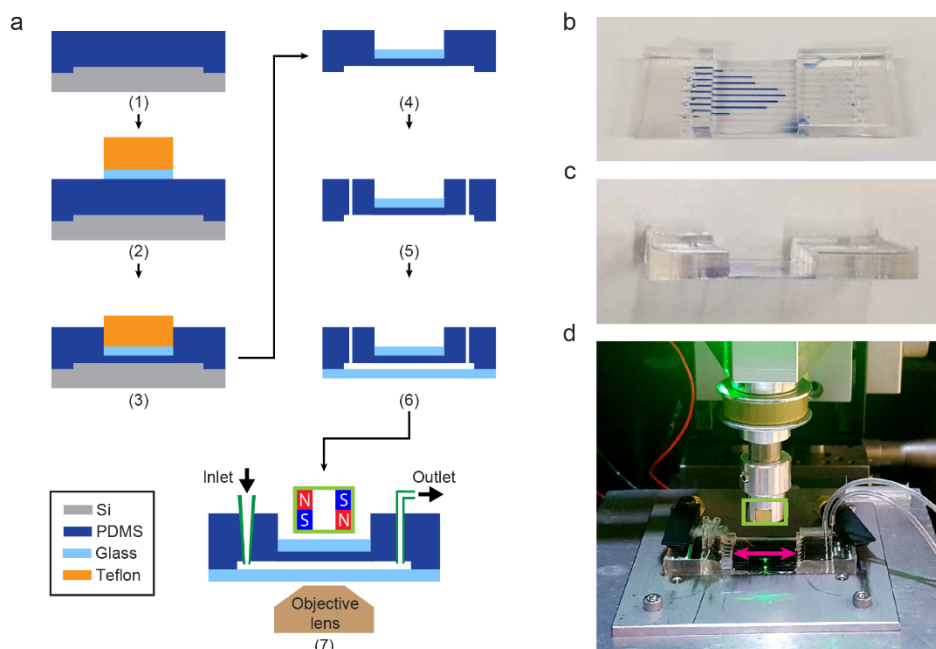


Figure S6.3. Fabrication of a magnetic tweezers-compatible (MTC)-SODA device. (a) Fabrication steps for an MTC-SODA device: (1) PDMS is poured onto a Si mold, as in step (8) in Fig. 6.2. However, a different cross-sectional view, along the length of a microfluidic channel, is shown. Hence, the protrusion of Si mold corresponds to the whole length of a microfluidic channel; (2) after partially curing the PDMS, a smaller coverslip and a Teflon block are positioned at the center; (3) gently pushing the Teflon block downwards deforms the PDMS layer and positions the smaller coverslip at the vicinity of channel; (4) after fully curing the PDMS, only the Teflon block is removed; (5) punching inlet/outlet holes into the thick parts of PDMS; (6) bonding PDMS block with coverslip following corona discharge treatment of both; (7) the assembled device is connected to the inlet/outlet tubing and loaded onto a TIRF microscope combined with magnetic tweezers. A pair of strong magnets (within light green box) can be closely positioned at the vicinity of the fluidic channel embedded in the thin part of PDMS block. Photographs taken from (b) slanted- and (c) side-views of an assembled device (similar to step (6) in panel (a)). From the slanted-view (b), the locations of channels are clearly visible as several channels are partially filled with blue solution. From the side-view (c), the recessed and uniformly thin PDMS layer covered with a smaller coverslip is clearly visible in the central region of the device. (d) A photograph of an MTC-SODA device loaded onto a magnetic tweezers setup (similar to step (7) in panel (a)). The width of the recessed region (indicated with double-sided arrow) was sufficiently wide to allow the approach of a pair of strong magnets (within light green box at center). Hence, successful application of magnetic force was possible.

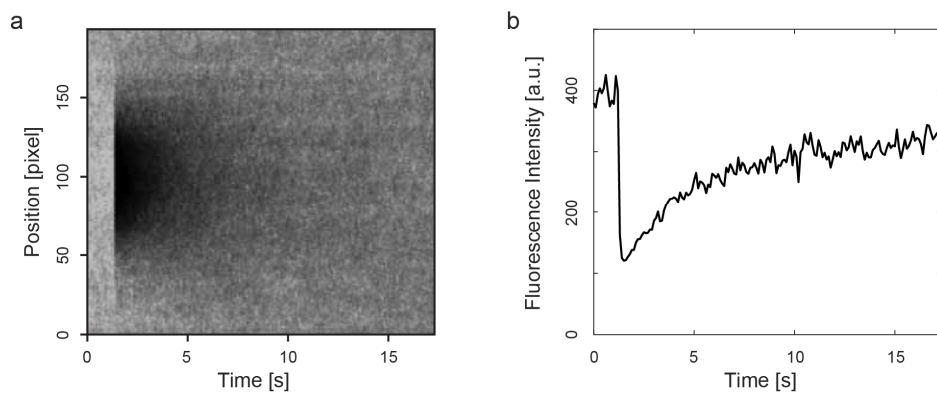


Figure S6.4. Fluorescence recovery after photobleaching (FRAP) on an SLB. (a) A kymograph for FRAP process on an SLB formed on a bare glass coverslip. An intense light pulse was irradiated at ~ 1 s to bleach fluorescently labeled lipid molecules within a spot (black) on an SLB layer. With time, the fluorescence intensity gradually recovers due to the diffusion of non-bleached molecules into the initially bleached region. (b) Fluorescence intensity over time, from the central position of the kymograph shown in panel (a). The dynamics of photobleaching and recovery processes are clearly visible.

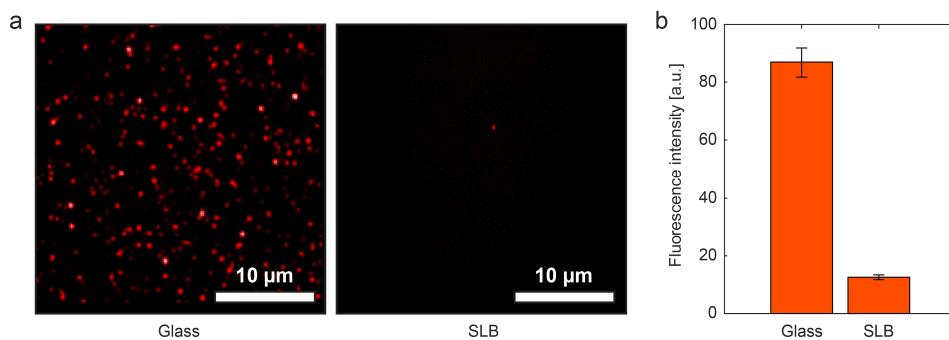


Figure S6.5. Non-specific binding of proteins on non-coated and SLB-coated glass surfaces. (a) Representative fluorescence microscopy images of non-specifically bound, fluorescently labeled proteins. Comparing the two images, it is clear that the SLB-coated surface (image at right) exhibits significantly reduced non-specific binding, relative to the non-coated glass surface (image at left). The protein used in this test is Cy3-labeled anti-HIS IgG, at concentration of 1.5 mg/mL ($\sim 10 \mu\text{M}$) (a kind gift from the Chirlmin Joo lab of the TU Delft). (b) The result of statistical analysis of multiple fluorescence images. The overall fluorescence intensity of each image is obtained by averaging the intensity of all pixels within a fixed region of interest (ROI). The height of each bar is the averaged fluorescence intensity from multiple images, while the error bar denotes the standard deviation ($N = 6$).

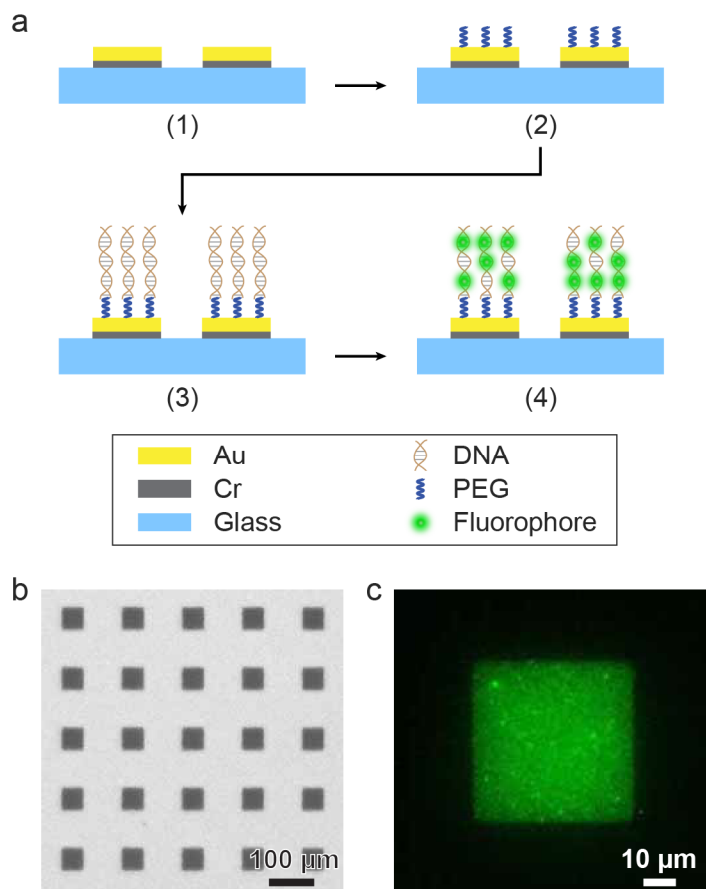


Figure S6.6. Highly selective surface functionalization between gold and glass. The selectivity in the functionalization of gold versus glass is cross-validated by using larger ($50\ \mu\text{m} \times 50\ \mu\text{m}$ square patterns) gold structures, than the submicron structures shown in Fig. 6.3e. (a) Au functionalization scheme: (1) gold patterns are prepared as depicted in Fig. 6.1a; (2) gold surfaces are selectively PEGylated by SH-PEG-COOH (MW 5,000) molecules; (3) DNA molecules (4.6 kbp NH_2 -dsDNA) are covalently bound to PEG by forming peptide bonds; (4) DNA molecules are labeled by intercalating fluorophores (YOYO-1). (b) A brightfield microscopy image showing the prepared gold patterns. Au appears as dark due to its reduced light transmission. (c) A fluorescence microscopy image of a square gold pattern that is selectively functionalized and labeled according to the steps in panel (a), demonstrating the high selectivity in functionalizing Au over glass.

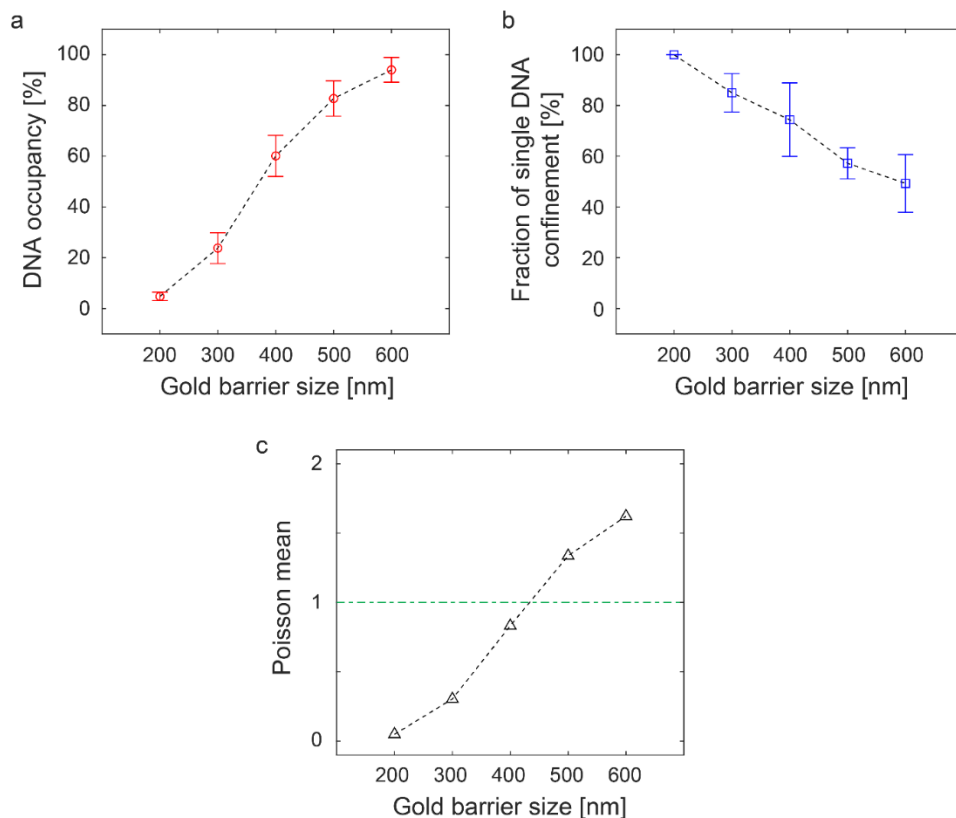


Figure S6.7. Statistics of the number of confined DNA molecules per barrier as a function of barrier size. (a) The DNA occupancy, defined as the probability of trapping at least one DNA molecule per each Au barrier by directional diffusion under weak buffer flow, is plotted as a function of gold barrier size. For the smallest barrier size ($L = 200$ nm), trapped DNA molecules were hardly found. In contrast, for the largest barrier size ($L = 600$ nm), most barriers contain one or more DNA molecules. (b) The fraction of single DNA confinement among all the barriers that confine one or more DNA molecules. The larger barriers have more probability to confine more than one DNA molecules. In panels (a,b), the symbols and error bars denote the average and standard deviation ($N = 168$), respectively. (c) The Poisson mean obtained from the fitting to Poisson distribution (Fig. 6.4d). The barriers with size $L = 400$ nm exhibit the mean closest to one (horizontal dash-dotted green line).

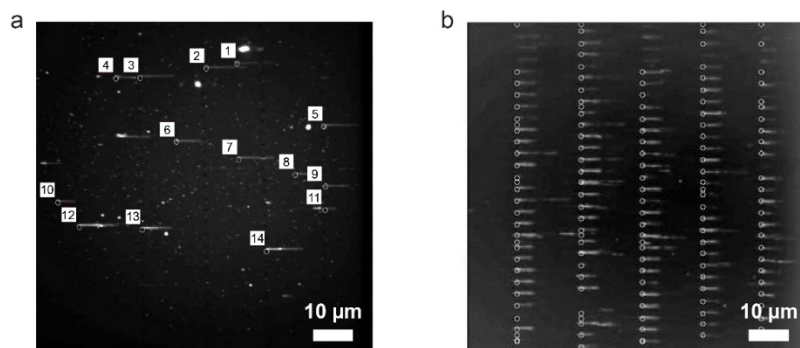


Figure S6.8. Advantages of DNA positioning in a dense array. Fluorescence microscopy images showing the results of different DNA positioning strategies. **(a)** A result from the random binding of DNA molecules, which shows a small number ($N = 14$) of flow-stretched DNA molecules on the surface. Such small number is resulting from using a reduced DNA concentration in buffer, as the random binding with high DNA concentration in buffer often results in overlapping DNA molecules that hinders proper image analysis. The overlaid numbers indicate the manually detected DNA strands in our home-made image analysis routine, while the overlaid white circles indicate the extremities of DNA molecules facing upstream. **(b)** A result from the DNA placement in a SODA device (the same image as shown **Fig. 6.5b**). Within the same field of view used in panel (a) image, it supports an order of magnitude larger number of DNA molecules ($N \sim 100$). The overlaid white circles indicate the automatically detected DNA molecules.

7

Conclusions and Recommendations

The overall achievements of this thesis, in the fields of force and torque spectroscopy with optical torque wrench (OTW) and high-throughput single molecule fluorescence imaging with stretched and oriented DNA arrays (SODA), are described. The use of single-crystal rutile TiO₂ as a newly proposed OTW probe material in this thesis is highly promising for answering diverse questions in biophysics and for applications in other scientific and engineering fields. Furthermore, the use of the SODA microfluidic device is expected to offer opportunities to obtain large single-molecule datasets to derive more statistically robust interpretations. In addition, possible improvements for more practical and efficient implementation of these techniques are discussed. For OTW, the advantages of differently shaped torque probes, possible routes for enhanced cleaving and mass production of torque probes, several alternative methods for the nanofabrication of highly-birefringent particles, and suggestions for the improvement of calibration and setup are discussed. In addition, possible routes to render SODA devices more accessible are presented.

A part of this chapter, 7.2.5. *Highly birefringent nanorods made from tailored metamaterials*, is a collaboration among the following authors: Ying Tang*, **Seungkyu Ha***, Thomas Begou, Julien Lumeau, Belen Solano, Nynke H. Dekker, Aurèle J. L. Adam, and Paul H. Urbach. Another part of this chapter, 7.2.8. *More accessible stretched and oriented DNA arrays*, is a collaboration among the following authors: **Seungkyu Ha**, Humberto Sanchez, Richard Janissen, Theo van Laar, Belen Solano, and Nynke H. Dekker. (*equal contribution)

7.1. Current research outcomes

7.1.1. Single-crystal rutile TiO₂ probes for the optical torque wrench

The capacities of the optical torque wrench (OTW) can be extended by employing single-crystal rutile TiO₂ nanocylinders as a novel probe particle that has been developed and extensively investigated in this thesis. The top-down fabrication protocol for single-crystal rutile TiO₂ developed here provides the means to fabricate TiO₂ nanocylinders with desired sidewall profile (cylinders, cones, and hourglass-shapes) and dimensions (diameter of 100–600 nm and heights of 1–2 μm). The developed surface functionalization approach uses epoxysilane mono-linker (GPDMES) for rapid and robust (high density and uniformity of coating) surface coating. This coating protocol is capable of covalently immobilizing diverse biomolecules while preventing particle aggregation. An improved protocol to fabricate exceptionally thick chromium etch masks has been additionally developed to allow precise control of cylinder dimensions. By integrating these individual developments, the utility of the novel particles in single-molecule studies has been demonstrated by successfully stretching and twisting single DNA molecules tethered to rutile TiO₂ nanocylinders. The advances made in this thesis have successfully overcome the difficulties of precise single-crystal rutile TiO₂ etching and efficient biomolecular coating to its surface for the first time.

To further elucidate the landscape of achievable performance with rutile TiO₂ particles, finite element method (FEM)-based numerical calculations and accurate measurements of differently sized nanocylinders were performed. First, particle dimensions supporting three-dimensional (3D) optical trapping of single-crystal rutile TiO₂ particles were investigated, since their high refractive index causes known difficulties in 3D trapping. Nanocylinders with diameters $< \sim 250$ nm are optically trappable, as demonstrated by both experiments and FEM calculations (for cylinders with aspect ratio range of 2–5, considering the practical limitations of the employed top-down fabrication method). In addition, several advantages of cylindrical torque probes are demonstrated by numerical calculations. The 3D-trappability can be enhanced by reducing light scattering, and all three rotational degrees of freedom (RDOF) can be confined due to the geometry-originated torque components.

For trappable nanocylinder dimensions, characterizations of both the linear and angular optical trapping properties are conducted. The results demonstrate that large forces up to ~ 1 nN range and torques in 1–10 nN·nm range at 1–10 kHz rotation frequencies can be applied, which is also supported by the performed numerical calculations. The angular trapping properties represents an order(s)-of-magnitude improvements compared to the performance of previously devised torque probes (e.g., quartz SiO₂). Such remarkable torque probe performance is possible as rutile TiO₂ possesses the highest birefringence among all naturally occurring crystals, which

permits maximized torque transfer to particles of size only $\sim 1 \mu\text{m}$ (compared to $\sim 30 \mu\text{m}$ for quartz SiO_2 particles, which are impractically large compared to the focal volume of a typical single-beam optical trap).

The application of Allan deviation (AD) analysis on angular dynamics is thoroughly investigated in this thesis for the first time. The use of AD analysis on torque/angle is analogous to the well-established case of AD analysis on force/position, and successfully reports achievable measurement precision and temporal resolution. First, the validity of applying AD analysis to angular dynamics is proven using datasets generated by stochastic simulations of rotational motion. Then, AD analysis is applied to measured datasets from OTW to prove that single-crystal rutile TiO_2 particles exhibit high measurement precisions that corresponds to $\sim 1 \text{ pN}$, $\sim 1 \text{ nm}$, $\sim 1 \text{ pN}\cdot\text{nm}$, and $\sim 1^\circ$ at timescales of (sub)milliseconds. These spatiotemporal resolutions are suitable for the measurement of single biomolecules, as their linear and angular dynamics occur at similar scales. The AD analysis results from OTW data are further compared to those resulting from (electro)magnetic torque tweezers (eMTT). The comparison indicates that OTW exhibits superior precision on short time scales from (sub)milliseconds to $\sim 10 \text{ s}$. However, the eMTT are complementary to OTW in the sense that they provide measurement precision higher than OTW only at longer time scales ($> \sim 10 \text{ s}$). Additionally, the conditions that should be fulfilled to perform a valid AD analysis on data acquired from different types of sensors (photodiodes for OTW versus cameras for eMTT) are discussed in depth, and a set of general recommendations is given to optimize spatiotemporal resolution as a function of particle drag and trapping stiffness. Further, the ability to detect diverse noise components in detail is demonstrated by comparing AD plots of OTW datasets obtained from either stable or noisy environments.

7.1.2. Stretched and oriented DNA arrays

The prototype stretched and oriented DNA array (SODA) devices are designed and fabricated to demonstrate the possibility of configuring a high-throughput single-molecule measurement platform equipped with real-time direct visualization functionality based on fluorescence imaging. A glass coverslip patterned with specifically designed shapes of gold nanostructures and coated with a supported lipid bilayer (SLB) forms the bottom of microfluidic channels. The SLB coating further provides effective passivation to suppress aspecific adhesion of DNA and other biomolecules. The other three sides of the microfluidic channels are provided by PDMS blocks patterned through casting on Si molds. A modified version of PDMS block with a thinner ($100\text{--}200 \mu\text{m}$) central region provides access for strong magnets in a magnetic tweezers setup. This is expected to add a force control functionality to SODA and extend its possible application.

In the aspect of device fabrication, the flexibility of the design process is enhanced by adopting maskless lithography techniques for both microscale and

nanoscale fabrications. The nanoscale features for gold nanostructures are patterned by e-beam lithography, while the micron-scale features for microfluidic channels are patterned by direct laser writing (DLW). As masks are not required for all levels of pattern sizes, modifications of pattern design can be rapidly implemented. During an experiment, the gold nanostructures fabricated prior to SLB formation first physically confine one end of a single DNA strand at V-shaped barriers, and then the DNA molecule is stretched by buffer flow. In a doubly-tethered scheme, the other end of the flow-stretched DNA can be anchored by specific chemical bonds to pentagon-shaped anchors, and its stretching can then be maintained without buffer flow. The dimensions and positions of gold nanostructures are designed in such a way that they permit colinear attachment of DNA molecules and control the tensions of doubly-tethered DNA molecules. Particularly, the size of the gold nanobarriers is optimized to host only one DNA strand per barrier while suppressing the probabilities of zero or multiple DNA confinement.

The proof-of-concept experiments were conducted with Rad51 proteins that have been widely studied, and they play a crucial role in the eukaryotic DNA repair mechanism. It has been previously shown that Rad51 proteins form nucleoprotein filaments that are stable within certain buffer conditions^{1,2}. This behavior is used to demonstrate the capability of the prototype SODA devices, in which tracking and analysis of ~100 DNA strands was possible with home-made image analysis routines. For each DNA strand, its nucleoprotein filament formation dynamics were visualized by a kymograph.

7.2. Suggestions for further development

7.2.1. Utilization of the various shapes of nanoparticle probes

In **Chapter 3**, different possible nanoparticle geometries achievable with the top-down fabrication protocol developed here are shown: cylinders, cones, and hourglass-shapes. Each of these shapes provides different advantages and disadvantages. The dimensions of cylinders can be defined by only two geometrical parameters (diameter and height), and this facilitates the optimization of probe design and the prediction of trapping properties, as demonstrated by the diverse calculated maps of trapping parameters and experimental results presented in **Chapter 4**. Cones may provide a better option to investigate angular dynamics of biomolecules, if selective surface coating is performed on their sharp tips (as shown in **Chapter 3**). When the coated tip is tethered to a biomolecule, the axis of rotation will be coincident with the center of mass of the particle. Then, the interpretation of the observed angular motion of the biomolecule can be more straightforward and precise, as wobbling or precession of the particle will be reduced. However, the yield of successful tethering of biomolecules might decrease due to the smaller surface area of the sharp tips. Also, optimizing the cone dimensions for

desired trapping parameters may not be straightforward, as trapping behavior highly depends on the taper angles, as shown in **Chapter 4**.

Hourglass shapes are expected to bring the axial equilibrium trapping positions (z_{eq} as explained in **Chapter 4**) closer to the focal plane, based on preliminary numerical calculations. In comparison, most of cylinder dimensions have z_{eq} values that are distant from the focal plane (**Chapter 4**). Hence, the end of a cylinder closer to the focal plane will experience tighter trapping compared to the other end. This imbalance might induce larger wobble and precession during torque and angle measurements, particularly for longer cylinders. The hourglass shape might be a solution to this issue, and can also be useful when configuring a dumbbell assay³. Unlike the microspheres used in the conventional dumbbell assays, pulling a rod-shaped particle from its side can tilt it if all of the tethering points, center-of-mass, and z_{eq} of a particle are not colinear. Such tilting is however undesirable, as it may result in a substantial change of trapping stiffness or difficulties in force and torque calibrations. However, there exist several challenges in the use of hourglass-shaped particles. It was observed that they break more easily during the cleaving process due to their thinner waist. In addition, for the use in dumbbell assays, a different method needs to be devised to selectively functionalize the middle of hourglass-shaped particles.

7.2.2. Alternative routes for cleaving single-crystal nanocylinders

A mechanical cleaving process is used to separate the top-down fabricated nanoparticles from the substrates, as shown in **Chapter 3**. However, such process can result in unevenly cleaved facets, as it can be observed in the SEM micrographs in **Chapter 3** and **Chapter 4**. Also, uniform cleaving result with fewer broken particles is dependent on operator skill. Such particle unevenness can result in a non-uniformity of optical trapping behavior, especially for particles with a high refractive index such as TiO₂. For example, the distribution of the measured trapping parameters of rutile TiO₂ nanocylinders (**Chapter 4**) is partially attributed to this geometrical non-uniformity. Another issue of mechanical cleaving is the low yield of cleaved particles. Using SEM, it was observable that a large portion of the cleaved particles were not collected into a buffer solution but adhered to the surfaces of substrates and blades. Therefore, the development of a more advanced method of cleaving is required to guarantee more clean cleaved facets and higher particle collection yield. For example, using a PDMS roller⁴ may increase the uniformity of cleaved facets, and embedding the nanocylinders within an water-soluble polymer scaffold^{5,6} (unlike the PDMS used in Refs. 5, 6) before cleaving might increase the collection yield.

7.2.3. Mass fabrication of nanoparticle probes for OTW

A top-down nanofabrication method is chosen in this thesis for production of nanoparticle probes for OTW because it permits the use of pure single-crystalline

structures and, within these, the realization of cylindrical geometries with precise control over dimensions. In addition, e-beam lithography is used to rapidly produce nanocylinders of different dimensions for comparative studies of their trapping parameters (**Chapter 4**). However, this combination exhibits a lower yield of particle production compared to other approaches based on bottom-up methods or photolithography. As a large number of mass-produced probe particles are generally required for practical use in biological or other applications, possible solutions to increase the particle production yield are discussed here.

If a spherical shape or a smaller birefringence than rutile TiO_2 suffices for a particular application, bottom-up methods based on chemical synthesis can be more practical, e.g., mass production of microspheres made of vaterite CaCO_3 ⁷ or nematic liquid crystal ⁸. For the opposite case, however, top-down approaches are necessary, and there exist techniques with a higher throughput than e-beam lithography. For example, diverse photolithography techniques including a stepper system ⁹, nanosphere lithography ¹⁰, and laser interference lithography ¹¹ have been successfully employed to mass-produce birefringent cylinders made of quartz SiO_2 to use in OTW setups. There are also other lithography techniques not based on photons but suitable for a mass-production, e.g., nanoimprint lithography ¹² and stencil lithography ¹³. Once the cylinder dimensions are optimized for a target application, using one of the abovementioned lithography techniques will facilitate the mass-production of birefringent particles from single-crystal rutile TiO_2 substrates.

7.2.4. Highly birefringent nanoparticles from the substrates of (001) orientation

All of the single-crystal rutile TiO_2 cylinders presented in this thesis are fabricated from substrates with the (100) crystal orientation. However, the (001) crystal orientation has the potential to be used for the fabrication of birefringent nanorods (not designated as cylinders because their cross-sectional shape is more close to a triangle in this approach due to the slanted etch direction, as shown in Ref. 14). For the (100) crystal orientation, the long axis of a nanorod should be vertically aligned with respect to the substrate during fabrication, to eventually allow the optic axis to be perpendicular to the beam propagation direction in an OTW (the stable angular manipulation of a birefringent nanorod becomes possible only under this configuration, as explained in **Chapter 3** and **Chapter 4**). Inversely, for the (001) crystal orientation, the long axis of a nanorod should be horizontally aligned with respect to the substrate to have the same configuration in an optical trap. A fabrication protocol is developed to enable this horizontal alignment of nanorods during fabrication, and a preliminary result is presented here.

Being inspired by the protocol that enabled fabrication of hourglass-shaped rutile TiO_2 particles (**Chapter 3**), the same etching condition is employed to fabricate nanorods that are horizontally aligned with the substrates (**Fig. 7.1a,b**). The etching

condition provides the means to achieve angled etch directions and hence permits to separate horizontal nanorods from a substrate, without using a Faraday cage¹⁴. One of the advantages of this approach is that there exists no limit on the achievable particle height, in contrast to the $\sim 2 \mu\text{m}$ height limit in the case of etching vertical cylinders (**Chapter 3**). This opens up a new possibility to use several crystals other than rutile TiO_2 to achieve maximal torque transfer. For example, as shown in **Chapter 4**, anatase TiO_2 has its optimal height for maximal torque transfer in the range of 3–4 μm , which exceeds the fabrication limit. Moreover, even exotic particle shapes are possible, e.g., alphabet-shaped particles¹⁵. Such asymmetric particle shapes can exhibit peculiar behaviors in an optical trap¹⁶ that might find other interesting applications. The optimization of this etching process or the introduction of an even more directional etching mechanism using a Faraday cage¹⁴ will enable a better controlled shape of nanorods than shown in this preliminary result. This approach also requires mechanical cleaving at the final stage of fabrication to detach the etched particles from a larger supporting structure (as shown in **Fig. 7.1a**), and hence a suitable cleaving method needs to be developed.

7.2.5. Highly birefringent nanorods made from tailored metamaterials

Although single-crystal rutile TiO_2 possesses superior optical properties as an OTW probe among all naturally occurring crystals, such properties are not tunable but fixed by the given crystalline structure. A tailor-made particle with optical properties tuned for each specific application is predicted to further broaden the applicability of OTW, including biophysics research and many other fields. Therefore, an alternative route is explored for obtaining highly birefringent particles from a metamaterial¹⁷ with a subwavelength multi-layer dielectric structure. The preliminary results are presented here.

The design principle of the artificially birefringent metamaterial probe is based on the effective medium theory (EMT)¹⁸. EMT predicts that a set of alternating layers of two different isotropic dielectric materials exhibits an effective birefringence. For this preliminary experiment, the two materials chosen are Nb_2O_5 ($n = 2.26$) and SiO_2 ($n = 1.47$). The multilayer is sputter-deposited on a Si wafer coated with a chromium (Cr) sacrificial layer. The thickness of each layer is 25 nm ($= d(\text{Nb}_2\text{O}_5) = d(\text{SiO}_2)$), and the total multilayer thickness is 300 nm. The filling ratio, defined as the relative ratio between the thicknesses of the two materials ($= d(\text{Nb}_2\text{O}_5)/(d(\text{Nb}_2\text{O}_5) + d(\text{SiO}_2))$), is set to be 0.5, and EMT predicts that this multilayer has an effective index $n \approx 1.8$ and a birefringence $|\Delta n| \approx 0.16$. The multilayer film is patterned by e-beam lithography to obtain particle dimensions with a width of 300 nm and a height of 1200 nm, and then dry-etched to a depth of 300 nm using a protocol similar to the one presented in **Chapter 3**. Hence, the resulting particles have a square cross-section (**Fig. 7.1c**). The particles were released from the Cr sacrificial layer by soaking the wafer in Cr etchant,

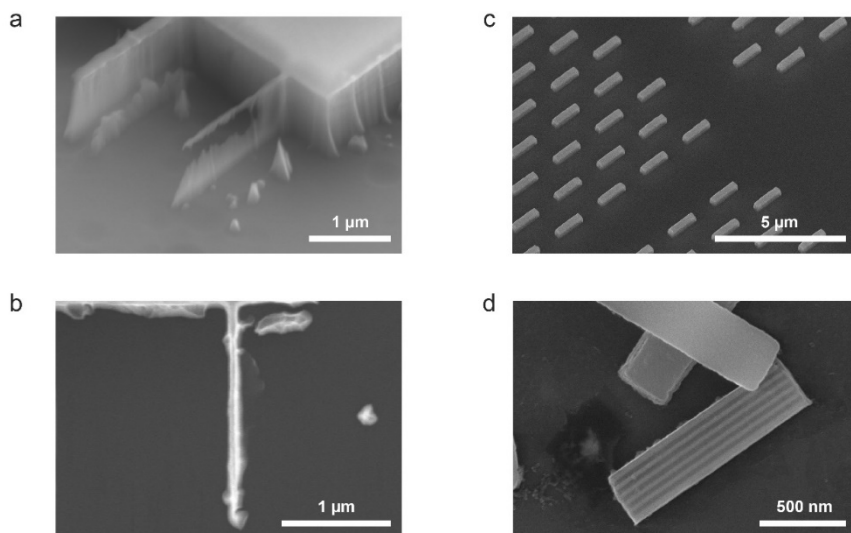


Figure 7.1. Preliminary results from the alternative fabrication routes for highly-birefringent nanoparticles for OTW. **(a,b)** SEM micrographs (taken before Cr etch mask removal) of the nanorod structures fabricated from a single-crystal rutile TiO_2 substrates with the (001) crystal orientation. The slanted view (a) clearly shows the separation between the nanorod (diameter of 100 nm) at center and the etched bottom of the substrate. The separation is less complete nearby the large supporting structure shown in the top part of the image. An extended etch time, a differently shaped (e.g., triangle as shown in Ref. 19) supporting structure, or a smaller nanorod diameter is expected to complete such separation. The nanorod pattern with a thicker diameter (200 nm) visible in the top-left corner is not separated from the substrate. The top view (b) shows the dimensions of the same nanorod shown in panel (a) (diameter of 100 nm and length of 2 μm). One end of the nanorod is connected to the large supporting structure shown in the top part of the image. **(c,d)** SEM micrographs (taken after Cr etch mask removal) of the metamaterial nanorods fabricated from $\text{Nb}_2\text{O}_5/\text{SiO}_2$ multilayer substrates. The slanted view (c) shows the etched metamaterial particles in an array on top of the Cr sacrificial layer. The top view (d) clearly shows the multilayer structure in the side wall of a metamaterial nanorod released after the removal of the sacrificial layer.

and then the Cr etchant solution containing the dispersed nanorods is diluted by a few hundred times with DI water. The collected particles were inspected by SEM and the multilayer structure was clearly identified (**Fig. 7.1d**).

The particles were measured in an OTW and resulted in ~ 11.1 nN·nm torque at ~ 3.2 kHz rotation frequency (at ~ 92 mW laser power). However, further characterization of their trapping properties as a function of particle dimensions and filling ratio is required. The correct estimation of their drag coefficients is also important, as these metamaterial particles have a square cross-section. A surface functionalization strategy and/or an alternative sacrificial layer material may be necessary to be further devised for biological applications. In addition, this approach is expected to provide more geometrically uniform particles as mechanical cleaving is not involved. This is also suitable for a mass-production of birefringent particles due to the availability of a larger substrate size (a 4-inch Si wafer was used in this experiment, compared to the typical 10 mm \times 10 mm substrate size for single-crystal rutile TiO_2).

Importantly, these particles were stable in aqueous environments, unlike the highly-birefringent calcite CaCO_3 crystal which has very similar optical properties ($n = 1.56$, $|\Delta n| = 0.16$). It is also of interest to explore metamaterial probes with other material combinations than $\text{Nb}_2\text{O}_5/\text{SiO}_2$ and different structural configurations of metamaterial than planar multilayers. Overall, the potential of metamaterial nanoparticles is demonstrated, and it is expected to expand the library of materials for optical torque transducers.

7.2.6. Position and tilt calibration of nanocylinders in an OTW

The position calibration of probe particles in an OTW is performed using back focal plane interferometry²⁰, which reports on the three-dimensional coordinates (x , y , and z) of a trapped particle. This method is well established and utilized in this thesis for both polystyrene microspheres and rutile TiO_2 nanocylinders (**Chapter 3** and **Chapter 4**). However, the cylindrical geometry allows tilted orientations, unlike the case of microsphere in which tilting does not change geometrical orientations. As trapped cylinders can wobble without rotation and exhibit precession under rotation, more accurate measurement and understanding of cylinder trapping dynamics will be possible if two orthogonal tilting angles (around the x - and y -axes when the laser beam propagates along the z -axis) can be precisely measured simultaneously in addition to the three-dimensional coordinates²¹.

It is noteworthy that the abovementioned polymer scaffold method^{5,6} can also be used to provide vertically aligned and immobilized cylinders as a reference for position calibration. In case of dielectric microspheres, a calibration reference can be easily prepared by attaching them to a flow cell surface. However, the same approach was not applicable for TiO_2 nanocylinders, because they lie down when attached to a flow cell and their long axes are perpendicular to the laser beam propagation direction. This is opposite to the actual trapping configuration, in which their long axes are parallel with the beam propagation direction. For the purpose of providing a calibration reference, index-matching polymers such as MY133 polymer²² are highly promising.

7.2.7. Solid-state implementation of the optical torque wrench

The OTW setup used in this thesis is based on bulk optical components. Therefore, it requires a tremendous amount of careful alignment, considering polarization effects and coupling between many different optical elements. Furthermore, as the laser beam path is in ambient air, detection is very sensitive to acoustic vibrations in the surrounding environment. The large number of optical components also decreases the stability of the overall OTW setup compared to much simpler magnetic tweezers, as shown by Allan deviation analysis in **Chapter 5**.

A solid-state OTW setup is highly promising to solve these issues. In general, the use of waveguide-based optical trapping has been proven to be more stable than

bulk optics setups due to the simpler configuration and the beam path confined in the solid-state waveguides²³⁻²⁶. Additionally, it has been shown that such waveguide-trapped particles can be rotated²⁷, and that minute torque can be measured and applied based on spin angular momentum using waveguide-based photonic circuits²⁸. Altogether, an integrated-photonics version of OTW is highly feasible, and this solid-state approach is also much more practical than bulk optics for multiplexing, as suggested in Ref. 23. It might even be coupled with SODA devices to permit dynamic control and measurement of force and torque in them.

7.2.8. More accessible stretched and oriented DNA arrays

The potential of SODA as a high-throughput single-molecule platform has been demonstrated in this thesis. Each SODA device is in principle considered to be disposable because it is difficult to perfectly clean organic residues adhered to surfaces, which would affect the reproducibility in the next round of experiments. However, the e-beam lithography patterning step for gold nanostructures is a bottleneck for the mass-production of SODA devices due to its slow patterning speed and the need for access to cleanroom facilities. Therefore, it is desirable to develop a method to mass-produce nanoscale gold patterns for SODA devices. Reducing the dependence on cleanroom facilities as much as possible is also an important factor to render SODA devices more broadly accessible to scientists, including ones who do not use cleanroom facilities on a daily basis. For example, PDMS blocks with microfluidic channels can be easily replicated at any time once the Si mold is fabricated in the cleanroom with an optimized design, and the Si mold can be used for years.

Stencil lithography is a probable solution, as it can replicate nanoscale features with high spatial resolution¹³. However, the fabrication of a stencil is rather complicated, and the stencil needs to be regenerated regularly by etching the deposited metals (chromium or titanium as an adhesion layer and gold for attaching biomolecules). Hence, the stencil might be damaged after several cycles of metal etching. Also, at least a vacuum machine is required for the deposition of metals.

A more viable solution could be micro-contact printing (mCP) to pattern an array of patches consisting of linker molecules (silanes or proteins such as antibodies and streptavidin) or gold nanoparticles. It has been previously shown that protein patches can be reproducibly patterned with diameters of 200–600 nm²⁹, which represents the desired length scale for attaching DNA molecules for SODA (**Chapter 6**). Moreover, this process relies on a patterned Si mold only to reproduce patterned PDMS stamps for mCP²⁹, which is almost the same as producing the PDMS microchannels for SODA, in the aspect of the required materials and equipment. Hence, the application of mCP for DNA attachment in SODA devices is highly promising.

7.3. References

1. van Mameren, J., Modesti, M., Kanaar, R., Wyman, C., Peterman, E. J. G. & Wuite, G. J. L. Counting RAD51 proteins disassembling from nucleoprotein filaments under tension. *Nature* **457**, 745 (2008).
2. Lee, M., Lipfert, J., Sanchez, H., Wyman, C. & Dekker, N. H. Structural and torsional properties of the RAD51-dsDNA nucleoprotein filament. *Nucleic Acids Research* **41**, 7023-7030 (2013).
3. Capitanio, M. & Pavone, Francesco S. Interrogating biology with force: single molecule high-resolution measurements with optical tweezers. *Biophysical Journal* **105**, 1293-1303 (2013).
4. Pevzner, A. et al. Knocking down highly-ordered large-scale nanowire arrays. *Nano letters* **10**, 1202-1208 (2010).
5. Park, H., Seo, K. & Crozier, K. B. Adding colors to polydimethylsiloxane by embedding vertical silicon nanowires. *Applied Physics Letters* **101**, 193107 (2012).
6. Go, G.-H. et al. Real-time monitoring and visualization of the multi-dimensional motion of an anisotropic nanoparticle. *Scientific Reports* **7**, 44167 (2017).
7. Arita, Y. et al. Rotational dynamics and heating of trapped nanovaterite particles. *ACS Nano* **10**, 11505-11510 (2016).
8. Ramaiya, A., Roy, B., Bugiel, M. & Schäffer, E. Kinesin rotates unidirectionally and generates torque while walking on microtubules. *Proceedings of the National Academy of Sciences* **114**, 10894 (2017).
9. Gutiérrez-Medina, B., Andreasson, J. O. L., Greenleaf, W. J., LaPorta, A. & Block, S. M. Chapter 15 - an optical apparatus for rotation and trapping. In *Methods in Enzymology* (ed Walter, N. G.) **475**, 377-404 (Academic Press, 2010).
10. Li, P.-C., Chang, J.-C., La Porta, A. & Edward, T. Y. Fabrication of birefringent nanocylinders for single-molecule force and torque measurement. *Nanotechnology* **25**, 235304 (2014).
11. Santybayeva, Z. et al. Fabrication of quartz microcylinders by laser interference lithography for angular optical tweezers. *Journal of Micro/Nanolithography, MEMS, and MOEMS* **15**, 034507 (2016).
12. Chen, H., Zhang, Q. & Chou, S. Y. Patterning of light-extraction nanostructures on sapphire substrates using nanoimprint and ICP etching with different masking materials. *Nanotechnology* **26**, 085302 (2015).
13. Vazquez-Mena, O., Sannomiya, T., Villanueva, L. G., Voros, J. & Brugger, J. Metallic nanodot arrays by stencil lithography for plasmonic biosensing applications. *ACS Nano* **5**, 844-853 (2011).
14. Burek, M. J. et al. Free-standing mechanical and photonic nanostructures in single-crystal diamond. *Nano letters* **12**, 6084-6089 (2012).
15. Hernandez, C. J. & Mason, T. G. Colloidal alphabet soup: monodisperse dispersions of shape-designed lithoparticles. *The Journal of Physical Chemistry C* **111**, 4477-4480 (2007).
16. Simpson, S. H. Inhomogeneous and anisotropic particles in optical traps: physical behaviour and applications. *Journal of Quantitative Spectroscopy and Radiative Transfer* **146**, 81-99 (2014).
17. Zheludev, N. I. & Kivshar, Y. S. From metamaterials to metadevices. *Nature Materials* **11**, 917 (2012).
18. Zhang, R. Z. & Zhang, Z. M. Validity of effective medium theory in multilayered hyperbolic materials. *Journal of Quantitative Spectroscopy and Radiative Transfer* **197**, 132-140 (2017).
19. Tasdemir, Z., Peric, O., Sacchetto, D., Fantner, G. E., Leblebici, Y. & Alaca, B. E. Monolithic fabrication of silicon nanowires bridging thick silicon structures. *IEEE Nanotechnology Express* **1**, 2-5 (2015).
20. Tolić-Nørrelykke, S. F., Schäffer, E., Howard, J., Pavone, F. S., Jülicher, F. & Flyvbjerg, H. Calibration of optical tweezers with positional detection in the back focal plane. *Review of Scientific Instruments* **77**, 103101 (2006).
21. Griebshammer, M. & Rohrbach, A. 5D-Tracking of a nanorod in a focused laser beam - a theoretical concept. *Optics Express* **22**, 6114-6132 (2014).
22. Kim, D. N. H., Kim, K. T., Kim, C., Teitell, M. A. & Zangle, T. A. Soft lithography fabrication of index-matched microfluidic devices for reducing artifacts in fluorescence and quantitative phase imaging. *Microfluidics and Nanofluidics* **22**, 2 (2017).
23. Soltani, M. et al. Nanophotonic trapping for precise manipulation of biomolecular arrays. *Nature Nanotechnology* **9**, nnano-2014 (2014).
24. Helle, Ø. I., Ahluwalia, B. S. & Hellesø, O. G. Optical transport, lifting and trapping of micro-particles by planar waveguides. *Optics Express* **23**, 6601-6612 (2015).
25. Ahluwalia, B. S., Helle, Ø. I. & Hellesø, O. G. Rib waveguides for trapping and transport of particles. *Optics Express* **24**, 4477-4487 (2016).
26. Ye, F., Soltani, M., Inman, J. T. & Wang, M. D. Tunable nanophotonic array traps with enhanced force and stability. *Optics Express* **25**, 7907-7918 (2017).

27. Kang, P., Serey, X., Chen, Y.-F. & Erickson, D. Angular orientation of nanorods using nanophotonic tweezers. *Nano letters* **12**, 6400-6407 (2012).
28. He, L., Li, H. & Li, M. Optomechanical measurement of photon spin angular momentum and optical torque in integrated photonic devices. *Science Advances* **2**, e1600485 (2016).
29. De Vlamincq, I. et al. Highly parallel magnetic tweezers by targeted DNA tethering. *Nano letters* **11**, 5489-5493 (2011).

Summary

Developments in single-molecule instrumentation for biophysical studies have enabled in-depth investigation of the physical behavior of biomolecules and cellular machineries that are workhorses for core cellular processes such as transcription, replication, translation, homologous recombination, and DNA repair. However, there remain myriads of unanswered biological questions, and the continuous development of new techniques is required to be equipped with proper tools to investigate biology at the nanoscale. With more advanced tools, it is expected that many crucial working mechanisms of life will be revealed earlier and eventually benefit healthcare and medicine. This thesis primarily presents technological advances in the force/torque spectroscopy on individual biomolecules, and secondarily in the high-throughput measurement of biomolecules based on fluorescence microscopy.

First, force/torque spectroscopy is suitable for answering questions regarding sophisticated mechanical properties and rapid dynamics of single biomolecules such as nucleic acids and proteins. There are many different such force/torque spectroscopy techniques, including optical tweezers, magnetic tweezers, and atomic force microscopy. In this thesis, optical tweezers have been chosen for further development because they currently represent the technique that allows the fastest and most precise measurement of minute forces and torques on individual biomolecules.

Control of light's polarization and, ensuingly, of optical angular momentum transfer provides an unrivaled method for precisely applying and measuring torque. Optical tweezers with such an extended torque application functionality are typically denoted as optical torque wrenches (OTW). With the possibility for accurately controlled application and high-precision measurement of both force and torque, the OTW has great potential to reveal a refined picture of the mechanical behaviors of biomolecules. Torque cannot be measured in conventional optical force spectroscopy, and hence there are still many domains to be explored with this technique. For example, it is known that accumulated torque plays an important role in cellular processes involving transcription and replication, but as yet investigations on such mechanism is not a routine compared to those on force-related mechanisms.

There have been continuous improvements to optical tweezers and OTW over the last decades, in terms of both optical setup configuration and optical trapping probe design. As the most widely used kind of optical tweezers is the single-beam optical tweezers, whose complex hardware is already quite sophisticated, this thesis focuses on the use of a novel probe material rather than upgrading the spectroscopic component of the setup. The suggested material is single-crystal rutile TiO₂ nanoparticles, and their use as optical probes is explored in depth.

This thesis thoroughly covers the whole aspects from preparation to utilization of single-crystal rutile TiO_2 nanoparticles. This material had not been utilized as an optical probe in prior to this thesis partly due to the known difficulties in etching and surface coating of TiO_2 . These challenges have been overcome by the developments of a tunable top-down nanofabrication protocol and an optimized surface functionalization and bioconjugation strategy in this thesis. Another challenge in its utilization had been the difficulties in stable three-dimensional optical trapping due to its high refractive index. This issue has been addressed in this thesis by employing cylindrical particle geometry and optimizing its dimensions for both tight optical trapping and maximal optical torque transfer. This optimization result has been verified by both experiments in OTW and finite element method (FEM)-based numerical calculations. With these developments, the range of applicable torque and rotation frequency have been expanded by order(s)-of-magnitude, and this is expected to enable the full characterization of powerful biological rotary motors such as bacterial flagellar motors. Simultaneously, its maximal torque transfer efficiency at small particle size permits substantially improved precision and temporal resolution of torque and angle measurements, as proven by Allan deviation analysis, which are suitable for investigation of the subtle dynamics of diverse biomolecules. At the same time, its high refractive index permits improved performance as a force probe as well, exhibiting a larger maximal applicable force and enhanced spatiotemporal resolution. Therefore, a single-crystal rutile TiO_2 nanocylinder is unique in the sense that it functions as a joint force and torque transducer that integrates the advantages of the previously developed transducer particles and outperforms them.

Second, the development of a high-throughput fluorescence microscopy technique that complements force/torque spectroscopy is presented. Although OTW offers precise quantification of force and torque (and their conjugate variables, position and angle) at high spatiotemporal resolution, it is limited in throughput, as it measures only single biomolecules at a time. Similarly, several other high-performance mechanical spectroscopy techniques such as optical tweezers and atomic force microscopy also exhibit low throughput. However, for certain biological questions, observing large datasets to obtain overall statistical behavior becomes the priority rather than in-depth investigation of individual molecular behavior. The single-molecule instrumentation with high-throughput capacity has been pioneered by multiplexed magnetic (torque) tweezers, acoustic force spectroscopy, and centrifugal force microscopy. Although possessing a multiplexing capacity, they are in principle indirectly probe biomolecules. However, specifically for the investigation of protein-nucleic acid interaction dynamics, direct visualization of differently labeled biomolecules based on fluorescence is helpful to obtain more straightforward and unbiased spatial information.

The DNA nanocurtain technique combines both high-throughput and direct-visualization capacities. The movement of a large number of labeled biomolecules can be tracked in real time using fluorescence. It is a highly accessible platform due to its straightforward coupling to fluorescence microscopy and much less complicated experimental configurations. It has proven its potential by investigating many important biophysical processes such as homologous recombination and chromosome organization. This thesis introduces preliminary experiments to develop an optimized DNA nanocurtain platform, which is denoted as stretched and oriented DNA arrays (SODA). Specifically, it is designed for large eukaryotic protein complexes such as the replisome.

Chapter 1 gives a general introduction to the field of biophysics research and single-molecule instrumentation, while **Chapter 2** provides an overview of the methods (optics, nanofabrication, and surface functionalization) used in the following chapters. In **Chapter 3**, a novel top-down nanofabrication protocol is presented, in which single-crystal rutile TiO_2 nanoparticles are plasma-etched with fluorine-based reactive species. With this protocol, a large number of nanoparticles can be fabricated with high geometrical uniformity in a desired shape and dimension. A surface functionalization strategy using epoxysilane linkers is also presented, and its successful use is demonstrated through bioconjugation with diverse biomolecules and maintenance of monodispersity in physiological buffers. Combining both developments, a successful demonstration of stretching and supercoiling of single DNA strands was possible in OTW.

Chapter 4 shows the first in-depth investigations of both linear and angular optical trapping behaviors of single-crystal rutile TiO_2 nanocylinders in OTW. By fabricating and measuring multiple batches of differently sized nanocylinders, the ranges of diameter and height that support tight optical trapping by a single focus beam were found. Also, the applicability of large torque (1-10 nN·nm) and rotation frequency (1-10 kHz) in aqueous environments with only moderate laser power (< 100 mW) was demonstrated. In addition, an improved fabrication method for chromium etch mask formation is briefly introduced, which allows a better control of sidewall angles across a wide range of nanocylinder dimensions. At the same time, using Allan deviation (AD) analysis, it has been shown that the OTW-measurable physical quantities from such nanocylinders achieve high measurement precision suitable for biomolecular measurements (~ 1 pN force, ~ 1 pN·nm torque, ~ 1 nm position, and $\sim 1^\circ$ angle) at (sub)milliseconds temporal resolution. All of these results could be predicted by FEM-based numerical calculations of electromagnetism and hydrodynamics, which are useful in the design of probes with tailored physical properties.

In **Chapter 5**, the theoretical background for and experimental proof of the applicability of AD analysis to rotational motion are presented for the first time and

discussed in depth. Also, the performance of OTW with single-crystal rutile TiO₂ nanocylinders is compared to that of (electro)magnetic torque tweezers with magnetic microspheres. OTW substantially outperforms its magnetic counterparts in terms of spatiotemporal resolution, as long as drift in the setup is not dominant. The chapter concludes with a set of informative advice on selection of particle size and trapping stiffness in single-molecule experiments, and their effect on achievable measurement precision and temporal resolution.

In **Chapter 6**, the development of the SODA microfluidic device is introduced. It presents protocols to fabricate gold nanostructures to confine and anchor DNA molecules, microfluidic channels made of transparent and flexible polymer block (PDMS), and final microfluidic devices. A surface functionalization strategy is also shown for selective binding of DNA molecules in a predefined array. The size of the gold nanobarrriers is optimized to increase the probability of tethering only single DNA molecules, which is crucial for observing protein-DNA interactions without interference from other DNA molecules. As a proof-of-concept for the SODA device, the loading of DNA-binding proteins (Rad51) onto single DNA strands is demonstrated. A modified SODA device that can be integrated with magnetic tweezers is also presented, which is expected to permit precise force control in addition to the high-throughput direct visualization capability.

Chapter 7 presents the overall summary of this thesis and further improvement points for a more straightforward, efficient, and wide-spread use of both OTW probes and the SODA microfluidic device. For OTW, potential uses of differently shaped birefringent particles, possible fabrication methods for an improved cleaving of nanocylinders and for a mass-production of birefringent nanoparticles, and recommendations for improved implementations of OTW setup are discussed. In addition, several alternative routes towards top-down fabrication of highly-birefringent particles, either from crystals with different optic axis orientation or multi-layered dielectric metamaterials, are introduced with the preliminary results. For SODA, potential routes to the fabrication of more easily replicable devices are suggested.

Samenvatting

Het is al mogelijk om met enkele molecuul instrumenten diepgaand biofysisch onderzoek te doen naar het fysische gedrag van biomoleculen en cellulaire machines, die de motor zijn achter belangrijke cellulaire processen zoals transcriptie, replicatie, translatie, homologe recombinatie en DNA reparatie. Er blijven echter talloze biologische vragen onbeantwoord; een voortdurende ontwikkeling van nieuwe technieken en juiste instrumenten is vereist om de biologie op de nanoschaal verder te kunnen onderzoeken. Meer geavanceerde instrumenten leiden tot een snellere onthulling van veel cruciale biologische werkingsmechanismen en zo uiteindelijk tot een verbetering van de gezondheidszorg en de geneeskunde. Dit proefschrift beschrijft in de eerste plaats de technologische vooruitgang in de kracht-/krachtmoment-spectroscopie van individuele biomoleculen en in de tweede plaats de fluorescentie-metingen aan vele biomoleculen tegelijkertijd.

Kracht-/krachtmomentspectroscopie is geschikt voor het beantwoorden van vragen betreffende geavanceerde mechanische eigenschappen en snelle dynamica van individuele biomoleculen, zoals nucleïnezuren en eiwitten. Er zijn verschillende kracht-/krachtmomentinstrumenten, waaronder het optisch pincet, het magnetisch pincet en de atoomkrachtmicroscop. In dit proefschrift is het optisch pincet gekozen voor verdere ontwikkeling, omdat deze techniek momenteel de techniek is, die de snelste en meest nauwkeurige metingen aan kleine krachten en momenten op individuele biomoleculen mogelijk maakt.

Controle over de polarisatie van licht, en daarmee over de overdracht van optische impuls, biedt een ongeëvenaarde methode voor het nauwkeurig uitoefenen en meten van krachtmoment. Het optisch pincet uitgebreid met een dergelijk krachtmoment-functionaliteit wordt gewoonlijk aangeduid als optische moment-sleutel. Met de mogelijkheid tot het nauwkeurig uitoefenen en meten van zowel kracht als krachtmoment heeft de optische momentsleutel een groot potentieel om een verfijnd beeld te geven van het mechanische gedrag van biomoleculen. Krachtmoment kan niet worden gemeten in de conventionele optische krachtspectroscopie en zodoende is er nog steeds een groot niet-verkend terrein voor deze techniek. Het is bijvoorbeeld bekend dat opgebouwd krachtmoment een belangrijke rol speelt in cellulaire processen rondom transcriptie en replicatie, maar tot nu toe is onderzoek naar dergelijke mechanismen nog verre van een routinekwestie vergeleken met het onderzoek naar krachtgerelateerde mechanismen.

De afgelopen decennia zijn er continu verbeteringen geweest aan het optisch pincet en de optische momentsleutel, zowel wat betreft de configuratie van de optische opstelling als het ontwerp van de optische probe. Aangezien de meest gebruikte implementatie een optisch pincet met enkele laserstraal is, waarvan de hardware al behoorlijk gecompliceerd is, zal dit proefschrift zich richten op het gebruik van een nieuw probemateriaal en niet op het verbeteren van spectroscopische componenten van de opstelling. Het voorgestelde materiaal is monokristallijn rutiel TiO_2 en de toepassing hiervan als probe wordt grondig onderzocht.

Dit proefschrift bestrijkt alle aspecten van de voorbereiding tot het gebruik van monokristallijn rutiel TiO_2 nanodeeltjes. Dit materiaal was voorafgaand aan dit proefschrift nog niet eerder als optische probe gebruikt, gedeeltelijk vanwege de bekende moeilijkheden bij het etsen en coaten van TiO_2 . Deze uitdagingen zijn in dit proefschrift overwonnen door de ontwikkeling van een top-down nanofabricatie-protocol en een geoptimaliseerde oppervlaktefunctionalisatie en bioconjugatie-strategie. Een andere uitdaging in het gebruik van TiO_2 is de moeilijkheid bij het stabiel vasthouden van TiO_2 in een optische val in alle drie dimensies. Dit komt door de hoge brekingsindex van TiO_2 . Dit probleem wordt in dit proefschrift opgelost door gebruik te maken van een cilindrische deeltjesgeometrie en van afmetingen die geoptimaliseerd zijn voor zowel het krachtig optisch vasthouden als een maximale overdracht van optisch krachtmoment. Dit optimale resultaat is geverifieerd door zowel experimenten in de optische momentsleutel als numerieke berekeningen gebaseerd op de eindige-elementmethode. Met deze ontwikkelingen is het bereik van het uit te oefenen krachtmoment en de rotatiefrequentie uitgebreid met orde(n) van grootte. Naar verwachting zal dit de volledige karakterisering van krachtige biologische rotatiemotoren, zoals de bacteriële flagellaire motor, mogelijk maken. Tegelijkertijd biedt zijn maximale efficiëntie van krachtmomentoverdracht bij kleine deeltjesgrootte een aanzienlijk verbeterde precisie en tijdresolutie in krachtmoment- en hoek-metingen, zoals bewezen door Allan deviatie-analyse die gebruikt wordt voor het onderzoeken van subtiele dynamica van verscheidene biomoleculen. Tegelijkertijd maakt zijn hoge brekingsindex ook een verbeterde prestatie van de krachtprobe mogelijk waardoor een grotere maximale kracht kan worden uitgeoefend met een verbeterde spatio-temporele resolutie. Nanocilinders van monokristallijn rutiel TiO_2 zijn dus uniek in de zin dat ze zowel grote krachten als grote krachtmomenten kunnen overdragen. Daarmee integreren ze de voordelen van eerder ontwikkelde overdragers en presteren ze zelfs nog beter.

Vervolgens wordt de ontwikkeling van een fluorescentiemicroscopietechniek met een hoge doorloop gepresenteerd. Deze microscopietechniek kan de kracht-/krachtmomentspectroscopie aanvullen. Hoewel de optische momentsleutel een precieze kwantificering biedt van kracht en krachtmoment (en hun geconjugeerde variabelen, positie en hoek) bij hoge spatio-temporele resolutie, is het beperkt door de lage doorloop, omdat het slechte één enkel biomolecuul tegelijkertijd meet. Hetzelfde geldt voor verschillende andere hoogwaardige mechanische spectroscopietechnieken, zoals het optisch pincet en de atoomkrachtmicroscopie. Bepaalde biologische vragen kunnen alleen beantwoord worden na het meten en analyseren van grote datasets, om zo een algeheel statistisch gedrag diepgaand te kunnen onderzoeken met behoud van individueel moleculair gedrag. De enkele-molecuulinstrumentatie met hoge doorloop is eerst ontwikkeld in veelvoudige magnetische (krachtmoment-)pincetten, akoestische krachtspectroscopie en centrifugale krachtmicroscopie. Hoewel ze een multiplexcapaciteit hebben, onderzoeken ze de biomoleculen in principe indirect. Specifiek voor het onderzoeken van de dynamiek van eiwit-nucleïnezuurinteracties is directe visualisatie van verschillend gelabelde biomoleculen op basis van fluorescentie echter nuttig om meer eenvoudige en onbevooroordeelde ruimtelijke informatie te verkrijgen.

De DNA-gordijn-techniek combineert een hoge doorloop met een directe visualisatiecapaciteit. De beweging van een groot aantal gelabelde biomoleculen kan in real-time worden gevolgd met behulp van fluorescentie. Het is een zeer toegankelijk platform

vanwege zijn ongecompliceerde koppeling aan fluorescentiemicroscopie en veel minder gecompliceerde experimentele configuraties. Het heeft zijn potentieel bewezen in onderzoek naar vele belangrijke biofysische processen zoals homologe recombinitie en de organisatie van chromosomen. Dit proefschrift laat de voorlopige resultaten zien om een geoptimaliseerd DNA-gordijnplatform te ontwikkelen. Dit platform wordt aangeduid als “stretched and oriented DNA arrays” (SODA, uitgerekte en georiënteerde DNA rijen). Deze techniek is specifiek ontworpen voor grote eukaryote eiwitcomplexen zoals het replisoom.

Hoofdstuk 1 geeft een algemene inleiding op het gebied van biofysisch onderzoek en enkel-molecuulinstrumentatie, terwijl **Hoofdstuk 2** een overzicht geeft van de methoden (optica, nanofabricage en oppervlaktefunctionalisatie) die in de volgende hoofdstukken worden gebruikt. In **Hoofdstuk 3** wordt een nieuw top-down nanofabricatieprotocol gepresenteerd, waarin monokristallijn rutiel TiO_2 nanodeeltjes geëst worden met een plasma van reactieve fluorhoudende soorten. Met dit protocol kan een groot aantal nanodeeltjes worden gefabriceerd met een hoge geometrische uniformiteit in een gewenste vorm en afmeting. Een strategie voor oppervlakte-functionaliserings met behulp van epoxysilaan-linkers wordt ook gepresenteerd en het succesvolle gebruik ervan wordt aangetoond door bioconjugatie met diverse biomoleculen en behoud van monodispersiteit in fysiologische buffers. Door beide ontwikkelingen te combineren was het mogelijk om het strekken en opwinden van enkele DNA-strengen in de optische momentsleutel succesvol te demonstreren.

Hoofdstuk 4 toont het eerste diepgaande onderzoek naar het lineaire en hoekgerelateerde gedrag van monokristallijn rutiel TiO_2 nanocilinders gevangen door een optische momentsleutel. Door het fabriceren en meten van meerdere partijen nanocilinders van verschillende grootte, wordt het bereik van diameter en hoogte gevonden waarbij het deeltje krachtig gevangen wordt door enkele gefocuste laserstraal. Ook wordt de toepasbaarheid van een groot krachtmoment (1–10 nN·nm) en hoge rotatiefrequentie (1–10 kHz) in waterige omgevingen bij slechts een schappelijk laser vermogen (< 100 mW) aangetoond. Bovendien wordt er kort een verbeterde fabricagemethode voor de vorming van chrometmaskers geïntroduceerd, die een betere controle over zijwandhoeken mogelijk maakt voor een groot bereik aan nanocilinderafmetingen. Tegelijkertijd is met behulp van Allan deviatieanalyse aangetoond dat de fysieke grootheden van deze nanocilinders, die gemeten kunnen worden met de optische momentsleutel, een hoge meetprecisie bereiken die geschikt is voor biomoleculaire metingen (~1 pN kracht, ~1 pN·nm krachtmoment, ~1 nm positie en ~1° hoek) bij (sub) milliseconden tijdsresolutie. Deze resultaten kunnen worden voorspeld door middel van eindige-elementenanalyse gebaseerde numerieke berekeningen van elektromagnetisme en hydrodynamica, die nuttig zijn bij het ontwerp van probes met aangepaste fysieke eigenschappen.

In **Hoofdstuk 5** worden de theoretische achtergrond en het experimentele bewijs van de toepasbaarheid van Allan deviatie-analyse op de rotatiebeweging voor het eerst gepresenteerd en diepgaand besproken. Ook wordt de prestatie van de optische momentsleutel met monokristallijn rutiel TiO_2 nanocilinders vergeleken met die van het (elektro-)magnetische krachtmomentpincet met magnetische micro-bolletjes. De optische momentsleutel presteert aanzienlijk beter dan zijn magnetische tegenhangers wat betreft de spatio-temporele resolutie, zolang de drift in de opstelling niet dominant is. Het hoofdstuk wordt afgesloten met een reeks informatieve adviezen over de selectie van

deeltjesgrootte en stijfheid van de optische val tijdens experimenten met één enkel molecuul en het effect van die deeltjes op de haalbare meetnauwkeurigheid en tijdsolutie.

In **Hoofdstuk 6** wordt de ontwikkeling van het SODA microfluidische apparaat geïntroduceerd. Het hoofdstuk presenteert protocollen voor het fabriceren van gouden nanostructuren om DNA-moleculen te beperken en te verankeren, microfluidische kanalen gemaakt van transparant en flexibel polymeerblok (PDMS) en uiteindelijke microfluidische apparaten. Een strategie voor oppervlaktefunctionalisatie wordt ook getoond voor selectieve binding van DNA-moleculen in een vooraf gedefinieerde locatie. De grootte van de gouden nanobarrières is geoptimaliseerd om de kans op het binden van één enkele DNA-molecuul te vergroten, wat cruciaal is voor het waarnemen van eiwit-DNA-interacties zonder interferentie van andere DNA-moleculen. Als een proof-of-concept voor het SODA-apparaat wordt het laden van DNA-bindende eiwitten (Rad51) op afzonderlijke DNA-strengen gedemonstreerd. Een gemodificeerd SODA-apparaat, dat kan worden geïntegreerd met een magnetische pincet, wordt ook gepresenteerd, waarvan wordt verwacht dat dit een nauwkeurige krachtrekking mogelijk maakt naast de direct visualisatie met hoge doorvoer.

Hoofdstuk 7 presenteert de algehele samenvatting van dit proefschrift en verdere verbeterpunten voor een meer eenduidig, efficiënt en wijdverbreid gebruik van zowel optische momentsleutel-probes als het SODA microfluidische apparaat. Voor de optische momentsleutel worden mogelijke toepassingen van dubbelbrekende deeltjes met verschillende vormen besproken. Verder worden mogelijke fabricagemethoden besproken voor een verbeterde splitsing van nanocilinders en voor de massaproductie van dubbelbrekende nanodeeltjes. Ook worden er aanbevelingen gegeven voor verbeterde implementaties van de optische momentsleutel-opstelling. Daarnaast worden er verschillende andere manieren voor het top-down fabriceren van sterk dubbelbrekende deeltjes geïntroduceerd met de bijbehorende voorlopige resultaten. De deeltjes worden dan gefabriceerd uit kristallen met verschillende optische as-oriëntatie of uit diëlektrische metamaterialen bestaande uit meerdere lagen. Voor SODA worden mogelijke manieren voorgesteld voor het fabriceren van apparaten die gemakkelijker te repliceren zijn.

Curriculum Vitae

Seungkyu Ha

- 2012-2018 **Ph.D.**
Department of Bionanoscience, Kavli Institute of Nanoscience,
Faculty of Applied Sciences,
Delft University of Technology, the Netherlands
Supervisor: Prof. dr. Nynke H. Dekker
- 2008-2012 **Research Scientist**
Nanophotonics Research Center,
Korea Institute of Science and Technology, Korea
- 2006-2008 **M.Sc.**
Department of Electrical Engineering and Computer Science,
Seoul National University, Korea
Supervisor: Prof. dr. Namkyoo Park
- 2002-2006 **B.Sc.**
Department of Electrical Engineering,
Seoul National University, Korea

List of Publications

S. Ha*, Y. Tang*, M. M. van Oene, R. Janissen, R. M. Dries, B. Solano, A. J. L. Adam, and N. H. Dekker, "Enhanced linear and angular optical trapping using single-crystal rutile TiO₂ nanocylinders", *Submitted* (2018). (*equal contribution)

M. M. van Oene*, **S. Ha***, T. Jager, M. Lee, F. Pedaci, J. Lipfert, and N. H. Dekker, "Quantifying the precision of single-molecule torque and twist measurements using Allan variance", *Biophysical Journal*, 114(8), 1970-1979 (2018). (*equal contribution)

S. Ha, R. Janissen, Y. Y. Ussembayev, M. M. van Oene, and N. H. Dekker, "Tunable top-down fabrication and functional surface coating of single-crystal titanium dioxide nanostructures and nanoparticles", *Nanoscale*, 8(20), 10739-10748 (2016).

P. Moon, J. D. Lee, **S. Ha**, E. H. Lee, W. J. Choi, J. D. Song, J. S. Kim, and L. S. Dang, "The effect of post-growth thermal annealing on the emission spectra of GaAs/AlGaAs quantum dots grown by droplet epitaxy", *Physica Status Solidi Rapid Research Letters*, 6(11), 445-447 (2012).

J. Y. Lee, S. F. Ahmed, M. H. Park, **S. Ha**, J. K. Park, J. H. Yun, S. J. Ahn, K. R. Lee, W. J. Choi, M. W. Moon, and C. W. Yang, "Self-assembled Cu(In,Ga)Se₂ nanocrystals formed by Ar ion beam irradiation", *Solar Energy Materials and Solar Cells*, 105, 119-124 (2012).

S. Ha, J. D. Song, D. Y. Ko, S. Y. Kim, E. H. Lee, and I. K. Han, "High-power 745-nm laser diode utilizing InP/InGaP quantum structures grown by using migration enhanced epitaxy", *Journal of the Korean Physical Society*, 59(5), 3089-3092 (2011).

S. Ha, J. D. Song, S. Y. Kim, S. Bounouar, L. S. Dang, J. S. Kim, and J. I. Lee, "Optical characterization of the excitonic states in low-density droplet GaAs quantum dots for single photon sources", *Journal of the Korean Physical Society*, 58(5), 1330-1333 (2011).

C. J. Yang, S. S. Lee, K. W. Shin, S. W. Oh, J. S. Park, C. Z. Kim, W. K. Park, **S. Ha**, W. J. Choi, and E. J. Yoon, "Growth of Si-doped GaInP on Ge-on-Si substrates and its photoluminescence characteristics", *Applied Physics Letters*, 99(9), 091904 (2011).

J. S. Kim, **S. Ha**, C. J. Yang, J. Y. Lee, S. H. Park, W. J. Choi, and E. J. Yoon, "Study of multi-stacked InAs quantum dot infrared photodetectors grown by metal organic chemical vapor deposition", *Journal of the Korean Vacuum Society*, 19(3), 217-223 (2010).



Casimir PhD Series 2018-37

ISBN 978-90-8593-367-0